## DISCLAIMER

# Device- and System-Level Thermal Packaging for Electric-Drive Technologies Final Technical Report

DATE OF REPORT: 5/15/2025

FEDERAL AGENCY: U.S. Department of Energy

AWARD NUMBER: DE-EE0008708

PROJECT TITLE: Device- and System-Level Thermal Packaging for Electric-Drive Technologies

PARTNERS: National Renewable Energy Laboratory (NREL), Oak Ridge National Laboratory (ORNL), SUNY Polytechnic Institute


| PRINCIPAL INVESTIGATOR(S): | | |
|---|---|---|
| Yogendra Joshi<br>yogendra.joshi@me.gatech.edu | Samuel Graham<br>sam.graham@me.gatech.edu | Satish Kumar<br>satish.kumar@me.gatech.edu |

## Acknowledgement:

This material is based upon work supported by the Department of Energy under Award Number EE0008708

## Disclaimer:

## Table of Contents:

## Executive Summary:

This project aimed to research, develop, and test electric traction drive system technology for use in vehicle applications that are capable of meeting the targets set by the Department of Energy Vehicle Technologies Office. The project is categorized into three major thrusts: Bonding interfaces for packaging, thermal management of electric vehicle (EV) power inverters, and electric motor thermal management.
Device- and System-Level Thermal Packaging for Electric-Drive Technologies project aimed to develop, analyze, and validate transformative approaches in thermal management and packaging for power electronics and electric motor systems, with the ultimate goal of enhancing power density, efficiency, and reliability in electrified transportation platforms.

The project objectives were:

**Objective 1:** To explore novel thermal management architectures using additively manufactured (AM) and traditionally fabricated metal foams for advanced inverter cooling, including both single-phase and two-phase flow configurations.

**Objective 2:** To design, fabricate, and validate an integrated in-slot heat exchanger that enables simultaneous slot and end-winding cooling for high-speed, high-power-density electric traction motors, compatible with mass-manufacturable geometries.

**Objective 3:** To develop advanced substrate bonding and metallization techniques, including transient liquid phase (TLP) bonding and printed copper-graphene hybrid conductors, to reduce thermal resistance and improve the reliability of high-temperature power modules.

### Comparison of Accomplishments to Goals and Objectives:

This program consisted of eleven phases carried out over a five-year period. An overview of key milestones contained within each phase is detailed below in Figure 1.

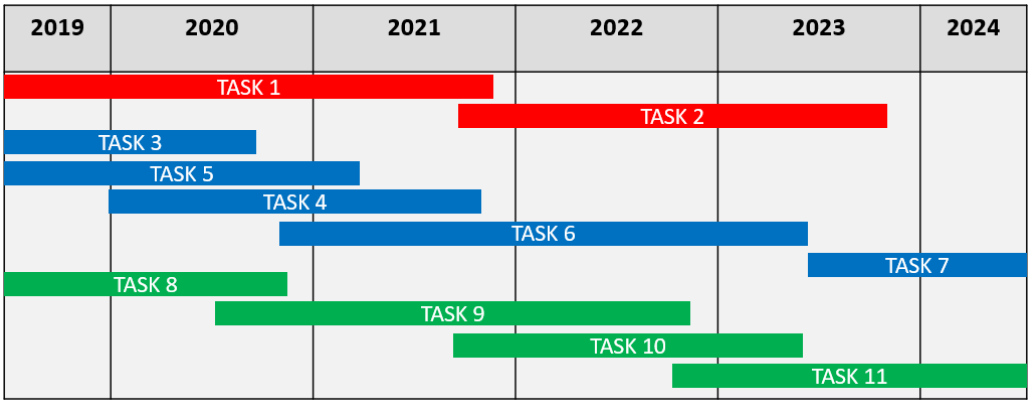


**Figure 1:** Overview of key milestones

## Accomplishments

### Bonding Interfaces for Packaging

In CY2020, a transient liquid phase (TLP) bonding technique was developed to directly bond copper substrates to AlSiC heatsinks, eliminating the need for Direct Bonded Copper (DBC) and integrating a streamlined substrate-to-cold plate assembly, enhancing performance and extending lifetime by at least 16 times, with interfacial adhesion strength around 80% and resistance to shear stress. Al coupons were successfully bonded to AlSiC using the Cu-Al TLP technique in CY2021, with Scanning electron microscope (SEM) and Energy-dispersive X-ray spectroscopy (EDX) confirming strong, defect-free bonds and no significant intermetallic phase formation where 25 μm Cu foil fully diffuses through the Al metal and into the Al-356 in the AlSiC coupon. In CY2022, EDX spectral results for the AlN-AlSiC and Al-SiC assemblies showed less than 1% atomic concentration of Cu. A computational model accurately predicted intermetallic compound formation during TLP bonding, showing dwell time's strong effect on bond interface compounds. In CY2023, a new additive manufacturing process was developed for printing conductive Cu nanoplatelets on AlN substrates, maintaining AlN's dielectric properties. The conductor's ampacity reached $390 \times 10^6$ A/m², and the copper-graphene conductor demonstrated thermal stability up to 400°C, with low resistance at 250°C for 140 hours.

### Thermal Management of EV Power Inverters:

In CY2020, experimental and numerical electric motor thermal management techniques were developed using additively manufactured (AM) metal foams, jet impingement, micro pin fin arrays, and integrated vapor chamber technologies. The microscale pin fin array also demonstrated superior single-phase heat removal, achieving a heat flux of 580 W/cm². In CY2021, a vapor chamber was fabricated using 200-micron sintered copper particles and sealed with arc welding. A silicon microgap cooler, enhanced with pin fins for embedded power electronics cooling, demonstrated over 1 kW/cm² dissipation while maintaining temperatures below 90°C with single-phase subcooled HFE 7200. Simulations of a representative power module were conducted, and flow boiling in microchannels was numerically evaluated to compare alternative geometries with a baseline straight microchannel. In CY2022, the performance of a novel package that uses a dielectric fluid as the cooling fluid for wide-bandgap (WBG) devices to maintain junction temperature below 200ºC with a heat flux maximum of 1 kW/cm2 has been investigated experimentally and numerically. Using high porosity 10 PPI and 100 PPI metal foams around a porosity of 0.9 for jet impingement cooling of power electronics has been numerically investigated in CY2023.

### Electric Motor Thermal Management:

Lumped Parameter Thermal Network (LPTN) offers much faster computation than finite element analysis (FEA) or computational fluid dynamics/heat transfer (CFD/HT) but lacks a full temperature map of motor parts. While a complete map isn't needed in the early design stages, accurately predicting hot spots is crucial. It is demonstrated in CY2020 that LPTN can predict high-temperature areas having a maximum relative error 2.1% with respect to FEA and 3.6% with respect to experimental data and can replace FEA or CFD/HT in iterative designs. In CY2021, a new end-winding cooling design was fabricated and tested at NREL using a Nissan Leaf electric

motor as the testbed. The design reduced external end-winding temperatures by over 35% and improved them by up to 15°C. A CFD/HT model calculated heat transfer coefficients and the LPTN was updated with an end-winding channel equivalent resistor network. The LPTN model, calibrated against experimental data, showed a maximum error of ~1°C. In CY2022, in-slot liquid cooling heat exchangers with integrated microchannels were optimized for end-winding cooling, showing a 28% increase in heat transfer efficiency (4080 W/m²K) compared to the baseline (3144 W/m²K). Additionally, a thermal modeling framework was developed to analyze motor cooling solutions at a multiscale level. In CY2023, experimentally validated component-level and motor-level models showed that the proposed heat exchanger (HX) design significantly improved thermal performance, enhancing the cooling of windings and end windings. The design increased coolant axial flow and contact length with the windings, resulting in a 30.5% reduction in total conduction resistance and a 33% reduction in convective resistance compared to the baseline. This improvement would enable the motor to operate with up to 24% higher winding root mean square (RMS) current density per slot, increasing power density while staying within the NEMA Class F insulation temperature limit of 155°C.

## 1. Interdiffusion and Formation of Intermetallic Compounds in Power Electronics Substrate Joints Fabricated By Transient Liquid Phase Bonding

### Background

Recent advancements in powertrain electrification have resulted in the need to enhance their power conversion capabilities and the need for efficient thermal management. Compared to traditional silicon-based electronic devices, wide band gap (WBG) devices such as silicon carbide (SiC) and gallium nitride (GaN) offer higher switching frequency capability, larger achievable power density, and high operating temperatures. Power electronic inverter modules within hybrid or electric vehicles usually consist of semiconductor devices, direct bonded copper (DBC) substrates, heat spreaders, and heat sinks bonded together using solders (die attach and substrate attach) and thermal interface materials (TIM). These bond materials are widely employed due to their low process temperatures (~220℃), ease of assembly, versatility, and low cost [98]. However, these materials often give rise to localized constraints in effectively dissipating heat from the semiconductor device to the heat sink, posing a challenge to efficient thermal management.

An alternative to conventional substrate-attach solders, transient liquid phase (TLP) bonding techniques have been shown to produce joints with remelting temperatures higher than their original process temperatures. The reliability of the Cu-Al bond formed is dependent on the percentage composition of the copper-aluminum constituents, the process temperature, bond time, and applied pressure. The resulting interfacial diffusion of Cu and Al molecules leads to the nucleation of the Cu-Al composite bond and intermetallic compounds (IMCs), which possess mechanical, electrical, and thermal properties that differ from pure Al and Cu. An intermetallic compound is a distinct chemical compound that emerges between two or more separate metallic elements, characterized by a well-defined crystal structure and composition.The formation of intermetallic compounds at the AlN-AlSiC interface may aid in the adhesion of the TLP bond; however, excessive IMC growth could lead to bond degradation and may result in cracks or

delamination. The microstructure and composition of the bonded materials were analyzed via field-emission scanning electron microscopy (FE-SEM), energy-dispersive X-ray spectroscopy (EDS), and X-ray diffraction (XRD).

This research task centers on the systematic investigation conducted to fabricate and characterize the bonds formed between AlSiC and metal heat spreaders composed of Cu and Al, as illustrated in Figure 2. The primary focus lies in analyzing the bond connections established within thermally conductive power electronics materials when coupled with AlN-AlSiC substrates. In this research task, a diverse array of advanced characterization techniques was employed to comprehensively analyze the structure and composition of the bonded interface materials. The chart presented in Table 1 provides a succinct overview of the specific material properties assessed, the desired results, and the corresponding characterization methodologies utilized in the investigation.

These analyses offer insight into the structure and behavior of the interface layer formed by TLP bonding and provide an understanding of the potential applications of TLP bonding in the fabrication of other mechanical and power electronics components.

**Table 1:** Material properties and characterization techniques

| Property/Result | Characterization Technique |
|---|---|
| Microstructure | Scanning Electron Microscopy (SEM) |
| Composition Analysis | Energy-dispersive X-ray Spectroscopy (EDS)<br>X-ray Diffraction (XRD) |
| Defects | C-Mode Scanning Acoustic Microscopy (C-SAM) |
| Thickness | SEM, XRD |

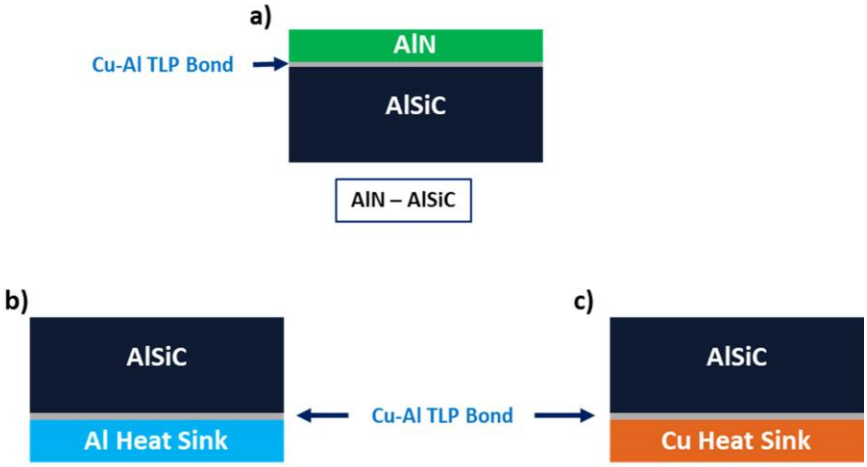


**Figure 2:** Schematic drawings of component assembly stacks studied: (a) Al-AlSiC, (b) Cu-AlSiC, and (c) AlN-AlSiC. The boxes represent the sample structure fabricated in this study.

## Method

The fabrication of AlN-AlSiC samples employs a 1:4 ratio of Cu and Al foils between an AlN ceramic substrate and an AlSiC heat sink, as illustrated in Figure 3. The AlSiC plates procured from CPS Technologies (MA-US) were composed of SiC particles within an Al 356 matrix, which contained around 7% SiC by weight. Sintered AlN dielectric ceramic with an average roughness, Ra of 0.4-0.5 µm was obtained from Accuratus (NJ, US). and precision-cut into square dimensions using a dicing saw. Cu and Al coupons with purity exceeding 98% and measuring 2 mm in thickness were sourced from American Elements and bonded to AlSiC. All samples were machined to a size of 25 mm x 25 mm.

The AlN and AlSiC coupons were laser cut and then carefully polished to ensure flat and even surfaces. Additionally, the bonding structure depicted in Figure 4 underwent an optimization process through iterative experiments. This optimization involved the strategic placement of bolts and spacers, ensuring an even distribution of pressure and maintaining proper alignment. These efforts were instrumental in achieving consistent and uniform bonds, effectively mitigating misalignment issues in the bonding process.

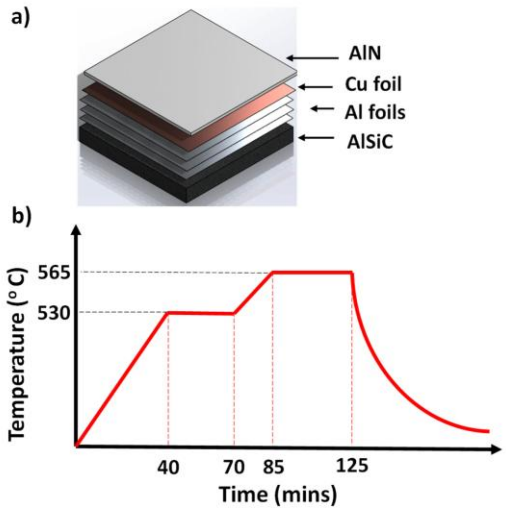


**Figure 3:** a) Assembly stack showing the sequence of the bonded sample layers b) TLP process temperature profile.

The bonding process involves placing one 0.25µm thick Cu foil (99.9% purity, American Elements, USA) and two 50 µm thick Al foils (99% purity, American Elements, USA) carefully between an AlSiC plate with a thickness of 5 mm and the designated material X, which could consist of AlN, Cu, or Al coupons as shown in Figure 3 and Figure 2. The layers are assembled in a steel and graphite rig and bonded according to the stack configuration and heating profile illustrated in Figure 3. To eliminate contaminants and improve interfacial bonding, the material

layers were immersed in 25% hydrochloric acid (HCl) solution at room temperature and rinsed with deionized (DI) water and isopropanol to minimize the formation of oxides. The layers were then stacked in a graphite rig and held under a clamping force of 2 kN to provide uniform pressure distribution and aid in diffusion.

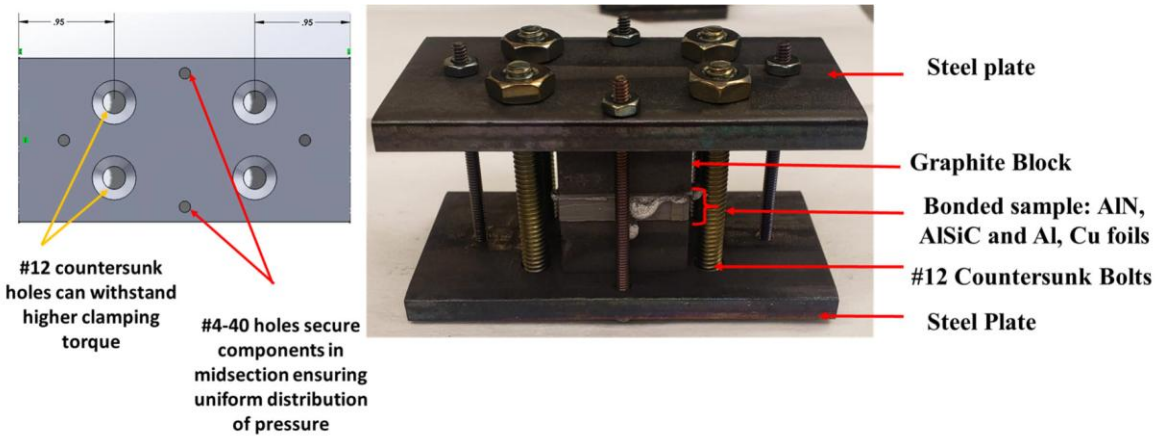


**Figure 4:** Bonding structure composed of steel and graphite plates designed for transient liquid phase bonding of Cu/Al.

The bonding structure containing the bond materials was transferred to a Thermolyne high-temperature glass tube furnace (Model 59300, Barnstead/Thermolyne Co., USA) and held under vacuum to approximately 20 µTorr, or 0.0026 Pa of pressure. The furnace was programmed to heat the samples according to the temperature profile shown in Figure 3 (b). A stepwise profile is used to control the formation of molten Al in stages as Cu diffuses through the foil layers, limiting the amount of melted Al lost through leakage from the rig. To prepare for the metallographic examination, the samples were cross-sectioned using electrical discharge machining, mounted in epoxy resin, ground with a series of SiC papers up to 4,000 grit (3-µm average particle size), and then polished to a fine finish using 1-µm diamond suspension followed by 0.05-µm colloidal silica suspension. A typical bonded sample is depicted in Figure 5.

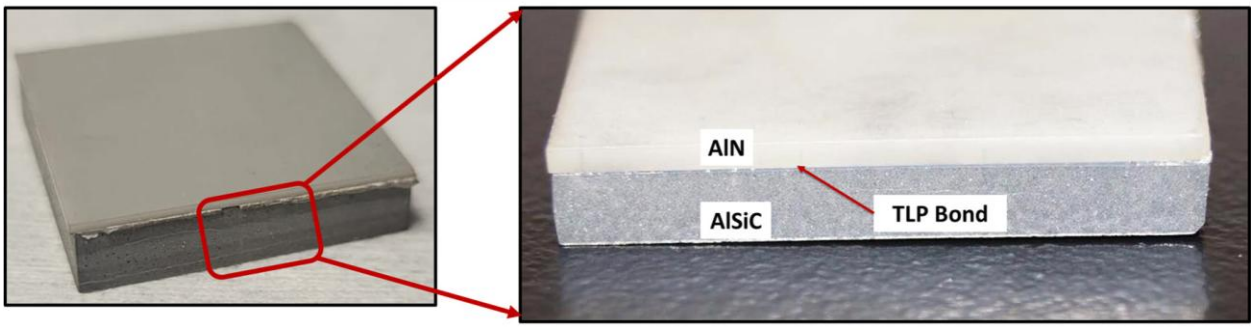


**Figure 5:** AlN dielectric ceramic bonded to AlSiC heat sink using copper-aluminum transient liquid phase bonding.

To assess the microstructure and composition of the bonds, the cross-sectioned samples were examined using a Zeiss Ultra 60 FE-SEM equipped with an Oxford Silicon Drift EDS detector.

The EDS analysis was performed using the embedded Aztec software to investigate the atomic composition of elements present within the interface layer. The test was operated at 10 kV with a working distance of 9 mm and a count rate of 10000−20000 counts/s. Microscopic images and EDS elemental data were obtained along the bonded interface at various locations. Typical SEM and EDS images of the cross-sectioned bonded samples are shown in Figure 6.

Researchers at the National Renewable Energy Laboratory (NREL) conducted Confocal Scanning Acoustic Microscopy (C-SAM) analysis of bonded samples using a Sonoscan Gen-6 C-Mode Microscope. This non-destructive technique utilizes ultrasound waves within the frequency range of 5 megahertz (MHz) to 230 MHz to identify defects by detecting variations in acoustic impedance. Samples were immersed in deionized water and subjected to ultrasound waves from a transducer. The reflected signals were transformed into intensity values by the Sonolytics software and translated into grayscale tones. These images provided insights into the characteristics of the interlayer, allowing the assessment of bonded interfaces, defects, and structural features.

The crystalline structure was analyzed via XRD to study the intermetallic phases formed between TLP-bonded material layers. A Malvern Panalytical Empyrean platform with a copper anode was used for the XRD analysis. The relationship between the wavelength of the incident X-rays produced by the source, angle of incidence, and crystal lattice spacing is known as Bragg's Law. Identification of Cu-Al intermetallic phases was executed by matching the resulting patterns to the built-in Joint Committee on Powder Diffraction Standards database software on the machine. These results were further compared with those of EDS. XRD analyses were conducted along the interfaces of all the samples to identify the compounds present. In each case, an XRD experiment was first performed on the AlSiC (bottom) surface and then on the top surface of AlN, Cu, or Al to determine a standard reference pattern for each of the known elements and compounds. This was done to enable the identification and elimination of these compounds. Next, XRD tests were carried out along the cross-sectioned surfaces of the different samples. Intermetallic phases were determined by first identifying the standard peaks from the XRD patterns previously obtained. Because the interface region consists of a small surface area (approximately 50 × 25 μm), the diffraction experiment was performed slowly over 12 hours for each sample, with the detector rotating through an angle of approximately 15° per hour in the Bragg–Brentano geometry.

**Results**

The SEM image of the AlN-AlSiC interface can be observed in Figure 6a. The findings illustrate a consistent cross-sectional profile and indicate the formation of a uniform bond between AlN and AlSiC. A unique aspect of the Cu-Al interlayer formed between AlN and AlSiC is the presence of SiC particles within the bond, as observed in Figure 6a. This indicates that the Cu in the TLP bond interacted with the AlSiC plate, melting the top layer of the Al-356 matrix and releasing SiC particles, which migrate into the bond to form a new metal matrix compound as it solidifies. It was determined that the average bond thickness measured 150 μm.

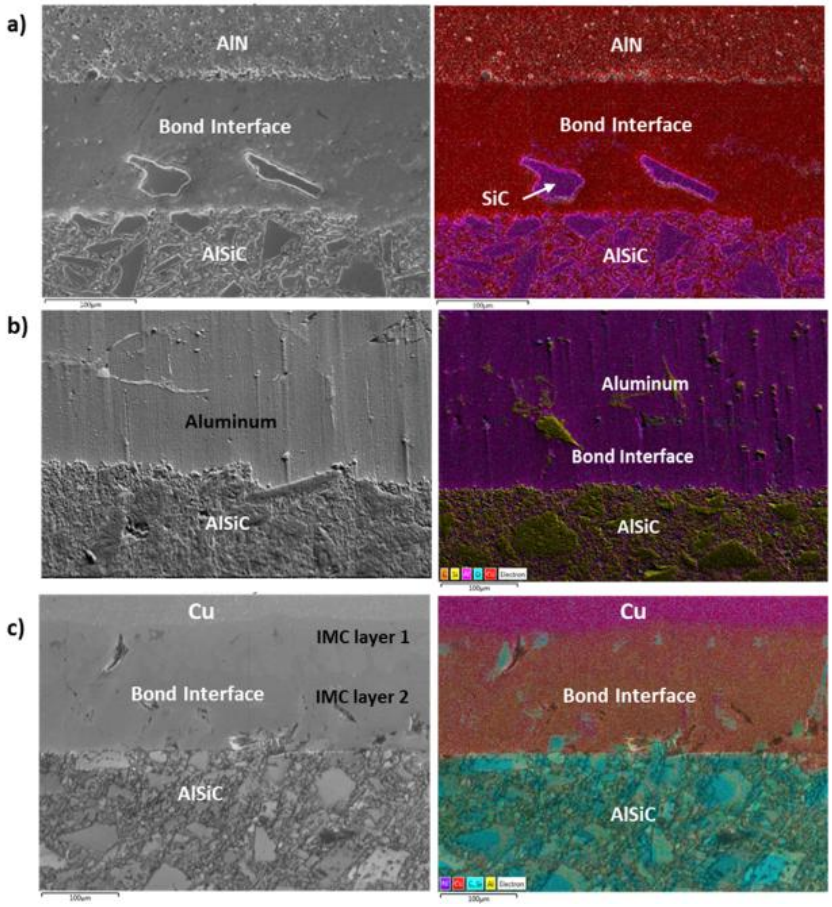


**Figure 6:** SEM (left) and EDS (right) images showing bonded interface along the cross sections of (a) AlN-AlSiC, (b) Al-AlSiC, and (c) Cu-AlSiC samples.

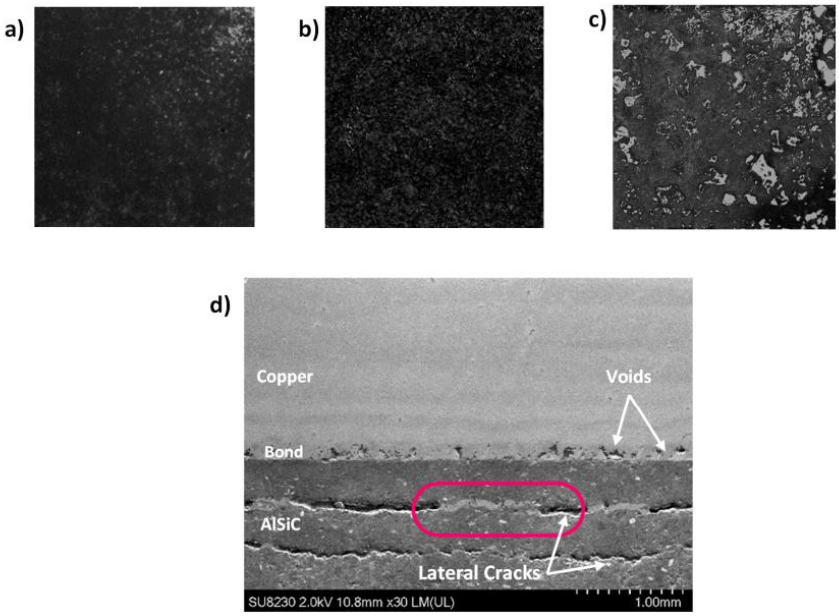


**Figure 7:** C-SAM images of interface between the TLP-bonded (a) AlN-AlSiC, (b) Al-AlSiC, and (c) Cu-AlSiC samples. (d) Kirkendall voids exhibited along with the interface of the Cu-AlSiC sample and lateral cracks along the length of the AlSiC plate.

Aluminum coupons were successfully bonded to AlSiC plates using the Cu-Al TLP bonding technique. C-SAM imaging revealed the Al-AlSiC bond interface to have a low void composition (Figure 7b), which is corroborated by the SEM image of the cross-sectioned sample in Figure 6b, showing no bond line defects. The Al-AlSiC assembly stack differs from the AlN-AlSiC samples in that, while the latter has an observable bond layer with a thickness of about 150 µm on average, in the case of Al-AlSiC, the bond is marked by a distinct interface between the Al metal and the AlSiC matrix without an identifiable interlayer width. This signifies that the Cu in the bond from the 25-µm foil completely diffuses through the Al metal and into the Al-356 in the AlSiC coupon, bonding the two without forming a significant intermetallic phase. The EDS analysis corroborates this conclusion.

The bond formed between a 2-mm Cu coupon and 5-mm AlSiC plate was peculiar in the sense that while a significant section of it possessed the qualities of a uniform bond—even diffusion between layers, interspersed SiC particles, and little to no discontinuity—three new occurrences were observed. First, the C-SAM images showed lighter contrast regions than the results for the interface between AlN-AlSiC and Al-AlSiC samples, possibly indicating a higher void composition (Figure 7); second, the cross-section along the diagonal revealed areas of Kirkendall voids between the metal layers; third, unlike in AlN-AlSiC bonded assemblies, lateral cracks were observed approximately 0.7–1.5 mm below the bond line and in the AlSiC layer in each of the Cu-AlSiC assemblies. At least two distinct reaction layers between the Cu and AlSiC layers parallel to the interface can be observed in the interfacial zone in Figure 6c.

The XRD patterns of the bonded samples in each of the three configurations are shown in Figure 8. The results were compared with standard peaks to determine possible compounds within each material stack. According to the data extracted, the interface between the Al-AlSiC and AlN-AlSiC samples was comprised predominantly of Al solid compound and SiC particles, as well as peaks of AlN compound in the AlN-AlSiC sample. The Cu-AlSiC sample, on the other hand, exhibited more varied intensity in Cu-Al diffracted peaks. In addition to Cu and SiC, CuAl2, CuAl, and Cu9Al4 were identified via XRD. EDS analysis conducted at various points within the bond shown in Figure 28 further elucidated the composition of the interlayer.

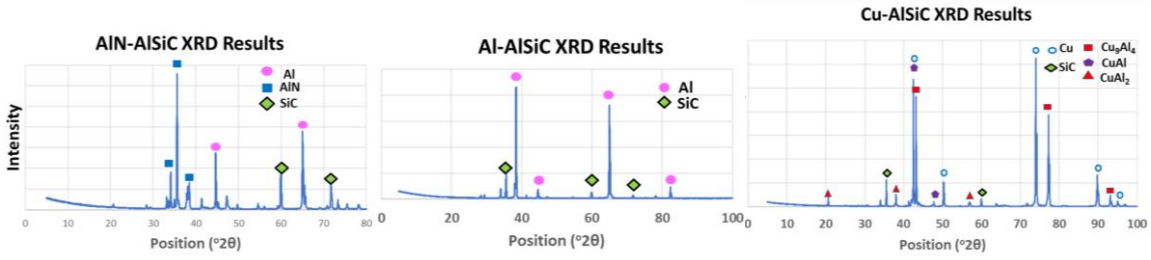


**Figure 8:** XRD analysis results

To model the Cu-Al TLP system, a two-dimensional geometry representing a cross-sectional view of the bond interlayer between the samples is developed. This adopts the assumption of isotropic

diffusion and assumes uniform diffusion in one direction, top to bottom. The Cu and Al elements of the bond are modeled as components. Since the sintered AlN substrate has been shown to have no influence on the formation of the bond, the AlN material was neglected in this analysis. For simplicity, the bond material is modeled as a binary material consisting of pure Cu and Al, although in practice, the SiC particles that migrate into the bond may play a role in impeding or decelerating diffusing atoms.

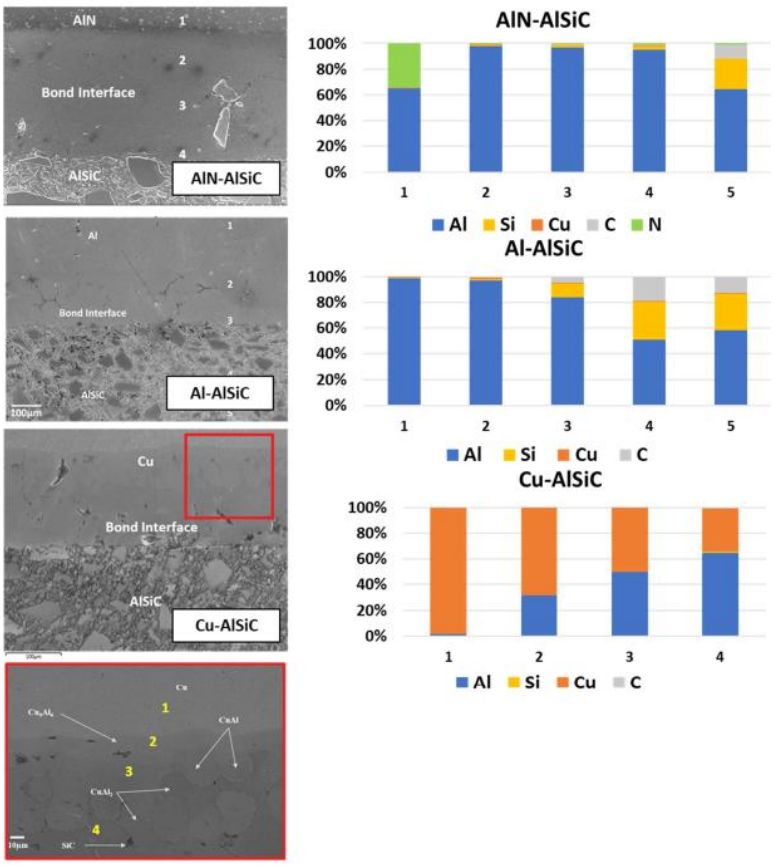


**Figure 9:** EDS spectroscopy analysis along (a) AlN-AlSiC, (b) Al-AlSiC, and (c) Cu-AlSiC cross sections. (d) Magnified SEM image showing interfacial microstructures of Cu/Al intermetallic compounds between TLP-bonded Cu and AlSiC plates

One 25 µm thick Cu foil and three 50 µm thick Al were used in the TLP bonding of the substrates to AlSiC. Representative uniform width, l, of 1 mm was used for all samples in the model (Figure 10), while the thickness of the Cu layer was varied according to the starting value in each of the three assemblies to examine the impact of Cu concentration on the final bond composition and intermetallic compound formation.

At the onset of the simulation (t = 0), Cu was assigned a concentration of 100% in the top domain and 0% in the lower segment, and Al a concentration of 0% and 100% in the top and bottom components, respectively. A boundary condition of zero flux was applied along all edges except the interface to allow for interlayer mixing. The temperature profile in Figure 3 is resolved into a

time-dependent function and imported as a global input. As the diffusion coefficient of Cu in Al changes with temperature, this value was parameterized over the temperature range of 500°C – 570°C.

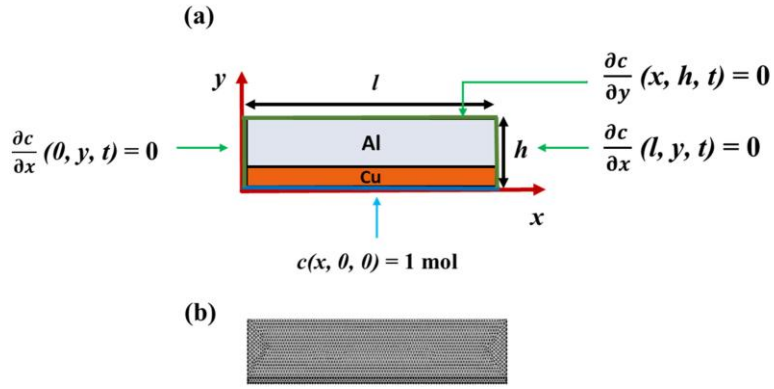


**Figure 10:** (a) Schematic illustrating Cu-Al bond geometry, depicting initial and boundary conditions. In the figure, l is fixed at 1mm, while h varies from 0.175mm – 2.15mm according to the sample concentration. (b) Meshed geometry discretized to solve domain.

The diffusion model predicts the formation of intermetallic compounds by simulating the atomic-level movement of elements within the system over time. It considers the input factors such as temperature, composition gradients, atomic mobility, and diffusion coefficients to simulate how the Cu or Al atoms migrate and interact at the interface. The Transport of Dilute Species (TDS) equations in COMSOL take into account Fick's laws of diffusion, which relate the concentration gradient to the flux of atoms. The model then generates composition profiles at various time intervals, showing how the elements' concentrations change within the material layers and at the interface. The COMSOL simulation outputs a three-dimensional matrix that showcases the concentration gradient of Cu in terms of mol/$m^3$ for all positions r over time t. The report was then analyzed using a MATLAB script to discretize the data based on the phase concentration ranges. Figure 11 shows the progression of Cu diffusion through the modeled geometry.

Comparing the simulated model to EDS results, it is shown in Figure 9 that spectral analysis for the AlN-AlSiC and Al-AlSiC assemblies showed less than 2% atomic concentration of Cu, while XRD patterns revealed an abundance of the α-Al solid compound. This is validated by simulation results exhibiting that over a hold time of 40 min at 565°C, the 12.5-µm Cu foil used in initiating the bond between AlN-AlSiC and for Al-AlSiC completely diffused through the system, leaving behind a mostly Al bond.

Conversely, when 2-mm-thick Cu was bonded to AlSiC at 565°C, the diffusion rate of copper, coupled with the high initial volume, dwell time, and favorable solubility limit on the Cu side, resulted in the nucleation of multiple phases. This is corroborated by the diffusion modeling results shown in Figure 11, which predicts the formation of intermetallic phases $Cu_9Al_4$, CuAl, and $CuAl_2$ given the starting concentration of Cu and dwell time at isothermal heating temperature. Although the sample is being held at a temperature of 565°C at t = 0 (leftmost image in Figure 11), the materials in the bond layer do not start to melt until the solid-state diffusion of Cu atoms into the

Al foils. This phenomenon is also exhibited in the modeling results presented in Figure 6, which shows no change in the Cu concentration at t=0, followed by a gradual interdiffusion as the Cu begins to react with Al to form the liquid phase. Subsequent phases entail the eutectic reaction and the progressive development of Cu-rich intermetallic phases.

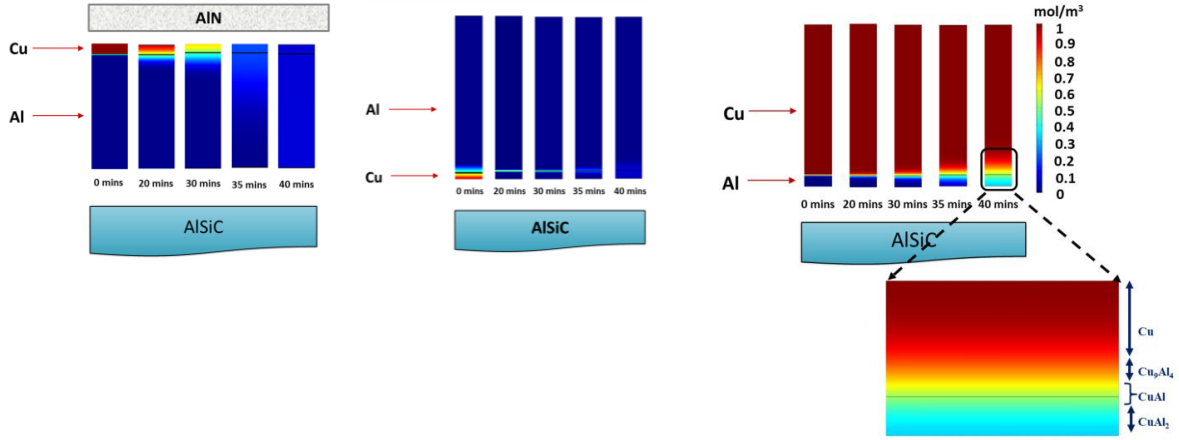


**Figure 11:** Modeling results over a time range of t = 0mins to 40mins at 565°C illustrating isothermal diffusion

It should be noted that although the diffusion model is likely to aid in the determination of intermetallic compounds formed between two materials given initial concentrations, thermal conditions, and time inputs, various other factors may influence the order of IMC formation, such as the heat of formation, thermodynamic stability of phases, bonding conditions, and cooling rate.

## 2. Enhanced Electrical Performance and Reliability of Hybrid Copper-Graphene Printable Conductor for Advanced Power Electronics Packaging

### Background

While the AlN-AlSiC substrate introduced in the previous project task may provide such insulation and heat conduction properties to establish electrical circuits and facilitate the attachment of components like devices, leads, and wire bonds for a complete package, as shown in Figure 12, the incorporation of a conductive metal layer is necessary [1]. Copper and aluminum, known for their exceptional electrical and thermal conductivity, are commonly employed as the metallization layer in power electronics. Consequently, direct bond copper (DBC) substrates are frequently favored in power electronics packages due to their high thermal conductivity and effective dielectric blocking capabilities.

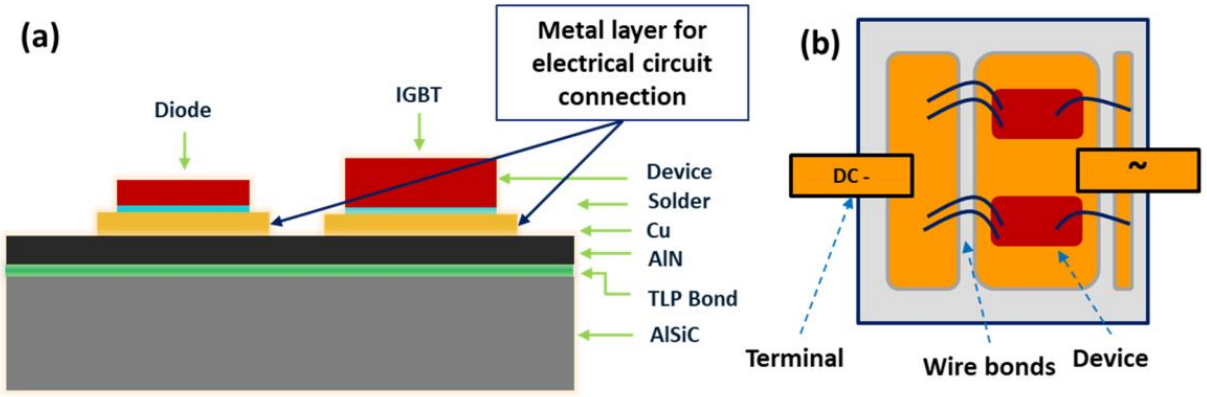


**Figure 12:** (a) Power Electronics Packaging with Cu Metallization on an AlN dielectric substrate TLP bonded to an AlSiC heat sink and (b) Representative Circuit Design

This research task focuses on 3D printing a metal layer for power electronics circuitry on AlN dielectric substrates using material jetting and aims to explore the use of additive manufacturing as an alternative to the conventional direct bond copper (DBC) manufacturing process for power electronics circuitry. Specifically, the task aims to 3D print a metal layer on aluminum nitride (AlN) dielectric substrates using material jetting. The task also investigates the effect of adding Graphene to the copper conductor, aiming to enhance its ampacity and thermal conductivity. By hybridizing copper nanoplates with Graphene, a material is formed that combines the desirable properties of both constituents, including high electrical conductivity and superior thermal stability. This task employs a printable Cu-Graphene ink conductor that was developed by Dr. Shenqiang Ren at the  State University of New York (SUNY) Buffalo. The ink formulation and processing techniques are proprietary to the Renewable and Emerging Nanomaterial (REN) Laboratory at the University of Buffalo. The research described in the subsequent sections was carried out in partnership with the REN lab.

**Method**

A large batch of copper nanoplates (CuNPLs) precursor is made by mixing copper chloride dihydrate ($CuCl_2 \cdot 2H_2O$, 38.4 g), D-glucose ($C_6H_{12}O_6$, 62.4 g), Hexadecyl-amine (HDA, $CH_3(CH_2)_{15}NH_2$, $\geq$ 90%, 232.8 g), and sodium iodide (NaI, 1.44 g) with 3600 mL deionized water. This mixture is placed in an oil bath with a mechanical stirrer for 16 hours at 100ºC. During heating, the HDA acts as a coordinating ligand and forms a Cu2+ - HDA complex. As time passes, the Cu2+ gradually reduces to Cu0 due to glucose, thus forming Cu seeds in the precursor solution. Once the seeds start to grow, iodide forces Cu growth parallel to the basal plane by preferentially absorbing onto the facets. Once the precursor feedstock is synthesized, it is filtered via a 160µm mesh, followed by centrifuging at 6000 rpm for 5 minutes. The solids are collected, re-dispersed in DI water and ethanol in a 1:1 ratio, and again centrifuged to obtain the CuNPLs feedstock. Once the CuNPLs feedstock is obtained, hydroxypropyl methylcellulose (HPMC) solution (2 wt. % in deionized water) and deionized water are mixed with the feedstock to make conductive, printable

ink. Dopamine hydrochloride is added to this conductive ink (0.3 wt.%), and the solution is mixed in a Thinky ARE-310 Mixer for 30 seconds to obtain a homogenous ink mixture.

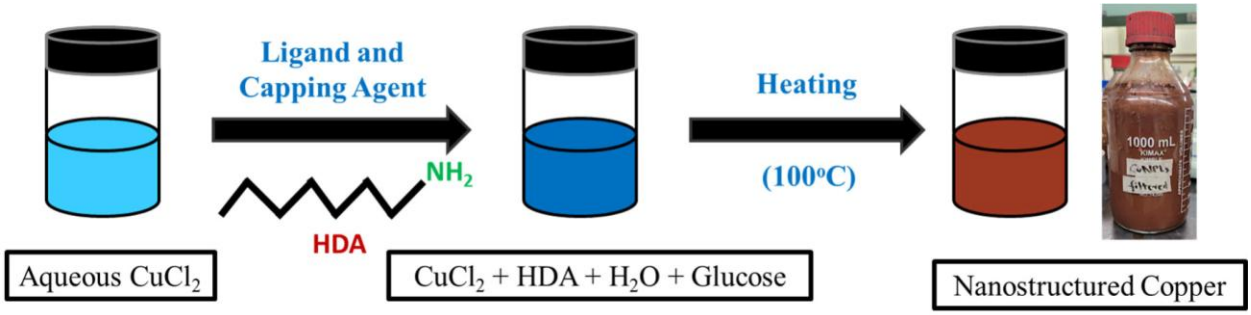


**Figure 13:** Schematic representation of the Cu nanoparticles synthesis through hydrothermal reaction from precursor preparation and nucleation to resulting growth of nanostructured copper.

The Cu-G ink is achieved via in-situ carbonization of polydopamine at elevated temperatures, as depicted in Figure 14, thus serving as a potential source of graphene, achieved via physical mixing. Moreover, as the polymerization of polydopamine is an oxidative process, it can potentially reduce oxides on the metallic Cu surface, which can assist in the removal of surface oxides. The presence of amine (-$NH_2$) and hydroxyl (-OH) groups ensure a uniform coating on the Cu-NPLs surface, which can be attributed to their strong adhesion as a result of non-covalent bonding (π–π stacking or hydrogen bonding), forming a metallic and covalent bond between the Cu-NPLs (111) and Graphene, offering enhanced electrical conductivity following high-temperature processing. The increase in ampacity observed in Cu-G conductors is due to the high thermal conductivity of graphene. Additionally, it significantly impedes Cu diffusion by preferential lattice matching, thus causing the hybridization of Cu and Graphene at the interface during in-situ conversion.

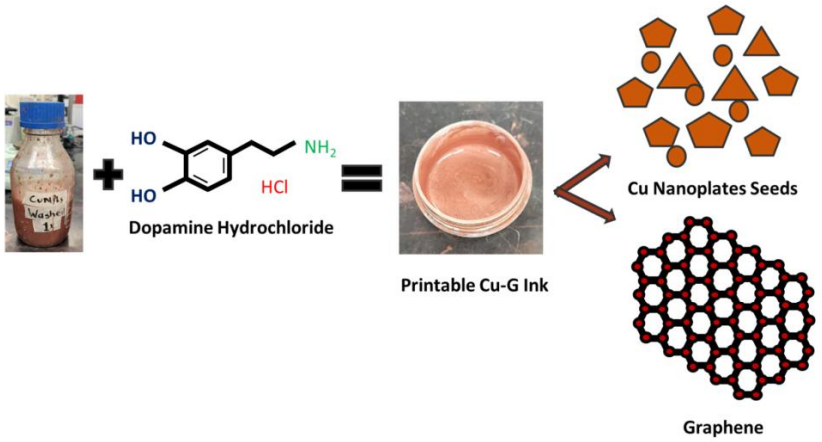


**Figure 14:** Illustration depicting the conversion of polydopamine to graphene during thermal processing of copper graphene conductive ink.

To prevent undesired coupling of signals between channels during electrical testing, 9$in^2$ bare AlN substrates (Accuratus, US) – each 630 µm thick – were cut into 25mm x 5mm pieces using a high-precision laser before printing. This ensured that each sample was subjected to an isolated testing

environment, mitigating the potential for crosstalk or spurious effects induced by neighboring samples. The bare AlN substrates were submerged in a 25% hydrochloric acid (HCl) solution at room temperature, sonicated in deionized (DI) water for 10 minutes, and then cleansed with an organic solvent to eliminate residual oils or greases.

The conductive inks were printed onto the AlN substrates using a direct-write approach with a Voltera V-One printer, depicted in Figure 15. The inks were loaded into the Voltera V-One dispenser cartridge and dispensed onto the AlN surface through a 0.225 mm nozzle via an extrusion process that facilitated controlled and precise deposition of the ink, as illustrated in Figure 16. Controlling the thickness of the print is an additive process that involves the iterative deposition of ink in multiple passes to meet specific requirements. Other factors influencing the print include the standoff distance, defined as the distance between the extruder nozzle tip and the substrate, and the print speed, which typically ranges from 400 mm/s to 600 mm/s.

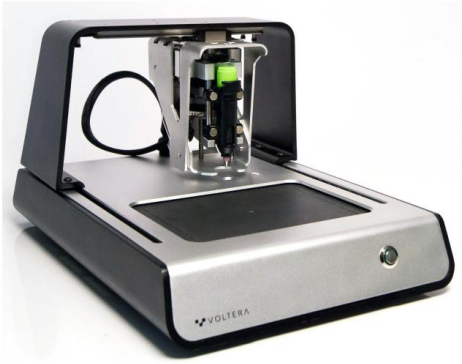


**Figure 15:** Voltera V-One: 3D Printer used in printing conductive traces on AlN substrates

The printed conductor was allowed to dry under ambient conditions for one hour, after which the substrates were transferred into a three-inch diameter alumina tube furnace (CM, Bloomfield, NJ). The CM furnace was equipped with a Eurotherm (Ashburn, VA) 3504 temperature controller, allowing precise internal temperature control. The samples were positioned in the furnace to closely approximate the center of the hot zone, ensuring uniform heating throughout the experiment.

The ink printed samples were fired in a forming gas atmosphere composed of 5% hydrogen (H) and 95% argon (Ar), supplied by Earlbeck (Baltimore, MD). The forming gas was continuously passed through the furnace at a flow rate of approximately 2 liters per minute throughout the furnace cycle. The temperature was ramped up at a rate of 1°C/min until it reached 350°C, where it was held for 1 hour to ensure furnace equilibrium. The temperature was then further increased at a rate of 1°C per minute until it reached 800°C, at which point it was held for 1 hour. After the hold, the furnace gradually cooled down at 2°C per minute until the samples reached room temperature. Once at room temperature, the flowing forming gas was turned off, and the end cap of the furnace was removed to allow retrieval of the sintered samples.

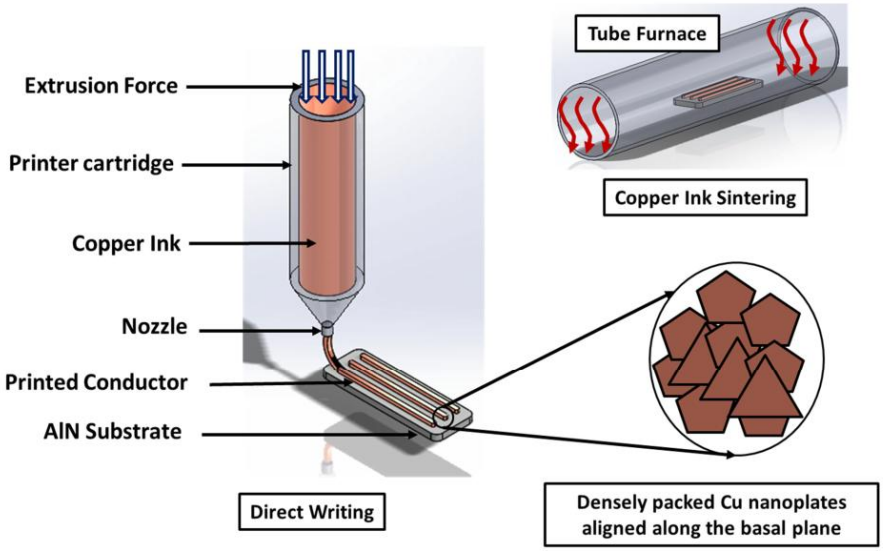


**Figure 16:** Illustration of Ink Jetting Process: Deposition of Copper Nanoplate-Based Ink onto AlN Ceramic Substrate

The diminished particle size of copper at the nanoscale results in a significantly increased surface-to-volume ratio, thereby amplifying the already low oxidation resistance of the metal. To tackle this concern, a promising approach to improving its performance is through the incorporation of a more resistant material, such as gold, platinum, titanium, or silver, using alloying or coating techniques.

Therefore, to investigate the impact of oxidation on the electrical performance of the conductive ink, a subset of the CuG printed samples was allocated for metal coating with silver (Ag) and a Nickel (Ni)-gold (Au) treatment. A 100-nm-thick Ni adhesion layer and 10-nm-thick Au layer were deposited onto a set of CuG conductor samples using an electron beam evaporator (Denton Explorer) at a deposition rate of 1 Å/s. Using a similar setup, 100 nm thick silver (Ag) was deposited onto the CuG-printed AlN substrates. The deposition was performed while maintaining a vacuum in the chamber.

Another plausible approach to enhance the passivation of the conductor is by depositing metal oxide layers on the conductor surface. Due to its high melting point, chemical stability, and excellent thermal and electrical insulation properties, Alumina exhibits outstanding oxidation resistance. It has been recognized as a promising candidate for the passivation of metallic conductors to protect against oxidation at high temperatures.

An atomic layer deposition (ALD) system was employed to deposit an ultra-thin layer of $Al_2O_3$ film. The deposition process was executed in a cyclic manner, where sequential pulses of trimethylaluminum (TMA) and $H_2O$ were interspersed with Nitrogen purged at a controlled flow rate of 20 standard cubic centimeters per minute (SCCM). The $Al_2O_3$ deposition process involved

a 0.015s exposure to TMA, followed by an 8-second dwell time, and a subsequent 0.015 s pulse of $H_2O$, succeeded by an additional 8-second hold time. The deposition was carried out at 200 °C to obtain a coating thickness of 100 nm. The growth rate of $Al_2O_3$ during this procedure was 1.06 Å per cycle.

To assess the microstructure and composition of the ink layer, the samples were examined using a Hitachi SU 8230 Field emission scanning electron microscope (FE-SEM) equipped with an Oxford Silicon Drift detector. Energy-dispersive X-ray spectroscopy (EDS) analysis was performed using embedded Aztec software to investigate the elemental composition of the sintered metal. The test was operated under 5-20 kV with a working distance of 15 mm and a 10000−20000 counts/s count rate.

The crystalline structure of the printed test samples was evaluated through X-ray diffraction (XRD) analysis. The XRD analysis was performed using a Malvern Panalytical Empyrean platform equipped with a copper anode (Cu-Kα, λ = 1.5416 Å) powder X-ray diffractometer. The analysis was carried out with a step size of 0.02° and a step time of 1 second, covering the 2θ range from 5° to 80°. Elemental identification was performed by comparing the obtained patterns with the comprehensive International Centre for Diffraction Data (ICDD) database [2] integrated into the software of the XRD machine.

Electrical conductivity and sheet resistance measurements were performed using an Ossila four-point probe system connected to a Keithley 2450 source meter. The system employed four equidistant and co-linear probes with rounded tips to establish electrical contact with the ink material. The probes were spring-loaded, ensuring a consistent 60 grams of force was applied on each sample during contact. Consequently, the resistance of the material was measured in a direction perpendicular to the thickness of the ink layer.

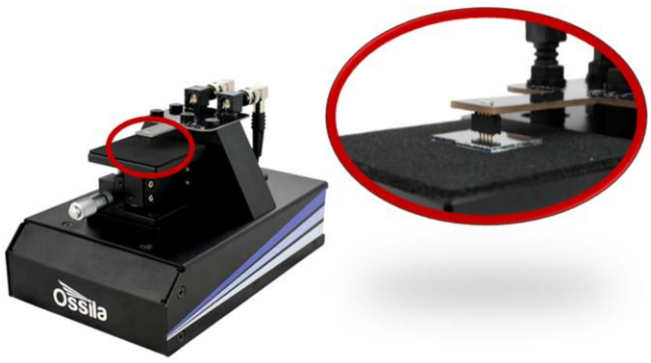


**Figure 17:** Ossila four-point probe used in conducting conductivity and sheet resistance measurements

A custom-built experimental arrangement was employed to measure the current density on the printed metal layer. This consisted of electrical wiring attached to opposite ends of Cu ink traces printed onto 25 x 5 x 0.63 mm3 AlN substrates. The wires were connected to a Keithley 2260B DC power supply capable of supplying up to 40.5 A of electrical current. Experiments were

conducted in the air by incrementally increasing the voltage flowing through the sample, as shown in Figure 18 while measuring the corresponding current. At each voltage step, the resistance was calculated from the correlation between current and voltage, and the resistance values were converted to resistivity using the measured length, width, and thickness of each sample trace, The measured cross-sectional area was used to calculate the current density at each voltage point. Direct bond copper substrates conventionally used in power electronics packaging from Stellar Industries (MA, US) were also subjected to identical test conditions using the aforementioned setup. The DBC samples had Cu-AlN-Cu layers with thicknesses of 0.3mm, 0.63mm, and 0.3mm, respectively.

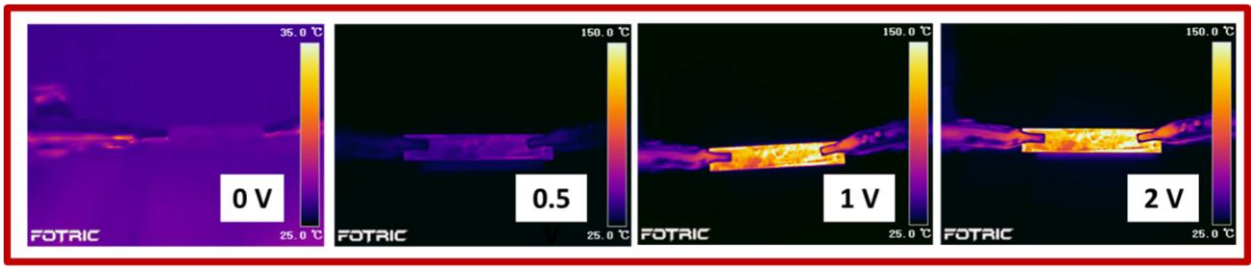


**Figure 18:** Infrared thermal imaging of sample during joule heating under current density assessment.

**Results**

The conductive ink used in this project task is a combination of copper nanoplates and Graphene from in-situ converted polydopamine hydrochloride. The hybridized copper-graphene material obtained combines copper's high electrical conductivity with Graphene's high thermal resilience, producing a metallic conductor with improved corrosion resistance and thermal stability.

The printed Cu nanostructures were evaluated through Scanning Electron Microscopy (SEM). Figure 19 presents Cu nanoplates' microstructural and dimensional properties after thermal processing for 1 hour at 800°C. The SEM results reveal the formation of plate-like structures from the Cu seeds present in the precursor. These plate-like structures exhibit an average width of 4.16 ± 1.47 µm.

This process promotes anisotropic growth due to the low thermodynamic energy associated with differential stacking along the crystal surface. During the thermal reaction, the Cu atoms tend towards equilibrium, leading to low surface energy facets emerging along the (111) planes that enclose the decahedral structure. This transformation produces Cu nanoplates with a face-centered cubic (FCC) structure. The development of nanoplates may be attributed to the abundance of decahedral Cu nanoparticles, which serve as nucleation sites for depositing Cu atoms. This process promotes anisotropic growth due to the low thermodynamic energy associated with differential stacking along the crystal surface. During the thermal reaction, the Cu atoms tend towards equilibrium, leading to low surface energy facets emerging along the (111) planes that enclose the

decahedral structure. This transformation produces Cu nanoplates with a face-centered cubic (FCC) structure.

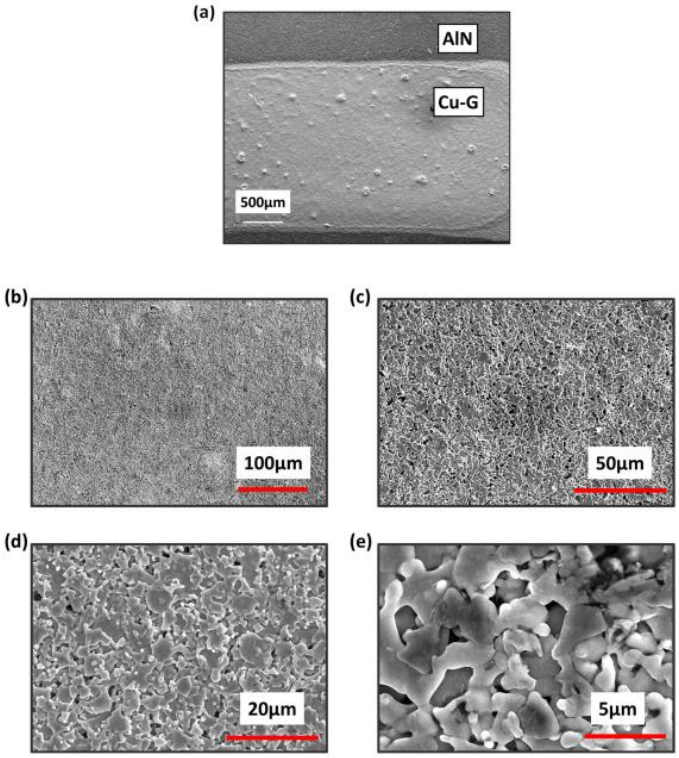


**Figure 19:** Scanning Electron Microscopy (SEM) images of sintered copper nanoplates at (a) 20× magnification (b) 300× magnification (c) 800× magnification dc) 2000× magnification and (e) 7000× magnification

The formulation of a dense percolation network, as depicted in Figure 19, has been shown to potentially enhance the flow of charge carriers, leading to higher electrical conductivities compared to smaller features, such as nanoparticles and nanorods, which may lack the same level of connectivity and continuity. The elemental composition of the conductive ink is further validated via energy-dispersive X-ray spectroscopy (EDS), as illustrated in Figure 20. Figure 21 presents optical images exemplifying the Cu-G ink conductor printed on an AlN substrate and subsequently passivated with silver or nickel-gold metallization.

X-ray diffraction analysis was employed to determine the phase and crystallinity of the Cu ink printed on AlN. The powder XRD diffractogram of the as-printed ink on the AlN substrate is presented in Figure 22. The diffraction pattern exhibits distinct peaks at 33.48°, 36.3°, 38.18°, 50.74°, 59.58°, 66.3°, 69.96°, 71.66°, and 72.86°, which can be attributed to the bulk AlN ceramic substrate. These peaks correspond to the (100), (002), (101), (102), (110), (103), (200), (112), and (201) crystallographic planes, respectively, of AlN's hexagonal wurtzite structure. The diffractogram of the Cu ink reveals a prominent 2θ peak at 43.6°, aligning with the (111) plane. This observation is consistent with the expected behavior, as the (111) plane is recognized as the

primary facet for the nanoplates [3]. In addition, two more 2θ peaks are observed at 50.06° and 74.34°, corresponding to the Cu (200) and Cu (220) crystallographic planes, respectively.

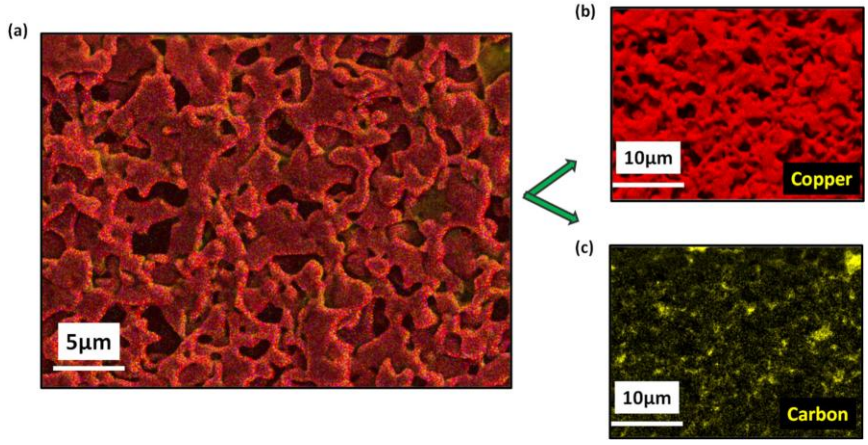


**Figure 20:** Energy-Dispersive X-ray Spectroscopy (EDS) analysis of copper nanoplates ink revealing distribution of elements in (a) a composite map, and individual micrographs of (b) copper and (c) carbon.

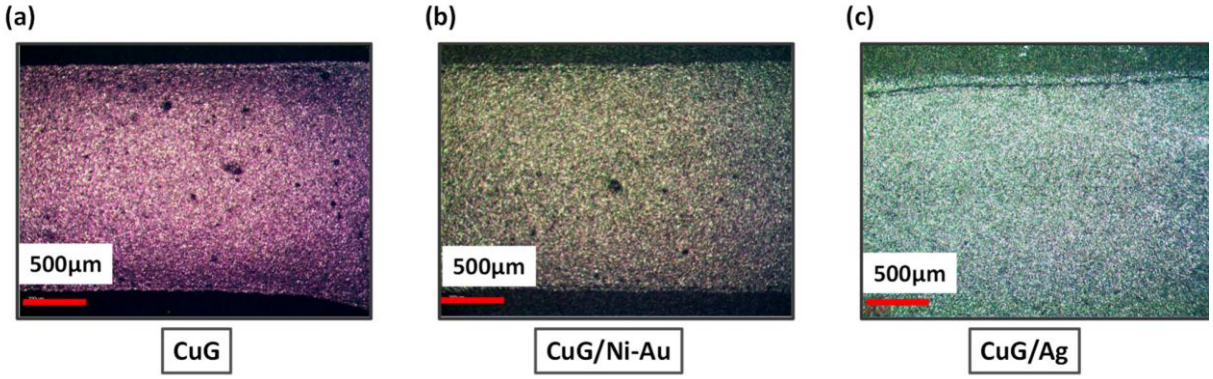


**Figure 21:** Optical microscopic images of (a) printed CuG ink (b) passivated with nickel-gold (Ni-Au) (c) and silver (Ag) coating

X-ray diffraction analysis was employed to determine the phase and crystallinity of the Cu ink printed on AlN. The powder XRD diffractogram of the as-printed ink on the AlN substrate is presented in Figure 22. The diffraction pattern exhibits distinct peaks at 33.48°, 36.3°, 38.18°, 50.74°, 59.58°, 66.3°, 69.96°, 71.66°, and 72.86°, which can be attributed to the bulk AlN ceramic substrate. These peaks correspond to the (100), (002), (101), (102), (110), (103), (200), (112), and (201) crystallographic planes, respectively, of AlN's hexagonal wurtzite structure. The diffractogram of the Cu ink reveals a prominent 2θ peak at 43.6°, aligning with the (111) plane. This observation is consistent with the expected behavior, as the (111) plane is recognized as the primary facet for the nanoplates [3]. In addition, two more 2θ peaks are observed at 50.06° and 74.34°, corresponding to the Cu (200) and Cu (220) crystallographic planes, respectively.

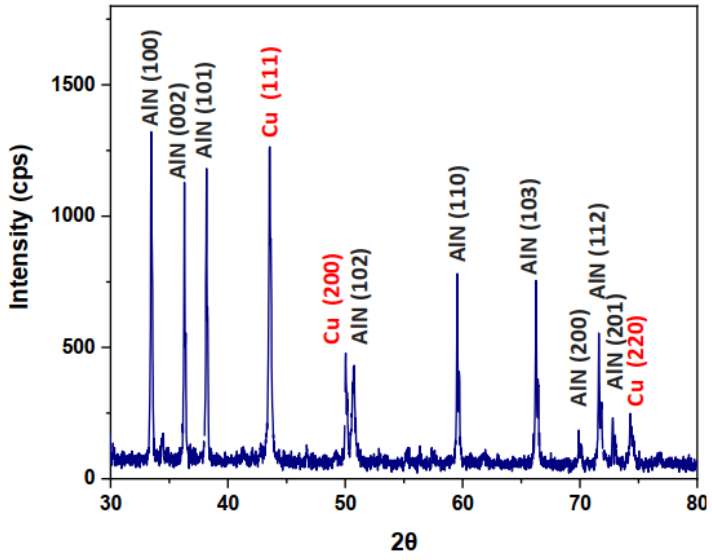


**Figure 22:** Powder XRD pattern of the copper conductor printed on AlN ceramic substrate.

The dielectric constant, κ, of a material represents the complex-valued permittivity εm of said material with respect to the fundamental permittivity of vacuum (8.854 x10-12 F/m), denoted $\varepsilon_0$, as expressed in equation (14). The dielectric properties of the samples were measured at room temperature across a wide frequency range from 20 Hz to 2 MHz using an LCR meter (Agilent E4980A), a specialized electronic device utilized in determining the inductance (L), capacitance (C), and resistance (R) of electronic components. Thin samples of copper-graphene printed AlN substrates measuring 25 mm x 5 mm in area, and 660 µm in total thickness were sandwiched between uniformly coated silver paste on both sides to create a ceramic capacitor structure. The materials' relative permittivity, $\varepsilon_r$, was determined from measured values of the sample's thicknesses, capacitance, and electrode area. The resulting impedance spectroscopy demonstrates the dielectric properties of the material as a function of frequency.


**Figure 23**: High frequency LCR Meter used in dielectric strength characterization.

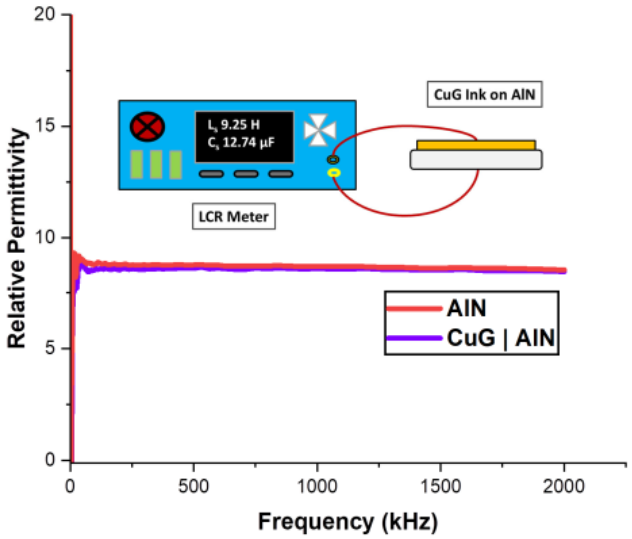


**Figure 24:** Frequency-dependent relative permittivity of CuG ink printed on AlN compared to as-ordered AlN measured using an LCR and Vector Network Analyzer. Results indicate the Cu ink sintering process has minimal impact on the dielectric strength of the AlN substrate.

The investigation encompassed an analysis of both pristine AlN substrates and substrates printed with Cu-ink conductors to analyze the potential impact of the printing and sintering procedures on the dielectric strength of the ceramic material. The results for the unmodified AlN samples maintained at room temperature demonstrated that the permittivity remained consistent across frequencies, yielding a value of $\varepsilon' = 8.6 \pm 0.04$ as illustrated in Figure 24. Comparatively, AlN substrates subjected to the CuG ink printing process demonstrated a frequency-independent relative permittivity value of $8.5 \pm 0.05$. This observation indicates that the entire process involving the printing and subsequent sintering of the copper-graphene ink does not adversely impact or alter the dielectric strength of the AlN substrate. The results presented in Figure 25 demonstrate the relationship between the electric conductivity and sheet resistance of Cu nanoplates and Cu graphene conductors to the printed ink thickness. The ink layer thickness was modulated by progressively increasing the number of passes during printing. An evident trend in both graphs indicates that an increase in conductor thickness correlates with a decrease in sheet resistance. However, as the thickness exceeds 15 µm, the decrease in sheet resistance becomes less significant. An inverse relationship is observed with conductivity, wherein the conductivity displays an upward trend with increasing thickness, plateauing after three passes, or when the ink thickness reaches 15 µm and 18 µm for CuNPLs and CuG ink samples, respectively.

Specifically, the electrical conductivity values of the copper nanoplates ink on AlN were found to range from 2.2 MS/m to 7.17 MS/m for five different thicknesses, namely 13 µm, 15 µm, 18 µm, 22 µm, and 27 µm. Prominently, a substantial increase in conductivity by 128% was evident between the initial two thicknesses. However, a gradual attenuation in the rate of conductivity enhancement was observed for the subsequent thicknesses.

Likewise, the conductivity of the printed Cu graphene ink on AlN increased by 80% from 4.77 MS/m for a 6 µm-thick layer to 8.61 MS/m for a 10 µm-thick ink layer – achieved by making a single or double pass on the substrate using the Voltera printer respectively. This progressive enhancement in conductivity gradually diminishes as the thickness of the layers increases, ultimately reaching a stabilized conductivity level of approximately 10.5 MS/m for thicknesses exceeding 15 µm.

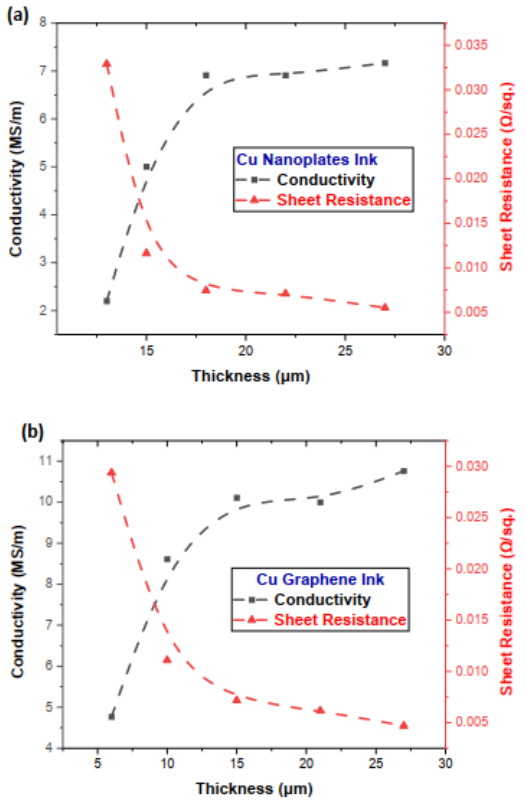


**Figure 25:** Impact of ink layer thickness on the electrical conductivity and sheet resistance of (a) Cu NPLs and (b) CuG ink-printed AlN substrates.

The observed variation in thicknesses between the CuNPLs and CuG ink layers for the same number of printer passes may be attributed to the differences in volumetric concentrations of hydroxypropyl methylcellulose (HPMC) and other dispersants in the printed ink due to the addition of polydopamine. During the thermal processing, the introduced dopamine undergoes carbonization, leading to the formation of Graphene and ultimately contributing to the creation of the copper graphene conductive ink. Although the initial volume of ink dispensed from the Voltera cartridge during a single pass may be consistent, the ultimate print thickness is subject to variation, contingent upon the concentration of Cu and the rate of decomposition of the viscosity modifiers during the thermal processing. Electrical conductivity was determined based on the precise measurements of ink thickness acquired post-processing.

While both the copper nanoplates and copper graphene (CuG) ink display comparable trends in terms of electrical conductivity and sheet resistance, it is worth highlighting that the CuG ink showcases a superior maximum electrical conductivity, measuring at 10.8 MS/m, in contrast to the pure nanoplates which attain 7.16 MS/m, despite an equal number of ink layer passes applied in both cases. This noteworthy distinction underscores the enhanced electrical performance offered by the CuG ink over its nanoplate counterpart within the specified conditions.

Compared to bulk Cu, characterized by an electrical conductivity of 58 MS/m, the copper graphene ink exhibits significantly lower conductivity, approximately one-fifth of the magnitude. Despite this discrepancy, opportunities exist to enhance the ink's conductivity to approach levels similar to that of copper. Nonetheless, the ink maintains a comparable order of magnitude to bulk copper and holds promising potential, particularly in its higher ampacity.

The current carrying capacity of the printed inks was evaluated by subjecting a series of Cu nanoparticle layers (Cu NPLs) and Cu-graphene (CuG) samples to testing, following the aforementioned method. The obtained results are presented in Figure 26. As seen in Figure 26a, at current densities up to 220 x 106 A/m2, the resistivity of the Cu-NPL ink printed on AlN substrates remained relatively unchanged. Beyond this limit, the thin ink traces experienced failure in the central region of the samples, leading to an exponential increase in resistivity. However, the CuG ink samples sustained their current carrying ability well beyond the Cu-NPL limit and went as high as 390 x 106 A/m$^2$, almost doubling the maximum ampacity results for pure Cu-NPLs. The increased ampacity observed can be attributed to Graphene's higher thermal conductivity than copper, which may provide improved heat dissipation during electrical conduction.

In contrast, direct bonded copper substrate samples tested in a similar setup displayed ampacities in the 4.1 – 5.6 x 106 A/m$^2$ range, a hundred times lower than the tested ampacities of both the copper nanoplates and copper graphene ink. This value is consistent with the known values of bulk copper (~ 106 A/m2).

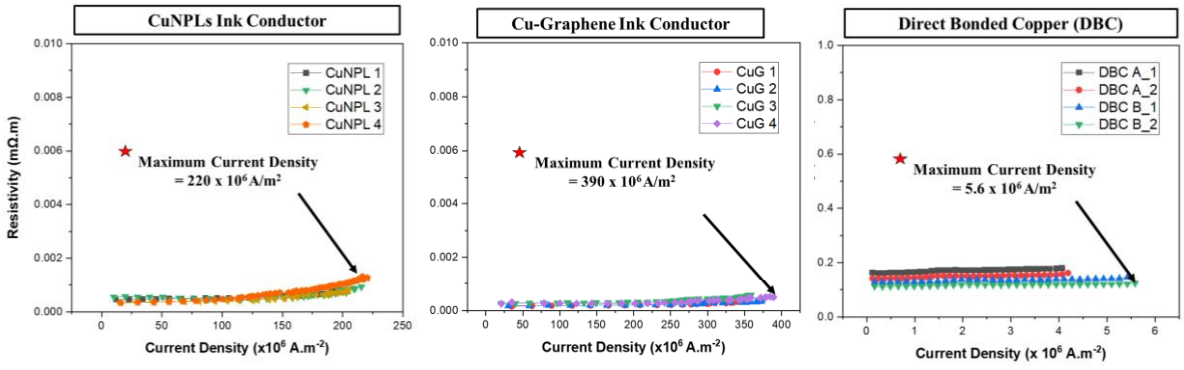


**Figure 26:** Current density measurements for copper nanoplates ink, copper graphene ink, and direct bond copper.

The significantly higher current density values may be attributed to the inherent ability of nanoplates to sustain elevated ampacities due to their 2-D geometry, which facilitates plate stacking, consequently bolstering their current-carrying capacity.

The technical guidelines for future advanced integrated power modules (AIPM) outline anticipated voltage ratings of near 1 kV and maximum device currents of 200 A. Considering the typical surface footprint of SiC devices varies in area, with a maximum assumed area of approximately 5 mm x 5 mm, the ideal maximum current density of a power module can be approximated by dividing the maximum current by the known area, resulting in 8 x 106 A/$m^2$. Comparatively, the ampacity of CuG ink significantly surpasses this requirement, making it a promising option for advancing power electronics packaging.

Figure 27 illustrates the resistance versus temperature curves for two inks tested in the air: copper nanoplates ink (Cu-NPLs) and copper graphene ink (CuG), and three different types of passivation layers, namely silver (Ag), alumina ($Al_2O_3$) and nickel-gold (Ni-Au). Among the different passivation options tested, a combination of 100 nm Ni and 10 nm Au demonstrated the highest level of oxidation resistance for the CuG ink. This metallization configuration maintained its robustness up to a temperature of 410 ºC. Under inert atmosphere conditions, however, pure CuNPLs have survived until a temperature of 950 ºC, whereas Cu-G (Cu-graphene) exhibits durability up to 1400 ºC.

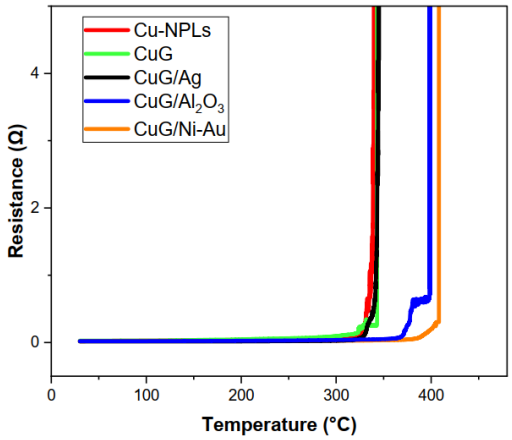


**Figure 27:** Resistance vs temperature curves for printed copper conductor with varying passivation layers

To assess the reliability of the printed metal ink conductors, accelerated aging tests were conducted on the samples near the maximum operating temperature of SiC devices. The printed samples were aged at a temperature of 250ºC for 140 hours. Figure 28 illustrates the results of the test conducted on CuG, CuG with Ag metallization, and CuG with Ni-Au metallization. Despite the absence of surface passivation, the Cu-G ink demonstrated notable stability, exhibiting a minimal increase in resistance to the current flow of less than 2.2% throughout the experiment. Similar results were obtained from identical tests on the CuG inks passivated with silver and gold metallization. The

CuG ink with alumina passivation has previously been demonstrated to survive at 500ºC for up to 90 hours [4]. These findings substantiate that integrating Cu-G in power module design offers remarkable reliability performance alongside additional benefits such as enhanced ampacity and electrical and thermal efficiency.

A fully assembled packaging prototype was successfully developed by integrating the results of the Cu-G ink development and characterization, along with the TLP material characterization. As displayed in Figure 29, this prototype involved bonding AlN dielectric to both AlSiC and an Al foam heat sink using the Cu-Al transient liquid phase bonding process. This package incorporates a Cu-G metal conductor layer that was additively printed onto the AlN surface. The conductor layer serves to establish electrical conduction pathways and is passivated with a gold finish to enhance oxidation resistance.

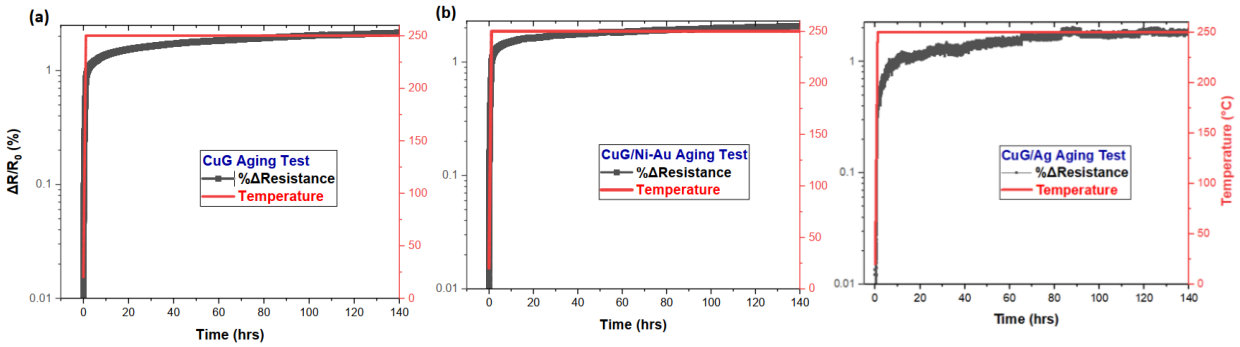


(a) (b) (c)

**Figure 28:** Reliability curve depicting results of aging test on copper graphene ink (a) printed on AlN substrate at 250°C for 140 hours (b) printed AlN samples, coated with Nickel and Gold. Samples were placed in a furnace and held at 250°C for 140 hours (c) printed AlN samples, coated with Silver. Samples were placed in a furnace and held at 250°C for 140 hours.

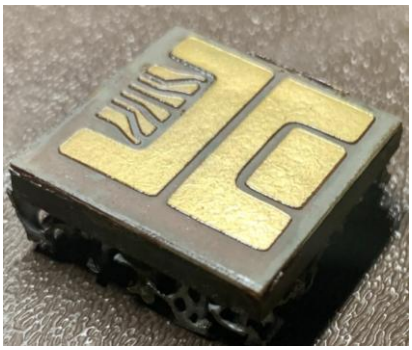

**Figure 29:** Power electronics packaging prototype: AlN dielectric TLP bonded to AlSiC plate and Al Foam, featuring 3D printed Cu-G conductor layer surface passivated with gold.

## 3. Single-phase Convection in Traditional Versus Additive Manufactured Metal Foams

### Summary

A commercial foam (nominally 5 pores per inch, 86.5% porosity) was analyzed using x-ray microcomputed tomography (x-ray μCT), and a designed foam based on the cell diameter and porosity of the commercial sample was manufactured. Reduced domain computational fluid dynamics/heat transfer (CFD-HT) models were compared against experimental data. Post validation, the flow behavior, effect of varying attachment thermal conductivities, and thermal performance were numerically investigated, demonstrating the usefulness of validated pore-scale models and the improved performance of AM metal foams over traditional foams.

### Method

The characterization is done in ImageJ, an open-source scientific image analysis tool, as well as BoneJ, a plugin developed for ImageJ that was developed for both trabecular and whole bone research that proved useful because of the porous nature of bone geometries.

The metal foam sample (referred to as commercial/stochastic/ERG foam) was purchased from ERG Aerospace Inc. The Duocel® aluminum foam was nominally labeled as 5 PPI, processed from 6101 alloy, and underwent T6 heat treatment. A Zeiss Metrotom 800 was used to perform x-ray μCT, a non-destructive imaging technique. A small section of the aluminum foam was scanned at 0.25-degree rotations with a voxel size of 18.43 μm, and the resulting 2D image files were subsequently imported to ImageJ. The images near both the top and bottom of the scan were deleted to remove distorted sections, and the files were cropped to only include the foam, without the dead space. The analysis of the properties (porosity, pore diameter, ligament diameter, ligament length, cell diameter, and specific surface area) began with the modified image files, and a flow chart illustrating the methodology can be seen in Figure 30.

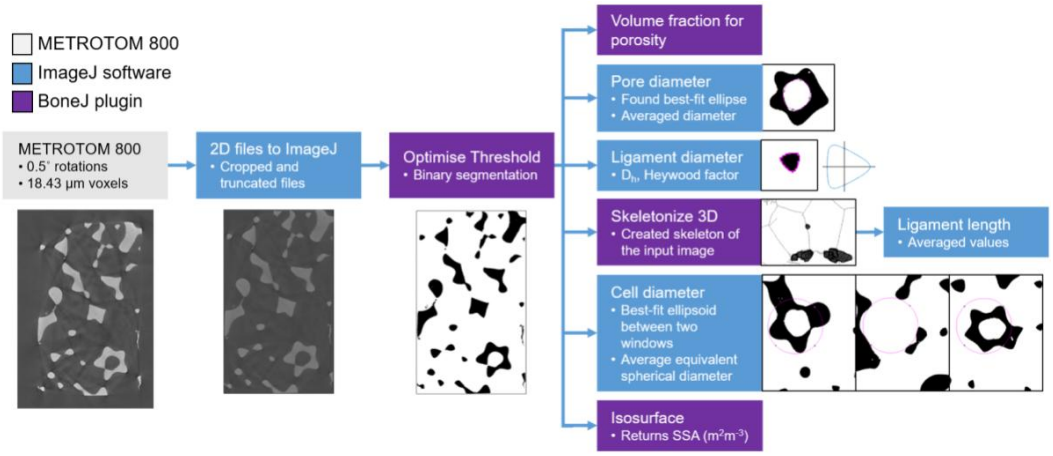


**Figure 30:** Illustration of steps for commercial stochastic foam characterization

Porosity (ε) was obtained by using the volume fraction command in BoneJ and subtracting the result from one, yielding a value of 86.5%. A cross-section with H = 1.086 is shown as a graph next to "Ligament diameter" in Figure 30. The ligament length was found by running Skeletonize 3D in BoneJ to create a skeleton image of the image sequence to measure ligament length more easily. Thirty ligament lengths from node to node were found and averaged. The cell diameter was calculated by finding the equivalent spherical diameter when compared to an ellipsoid of ten unbroken cells. The three ellipsoid axes were obtained by finding the two axes at the middle of the cell and the distance between the two pores that make up the cell. BoneJ's Isosurface was used to find the specific surface area. The calculated values can be seen in Table 2. A rhombic dodecahedron was chosen for the AM unit cell. Two views of this unit cell can be seen in Figure 31.

**Table 2:** Comparison of foam properties from x-ray μCT analysis, literature [5], and AM foam

| Parameter | Result | Literature comparison | Rhombic dodecahedron |
|---|---|---|---|
| *PPI* | 5 | 5 | 5 |
| *Porosity* | 86.5% | 92% | 86.5% |
| *Ligament diameter (mm)* | 0.508 | 0.505 | 0.548 |
| *Ligament length (mm)* | 1.94 | 1.72 | 2.01 |
| *Pore diameter (mm)* | 2.58 | 2.61 | 1.35 |
| *Cell diameter (mm)* | 4.65 | 4.60 | 4.65 |
| *Surface area ($m^2m^{-3}$)* | 571 | 510 | 927 |

**Figure 31:** Dimetric and diagonal views of a rhombic dodecahedron-based unit cell

The rhombic dodecahedron-based foam was constructed by setting the cell size and porosity equal to that found from the x-ray μCT analysis. Cell size and porosity were chosen as the two parameters due to their prevalence in literature, which are the most commonly reported parameters (as shown in Table 2), and the fact that they largely determine other geometric characteristics. The results matched closely for all parameters except the pore diameter and specific surface area.

The ERG foam was cut to the appropriate nominal size of 100 mm x 40 mm x 9.3 mm using electrical discharge machining (EDM). The foam was then attached to an aluminum plate (sanded

with 1000 grit sandpaper) using Omegabond 200 Epoxy Adhesive (k = 1.38 W/m·K, thickness 0.3 mm). The assembled foam and substrate were placed in a ThermoScientific Lindberg Blue M oven for 3 hours at 150 ˚C to cure per supplier recommendation. Figure 34a shows the attached foam with the layer of cured, black epoxy between the substrate and the foam. The AM foam was assembled using Materialise Magics, a software for STL file editing for 3D printing. The lattice unit cell was created in Solidworks then imported into Materialise. STL file corruptions and errors were handled using the Fix Wizard in-software. The AM manufacturing was outsourced to Forecast 3D who used direct metal laser sintering (DMLS) of AlSi10Mg particles to manufacture the designed foam structure. A vertical band saw was used to cut the structure out of the baseplate. Then, an end mill and electric discharge machining were used to bring the plate to the correct dimensions, and the plate was heat treated at 600 ˚F for 2 hours to relieve stresses created during machining so as to not break or warp the structures. The finished product post-machining and heat treatment can be seen in Figure 34b.

The numerical modeling examined and compared the thermo-hydraulic performance of both the ERG foam and the AM foam. The numerical model was experimentally validated to ensure model fidelity. The numerically simulated AM geometry measured 9.30 mm x 2.33 mm x 46.5 mm and can be seen in Figure 32a. The commercial foam geometry used in CFD-HT simulations was obtained from the image stack from the x-ray μCT analysis. A surface was created using the Isosurface command in BoneJ and then exported as a binary STL file.

The final foam geometry used in the modeling measured 9.30 mm x 4.65 mm x 25.0 mm, with the directions oriented in the same way as the experimental sample to ensure any directional bias in the foam is replicated in the simulations. Floating mesh points and triangles were removed using Meshlab, an open-source software used for mesh processing and repair, which was then subsequently used to smooth the geometry to decrease the mesh resolution. The geometry was assembled in Solidworks and subsequently exported to Fluent for CFD-HT analysis. The assembly can be seen in Figure 32b, with an inlet and outlet section added on either side. The 0.3 mm thick thermal interface material (TIM) layer between the substrate plate and the metal foam matrix is shown in the magnified view as the greyed out layer. The AM foam's simulation boundary conditions were the same as the ERG foam model. Both samples had Al 5083 substrates, and the thermophysical properties for the materials in the numerical analysis can be seen in Table 3. Despite the difference in materials used for the foams, their values were nearly identical, so that the thermal performance differences are not attributable to the material selection. The ERG foam was Al 6101, the AM foam was AlSi10Mg, and the working fluid was DI water.

The stochastic foam domain was reduced length-wise, as a full-length simulation would not import properly into the 3D modeling software utilized unless the mesh was simplified to the point of losing too many of the geometrical details. The domain reduction was necessitated by hardware and software, and it was assumed that the reduction in total domain length would have a small enough impact on the thermo-hydraulic parameters studied that it would be possible for us to still maintain model accuracy. Additionally, it was assumed that the scanned section was large enough

that it would encompass a sufficient quantity of foam cells that it could be considered a representative elementary volume (REV). The current geometry would be able to hold over ten cells total. It was also assumed that the inlet effects would be small enough so as to still give reasonable agreement between the CFD-HT simulation and experimental results.

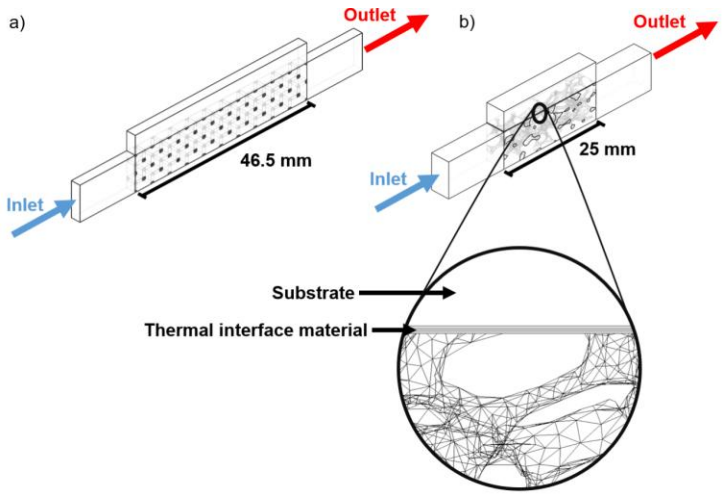


**Figure 32:** a) Reduced AM geometry and b) reduced ERG sample geometry with TIM with magnified view showing TIM layer

**Table 3:** Material properties at 25 ˚C used for CFD-HT models

| Property | Al 6101 | AlSi10Mg | Al 5083 | Water |
|---|---|---|---|---|
| $\rho$ (kg/m$^3$) | 2700 | 2670 | 2660 | 998 |
| $c_p$ (J/kg•K) | 896 | 890 | 900 | 4182 |
| $k$ (W/m•K) | 167 | 173 | 117 | 0.6 |
| $\mu$ (Pa•s) | - | - | - | 0.001003 |

The simulations assumed steady state, laminar, incompressible flow with negligible viscous dissipation. Buoyancy and radiative heat transfer effects were ignored, and material properties were considered constant. Prior studies defined the transition for open-cell, high-porosity foams in terms of pore diameter-based Reynolds number $Re_p$ and permeability-based Reynolds $Re_K$, where the length scale is the square of permeability. The turbulent Reynolds numbers corresponded to 10.2 cm/s for the ERG foam and 15.5 cm/s for the AM foam, so the assumption of laminar flow was reasonable. It must be noted that the experimental overall heat transfer coefficient differed from the computed values due to the additional resistances from the thermal paste applied onto the thermocouples.

A uniform inlet velocity condition was applied on one end of the computational domain normal to the boundary. The inlet speeds (u) were limited by the equipment discussed in the section detailing experimental setup and consequentially varied from 2.5 cm/s to 12.5 cm/s. The inlet temperature (Ti) was set as 300 K. Both side walls were set as symmetry conditions, as this computational

domain represents a relatively thin slice of the overall width. The solid-fluid interfaces were set as no-slip walls with temperature and heat flux continuity. The top section directly above the porous medium was a no-slip wall with a prescribed a heat flux of q" = 10 W/cm$^2$, and the outlet was prescribed a pressure outlet boundary condition.

ANSYS Fluent 19.2 was utilized for the CFD-HT simulations. A second order upwind scheme was used for the momentum and energy equations discretization. The pressure was interpolated using a second order scheme, and the gradients were discretized using the least squares cell based method. The SIMPLE algorithm was used for pressure-velocity coupling. Convergence was reached after the average topside temperature and pressure drop qualitatively leveled off and the residuals dropped below $10^{-3}$ for mass and momentum and $10^{-6}$ for energy. Both pore-scale simulation geometries were examined for mesh independence. This was achieved by refining three separate meshes with u = 10 cm/s and examining both the pressure drop and average surface temperature for convergence. The ERG foam model elements numbered from 2.7 M to 14.8 M, with the coarsest mesh being used for analysis. The AM model ranged from 5.2 M to 14.8 M, and the mesh of 5.2 M elements was selected. Both the solid and fluid domains for the two geometries were meshed using tetrahedral elements.

The samples were tested in the closed flow loop shown in Figure 33. Prior to charging with degassed, DI water, the flow loop was evacuated using a commercial vacuum pump. A gear pump (Micropump® GJ-N27) mounted on a variable-speed gear pump system (Cole-Parmer® EW-75211-30) continuously circulated the working fluid around the loop. The coolant then passed through a liquid-to-liquid heat exchanger (Lytron® LL520FG12) connected to a constant temperature bath (Thermo ScientificTM A25 refrigerated circulator) for finer temperature control, and a flowmeter (McMillan® S-114-8-D-S6) measured the volumetric flow rate. Three pressure sensors (Omega® PX219 series) and in-line type-T thermocouples (Omega® MQSS series) were placed in various locations around the loop for continuous monitoring of both values. For the test section itself, shown in Figure 34c, a differential pressure sensor (Omega® PX2300 series) measured the pressure drop across the samples. Five additional type-T thermocouples were attached to the test section along the midline for calculating the heat transfer coefficient using the average wall temperature, and the data acquisition was handled by an Agilent® 37940A DAQ unit. A liquid-to-air heat exchanger (Lytron® M14-120) cooled the fluid back to near room temperature. A DC power supply (Agilent® E3620A) provided the electrical power necessary for the instrumentation.

The uniform heat flux heating condition was achieved by placing five cartridge heaters into an aluminum block. A DC power supply (Keysight N8742A, 600V, 5.5A) provided electrical power to the heaters. The test samples were nominally 4 cm x 10 cm x 0.93 cm, and the heated section had the same area of 4 cm x 10 cm. A thermal pad was used to decrease the contact resistance between the heater block and the test section. The system reached steady state before data collection, and this was ensured by ensuring the thermocouples measured a < 1 ˚C change over 5 minutes, which was typically reached in 25 minutes between each collection point. The flow rate

was measured by filling a graduated cylinder and timing it while simultaneously recording flowmeter output voltages. The pressure drop was calibrated using an Omega DPI 610 portable pressure calibrator, and the thermocouples were calibrated with an Omega CL122-4 block calibrator.

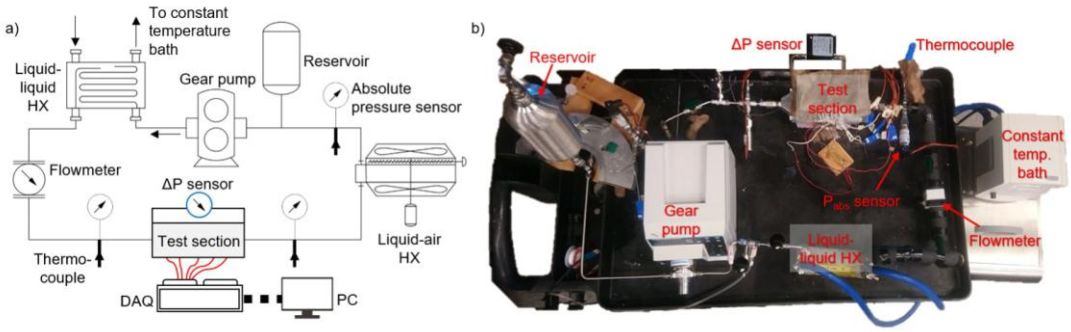


**Figure 33:** a) Schematic and b) image of closed flow loop and data acquisition setup

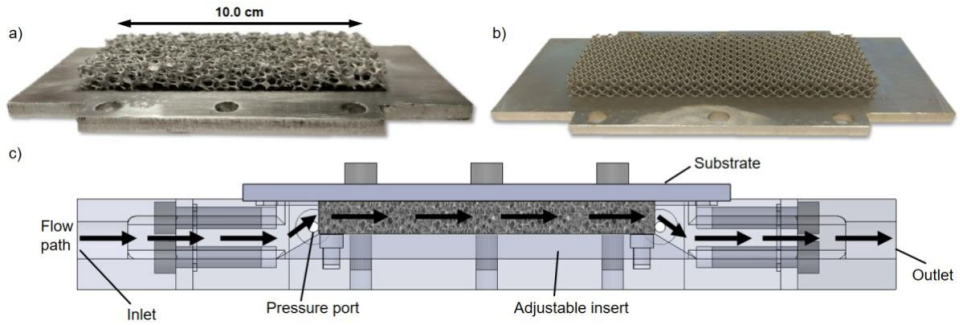


**Figure 34:** a) Stochastic ERG foam with visible thermal epoxy layer, b) designed foam, and c) Test bed used for testing the foam samples

The pressure drop results were curve-fit to a second-order polynomial to conform to the Darcy-Forchheimer Law, which applies to the range studied. A power law fit was selected for the Nusselt number, as is commonly done for thermal behavior with varying Reynolds numbers. Figure 35 showed good agreement between experimental and numerical results, which ensured model validity. Regarding the pressure drops for experimental and CFD datasets, there was a slight behavioral difference for the ERG sample. This was attributed to using a smaller representative section, which does not perfectly replicate the entirety of the foam sample and, therefore, introduces small discrepancies. Modeling more of, or the entirety of the sample, would yield better agreement but at a severe computational cost relative to the small improvements in accuracy. The figure also demonstrated that although the pressure drop is higher (66%) for the AM sample (as to be expected due to the rhombic shape as opposed to the more circular shape of the ERG foams), the penalty came with approximately 60% increase in effective heat transfer coefficient.

Figure 36 compares the non-dimensional thermal performance of the two thermal management solutions with respect to pressure drop per unit length. The increase in pressure drop by using the AM structure contributed primarily to the pore window shape, which was rhombic, instead of a

more circular shape of traditional foams. The pressure drop was approximately 60% higher for the designed structure when compared to the ERG structure, and the Nusselt number was also around 60% higher for the same inlet speeds, as seen in Figure 35. However, when comparing the thermal performance as a function of pumping power, the AM sample was clearly superior at the studied pressure drops.

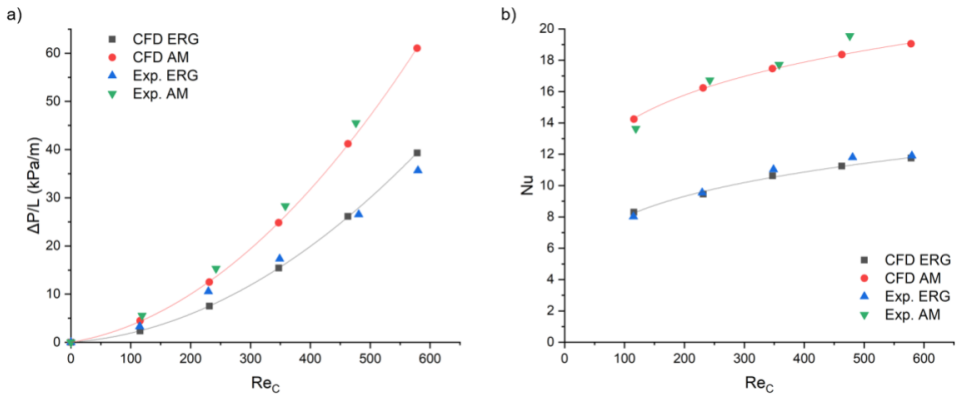


**Figure 35:** a) Pressure drop per unit length (left) and Nusselt number (right) for computational and experimental data for both the ERG and AM samples

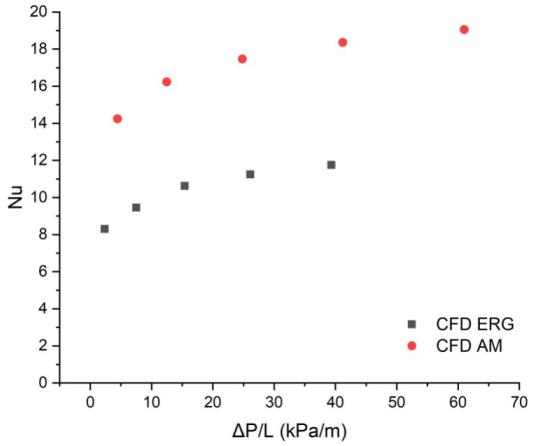


**Figure 36:** Nusselt number of both samples as a function of pressure drop per unit length

In these structures, the variations in local fluid velocity about the mean flow velocity caused mixing and increased heat transfer. Flow mixing can be seen in Figure 37, which shows the streamlines in the ERG foam at two different inlet flow speeds and compares them to the AM sample's streamlines. Unlike pore-level simulations, volume-averaging can decrease computational time at the expense of intrafoam detail. The contribution to heat transfer from mixing was accounted for by augmenting the effective fluid conductivity $k_f$ with the dispersion conductivity $k_d$. Generally, the dispersion conductivity increases with flow speed and streamline tortuosity.

Figure 37a and Figure 37b display the streamlines for u = 2.5 cm/s and 12.5 cm/s with both the streamlines with the solid structure as well as just the streamlines in black without the solid to emphasize the path of the streamlines. It was clearly visualized that the fluid path was more erratic with increasing inlet velocity, which would increase flow mixing and support the assumption of increasing dispersion conductivity with respect to velocity. Examination of the streamlines also illustrated that the majority of the particle paths were not heavily disturbed by the foam, as they traveled in a mostly linear path. This was also confirmed by the later tortuosity calculations, which demonstrated a total average increase in streamline length of 9.3% when compared to the length of the ERG foam.

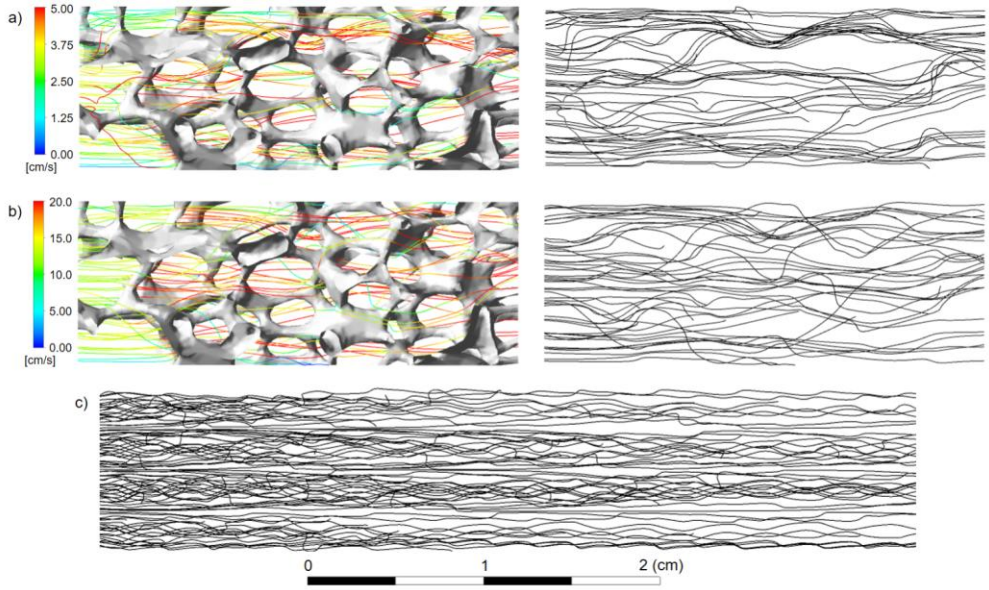


**Figure 37:** Streamlines visualized for a) stochastic geometry with u = 2.5 cm/s and b) u = 10 cm/s, and c) streamlines for the additive manufactured sample with u = 10 cm/s

The streamlines were also compared for the traditional and designed foams. The position coordinates for several hundred particles were exported to MATLAB, where the particle paths were analyzed for their total distance traveled over the foam structure. The code ensured that the tortuosity calculation only used paths that traversed the entirety of the structure (as some streamlines were truncated before exiting the foam). 500 and 161 particles were used after the elimination of the aforementioned incomplete pathlines, respectively. The average distances traveled were 2.732 cm and 4.828 cm for the ERG and AM foams. The tortuosity values were calculated to be 1.093 and 1.038 for the stochastic and AM foam. Increasing $\tau$ corresponds to increasing thermal dispersion conductivities. As the extra distance traveled grew by 2.45x when comparing the ERG and AM samples, it implied that the dispersion conductivity should be greater for the stochastic foam. It was also reasonable to assume that the randomness of the ERG foam promotes greater mixing, and although the effect of the dispersion conductivity is small at these velocities, it may warrant additional investigation at higher flow speeds and Reynolds numbers. Comparing the streamlines for u = 10 cm/s in Figure 37b with those in Figure 37c visually demonstrated the differences in mixing, with some streamlines in the ERG geometry spanning

more than half the breadth of the sample height, as opposed to the AM's streamlines, which did not mix significantly with the fluid in adjacent foam cells.

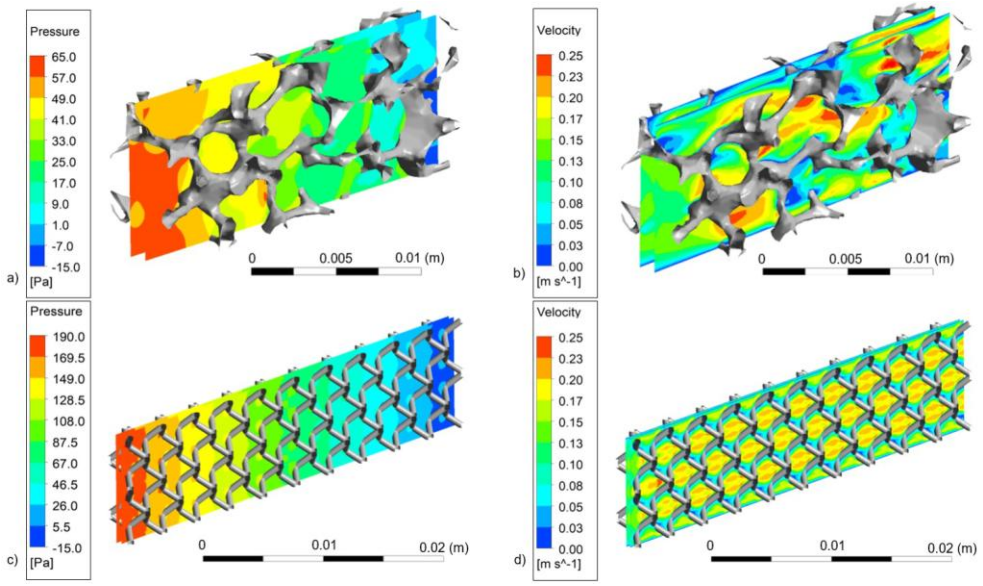


**Figure 38:** Flow fields for u = 10 cm/s for the commercial and AM foams a) Pressure contours, b) Velocity contours, c) Pressure contour, and d) Velocity contour for AM

Figure 38 shows the pressure and velocity contours for the commercial and AM geometries along a plane parallel to the flow direction. The flow patterns for the AM foam repeat due to the ordered structure, whereas a consistent flow pattern was not established for the stochastic sample. Stagnation regions can be seen in both geometries when the working fluid encounters a ligament. Downstream of the ligament, there were recirculation zones where the velocity was significantly lower than the bulk fluid velocity. The pressure values decreased to below 0 Pa relative pressure due to the outlet being constrained to 0 Pa, and the fluid velocities were higher due to the presence of the metal foam. The pressure contours implied significantly more mixing in the stochastic structure due to the uneven contour lines. Another difference between the two structures was the existence of large stagnant zones in the ERG sample, contrasting with the relative lack of such large low-velocity zones in the AM geometry.

While Figure 36 demonstrated the AM sample's superior thermal performance, the causes of improved performance – namely, structural differences in the foam versus elimination of the thermal interface material between the foam and substrate, were further investigated. Using a one-dimensional resistive network (Figure 39a), the effective Nusselt number was recalculated with an updated overall heat transfer coefficient $U_{new}$ for three $k_{TIM}$ values ($k_{TIM}$ = 4.0, 40, and ∞ W/m•K), in addition to the original $k_{TIM}$ (1.38 W/m·K). These values were chosen to be representative of a high-conductivity epoxy, a solder, and no TIM layer.

The results of the calculations can be seen in Figure 39b, where (N) designated the data points obtained by using a resistance network. To ensure the accuracy of the 1D assumption, additional

simulations with $k_{TIM}$ = 4.0 W/m·K were performed, and the numerical results were compared graphically with the resistance network results in Figure 39b. As the numerical and semi-analytical results demonstrated good agreement, the 1D assumption was considered reasonable. The effect of incrementally improving TIM thermal conductivity had a significant impact at lower values. However, the returns diminished at higher $k_{TIM}$ values, and increasing $k_{TIM}$ from 40 W/m·K to effectively infinite had much smaller performance benefits. Figure 39b also shows the effect of eliminating the TIM versus changing the structure to the AM's rhombic dodecahedron unit cell. At lower Reynolds numbers, the difference in Nusselt number was approximately half due to the TIM layer, and the other half was attributed to the structural differences. However, at higher Reynolds numbers, the performance reduction due to the ERG foam structure was much smaller than the TIM's thermal resistance effect. Additionally, the performance of the ERG foam approached the AM foam with increasing flow speeds, which may have been caused by the differences in $k_d$. Generally, the wall heat transfer coefficient is presented for metal foams, as it is more easily applicable for use in electronics cooling via resistance networks and simple numerical simulations. However, the interfacial heat transfer coefficient ($h_{sf}$), which represents the heat transfer between the solid phase and the working fluid, has also been reported and can be used in volume-averaging simulations.

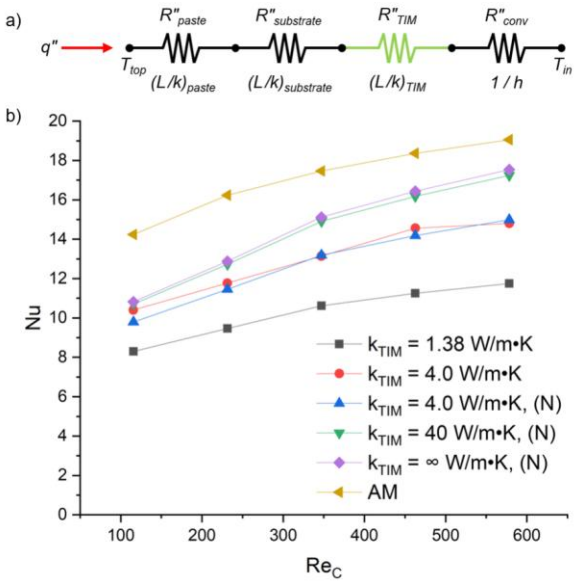


**Figure 39:** Non-dimensional heat transfer performance for AM foam and ERG Inc. foam with varying $k_{TIM}$ values – (N) denotes values found using a resistance network approach

A fin efficiency (η) analysis was conducted for both models, where η is defined as the ratio of convected heat to the heat that would be convected with an ideal fin. For the ideal fin, all solid geometries were set to a uniform temperature of 320 K. The real fin simulations were done by setting the lower substrate surface or the fin base to T = 320 K. Additionally, to provide a more one-to-one comparison of the two foam structures, the heat dissipated by the fluid was measured at 2.5 cm into the AM structure as opposed to at the exit, which was at an additional 2.15 cm downstream. Temperature contours of the solid phase can be seen in Figure 40 for an inlet velocity

of u = 10 cm/s. Increasing $h_{sf}$ and $k_f$ or decreasing $k_s$ were accompanied by a resulting decrease in η, as the heat was convected before it could travel down the finning surface. Figure 40 demonstrates how the temperature decreases more quickly for the ERG foam, which implies that the fin efficiency would be lower. This is shown quantitatively in Figure 41, which illustrates the fin efficiencies, as well as the nondimensional outlet temperatures. The reason the heat was able to penetrate further down the foam was primarily due to the thicker nodes, which allowed for more heat transfer in the fins.

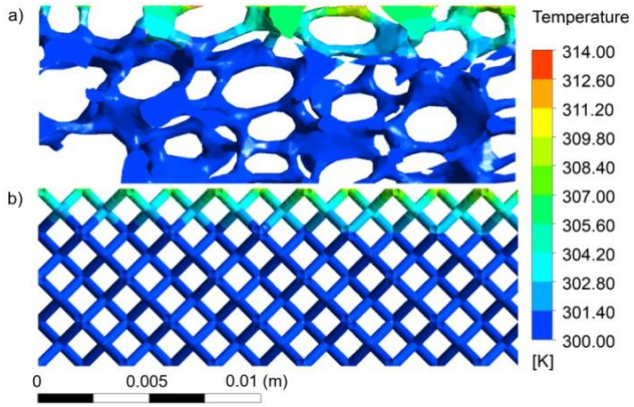


**Figure 40:** Temperature contours for the solid phase for u = 10 cm/s inlet velocity and $T_b$ = 320 K for a) the ERG foam and b) the AM foam

Figure 41a shows that the ERG foam had better fin efficiency than the AM foam, except at lower inlet velocities. Figure 41b illustrates the outlet temperatures at a location 2.5 cm downstream of the foam inlet, which were used for calculating η. Although upon initial examination, it seemed that the commercial foam performs as a better finning surface than the AM foam, the isothermal simulation results for both geometries showed that the AM geometry had a higher heat transfer rate at a given Reynolds number. The AM geometry also transported more heat than the commercial foam in the conjugate heat transfer model, which was due to the TIM and to the AM cell's more favorable geometry, particularly the rhombic windows.

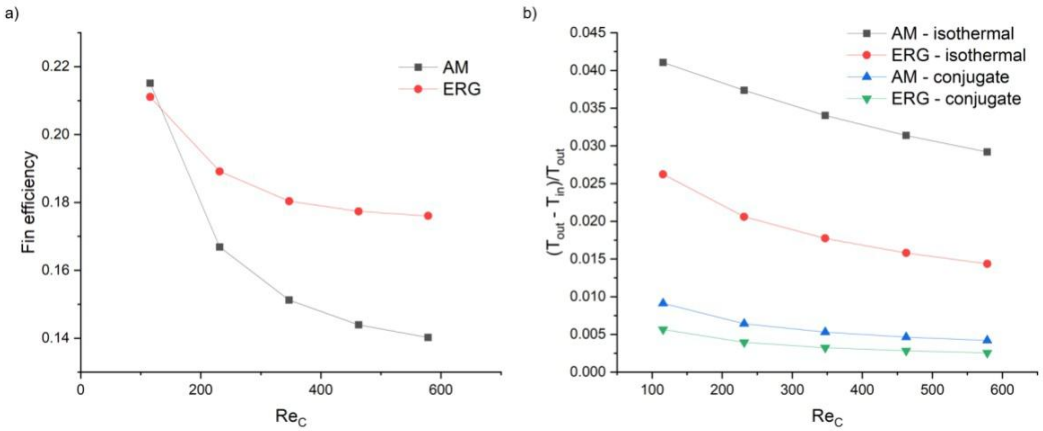


**Figure 41:** a) Fin efficiency for a 2.5 cm sample length and b) nondimensionalized outlet temperature comparison for constant and variable ligament temperature

## 4. Numerical Investigation of Metal Foams and Additive Manufactured Metal Foams for Module-level Cooling

### Summary

Module-level numerical studies were performed on metal foams and additively manufactured metal foams (AMMFs). Initial pore-scale simulations (validated with experimental results) gave closure terms for volume-averaged (VA) simulations, allowing for rapid, module-level simulations. Traditional metal foams were compared with straight fins for module-level thermal management. Additional VA simulations were performed for tailored hotspot cooling structures. They were examined specifically for their ability to locally control relevant parameters to tailor the heat transfer performance. Two geometries – one with local, spanwise densification and another with uniform features throughout – were investigated for the thermal management of several discrete heaters.

### Method

A reduced computational domain (with foam size 9.3 mm x 25.0 mm x 4.65 mm) was used to obtain closure terms for the volume-averaged (VA) simulation. The domain assumed that this region would be representative of the entire foam sample and therefore, give reasonable accuracy. The simulations also assumed a steady-state, laminar, incompressible flow, and neglected viscous dissipation, buoyancy, and radiation.

Figure 42 illustrates the geometry used for pore-scale CFD/HT analysis with a thermal epoxy layer (thickness 0.3 mm, k = 1.38 W/m-K) connecting the substrate to the metal foam. A velocity inlet ranging from u = 2.5 cm/s to 12.5 cm/s with $T_{in}$ = 300 K was applied, and the right boundary was set to a pressure outlet. Both sides were set to a symmetry condition, and the lattice was set as an isothermal no-slip wall at $T_w$ = 320 K.

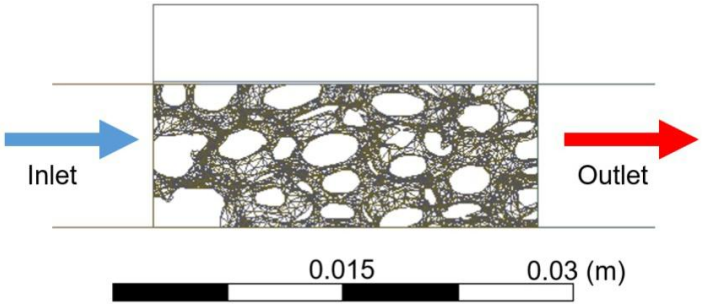


**Figure 42:** Assembly with foam, TIM, and substrate used in pore-scale CFD/HT simulations

The pore-scale pressure drop per unit length and interfacial heat transfer coefficient were calculated using isothermal boundary conditions for the metal foam structure. The results are given as functions of inlet velocity in Figure 43. The interfacial heat transfer coefficient ($h_{sf}$) was calculated and then fitted to a power law equation, and the effects of the varying Prandtl number

due to the water's temperature dependence were lumped into other terms. For $a_{sf}$, the specific surface area (SSA) was multiplied by the simulated foam volume. The SSA was calculated using the correlation from Inayat et al. [6], based on the tetrakaidecahedron approximation of foam morphology. The correlation yielded the sample's SSA to be 509.1 $m^2/m^3$.

Fitting the data to a second-order polynomial allows the values for the permeability (K) and inertial coefficient ($C_f$) to be extracted, and they were found to be $2.421 \times 10^{-7}$ $m^2$ and 0.108, respectively. The $R^2$ value for both of the trend lines was greater than 0.99, demonstrating the validity of these selected curve-fits.

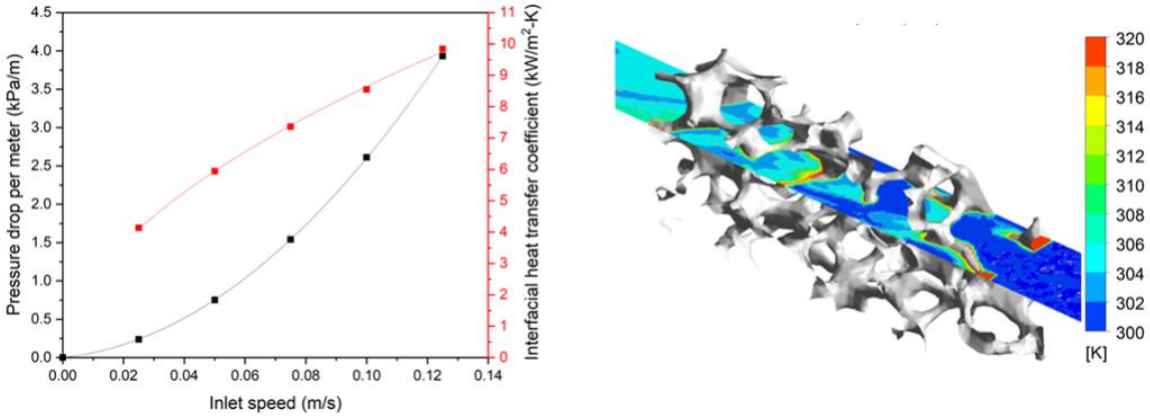


**Figure 43:** ΔP/L and $h_{sf}$ for isothermal simulations (left) and an associated temperature contour for u = 10 cm/s (right)

The VA parameters (K, $C_f$, $a_{sf}$, $h_{sf}$, and $k_d$) were put into a uniform heat flux model to experimentally verify the computational results and ensure reasonable accuracy before proceeding. ANSYS CFX 19.2 was used for the VA CFD/HT analysis.

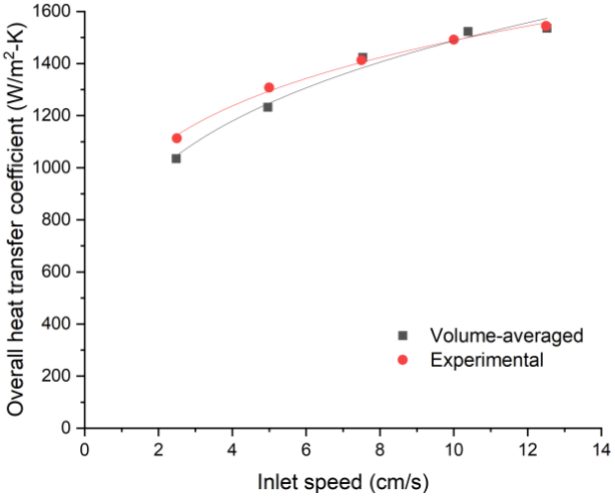


**Figure 44:** Overall heat transfer coefficient for the VA and experimental results

Two geometries were used for the three cases studied, which are shown in Figure 45. The geometric parameters for the simulations can be seen in Table 4. Both simulated five 1 x 1 cm silicon heat sources in order to simulate silicon power devices. The first case was for a metal foam-filled channel with the thermal interface material's k = 1.38 W/m·K. The second case used the latter straight-finned geometry. The final case used the first geometry but with $k_{TIM}$ = 40 W/m·K. A velocity inlet (ranging from 2.5 cm/s to 12.5 cm/s with $T_{in}$ = 300 K) and a pressure outlet were defined, and a heat flux of 100 W/cm$^2$ was applied to the top side of each chip heater.

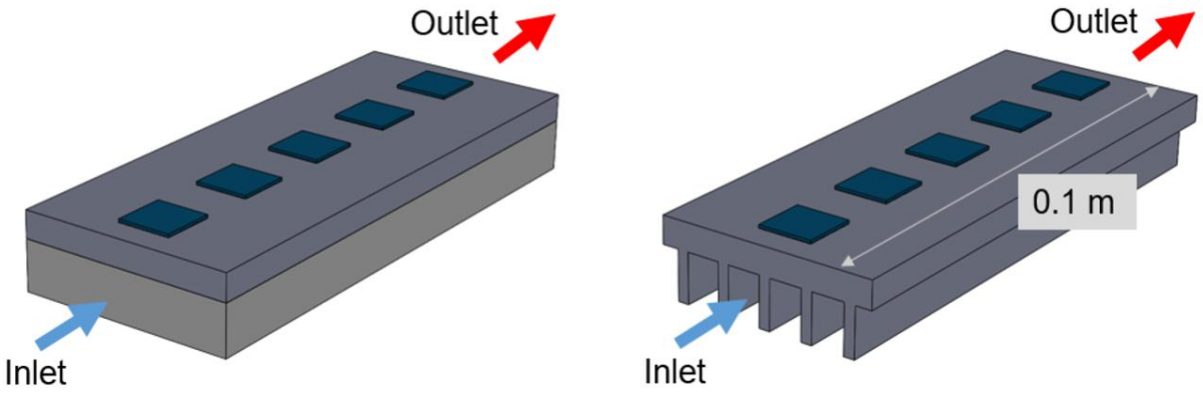


**Figure 45:** Module-level geometries using metal foam (left) and straight fins (right)

**Table 4:** Geometric parameters used for module-level simulations

| Geometry | Dimensions (mm) | *k* (W/m·K) |
|---|---|---|
| Heaters | 10 x 10 x 0.5 | 130 |
| Die attach | 10 x 10 x 0.1 | 200 |
| Substrate | 100 x 40 x 5 | 120 |
| Foam section | 100 x 40 x 9.3 | 160 |
| Fins | 100 x 2 x 9 | 120 |

**Results**

Figure 46 (left) illustrates the average chip temperature rise above the inlet temperature for the three thermal management schemes discussed. At lower speeds, the foam is superior even with poor epoxy thermal conductivity. However, at higher inlet velocities, the thermal performance degradation from the thermal epoxy connecting the foam and substrate causes the finned solution to be superior with regard to both pressure drop and chip temperature. Replacing the foam's low conductivity epoxy with a higher performing option (with thermal properties more similar to that of a solder) yields much more favorable results. The foam dissipates heat much more effectively, with a temperature rise of ~60 K as opposed to 87 K and 76 K. Figure 46 (right) shows the temperature contours for both interface material conductivities, and it is found that the decreased

thermal resistance causes the module to be ~20 K cooler. As some thermal degradation mechanisms have an inverse relationship with temperature, using a foam with a higher-performing thermal interface material may be the superior option despite the higher pressure drop penalty.

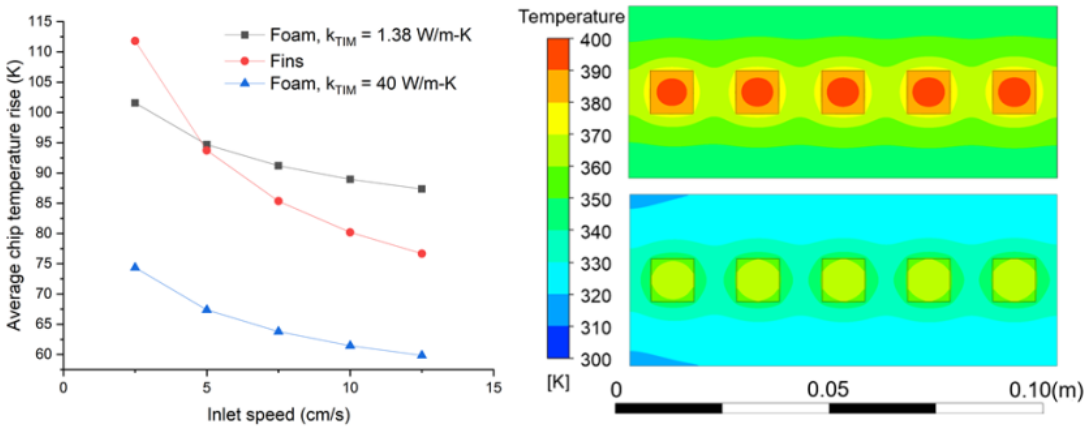


**Figure 46:** Average chip temperatures for module-level geometry simulations (left) and temperature contours using foams with $k_{TIM}$ = 1.38 W/m·K (top) and $k_{TIM}$ = 40 W/m·K (bottom) for u = 10 cm/s and q" = 100 W/cm2 (right)

Figure 48 compares the simulated modules' specific thermal resistances with the 2012 Nissan Leaf and the 2014 Honda Accord's inverters. Due to equipment limitations, the simulated flow rates were significantly lower than typical for EV inverters. However, it can be seen that the thermal resistances are comparable to the direct cooling module of the Honda Accord, even at flow rates that are over a magnitude lower. Additional benefits regarding weight and potential cost can be realized by using metal foams, which are both typically lighter per unit volume, and the decreased material required may improve costs.

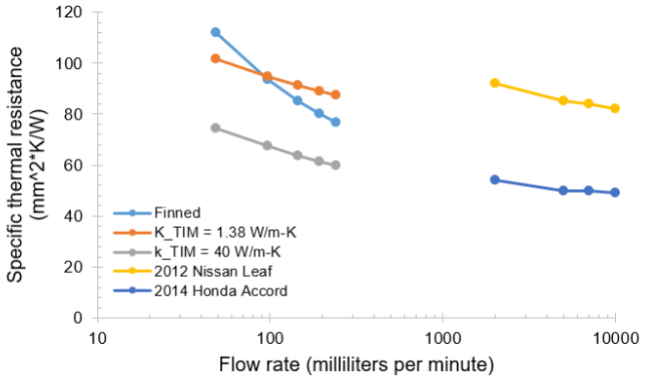


**Figure 47:** Comparisons for the discussed solutions versus commercial inverter modules from [7]

Two pore-scale models were used in this work. Pore-scale models of the 5 and 30 PPI AM foams (seen in Figure 48) were imported into ANSYS Workbench, and Fluent 19.2 was used for analysis. The geometric parameters for both PPI sizes are presented in Table 5. An isothermal simulation (constant temperature applied to the topside and the foam structure) and a conjugate heat transfer

simulation (with only topside heating) were performed to find the interfacial heat transfer coefficient and pressure drop as a function of inlet speed.

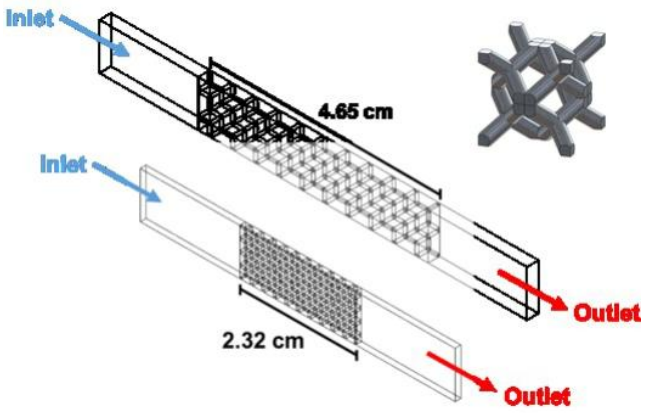


**Figure 48:** 5 PPI pore-scale model (top) and 30 PPI pore-scale model (bottom) with unit cell shown

**Table 5:** Geometric parameters list for both PPIs

| Parameter | Smaller PPI | Larger PPI |
|---|---|---|
| *PPI* | 5 | 30* |
| *Porosity* | 86.5% | 73.0% |
| *Ligament diameter (mm)* | 0.548 | 0.398 |
| *Ligament length (mm)* | 2.014 | 1.001 |
| *Pore diameter (mm)* | 1.35 | 0.55 |
| *Cell diameter (mm)* | 4.65 | 2.325 |
| *SSA* ($m^2m^{-3}$) | 927.4 | 2465 |

Figure 49 shows the pressure drop per unit length and the interfacial heat transfer coefficient for both the 5 and 30 PPI foams as functions of inlet speed and the accompanying equations. $K$ and $C_f$ are given in Table 6.

**Table 6:** Hydraulic closure terms for VA simulations

| Parameter | Smaller PPI | Larger PPI |
|---|---|---|
| $K$ ($10^{-8}$ $m^2$) | 9.340 | 1.398 |
| $C_f$ | 0.094 | 0.191 |

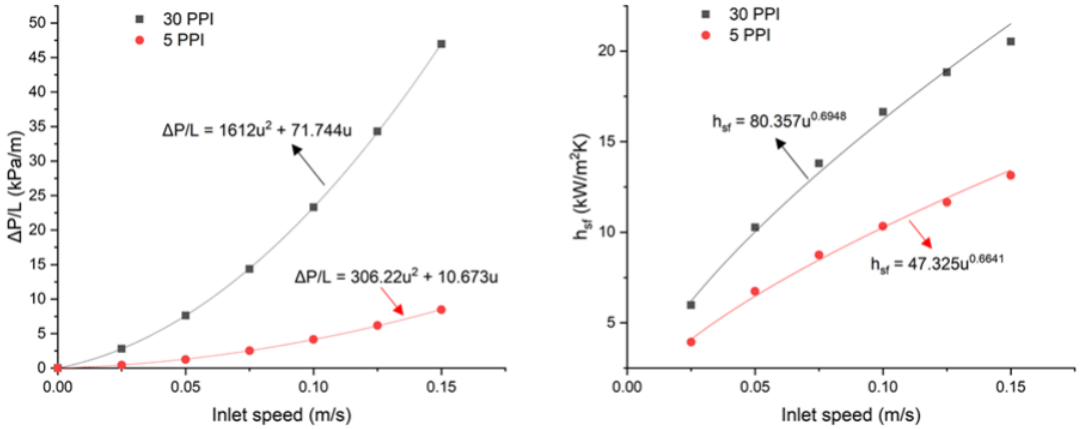


**Figure 49:** Pressure drop (left) and interfacial heat transfer coefficients (right) for pore-scale models

The accuracy of the closure terms was first investigated by comparing the two isothermal models. The pressure drop and heat rejection demonstrated excellent agreement. Figure 50 (left) displays the total heat rejected by both 5 and 30 PPI isothermal models. However, Figure 50 (right) demonstrates the error from not properly weighing $k_{s,eff}$ by a factor to account for its geometry. The model consistently over-predicted the convected heat by approximately 35%. The results show excellent agreement after incorporating a reduction in effective solid thermal conductivity to account for tortuosity τ. The solid thermal conductivity was iteratively adjusted until the agreement was satisfactory.

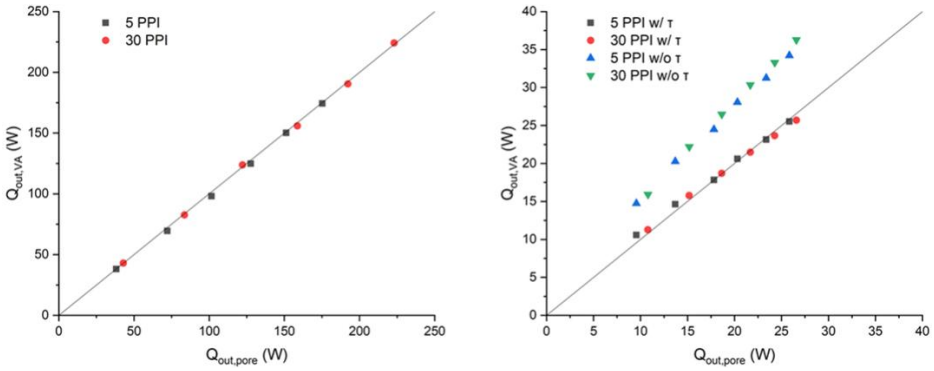


**Figure 50:** Isothermal (left) and conjugate model (right) comparisons of heat rejected for VA and pore-scale simulations

Two configurations representative of a typical power electronics assembly were used for coupled CFD/HT simulations with volume-averaging to demonstrate the ability of localized cooling for higher heat flux sources. Both configurations, seen in Figure 51, use five chip heaters mounted onto a substrate with a die attach. The first geometry (referred to as uniform geometry) uses a uniform metal foam for convective heat transfer, and the second (referred to as hotspot mitigation geometry) uses the 30 PPI metal foam characterized earlier for a densified middle section in addition to the 5 PPI designed foam on either side.

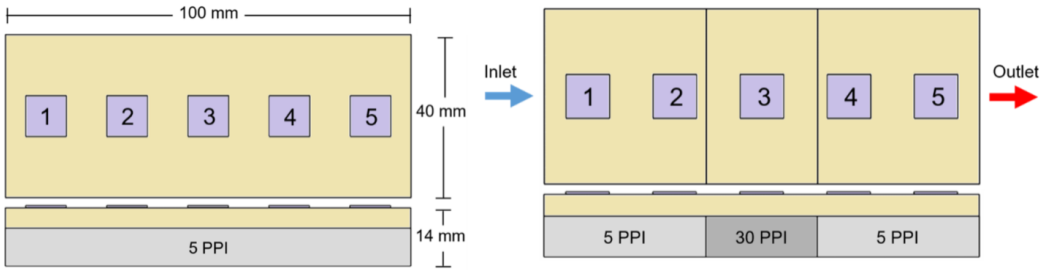


**Figure 51:** Assembled geometries with uniform foam PPI (left) and hotspot mitigating structure (right)

**Table 7:** Parameters for full-scale simulations

| Geometry | Dimensions (mm) | k (W/m·K) |
|---|---|---|
| Heaters | 10 x 10 x 0.5 | 130 |
| Die attach | 10 x 10 x 0.1 | 200 |
| Substrate | 100 x 40 x 5 | 117 |
| Uniform 5 PPI | 100 x 40 x 9.3 | 173 |
| Hotspot 30 PPI section | 25.6 x 40 x 9.3 | 173 |
| Hotspot 5 PPI section | 37.2 x 40 x 9.3 | 173 |

The geometric and relevant thermal parameters for the following steady-state full-scale simulations can be seen in Table 7. Heaters 1, 2, 4, and 5 were set with constant heat fluxes of 150 W/cm$^2$. Heater 3 had heat flux boundary conditions of 150–250 W/cm$^2$. The foam sections were set as porous domains, and velocity inlet and pressure outlet conditions were applied at the surfaces nearest to chips 1 and 5. All remaining boundary walls were set as adiabatic.

The effects of hotspots for varying flow speeds are demonstrated in Figure 52. The heat spreading in the substrate can also be seen in these graphs as the temperatures of 4 and 5 are similar for the uniform structure. Heater 3 influences the temperatures as the higher heat fluxes spread out towards the adjacent heaters. As shown for both scenarios, the effects of increasing flow speed decrease, and chip temperatures begin approaching a minimum. This is due to the significant resistances aside from the convective resistance. The resistance network has, in addition to the convective resistance of the metal foam, components from the heater, die attach, spreading in the substrate, and through-resistance of the substrate. Even if the convective resistance were to be eliminated, the maximum temperatures would remain thermally bottlenecked by the remaining elements.

Figure 53 shows the pressure drop for both structures. Although the low-pressure drops make pumping power less of a priority than other systems, a locally densified (instead of spanwise densified) structure may mitigate the pressure drop. However, as the current setup has significant heat spreading, so more targeted thermal management may improve pressure drop but at the cost of hotspot management.

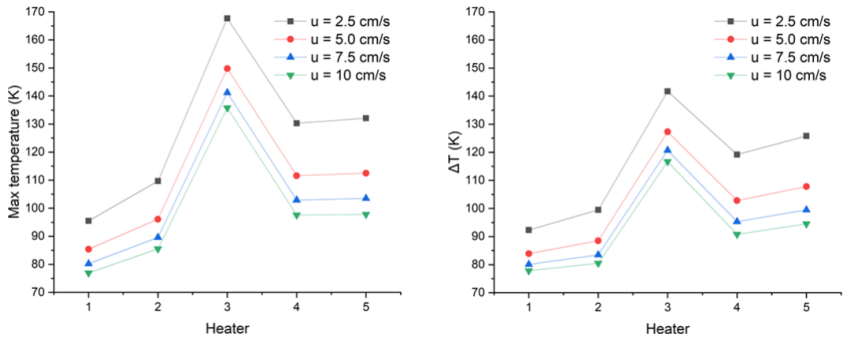


**Figure 52:** Temperatures for u = 2.5, 5.0, 7.5, and 10.0 cm/s for uniform (left) and hotspot mitigating (right)

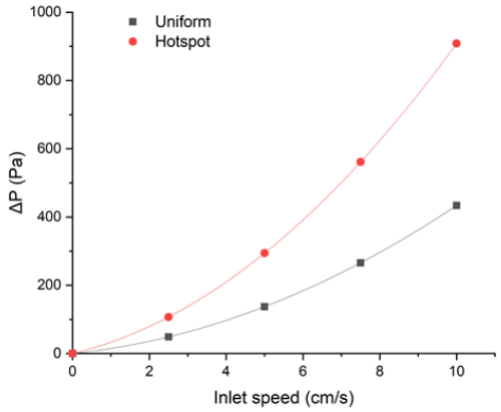


**Figure 53:** Pressure drop for both geometries

## 5. Computational Investigations of Flow Boiling in Alternative Geometry Microchannels

### Summary

This research task numerically investigates several passive methods of mitigating microchannel thermohydraulic instabilities and compares it to a baseline case. The purpose of this was to investigate a problem with more readily available experimental data while simultaneously gaining experience in the complexities of modeling flow boiling and researching a compelling research area that has been scarcely addressed. This work was then leveraged for experimental and numerical flow boiling in AMMFs, which is a more complex problem with no available prior literature for AMMF flow boiling simulations. Four separate cases (straight, constricted, diverging, and auxiliary jetting flow microchannels) representing singular 3D microchannel geometries of similar dimensions were simulated using the volume of fluid (VOF) method for interface generation. The effects of implementing these strategies are compared and evaluated with regard to overall thermohydraulic performance. The flow regimes from the computations are compared to flow regime maps in the literature. The advantages of CFD/HT simulations are leveraged to

closely examine the bubble dynamics, and heat transfer and pressure drop characteristics as well as bubble dynamics, were evaluated against available literature.

**Model**

The present models use the VOF model, which was implemented using the commercial software ANSYS Fluent 2020 R1. The current task examines four different geometries, the first being a baseline and the latter three utilizing instability mitigation methods experimentally demonstrated in the literature. In order to make the comparison as direct as possible, the geometric parameters remain the same for all cases whenever feasible. Table 8 shows the geometric parameters and inlet mass flux conditions. Each configuration has the same heated section length L =10.5 mm and an adiabatic entrance length $L_{ent}$= 0.5 mm. The total width of each assembly is constant at 300 µm. Figure 54 illustrates the baseline straight microchannel configuration (referred to as case 1). The fin height $H_1$ and thickness $d_1$ are 250 µm and 50 µm, respectively, wherein the values for the case number are denoted with a subscript of the same number. The substrate, upon which the fins are mounted, has a thickness t1 of 50 µm, and the channel width $W_1$ is 200 µm. A mass flux condition G = 1,000 kg/m$^2$·s is applied at the inlet, and a pressure outlet condition with a gauge pressure of 0 Pa and backflow temperature of 373.15 K is applied at the outlet. These operating conditions give a Reynolds number $Re_{L0}$ = 790 (with the characteristic length defined as the hydraulic diameter) and a Prandtl number of Pr = 1.74. A heat flux condition q" = 200 W/cm$^2$ is applied at the heated wall, which is indicated on the geometries with bold or dashed red lines.

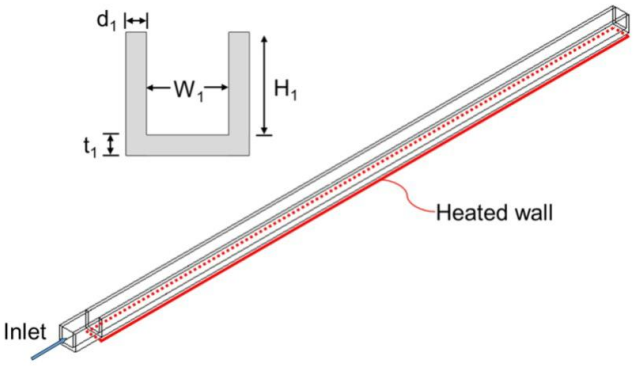


**Figure 54:** Computational geometry for baseline straight microchannel (case 1)

Test cases 2 – 4 are shown in Figure 55 through Figure 57. Figure 55 shows frontal and partial topside views of the inlet for case 2 – a microchannel with a constricted inlet. Inlet constriction, also referred to as upstream throttling, increases pressure requirements for upstream expansion and the accompanying instabilities. Case 2 has the same dimensions as case 1, except for the adiabatic entrance section. Whereas the base thickness $t_2$ and fin height $H_2$ are the same as for the benchmark simulations, the inlet channel width $W_2$ is 40 µm, or a fifth of the baseline value, and consequentially, the fin thickness $d_2$ is increased to 130 µm.

**Table 8:** Geometric parameters and simulation setup for the four cases

| Parameter | Case 1 | Case 2 | Case 3 | Case 4 |
|---|---|---|---|---|
| Fin thickness (μm) | $d_1$ = 50 | $d_2$ = 50<br>$d_{ent,2}$ = 130 | $d_3$ = 50 | $d_4$ = 50 |
| Channel width (μm) | $W_1$ = 200 | $W_2$ = 200<br>$W_{ent,2}$ = 40 | $W_3$ = 200 | $W_4$ = 200 |
| Channel height (μm) | $H_1$ = 250 | $H_2$ = 250 | $H_{3,i}$ = 250<br>$H_{3,o}$ = 424 | $H_4$ = 250 |
| Substrate thickness (μm) | $t_1$ = 50 | $t_2$ = 50 | $t_{3,i}$ = 224<br>$t_{3,o}$ = 50 | $t_4$ = 50 |
| Total length (mm) | $L_{tot}$ = 10.5 | $L_{tot}$ = 10.5 | $L_{tot}$ = 10.5 | $L_{tot}$ = 10.5 |
| Entrance length (mm) | $L_{ent}$ = 0.5 | $L_{ent}$ = 0.5 | $L_{ent}$ = 0.5 | $L_{ent}$ = 0.5 |
| Mass flux ($kg \cdot m^{-2} \cdot s^{-1}$) | $G_1$ = 1,000 | $G_2$ = 5,000 | $G_3$ = 1,000 | $G_4$ = 625.6<br>$G_{4,jet}$ = 4,793 |

The diverging microchannel geometry shown in Figure 56 expands at an expansion angle θ = 1˚ beginning after the adiabatic entrance. These geometries are also termed expanding microchannels due to the increasing cross-sectional channel area. The increase in area promotes downstream bubble growth due to channel divergence as well as surface tension force differences. As a result of the expansion, the entrance substrate thickness $t_{3i}$ increases while the entrance fin height $H_{3i}$ remains the same as cases 1 and 2 at $t_{3i}$ = 224 μm and $H_{3i}$ = 250 μm. The outlet substrate thickness $t_{3o}$ and fin height $H_{3o}$ measure 424 μm and 50 μm. $W_3$ and $d_3$ measures are the same as those in the baseline case. The final case examined is an auxiliary jetting microchannel seen in Figure 57. The introduction of liquid after flow boiling begins has shown to improve thermohydraulic performance, as well as flow instabilities by accelerating bubble collapse and disrupting/suppressing bubble growth. Figure 57b gives magnified views of the auxiliary jet. The jet's center is located at the midpoint of the heated length L, and it spans the breadth of the channel with a width $W_{jet}$ of 20 μm. A mass flux (G) condition of 1,000 kg/m$^2$·s with $T_{in}$ = 373 K is applied at the inlet for case 1 and case 3, but cases 2 and 4 required adjusting G to maintain equivalent mass flow rates. For case 2, the mass flux was increased fivefold to 5,000 kg/m$^2$·s so that the mass flow rate at the start of the diabatic section would be equivalent to the benchmark case. Case 4 was also adjusted accordingly to be 625.6 kg/m$^2$·s for the primary inlet, which accounted for an inlet velocity of 5 m/s at the jet inlet. For all scenarios, a pressure outlet condition with a gauge pressure of 0 Pa is applied at the outlet, and a heat flux q" = 200 W/cm$^2$ is applied at the heated wall (indicated on the geometries with bold or dashed red lines). The remaining walls were adiabatic.

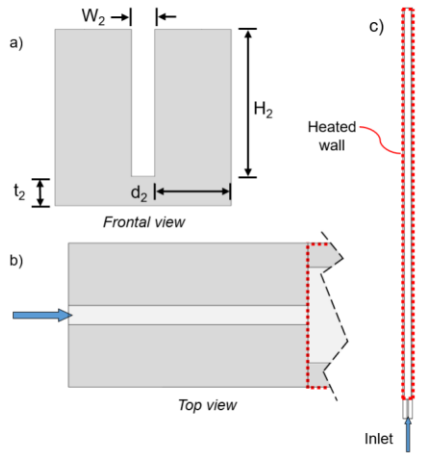


**Figure 55:** a) Frontal view and b) top view of inlet constriction, and c) full top view of constricted inlet microchannel geometry (case 2)

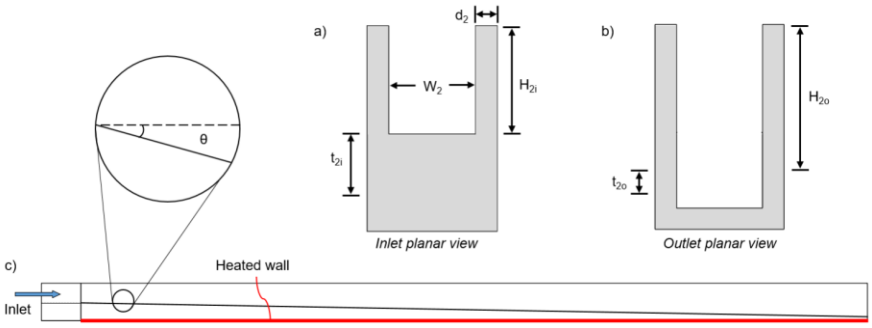


**Figure 56:** Views of diverging microchannel geometry (case 3) with θ = 1˚ showing a) inlet, b) outlet, and c) side profile

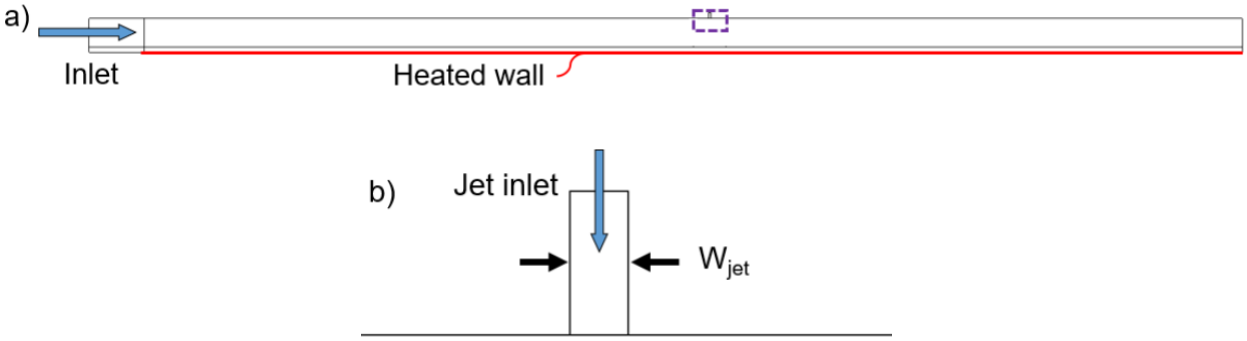


**Figure 57:** View of case 4 (auxiliary jetting microchannel) showing a) side view of the assembly with close-up location indicated and b) close-up of auxiliary jet

The CFD/HT models assumed the following:
1) Transient laminar flow
2) Continuum flow (Knudsen number Kn = 0.0018 when $u_v$ = 30 m/s)
3) Negligible radiative heat transfer
4) Constant material properties
5) Negligible viscous dissipation

Table 9 lists the thermophysical properties used in the simulations. Water was used as the coolant with the properties given at a saturation temperature Tsat at 100 ˚C at atmospheric pressure. The solid phase (fins and substrate) was pure copper, and the properties were also chosen at a temperature of 100 ˚C.

**Table 9:** Thermophysical properties of materials used in the present simulations for T = 100 ˚C from the Engineering Equation Solver software

| Property | Symbol | Copper | Liquid water ($T_{sat}$ = 100 ˚C) | Water vapor ($T_{sat}$ = 100 ˚C) |
|---|---|---|---|---|
| Density (kg·m$^{-3}$) | $\rho_{Cu}$, $\rho_l$, $\rho_v$ | 8924 | 958.5 | 0.5951 |
| Thermal Conductivity (W·m$^{-1}$·K$^{-1}$) | $k_{Cu}$, $k_l$, $k_v$ | 392.8 | 0.6828 | 0.02459 |
| Specific heat (J·kg$^{-1}$·K$^{-1}$) | $c_{Cu}$, $c_l$, $c_v$ | 3681 | 4216 | 2079 |
| Dynamic viscosity (Pa·s) | $\mu_l$, $\mu_v$ | – | 2.822 x 10$^{-4}$ | 1.226 x 10$^{-5}$ |
| Surface tension coefficient (N·m$^{-1}$) | $\sigma$ | – | 0.05894 | |
| Latent heat of vaporization (kJ·kg$^{-1}$) | $h_{fg}$ | – | 2257 | |

ANSYS Fluent 2020 R1 was used to solve the governing equations using the finite volume method. The single-phase solution was solved for each simulation to implement as the initial condition to the two-phase solutions in order to increase numerical stability. The converged single-phase solution (as indicated by the convergence of total pressure drop across the domain) was then used as solution initialization for a constant temperature solution. In this secondary initialization, identical boundary conditions to the boiling simulations described earlier were used, with the exception of the heat flux condition. An estimated wall temperature was used in lieu of said boundary condition to allow for faster convergence, as the thermal capacitance of the solid regime requires longer simulation times to reach quasi-steady-state. Finally, after quasi-steady-state was qualitatively reached with volume fractions and pressure drop values steadying, the topside boundary condition was switched to a heat flux condition. The simulation time was reset, the accompanying data files were imported into the two-phase case file, and the boiling simulation was initiated with a prescribed wall heat flux. The heat flux condition case was run for an additional period at which point the temperature and volume fraction reached quasi-steady state, defined as < 2% and < 5% change over 0.5 ms in these respective parameters, following which the simulation times were reset. The pressure drop was not an explicitly quantified quasi-steady state requirement, as the values can vary significantly with each time step, leading to occasional spikes due to bubble formation.

Gradients were discretized using the least squares cell-based method, pressure and velocity were coupled using the SIMPLE algorithm, and the PRESTO! scheme was used for pressure discretization. The second-order upwind scheme discretized both momentum and energy equations. Values of $10^{-3}$ and $10^{-6}$ were set as the convergence criteria for mass and momentum

equations and energy equations, respectively, with 20 iterations per time step. The explicit VOF formulation with a Courant number (*Co*) of 0.25 was employed. The time step depended on the global *Co* which was set to 1, with resulting time steps typically around 0.2 μs. The simulations were performed using a high-performance computing cluster, utilizing 192 cores in AMD EPYC 7281 processors in parallel, with each solution requiring approximately 1 week of runtime, due to the small time steps resulting from high vapor velocities and relatively small mesh size.

**Table 10:** Mesh independence analysis via surface temperature and pressure drop comparison

| Mesh | Elements | $\Delta P$ (kPa) | $\lvert(\Delta P^k - \Delta P^{k+1})/(\Delta P^k)\rvert$ | $T_w$ (K) | $\lvert(T_w^k - T_w^{k+1})/(T_w^k - 373)\rvert$ | Flow regime |
|---|---|---|---|---|---|---|
| 1 | 117,075 | 11.2 | 45.6% | 389.9 | 6.29% | Slug |
| 2 | 236,616 | 20.6 | 4.04% | 388.9 | 7.56% | Annular |
| 3 | 483,264 | 19.8 | 2.59% | 390.2 | 1.15% | Annular |
| 4 | 945,000 | 19.3 | – | 390.4 | – | Annular |

A mesh independence study was done with the benchmark case 1 geometry with identical inlet mass and heat flux. The simplicity of the computational domain allowed for a mesh that utilized exclusively hexahedral elements, which can improve accuracy and decrease cell counts. For mesh convergence verification, the baseline case geometry was used, with mesh elements that approximately doubled across each finer mesh iteration. Four meshes of increasing fineness, seen in Table 5-3, were compared by examining the topside wall temperature, net pressure drop, and flow regime. Although the nature of boiling is inherently transient, the simulations were defined as quasi-steady-state when the area-averaged temperature of the heater, void fraction, and net pressure drop across the entire microchannel steadied. The percentage change in surface temperature and pressure drop (averaged over 2 ms) was calculated for each mesh iteration, with the criterion < 3% change being chosen as sufficient for mesh independence. The mesh analysis also comes with a qualitative assurance that the flow regime no longer changes with increasing mesh fineness, demonstrated by the flow regime remaining annular for meshes 2 through 4.

Figure 58 shows the spatially evolving flow regimes in the baseline case microchannel. The regime is briefly bubbly flow at the entrance (Figure 58a), and the bubbles are primarily generated closer to the finned walls and substrate. But it rapidly evolves into churn and then confined annular flow, which combine to occupy the significant majority of the microchannel. Figure 58b shows the highly disturbed phases characteristic of churn flow. Similar to bubbly flow, the effect of conduction along the fins can be seen in that there is more vapor generation near these features. More than half of the heated section of the microchannel is confined annular flow (Figure 58c), where the vapor core and thin annulus occupy the entire microchannel cross-section with sparse liquid droplets entrained in the vapor core. This analysis could also be applied to the other case geometries, albeit with less confidence due to the modified configurations. The flow regime map predicted cases 1 and 2 to be churn/annular, case 3 to be confined slug flow at the outlet due to the

increase in cross-sectional area), and case 4 was predicted to be confined slug before the jet and churn/annular after. The different flow regimes for each case can be seen in Figure 59. As predicted, cases 1 and 2 are primarily churn/annular, case 3 is confined slug, and case 4 is confined slug then annular, except for where the auxiliary jet has collapsed the bubble.

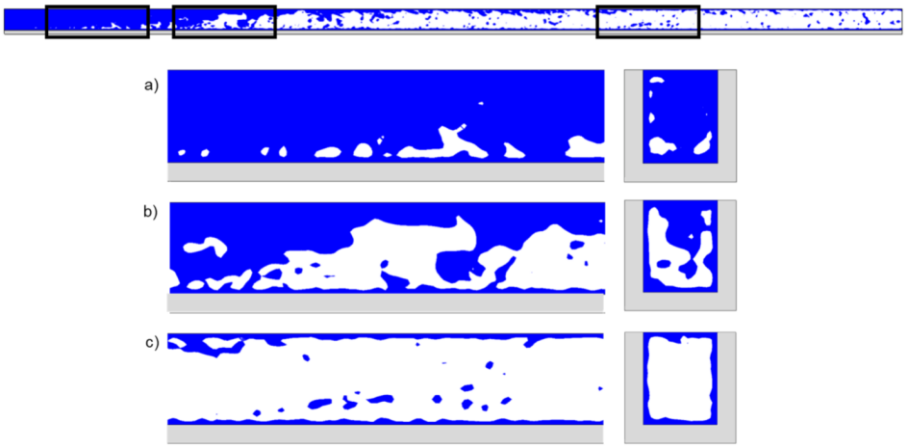


**Figure 58:** Liquid (blue) and vapor (white) regime visualization in baseline case showing magnified side views along the centerline and frontal views normal to flow direction of a) bubbly flow, b) churn flow, and c) confined annular flow phase contours

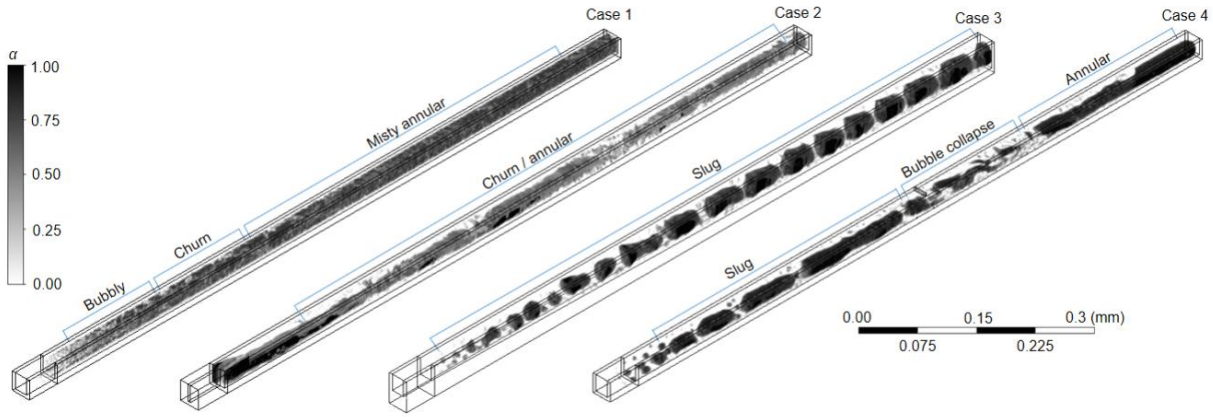


**Figure 59:** Void fractions volume renderings for each case after quasi-steady-state, showing flow regimes

Case 2 saw a moderate increase in pressure drop while the thermal performance was relatively unaffected. However, inlet restrictors have been shown to improve stability not by the same mechanisms of cases 3 and 4 but rather by altering the internal boiling pressure curve. Microchannel flow boiling systems often see instabilities associated with the negative sloped portion of the curve, and the inclusion of inlet restrictors can eliminate this portion to the effect of higher pressure drops and mitigated instabilities.

Cases 3 and 4 showed improvements in both two-phase heat transfer coefficient and net pressure drop. For case 3 (the expanding geometry), there is the benefit of increased surface area (12.5%), but this is not sufficient to explain the noticeable improvements in surface temperature or the $h_{tp}$. The change in ΔP is mostly a result of the acceleration pressure drop decrease – ΔPa in the baseline accounts for 12.4 kPa or 64% of the total pressure drop. Case 4's pressure drop was likewise affected by the bubble collapse, which decreased the outlet void fraction and, consequentially the outlet velocity (see Figure 60) and acceleration pressure drop. The centerline velocities at a representative time show that cases 1 and 2 have similar profiles and magnitudes, with the most significant and obvious exception being an elevated inlet speed for case 2. The inlet-restricted geometry also shows very low velocities right after the inlet, resulting from low-velocity vapor recirculation zones. Cases 3 and 4 demonstrate significant decreases in magnitude from ~30 m/s to ~6 m/s and ~15 m/s, respectively. The diverging microchannel shows regular peaks and valleys in velocity correlating to the vapor and liquid slugs, with a constant, slow rate of increase. The auxiliary jetting case, which shows the velocity speeds at a time during downstream bubble collapse, shows somewhat constant velocities around after the secondary inlet due to the bubble collapse and mixing.

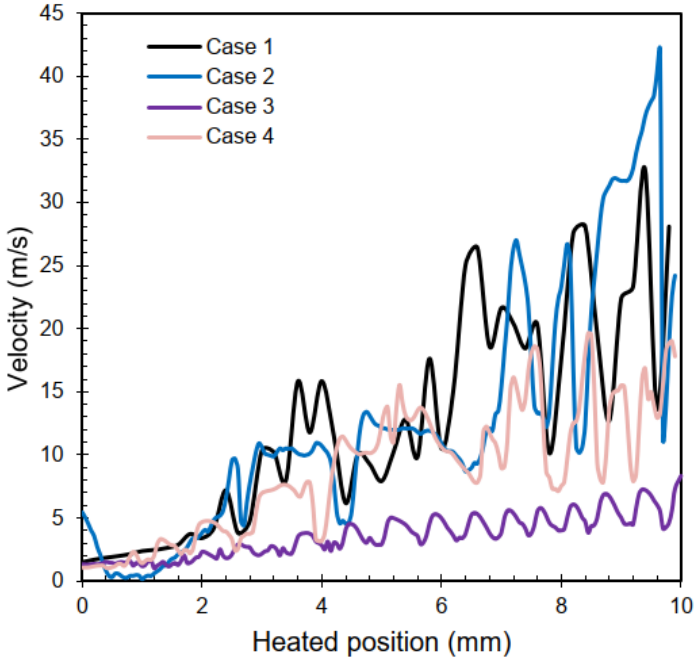


**Figure 60:** Centerline velocities for all cases at representative time steps. Case 4 is at a time step where the bubble is collapsing and increasing mixing downstream of the jet

Examination of the restricted microchannels showed a somewhat different flow regime and some bubble behavior resulting from the inlet constriction. Cases 1 and 2 can both be defined as the same regime (i.e., annular) according to either flow regime map. However, the specific regimes would differ, where case 1 can be specified as annular mist flow and case 2 as wavy annular. Additionally, the inlet restriction creates a jetting effect, where the high-velocity saturated liquid penetrates into the diabatic section. Figure 61a gives a top view of the void fraction, where the

flow regime is primarily wavy annular. Additionally, the entire channel is filled with vapor, as shown in Figure 61a, whereas the baseline and other cases have spatially varying regimes and different bubble sizes, progressing from bubbly to slug to misty annular. And where all three other cases have bubbly flow and the characteristic small vapor bubbles near the inlet, two distinct vapor bubbles – one smaller and one larger that eventually merge with the downstream vapor – have accumulated near the case 2 inlet (Figure 61b). This is due to the two low-velocity zones located on either side of the inlet jet. The jet stream's viscous effects drag a portion of the bubbles along with it, and the wall heating combines with this to cause the vapor bubbles to recirculate, as illustrated by Figure 61c. The bottom vapor bubble's size results in multiple smaller recirculation zones reminiscent of natural convection cells (Figure 61d). The two recirculating bubbles straddling the restricted inlet measure 0.47 mm and 1.71 mm. The strong jetting effect dissipates with the end of the larger recirculating bubble zone, after which the velocity increases gradually due to vaporization and corresponding acceleration effects.

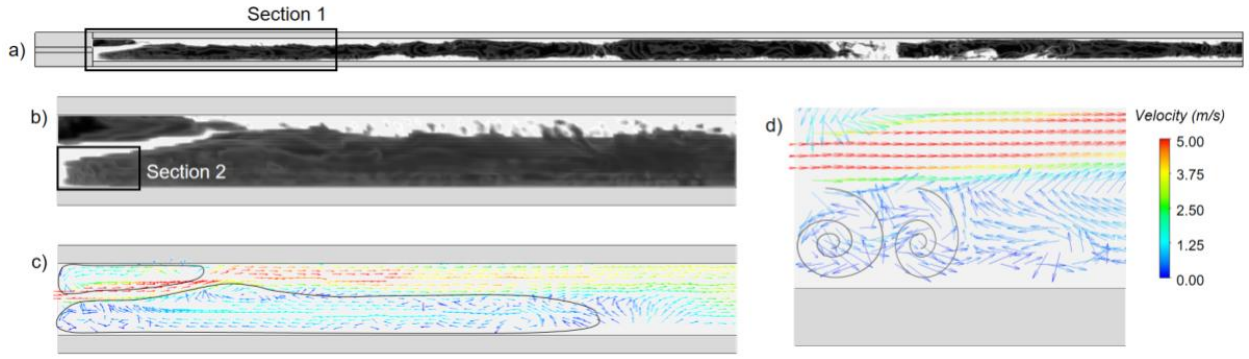


**Figure 61:** a) Top view of the microchannel with inlet restrictors illustrating vapor volume fraction in black with 3x magnification area labeled section 1, b) section 1 view of void fraction with 9x magnification area labeled section 2, c) velocity vector field at the middle of channel height for section 1 showing two large zones of recirculation, and d) section 2 velocity vector field showing multiple small eddies near the inlet

The formation of two large bubbles creates an unstable operating condition where the jet will be pushed to one side or the other. The jet inevitably biases towards one direction to create a stable operating condition. Asymmetrical behavior results from the bubble formation in the form of a modest redirection of the inlet jet. This asymmetrical flow pattern results in both temperature and flow changes in the microchannel. The low-velocity zone combined with the liquid jet causes moderately differentially cooled surfaces, as per Figure 62.

A critical Capillary number $Ca = 0.02$ was shown to change the cross-sectional profile, above which the vapor slugs exhibit axisymmetric profiles and below which they become non-axisymmetric as per Figure 63a and Figure 63b, respectively. Figure 63c demonstrates how results for the diverging case showed that low velocities caused by the increasing microchannel depth affected a similar axisymmetric profile (with the obvious dissimilarity of rectangular versus square cross sections). Ferrari et al. [8] also found that the film thickness decreases in square channels

with non-axisymmetric bubbles, where they become longer, and secondary flows (draining flows) remove liquid from the center liquid film regions (denoted by the dashed lines) towards the bubble rear. They further noted that this could result in liquid film dryout with sufficient bubble length.

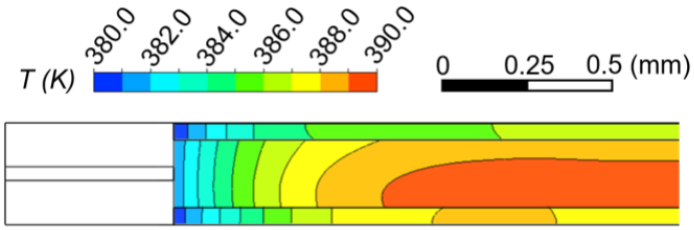


**Figure 62:** Temperature contours showing differentially cooled surface due to inlet jetting asymmetry

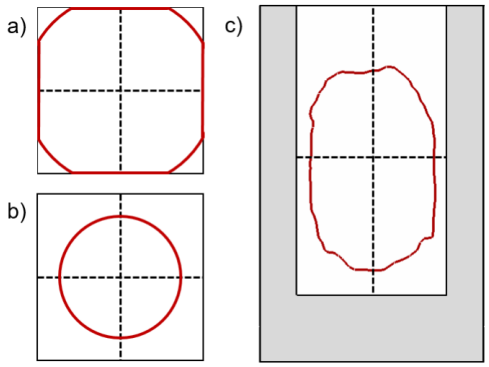


**Figure 63:** a) Non-axisymmetric bubble shape, b) axisymmetric bubble shape adapted from [8], and c) non-axisymmetric bubble in diverging channel geometry

Figure 64 compares case 1 and 3's liquid film thickness and thermal boundary layer thickness. It is well known that the thickness of the liquid film plays a critical role in heat transfer performance. The vapor slugs, as demonstrated in Figure 64a, exhibited the characteristic taper of non-axisymmetric slugs, as discussed in [8], with some dryout appearing on the side walls in black. The foremost contrast between Ferrari et al. and the case 3 geometry is the continuously changing aspect ratios, which begins nearly square but evolves with increasing rectangularity. This difference in aspect ratios, with the diverging microchannel eventually being more than twice deep than wide, results in a non-axisymmetric bubble shape that is constrained by two walls as opposed to four. The liquid thin films at the top and bottom of the channel thus see less thinning and virtually never see dryout.

Figure 64b graphs case 3's liquid film thickness across the nose to the rear of a bubble at the middle and side of the microchannel as well as the film thickness for case 1 at similar locations. The liquid film thickness strongly influences the heat transfer. Although there is a brief film dryout at the side walls of the vapor slug (due to draining flows and evaporation), the majority of the slug does not see more than a small quantity of local dryout. The film gradually decreases until the dryout, after which the rewetting rapidly increases due to the slug ending. In slug flow, vapor slug passage somewhat resets the boundary layer, which promotes improved performance in subsequent slugs.

Figure 65 illustrates this phenomenon for case 3. Figure 65a-c shows zoomed-in views of the isotherms grouping together after three representative vapor slugs, and their location can be seen in Figure 65d. Figure 65e demonstrates the continuous growth and shrinking of isotherms due to the liquid and vapor slugs passing. The film thickness decreases with decreasing velocity and evaporation [116], and this may further explain why increasing θ oftentimes improves heat transfer in expanding microchannels.

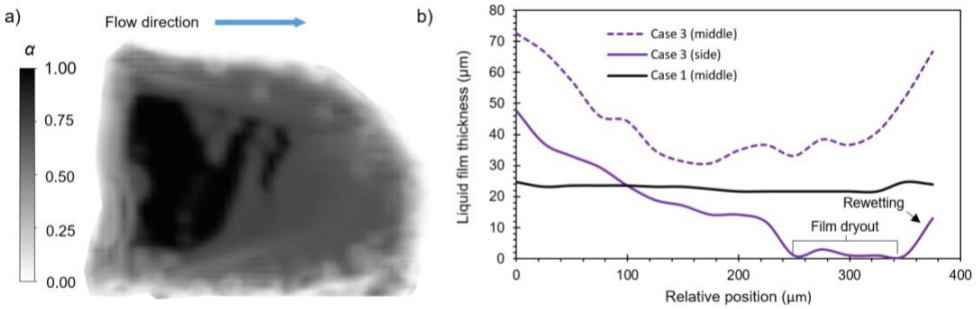


**Figure 64:** a) Tapering vapor slug with local dryout on the side centerline and b) liquid film thickness for the visualized slug for case 3 and for the baseline case 1

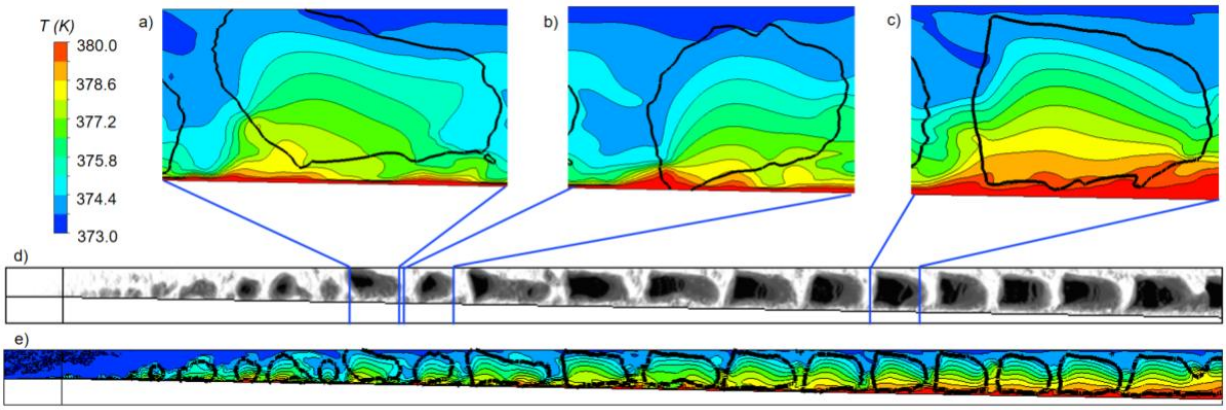


**Figure 65:** Midline cross-sectional views showing a-c) zoomed-in temperature contours with black vapor slug outline, d) bubble visualization with side view of channel, and e) side view of channel illustrating thermal boundary layer soft reset

Figure 66 compares the void fraction contours between cases 1 and 3 along the center plane, nominally halfway downstream. The bottom void fractions illustrate distinguishing features, where the liquid annulus is an approximate thickness for case 1, and the liquid layer for case 3 varies, as discussed earlier. The liquid portion near the nose of the vapor slug is considerably thicker (~50 microns compared to film dryout towards the rear), and this allows for some nucleate boiling bubble formation. Bubble formation augments the heat transfer in case 3 due to agitation and latent heat.

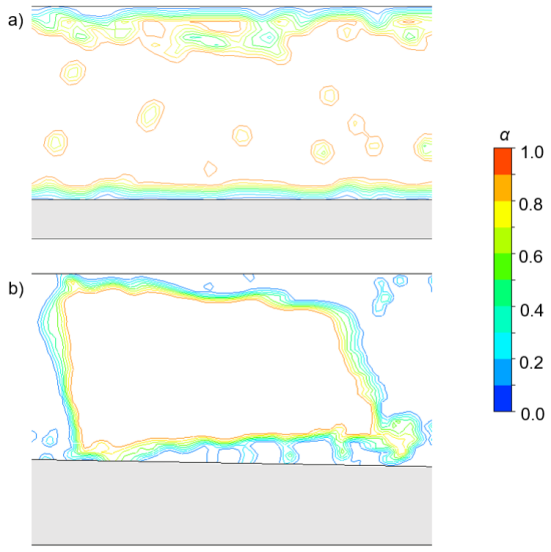


**Figure 66:** Vapor volume fraction α contour lines for cases a) 1 and b) 3, showing the bubble formation in the case 3 areas with thicker liquid films

The total mass flow rate at the outlet was kept constant in order to maximize similitude between the different configurations. This unsurprisingly results in different flow boiling regimes because of differential cross-sectional mass fluxes before and after the auxiliary jet, where slug flow happens upstream, and annular flow happens downstream, with the exception of bubble collapse dynamics, which is the primary focus of the following deliberations. Figure 67 shows a side view of the bubble collapse and subsequent advection phenomena with additional wall temperature contours. The jet can be seen injecting saturated liquid at 373 K. The jet keeps the bubble somewhat smaller, as there is always the liquid area around the jet penetrating into the vapor and pushing it towards the bottom of the channel. The bubble begins shrinking both in height and length at 0.2 ms, with the shrinking beginning from the inlet direction. Then, at 0.4 ms, the bubble begins to collapse, causing highly disturbed flow. 0.6 ms shows complete bubble collapse, which is then advected out of the channel, as seen at 0.8 ms before the cycle begins anew.

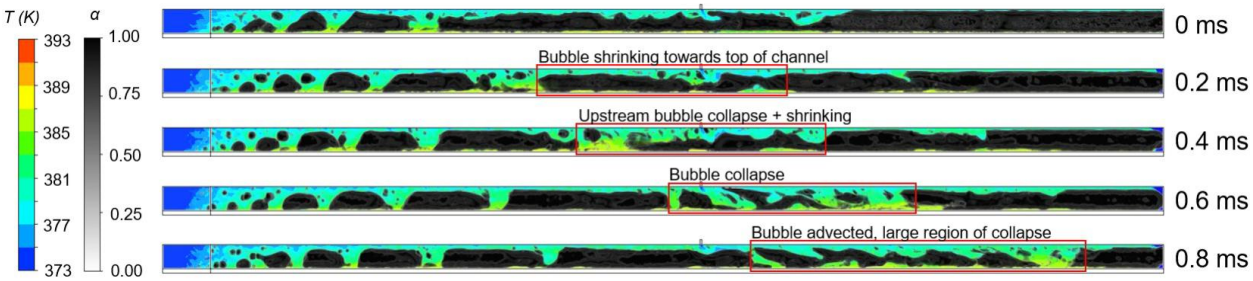


**Figure 67:** Side view visualization of transient bubble collapse and advection phenomena with wall temperature contours and void fractions

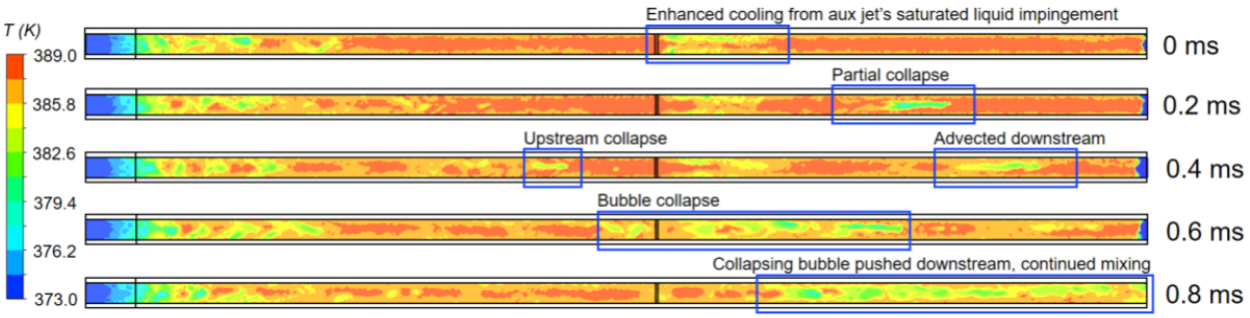


**Figure 68:** Top view visualization bubble collapse's impact on bottom wall temperatures

The bubble collapse impacts the transient and locational thermal performance more so than the other geometries, which could be intuited due to the jet's location and the periodic nature of bubble collapse. Figure 68 illustrates the changing bottom wall temperatures (at the fluid-solid interface) caused by the auxiliary jetting. The shrinking and collapse causes the wall temperatures to vary with time, although primarily downstream or upstream in close proximity to the jet. From 0 ms to 0.6 ms, the auxiliary jetting impinges on the vapor, and the combination of impingement and fully saturated liquid improves cooling directly downstream of the jet for a short length. This effect disappears temporarily, as it partially disappears at 0.6 ms and fully at 0.8 ms. At 0.2 ms and 0.4 ms, the effect of liquid impingement and partially collapsed bubble (which can be seen as an incomplete collapse/compression of the vapor in Figure 67) can be seen. This corresponds to the decreased temperatures. After the bubble bursts, the chaotic flow continues to mix and condense the vapor, which allows for decreased velocities (and hence pressure drop, as discussed prior to this section) and enhanced cooling. The continued condensation and augmented performance are evidenced by the increasing volume of chaotic flow (indicating mixing) in Figure 67 and the increasing area of the green contours in Figure 68. Aside from during the brief period after bubble collapse and during bubble advection, a region 1.3 mm in length downstream of the jet exhibits improved cooling. This suggests that the addition of multiple nozzles could provide for improved cooling for the entire length of the channel as opposed to the more localized cooling seen herein.

## 6. Experimental and Computational Studies of Flow Boiling in Additive Manufactured Metal Foams

### Approach

This project task investigates flow boiling in AMMFs for both uniform and vapor pathway geometries with both experimental and numerical methods. The prior project task in Chapter 4 was leveraged by using the same CFD-HT flow boiling models as the flow boiling in microchannels – VOF for interface generation and conservation equations, and the Lee Model for the phase-change model. Additionally, the experience gained improved confidence in the numerical models, as there was not the same quantity of either experimental or numerical work available for metal foams. The dielectric HFE-7200 was selected as the working fluid, and saturated flow boiling conditions were applied to study its phase change in AMMF structures, including the pressure drop, heat transfer

performance, and two-phase flow behavior. A computational fluid dynamics and heat transfer (CFD-HT) numerical model used the experimental data for validation, providing the layout for future modeling capabilities for boiling flows in metal foams, with the potential for future applications for direct cooling using dielectric flow boiling in AMMFs.

**Method**

Two test samples were fabricated using DMLS based on the unit cell in Figure 69. The first was uniformly populated and consequently named “uniform sample”, whereas the second, termed “vapor pathway sample”, was non-uniformly populated by removing each alternate row from the halfway point downstream. Figure 70 displays and compares both the CAD files and the manufactured pieces prior to finishing machining operations but post-heat treatment. The surface roughness can be clearly visualized, which results from the copper particle size during DMLS operations. Exposed substrate surfaces were sanded for improved o-ring sealing and heater block soldering. Additionally, several unit cells from the bottom were removed, as their purpose was to provide thermal and structural support during the printing process.

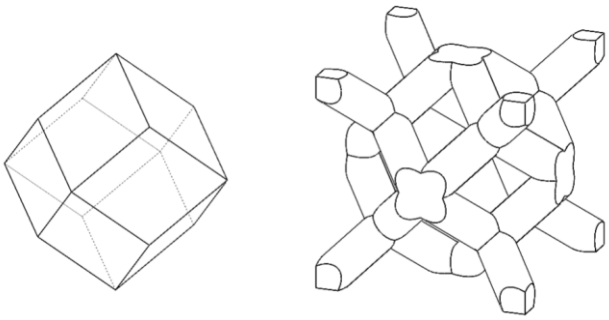

**Figure 69:** Rhombic dodecahedron shape (left) and unit cell based on the shape (right)

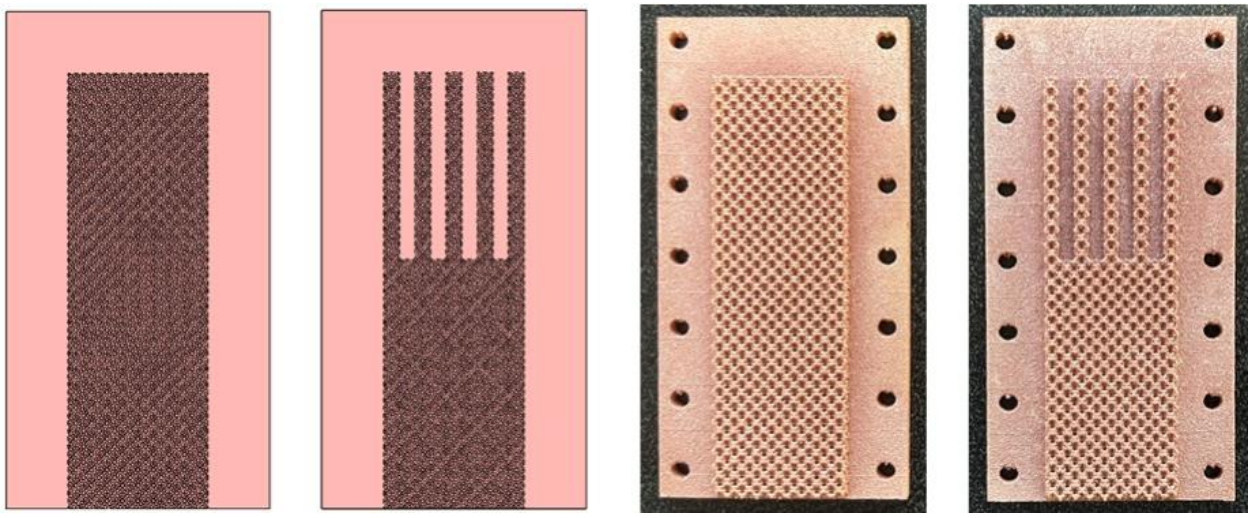

**Figure 70:** CAD files of the printed AM cold plates for the uniform and vapor pathway structures (left), and corresponding printed structures (right)

The vapor pathway design was chosen based on prior literature showing that expansion, whether via dedicated vapor removal routes or increased feature sizes, can improve thermohydraulic performance.

A test section made of polyetheretherketone (PEEK) provided the means to mount and quantify cold plate performance. PEEK is known for both its chemical resistance and mechanical strength, even at high temperatures, which are maintained well beyond the saturation temperature for the selected working fluid. Cross-sectional diagrammatic test bed views, seen in Figure 71, illustrate its important aspects, including the heating, general assembly, and fluidic routing. Ports and accompanying fluidic pathways for pressure measurement can be seen near the ends of the foam sections. Additionally, three stainless steel sheathed T-type thermocouples (1/16” diameter) have been embedded near the cold plate inside the heater block. A DC power supply (Agilent® N8742A) provided the power supply for the three cartridge heaters embedded in the heater block. An ethylene propylene diene monomer (EPDM) o-ring sealed the cold plate and the PEEK package. Two solid-state pressure transducers (Omega PX319, calibrated using an Omega DPI 610 portable pressure calibrator) measured the absolute pressure before and after the test section, allowing the differential pressure to be measured using the two values.

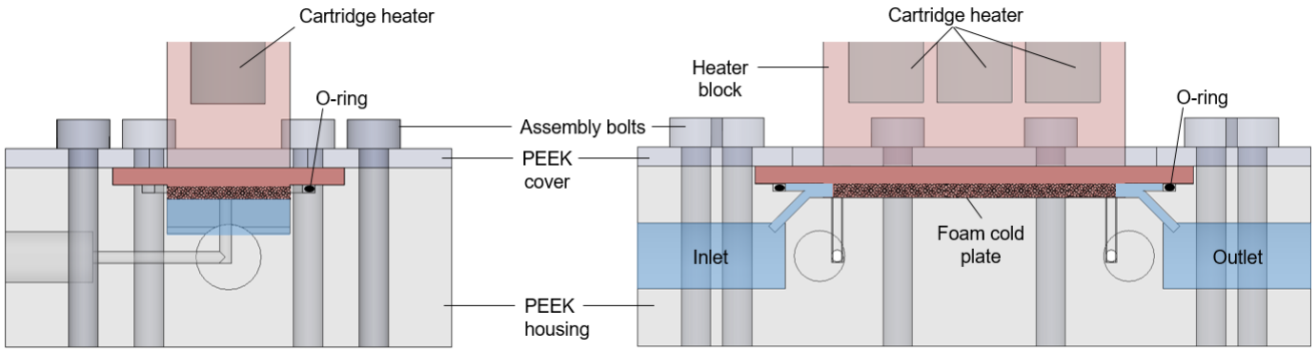


**Figure 71:** Front cross-section (left) and side cross-sectional view (right) of test section

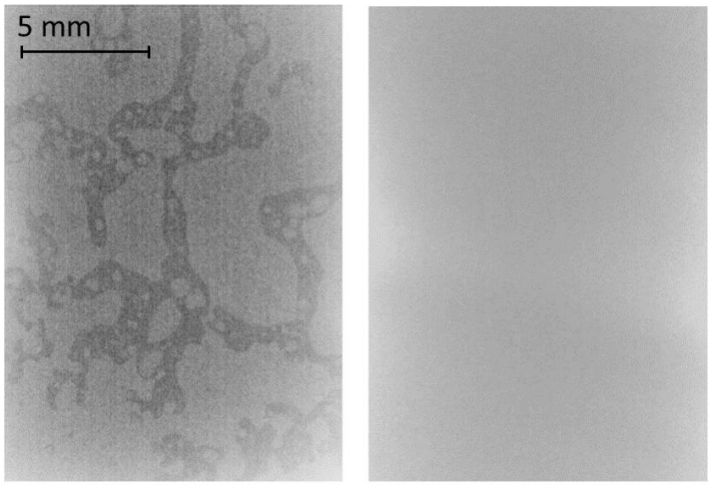


**Figure 72:** X-ray images of the solder cross-section with low (left) versus high (right) pressure applied during processing

A tin-based solder (96.5Sn/3Ag/0.5Cu, liquidus temperature TL = 220 ˚C) mechanically and thermally attached the copper heater blocks to the cold plate. Three cartridge heaters, capable of providing 200 W each, were embedded into the copper heater block to provide uniform heat flux thermal loads for subsequent experimentation. Initial soldering tests were undertaken to ensure a sufficiently low void percentage prior to soldering the heater blocks to the cold plate. Both sides were sanded with 1000 grit prior to the application of liquid flux on both sanded surfaces and the placement of the solder ribbon between the pieces. An aluminum jig mechanically aligned the two pieces, after which it was placed within a Heraeus vacuum oven capable of providing a nitrogen environment or vacuumed conditions. The assembly was placed into the oven, after which the ambient air was replaced with nitrogen to prevent oxidation, and the oven was then gradually raised to 20 ˚C below liquidus for 50 minutes to ensure the entire assembly was near the liquidus temperature. The oven was subsequently evacuated, and the temperature increased to 250 ˚C for 4 minutes in order to form a sufficient but not overly thick and resultantly brittle intermetallic layer. The heating was turned off, and the oven was allowed to cool down. Inspection of cross-sectional x-ray images, taken using a Dage XD7600NT x-ray inspection system, can be seen in Figure 72. The right image shows excellent joint quality when the process flow is followed as described alongside the application of added pressure. Significant voiding occurs in the joint without this additional force (Figure 72, left). Additional pressure was applied during the test sample soldering, after which a 0% void percentage was assumed for the cold plate solder joint.

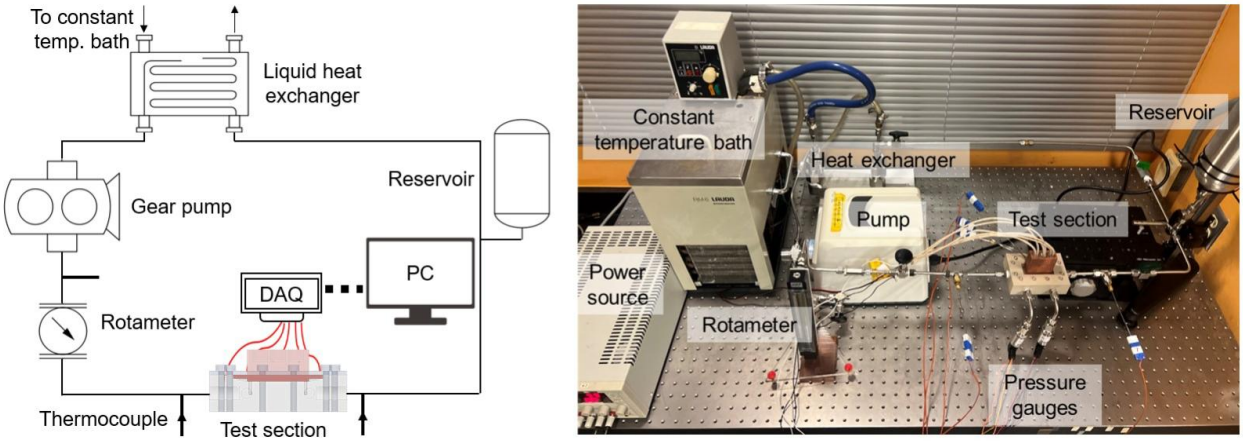


**Figure 73:** Experimental setup diagram (left) and photograph (right) of flow loop components prior to test section and tubing insulation

The test section was subsequently attached to a closed fluidic test loop by way of the inlet and outlet ports, which have female 1/4 NPT fittings NPT ports. Figure 73 shows a diagrammatic view of the aforementioned loop with an accompanying photo showing the data acquisition unit, laptop computer, and power supplies. ¼" OD stainless steel tubing connects the separate components using Swagelok compression fittings. A gear pump and pump drive assembly (Micropump® GJ-N21 and Cole-Parmer® EW-75211-30) circulates the fluid through the closed loop, where a Cole-Parmer® PMR1-010423 analog rotameter measures the volumetric flow rate. The rotameter was calibrated for the range of 0 – 160 mL/min using a graduated cylinder that was covered to minimize evaporation. The fluid subsequently passes into the test section, which was described prior, before

and after which sheathed T-type thermocouples (Omega) measures the fluid temperature. DI water at boiling and freezing conditions were used for thermocouple calibration. The liquid undergoes a phase change, and then the liquid-vapor mixture enters the brazed plate liquid heat exchanger (Lytron® LL520FG12), which is connected to a constant temperature bath (RM6 Lauda Brinkmann) for condensing the evaporated liquid. A liquid reservoir (Swagelok 304L-HDF8-1000) functions both as a vapor trap and eponymously as a reservoir. The instrumentation outputs the signals to a data acquisition unit (Agilent 34970A, Keysight Technologies Inc.).

A commercial vacuum pump evacuated the loop to a nominal absolute pressure of 6 kPa via a connection at the reservoir, which was held for 1 hour. The system was charged using a connection adjacent to the rotameter. The evacuated system was charged with the dielectric HFE-7200. The discussion regarding fluid selection is expanded upon in the following section. After adiabatic conditions with appropriate inlet temperatures were attained, testing was performed by discretely increasing heat fluxes from adiabatic conditions to system limitations. Steady state at each heat flux was verified once the deviations in temperature and pressure transducers were no longer visible on the DAQ user interface, or after a time interval of 10 minutes passed.

The CFD-HT simulations leveraged several simplifications to make the domain computationally manageable. Due to uniform heating conditions, the numerical domain was reduced to a single lane with inlet and outlet lengths for flow stability. Simulated portions of the total geometries measured 1 unit cell in width and took advantage of symmetry on either side. Figure 74 and Figure 75 illustrate multiple views of both the uniform and vapor pathway computational domains. Both figures show zoomed-in portions of the unit cell with the substrate made transparent, where Figure 74a specifically illustrates the partially removed unit cell to function as a vapor conduit. Figure 74b and Figure 75b show isometric views of the simplified numerical domain, which uses a small strip 1 unit cell wide, designated by the blue volume in c. Bounding box measurements are approximately 3.3 x 2.3 x 55.8 mm (height x width x length), with the copper substrate thickness decreased from 3 to 1 mm to further decrease unnecessary element count. The boundary conditions, which are identical for the two cases, utilize symmetry on either side of the geometry. Velocity inlet conditions ($u = 0.125$ m/s, corresponding to $G = 160$ kg/m$^2$·s, with $T_i = 354$ K) and pressure outlet conditions were applied at the inlet and outlets. The topside boundary condition was a uniformly applied heat flux of 20 W/cm$^2$.

The present experiments and simulations utilized the dielectric HFE 7200 (trade name NovecTM 7200, chemical formula $C_4F_9OC_2H_5$, molecular weight 264 kg/kmol) from 3M. Its thermophysical properties are given at atmospheric pressure in Table 6-2. The engineering software EES (Engineering Equation Solver) gives the properties for HFE 7200 at different thermodynamic values. From the given values, the disadvantages of this fluid are apparent, as several quantities are much worse for cooling when compared to water (e.g., thermal conductivity and latent heat of vaporization are more than an order of magnitude lower than liquid water). However, using dielectric fluids allows for the direct contact of the working fluid with current-carrying parts without the need for electrical isolation, although additional considerations, such as fluid

decomposition at high operating temperatures (>150 ˚C), should be taken into account. The contact angle used was set to 20˚, which is near to the values seen for highly wetting fluids.

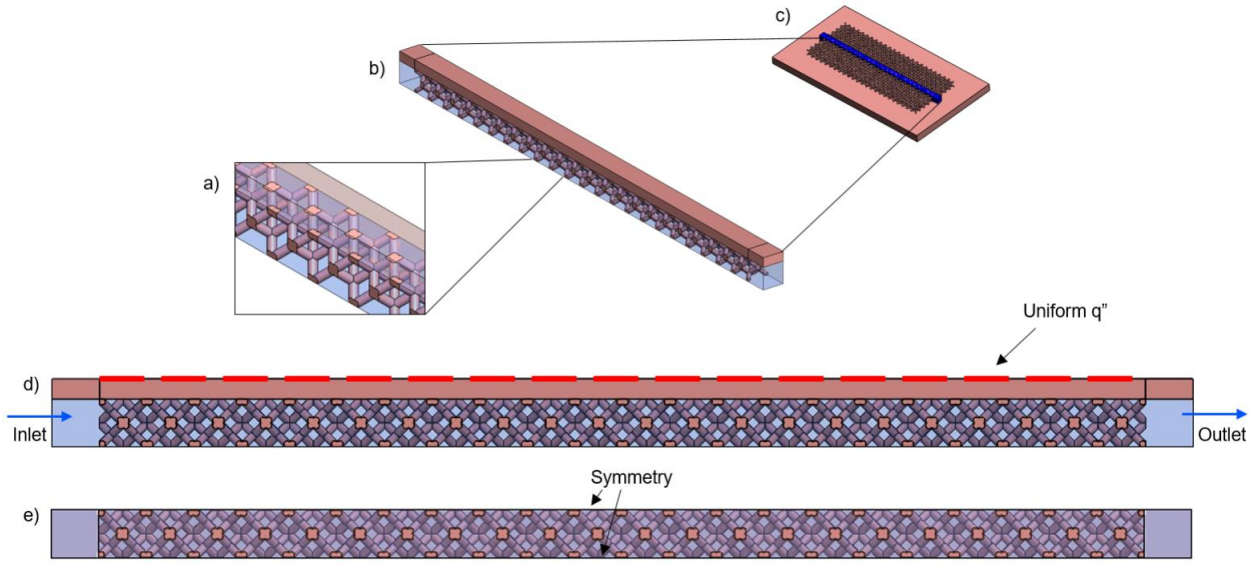


**Figure 74:** Views of the uniform foam showing a) Zoomed-in view with transparent substrate showing unit cell, b) Isometric view of computational domain, c) Numerical domain versus test piece, d) Side view of numerical domain with boundary conditions, e) Bottom view of numerical domain showing symmetry conditions

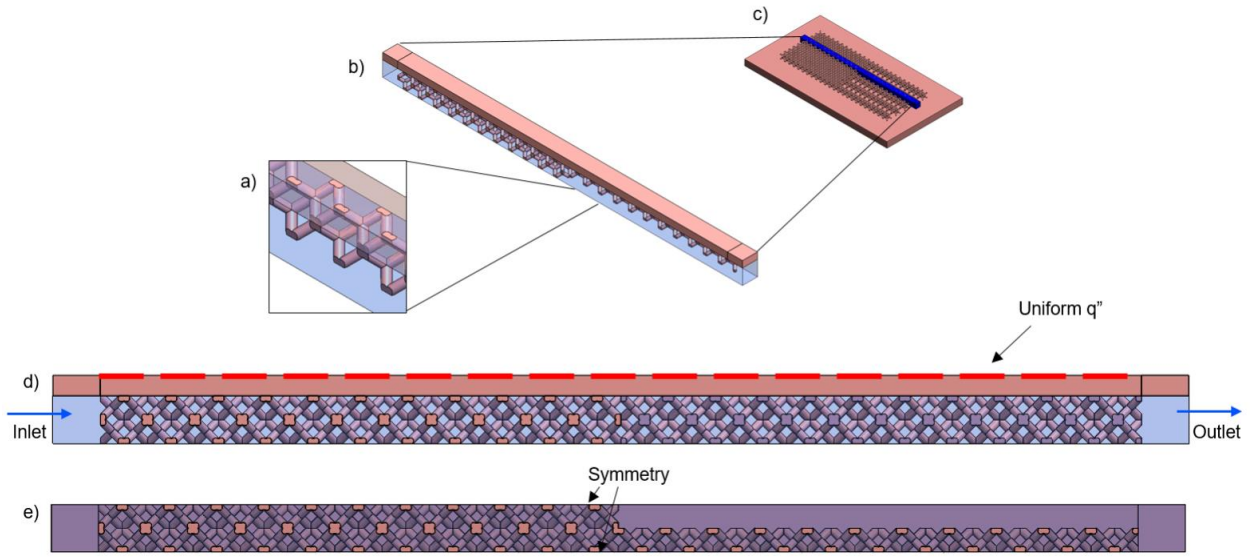


**Figure 75:** Views of the vapor pathway foam showing a) Zoomed-in view with transparent substrate showing unit cell, b) Isometric view of computational domain, c) Numerical domain versus test piece, d) Side view of numerical domain with boundary conditions, e) Bottom view of numerical domain showing symmetry conditions

The commercial CFD-HT software ANSYS Fluent 2021 was used to solve the governing equations discussed in the prior sections using the finite volume method. The built-in VOF model was coupled with the Lee model calibrated according to experimental data as $\lambda_{l,v} = 10\ s^{-1}$ for simulating evaporation and flow boiling, which gave the best agreement when considering both cases

simultaneously. The model simulates a transient, laminar flow, the former of which is necessary based on the nature of boiling and phase-change phenomena.

**Table 11:** Thermophysical properties of materials used in the present simulations for T = 81 ˚C from EES

| Property | Symbol | Copper | Liquid HFE 7200 ($T_{sat}$ = 81 ˚C) | HFE 7200 Vapor ($T_{sat}$ = 81 ˚C) |
|---|---|---|---|---|
| Density (kg·m$^{-3}$) | $\rho_{Cu}$, $\rho_l$, $\rho_v$ | 8924 | 1287 | 11.57 |
| Specific heat (J·kg$^{-1}$·K$^{-1}$) | $c_{Cu}$, $c_l$, $c_v$ | 3681 | 1107 | 1001 |
| Thermal Conductivity (W·m$^{-1}$·K$^{-1}$) | $k_{Cu}$, $k_l$, $k_v$ | 392.8 | 0.05586 | 0.009317 |
| Dynamic viscosity (Pa·s) | $\mu_l$, $\mu_v$ | – | 3.354 x 10$^{-4}$ | 1.243 x 10$^{-5}$ |
| Surface tension coefficient (N·m$^{-1}$) | $\sigma$ | – | 0.00908 | |
| Latent heat of vaporization (kJ·kg$^{-1}$) | $h_{fg}$ | – | 108.8 | |

The SIMPLE algorithm was used for pressure-velocity coupling, with gradient discretization using the least squares cell-based method. PRESTO and second-order upwind spatial discretization were used for pressure and momentum, and volume fraction discretization was handled using the compressive scheme. Although advanced piecewise linear interface construction (PLIC) methods claim higher accuracy, compressive VOF methods demonstrate a similar ability for interface capturing. The compressive or implicit VOF method allowed for increased Courant (Co) numbers so that it could be set to Co = 20 before the quasi-steady state and adjusted after this stage was reached to Co = 2, allowing for accelerated convergence. Compressive VOF schemes can also provide solutions where the intermediate transient simulation is not the primary focus. The simulations utilized a secondary initialization to bypass the thermal capacitance to quicken the simulations, as the transient solution is not of current interest. Later discussions on boundary and initial conditions give further details regarding the dual initialization procedure. Convergence residuals were set to $10^{-3}$ for mass and momentum and $10^{-6}$ for the energy equations. Automatic variable time stepping was implemented (limited by Co = 20). The cases were simulated using 64 – 192 cores in AMD EPYC 7281 processors in parallel, which required approximately 3 weeks of run time for each case. The computational domain was meshed with a mix of hexahedral and tetrahedral elements, with inflation layers at all fluid-solid interfaces. Tetrahedral elements were allowed due to the foam's complex geometry. The following analysis ensures that results are independent of grid sizing by comparing several relevant parameters across four mesh grid sizes, which increase by a nominal factor of 1.5 in element count across each iteration. The mesh used a mix of tetrahedral and hexahedral elements, although the former was more common due to the relatively complex geometries simulated. Inflation layers were generated at fluid-solid interfaces

and symmetry boundaries. Mesh independence studies were performed with a uniform structure, where the topside temperature was 365 K.

Table 12 illustrates the studied variables, which encompass fluid-solid interface wall temperature $T_w$, differential pressure ΔP (time-averaged over a 10 ms span prior to the given time), and void fraction α. Prior to applying a constant topside temperature, the steady-state isothermal solution was computed as the initialization for these studies. Mesh 3 demonstrated the best compromise between computational time and accuracy. Each variable that was examined across the varying mesh densities needed to see a percent change of less than 3% before a grid-independent solution was considered to be achieved. Mesh 3 provided mesh independence, while the relative fineness of the mesh mitigated occasional numerical divergence seen at higher void fractions of the coarser grids, and its meshing parameters were consequentially selected.

**Table 12:** Increasing grid fineness percentage effect on relevant variables for mesh independence analysis at t = 100 ms

| Mesh | Cell count | $\lvert(T_w^k-T_w^{k+1})/(T_w^k-T_{in})\rvert$ | $\lvert(\Delta P^k-\Delta P^{k+1})/(\Delta P^k)\rvert$ | $\lvert(\alpha^k-\alpha^{k+1})/(\alpha^k)\rvert$ |
|---|---|---|---|---|
| 4 | 9,119,474 | – | – | – |
| 3 | 6,049,449 | 1.49 | 2.89 | 0.55 |
| 2 | 4,234,283 | 37.7 | 0.83 | 3.99 |
| 1 | 2,352,766 | 39.4 | 14.7 | 544 |

## Results

CFD-HT simulations, in the case of complex multiphase flows, require validation to ensure model fidelity. The prior discussions reviewed some of the relevant literature; the particular structure lacks available correlations. Due to the dearth of correlations, experimental results can substantiate the numerical results for generally boiling flows in the metal of these configurations. The selected methods of validation were thermal and hydraulic performances. Post-validation, numerical results can provide insight into the microscale flow phenomena behind these new structures without the use of expensive imaging or visualization technologies. The performance of the vapor pathways structure showed mild changes for the two-phase heat transfer coefficient $h_{tp}$ but a more significant improvement in the pressure drop ΔP across the test samples. The experimental and numerical results aligned with expectations of improved thermohydraulic performance resulting from incorporating dedicated vapor expulsion channels.

Both structures were tested under similar conditions, with a mass flux G = 160 kg/m$^2$·s, while ramping the heat flux beginning from adiabatic flow. The experimental performance fulfills the purpose of validating the numerical results. However, additional interesting behaviors can be observed due to the wider operating conditions ranges and the interaction between the other flow

loop components. This provides additional information on how the application of these thermal management solutions would perform outside of a computational simulation environment.

Figure 76 represents the key experimental results from the tests. The graphs show both $\Delta P$ and $h_{tp}$ as functions of heat flux q". Additional solid thermal resistances (i.e., the substrate, solder, and heater block's) are included into the two-phase heat transfer coefficient, which somewhat lowers the actual convective thermal resistances. Nevertheless, the $h_{tp}$ graph incorporated these effects into the heat transfer coefficient due to the practical nature of implementing such a thermal management solution.

As expected, integrating vapor pathways into the foam structure considerably lowers the pressure drop. The maximum pressure drop reached 6.5 kPa for the uniform structure. The addition of vapor pathways decreased the pressure drop to 1.3 kPa (at the same q" values) for the second tested thermal management solution. A corresponding drop in pumping power occurs as well. A graph illustrating the differences in required pumping power was not presented because the pumping power's relative improvement would be the same as for the pressure drop, given the constant inlet mass flow rate. Another interesting pattern was observed from best-fit curves for either structure. The uniform structure's $\Delta P$ graph follows the more expected second-order polynomial trend, whereas the vapor pathway structure looks to be nearly linear, with the exception of a brief uptick around a nominal value of 13 W/cm$^2$. It is possible, however, that differences in pressure drop trend line curves possibly result from the low-pressure drops, obscuring the perceived trends. R-squared values further support this hypothesis, as the values decreased from 0.97 to 0.96 when curve-fitting a second-order polynomial versus a linear fit.

The two-phase heat transfer coefficient $h_{tp}$ shows less significant differences between the two structures. The vapor pathway performs negligibly better than the uniform structure for most of the data points. There is a slight deviation at lower heat fluxes and higher heat fluxes. Measurement uncertainties may explain the variance for the former. The heat transfer coefficient drops sharply after 20 W/cm$^2$ for the first test sample, whereas the vapor pathway sample sees a more moderate drop, after which it reaches a maximum heat flux at a nominal value of 33 W/cm$^2$.

System-level effects, which are not captured in the evaporator-level reduced domain numerical model, account for the differences in performance at higher q" values. The second test sample reached equipment limitations, whereas the uniform sample did not. This was due to the flow loop's internal pressure curve, as well as the compressibility effects due to non-condensable gases. With increasing evaporator heat fluxes, the pressure drop across the metal foam likewise increased. This alters the internal pressure curve of the flow loop, which is inherently linked to the evaporator performance. The interplay between the compressible tank pressure and evaporator can cause dynamic instabilities known as pressure drop oscillations. The dynamic instabilities manifested in visible oscillations, where vapor was jetting upstream of the test section after being generated within the AMMF. This affected negative thermal performance, as seen with the significant 20% decrease in $h_{tp}$ that was conversely not seen in the vapor pathway sample.

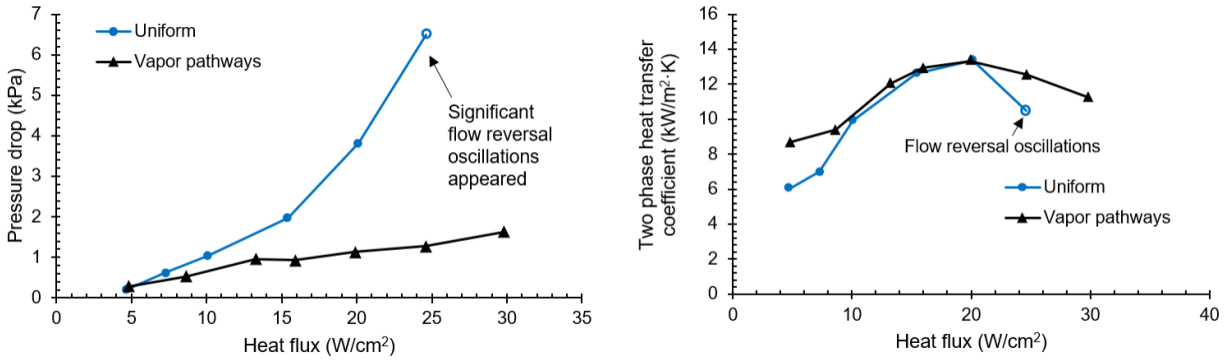


**Figure 76:** Pressure drop (left) and two-phase heat transfer coefficient (right) versus heat flux comparison plots for both structures at G = 160 kg/m$^2$·s

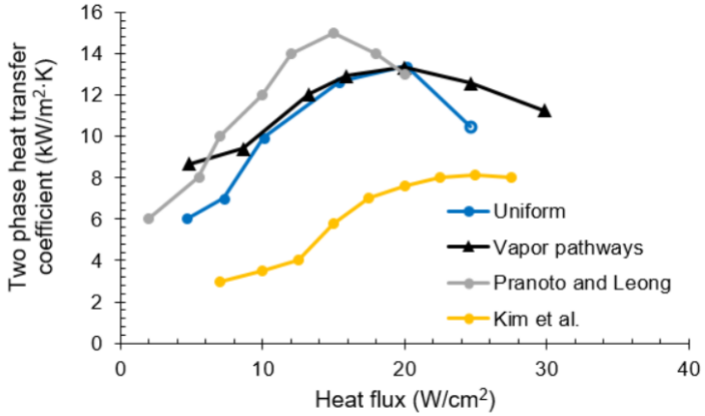


**Figure 77:** Two-phase heat transfer coefficient (right) versus heat flux comparing both structures to Wong and Leong [9] and Kim et al. [10]

Figure 77 compares the two structures to two-phase heat transfer coefficients found in the literature for metal foams with flow boiling. The comparisons serve more as a reference, as there are several properties and operating conditions, and no experimental results with identical conditions could be found. However, the foams studied herein demonstrate a similar performance to that of Wong and Leong, who used additive-manufactured foam-type structures [9]. Additionally, all AMMFs outperformed the metal foam from Kim et al. [10].

Simulations are a valuable tool for adding further analysis without the addition of complex and expensive visualization equipment. The following section presents 3D flow boiling simulations, which are validated using experimental pressure drop and two-phase heat transfer coefficient measurements presented in the prior discussion. Both AMMF flow boiling simulations used heated thermal boundary conditions where q" = 20 W/cm$^2$. Table 13 lists the values for $\Delta P$ and $h_{tp}$, which confirmed model fidelity via good agreement between the predicted and experimental values.

Bubble physics and accompanying phenomena are of interest due to the additional insight that can be gained. Figure 78 presents isometric views of both structures. Immediately, stark differences past the midway point (where the vapor pathway begins) can be seen in bubble behavior. The two

results resemble each other upstream before the vapor channels, but a small difference is increased coalescence and larger bubbles in the vapor pathway sample's foam cells. The vapor channel contains a vapor column reminiscent of annular flow, where the pathway is shown to function as intended.

**Table 13:** Model validation using experimental and computed values for heat transfer coefficient and pressure drop

| Mesh | $h_{tp}$ (W/m$^2$·K) | | $\Delta P$ (Pa) | |
|---|---|---|---|---|
| | Experimental | Numerical | Experimental | Numerical |
| Uniform | 13,378 | 13,256 | 3,825 | 4,231 |
| Vapor Pathway | 13,338 | 14,157 | 1,131 | 1,145 |

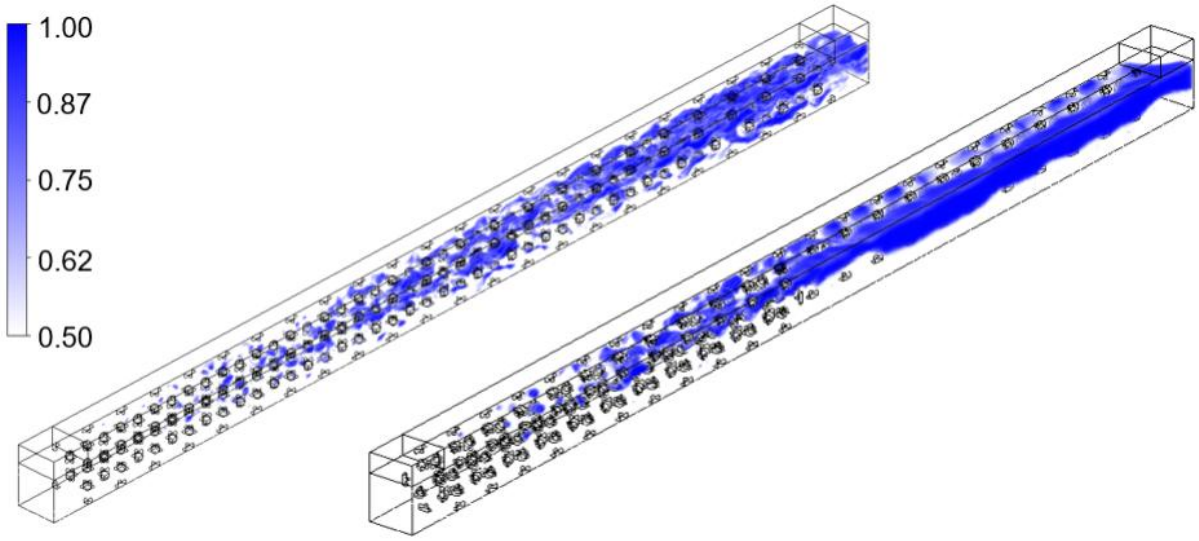


**Figure 78:** Isometric views showing vapor volume fraction renderings for both structures (left: uniform, right: vapor pathway)

Additional views further clarify differences in the multiphase flow behavior. Figure 79 and Figure 80 illustrate the liquid/vapor volume fractions at some representative time step after a quasi-steady state. The former gives only one side view due to the symmetrical formulation of the problem; added insight from presenting the opposite side proved trivial. Extensive literature exists on microchannel flows, where common two-phase flow regimes include bubbly, slug, churn, and annular. However, these flow regimes typically result when the fluid paths are not impeded by solid barriers. Both the top and side views demonstrate similar flow regimes that appear more as churn flows seen in microscale literature, with some bubbly flow closer to the entrance before significant void fractions form. The reason behind this is not liquid-vapor interaction physics but an inevitable effect of the solid foam matrix's presence. These bubbles form thin vapor columns

where the foam morphology encourages, seen particularly in the side view near the outlet, where two prominent vapor columns wind between the foam struts. The vapor column near the top of the channel shows a higher vapor volume caused by its proximity to the diabatic surface.

The uniform structure's flow behavior demonstrates the chaotic, disconnected flow that is characteristic of churn flow. However, this result is not from liquid-vapor interaction physics but rather is an inevitable effect of the solid foam matrix's presence. The chaotic, churn-type flow seen in the uniform structure aligns with expectations based on the limited relevant literature.

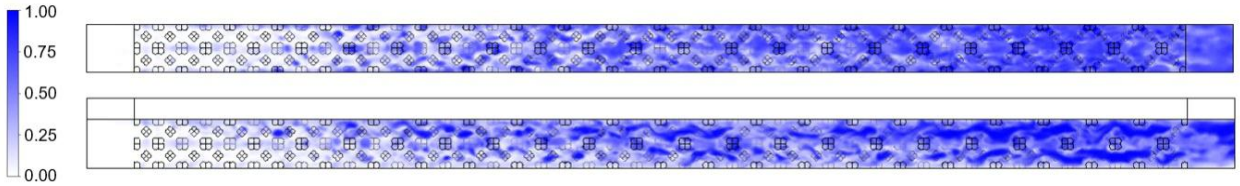


**Figure 79:** Vapor volume fractions for uniform structure showing top and side views

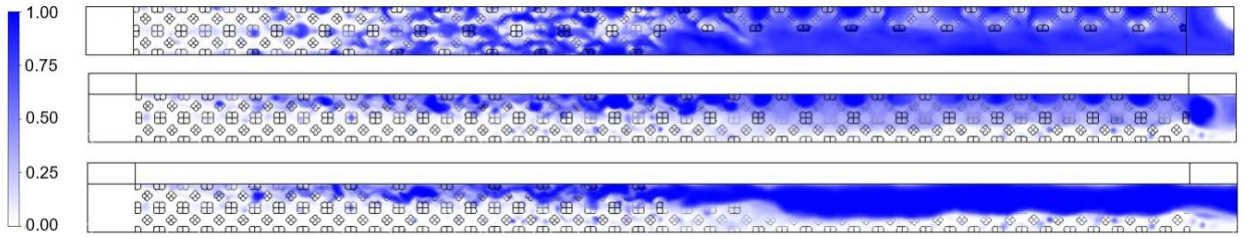


**Figure 80:** Vapor volume fractions for vapor structure (in descending order) top view, side view showing uniform portion horizontally mirrored for illustrative purposes, and opposite side view for vapor pathway visualization

Integrating vapor escape channels changes the vapor behavior, and they function as designed and anticipated. But Figure 80 shows that there are further significant changes in flow behavior. The images show multiple angles of the vapor in the reduced domain, beginning from the top view. Initially examining the aforementioned looks to be alike with the same angle for the original structure. Upstream of the midway point, initial bubble formation occurs symmetrically. The bubbles coalesce and turn into longer bubbles, again mimicking the other AMMF, before exhibiting some small asymmetry, approximately one unit cell upstream of the vapor channel beginning due to the foam's flow impedance.

Vapor volume fraction renderings demonstrate the effect of vapor channel integration. Figure 80's top and side views (from the vapor channel side) illustrate how the vapor travels towards the channel, from where the majority of the vapor vents. The top view shows the effect of removing the foam struts, which decreases fluid mixing, resulting in an uninterrupted flow with markedly less chaotic features. The view from the uniform side further elucidates the magnitude of the vapor's bias towards the channel. Due to the remaining gaseous phase venting outwards, small pockets of vapor exist only near the top of the cold plate within the larger volumes created by the unit cells. The vapor pathway side shows what would be best described as annular flow. The effects

of gravity come into play due to the hydraulic diameter increasing from the foam to the vapor channel, shown by the vapor core's proximity to the cold plate's top surface.

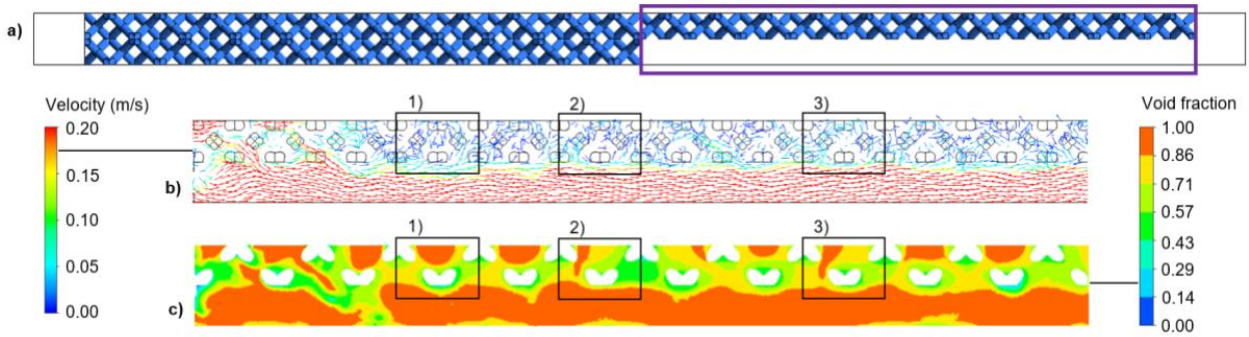


**Figure 81:** a) Reduced computational domain for vapor pathway sample, b) velocity vectors at 0.2 mm below the substrate over area indicated in a), and c) vapor volume fraction for the indicated area at 0.2 mm below the substrate

A closer examination of the vapor pathway's effects shows that the multiphase flow behavior has fundamentally changed. Introducing vapor pathways significantly changes the flow behavior by not only introducing annular-like flow in the pathways, but also by altering the bubble velocity, behavior, and shape inside the foam. Figure 81 presents a velocity field and volume fraction contour located 0.2 mm below the cold plate cover. The velocity vectors in Figure 81b indicate decreasing flow velocity and recirculation effects. The uniform structure demonstrates fairly constant flow behavior throughout its entirety, with chaotic, winding flow resembling churn flow that increases in velocity due to the increasing vapor. In contrast, the liquid-vapor mixture suddenly slows to near-stagnant conditions in the foam adjacent to the vapor channel. The low flow rate is a consequence of the higher flow impedance caused by the dense foam structure. This, in turn, causes recirculation in these areas, which are denoted by numbers in Figure 81b. Below, the vapor volume fraction shows bubbles in the stagnant region in Figure 81c. The bubbles expand and then eject vapor into the vapor column. Section 1 shows a vapor bubble and sections 2 and 3 show vapor bubbles ejecting into the channel. The vapor formation and ejection, coupled with the strong tendency for flow to go through the low resistance channel, improve the cold plate performance.

## 7. Evaluation of Thermal Performance of Triply Periodic Minimal Surface Lattice Structures in Single-phase Dielectric Fluid Cooling of Power Electronics

### Summary

This project task investigates the use of TPMS structures with graded porosity in different flow orientations. Dielectric cooling fluid is utilized under single-phase flow conditions; most prior studies on TPMS use a water-glycol mixture as the coolant. Also, the effects of graded porosity remain largely unexplored.

**Method**

This project task investigates the gyroid TPMS structures formed by surfaces derived from implicit functions. The surfaces are generated using the level-set approximation equation [11]:

$$\sin(X)\cos(Y) + \sin(Y)\cos(Z) + \sin(Z)\cos(X) = c$$

The periodicity is represented as $X = 2\pi n_x x$, $Y = 2\pi n_y y$, and $Z = 2\pi n_z z$ in each Cartesian coordinate. Therefore $n_x$, $n_y$, and $n_z$ define the unit cell dimensions.

The parameter $c$ on the right-hand side of the Eq. (1) controls the gyroid minimal surface. The solid structure is formed by solidifying the volume enclosed by a specific c value. Therefore, adjusting $c$ alters the porosity of the generated TPMS lattice structure. TPMS lattices with varying porosities are shown in Figure 82.

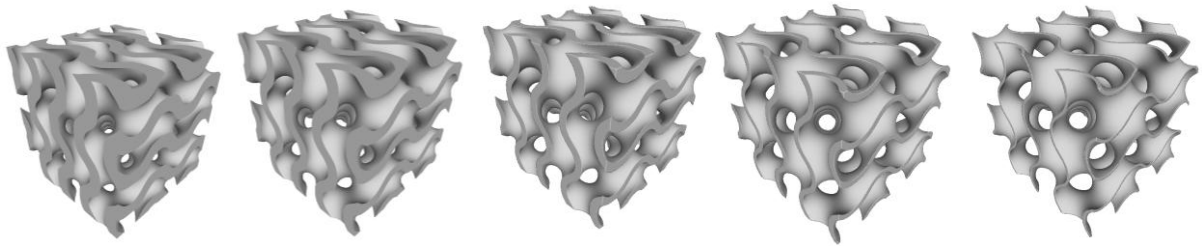

**Figure 82:** Different TPMS lattices having different porosities (0.5, 0.6, 0.7, 0.8, and 0.9).

The functional graded TPMS is assumed to be used in a half-bridge inverter as shown in Figure 83. The cold plates here have a dimension of 10 mm x 10 mm and a height of 4 mm. For reducing computational cost, the flow domain is selected having a width of 1.8 mm, corresponding to the unit cell length, as the geometry exhibits periodicity with this dimension.

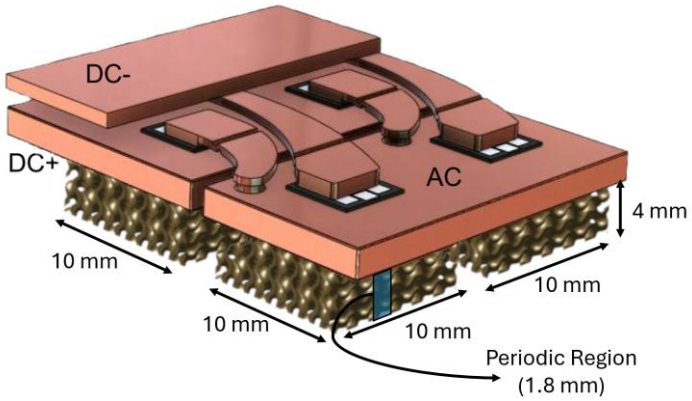


**Figure 83:** Conceptual half-bridge module for the use of dielectric fluid and TPMS structure

Three different flow configurations were investigated in this study, all derived from a gyroid TPMS structure, featuring a porosity of 0.5 at the bottom and 0.8 at the top, resulting in an average porosity of 0.65.

The flow orientation differs for each model:

- Wide slot configuration (Figure 84a): This model has a slot jet width of 9 mm. The flow enters from above and exits from the sides.
- Narrow slot configuration (Figure 84b): This model has a slot jet width of 2 mm, with an opening in the flow path at the center. As a result, the flow directly impinges on the heated surface. The flow then exits from the sides like the previous model.
- Parallel flow configuration (Figure 84c): Unlike the jet impingement configurations, this model features a parallel flow configuration, where the fluid enters from one side and flows through the structure.

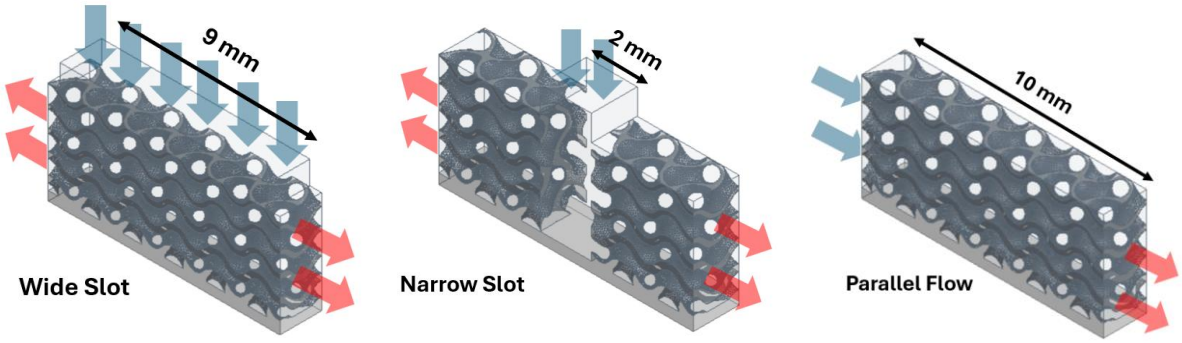


(a) (b) (c)

**Figure 84:** Different flow orientations

The research task covers a range of inlet velocities, volumetric flow rates, and Re, as summarized in Table 14. The flow is assumed to be laminar and incompressible. A heat flux of 50 W/cm² is applied from the bottom of the heat spreader. Symmetry boundary conditions are imposed on the sides of the unit cell model. The inlet boundary condition is set to 70 °C, with a pressure outlet at the exit.

**Table 14:** Numerical parameter ranges

| Parameter | Range |
|---|---|
| Inlet Velocity (m/s) | 0.01 – 1.2 |
| Volumetric Flow Rate (m3/s) | 1.6x107 – 6.5x106 |
| Volumetric Flow Rate (l/min) | 0.01 – 0.4 |
| Re based on height | 10 - 850 |
| Re based on the hydraulic diameter | 15 - 600 |

Dielectric fluids offer a promising alternative by enabling direct contact cooling of heated surfaces by avoiding DBC layers without the risk of electrical short circuits, thus reducing thermal resistance. Among the available dielectric fluids, AmpCool® AC-110 stands out as a high-performance synthetic fluid tailored for electronics cooling applications. It combines key features such as high dielectric strength, thermal stability, and low viscosity. While its thermal conductivity is lower than that of water-based coolants, its electrical insulation allows placement much closer to the heat source, partially compensating for the difference. The properties of AmpCool110 used in the simulations are shown in Table 15.

A mesh dependency test is performed for the parallel configuration. Table 16 presents the results, indicating that a mesh size of around 5-6 million elements is sufficient for the simulations. Furthermore, the mesh is converted into a polyhedral structure to enhance the numerical accuracy and convergence at a lower computational cost.

**Table 15:** AmpCool® AC-110 properties

| | |
|---|---|
| Density (kg/m3) | 783 |
| Specific heat (kJ/kgK) | 2326 |
| Thermal conductivity (W/mK) | 0.134 |
| Viscosity (kg/ms) | 0.0034 |
| Dielectric Constant | 2.08 |

**Table 16:** Mesh dependency results

| Wide Slot | | | | | Narrow Slow | | | | | Parallel Flow | | | | |
|---|---|---|---|---|---|---|---|---|---|---|---|---|---|---|
| Mesh elem. (M) | h ($W/m^2$ K) | Diff. % | Ppump (W) *104 | Diff % | Mesh elem. (M) | h ($W/m^2$ K) | Diff. % | Ppump (W) *103 | Diff % | Mesh elem. (M) | h ($W/m^2$ K) | Diff. % | Ppump (W) *103 | Diff. % |
| 1.14 | 21810 | 10.9 | 6.0122 | 1.2 | 1.00 | 29528 | 2.6 | 2.6974 | 0.8 | 1.08 | 32654 | 3.6 | 3.4165 | 0.5 |
| 2.63 | 21648 | 10.1 | 6.0250 | 1.1 | 2.36 | 29301 | 1.8 | 2.6965 | 0.8 | 2.5 | 32613 | 3.4 | 3.4240 | 0.3 |
| 6.31 | 19556 | 0.6 | 6.0755 | 0.2 | 5.30 | 28618 | 0.6 | 2.7166 | 0.1 | 5.78 | 31619 | 0.3 | 3.4292 | 0.1 |
| 8.55 | 19666 | - | 6.0896 | - | 7.16 | 28776 | - | 2.7195 | - | 7.56 | 31533 | - | 3.4336 | - |

The numerical model with an identical mesh element size is validated against the experimental results of Deng et al. [12], as their study presents a geometry most comparable to the TPMS, with characteristic sizes around 500 µm. The model used for the validation is shown in Figure 85, and the comparison between the experimental data and numerical results is presented in Figure 86, demonstrating reasonable agreement. However, the numerical Nu is slightly higher due to idealizations related to flow and heat transfer in the simulations, such as perfectly smooth and insulated walls.

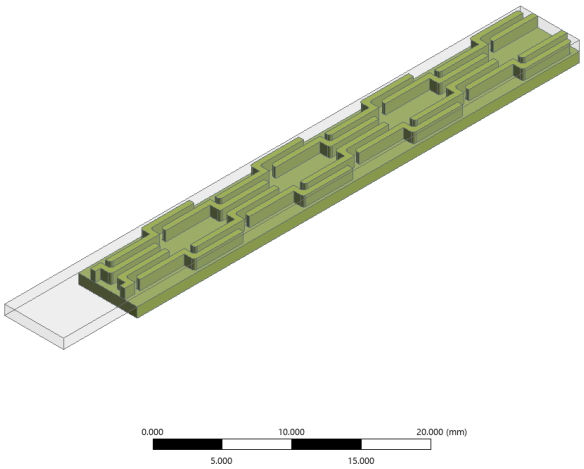


**Figure 85:** Validation model

**Results**

The comparative heat transfer results with the variation of Re for different geometries and flow orientations are presented in Figure 87. The 2 mm slot configuration exhibits a higher Nu compared

to the 9 mm slot, as direct impingement onto the heated surface enhances heat transfer. Interestingly, despite the absence of impingement, the parallel flow configuration achieves a comparable Nu to the 2 mm slot configuration and surpasses it at higher Re.

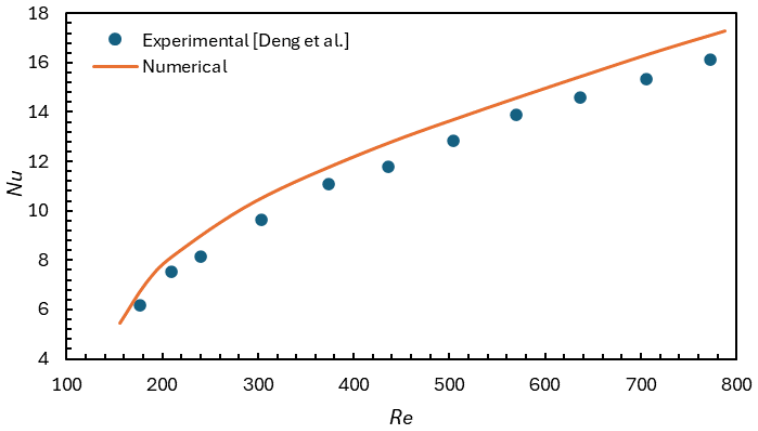


**Figure 86:** Agreement between experimental and numerical results.

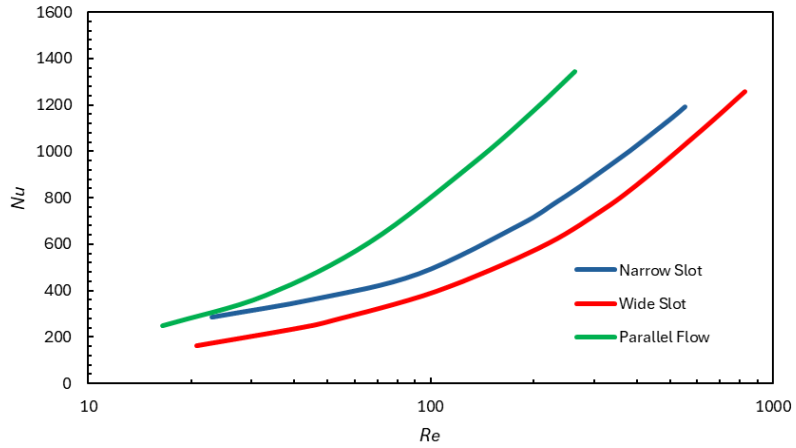


**Figure 87:** Nu with varying Re for different configurations.

Evaluating Nu across different Re conditions helps understand the hydrodynamic effects on heat transfer. However, analyzing Nu at a fixed pumping power is also crucial, as shown in Figure 88. The results indicate that all three configurations exhibit similar Nu trends with increasing pumping power. However, the parallel flow configuration slightly outperforms the narrow slot and wide slot configurations with increases of 8.2% and 10%, respectively, under higher pumping power conditions.

The streamlines in the 9 mm slot configuration are shown in Figure 89 for 0.4 m/s inlet velocity, plotted as it starts from a plane with 1 mm thickness to track them better. Figure 89a illustrates the flow distribution within the TPMS geometry, where no direct impingement occurs, preventing the flow from directly reaching the heated surface. Instead, the flow is directed toward the outlet section near the heated surface. The flow farther from the center, shown in Figure 89b, exits through the upper regions, unable to reach the heated surface effectively. Similarly, the flow near the edges, shown in Figure 89c, is guided toward the outlet through upper regions, where the heat transfer rate per unit pressure drop is lower due to reduced solid temperatures.

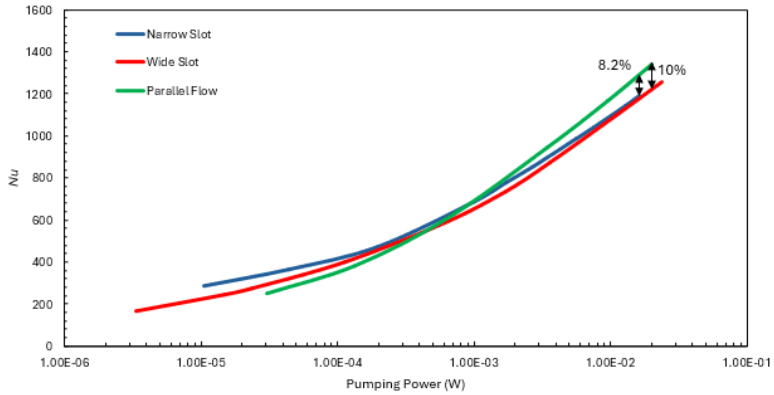


**Figure 88:** Variation of Nu with pumping power for different configurations.

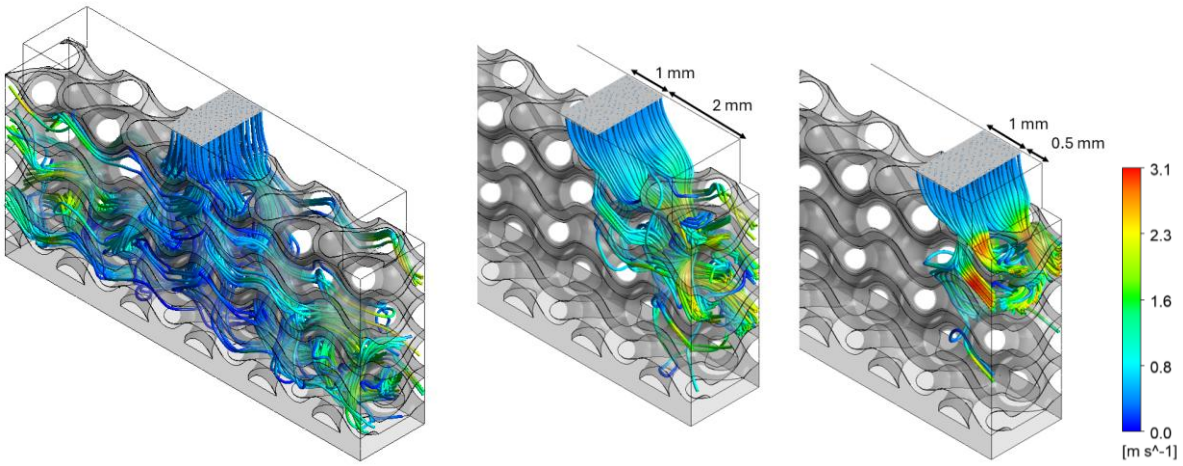


(a) (b) (c)

**Figure 89:** Streamlines for the 9 mm slot configuration with an inlet velocity of 0.4 m/s.

Streamlines for the 2 mm slot configuration is shown are shown in Figure 90 for 1.2 m/s inlet velocity. The flow originating from a 1 mm thickness in the center of the 2 mm slot, shown in Figure 90a, travels directly to the heated surface, where it is distributed throughout the TPMS geometry and exits the outlets homogenously. In contrast, the flow originating from the 0.5 mm section near the edge, illustrated in Figure 90b, enters into the TPMS geometry and exits primarily from the upper regions of the outlet. In general, this configuration generates more vorticity compared to the 9 mm slot configuration.

The streamlines for the parallel configuration are shown in Figure 91 for 0.4 m/s inlet velocity. Figure 91a shows the streamlines originating from the upper part of the inlet section, and Figure 91b shows the streamlines originating from the lower part of the inlet section. The upward spreading of the flow from the lower part of the inlet is more dominant compared to the downward spreading from the upper part of the inlet. This is due to the reduced porosity and flow resistance in the upper region.

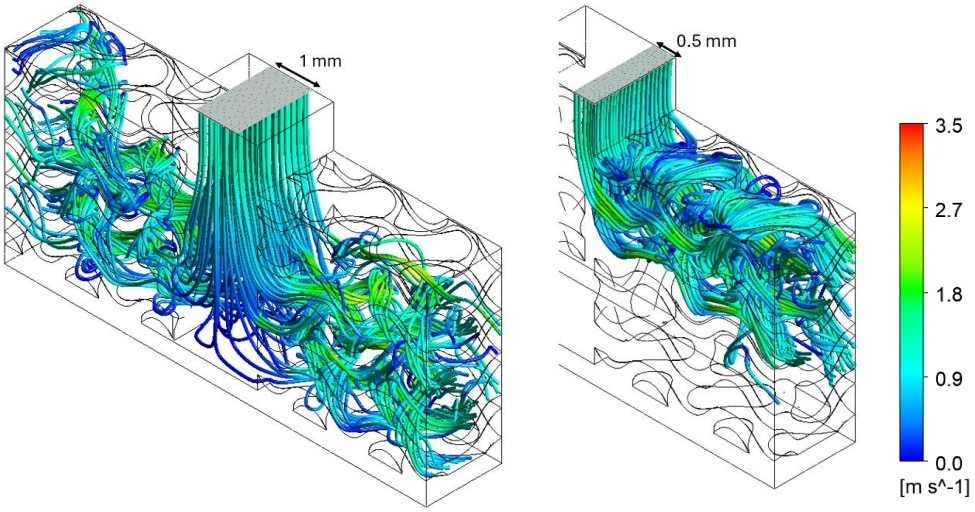


**Figure 90:** Streamlines for the 2 mm slot configuration with an inlet velocity of 1.2 m/s.

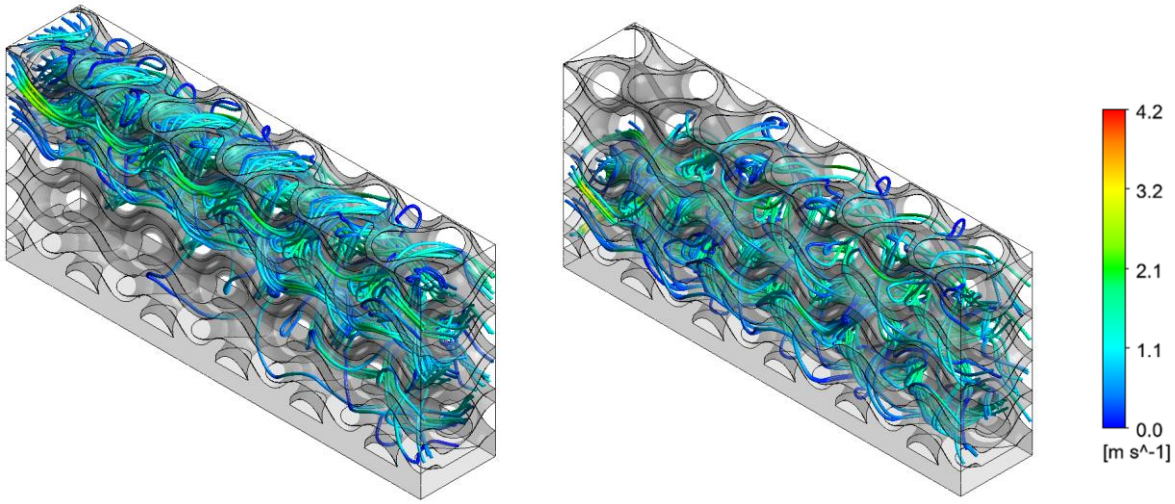


**Figure 91:** Streamlines for the parallel flow configuration with an inlet velocity of 0.4 m/s.

The vorticity results for the 9 mm slot geometry are shown in Figure 92. The central region generates minimal vorticity, resulting in reduced heat transfer. In contrast, vorticity is higher near the sides, especially close to the outlet. Notably, strong vorticity is observed along the surfaces as the flow navigates through curves.

The vorticity results for the 2 mm slot configuration are shown in Figure 93. In contrast to the 9 mm slot configuration, vorticity is more homogeneously distributed within the TPMS geometry, indicating more efficient flow mixing. Unlike the 9 mm slot configuration, high vorticity near the surfaces is not observed when turning through curves. Additionally, the impingement channel in the middle of the geometry does not generate notable vorticity.

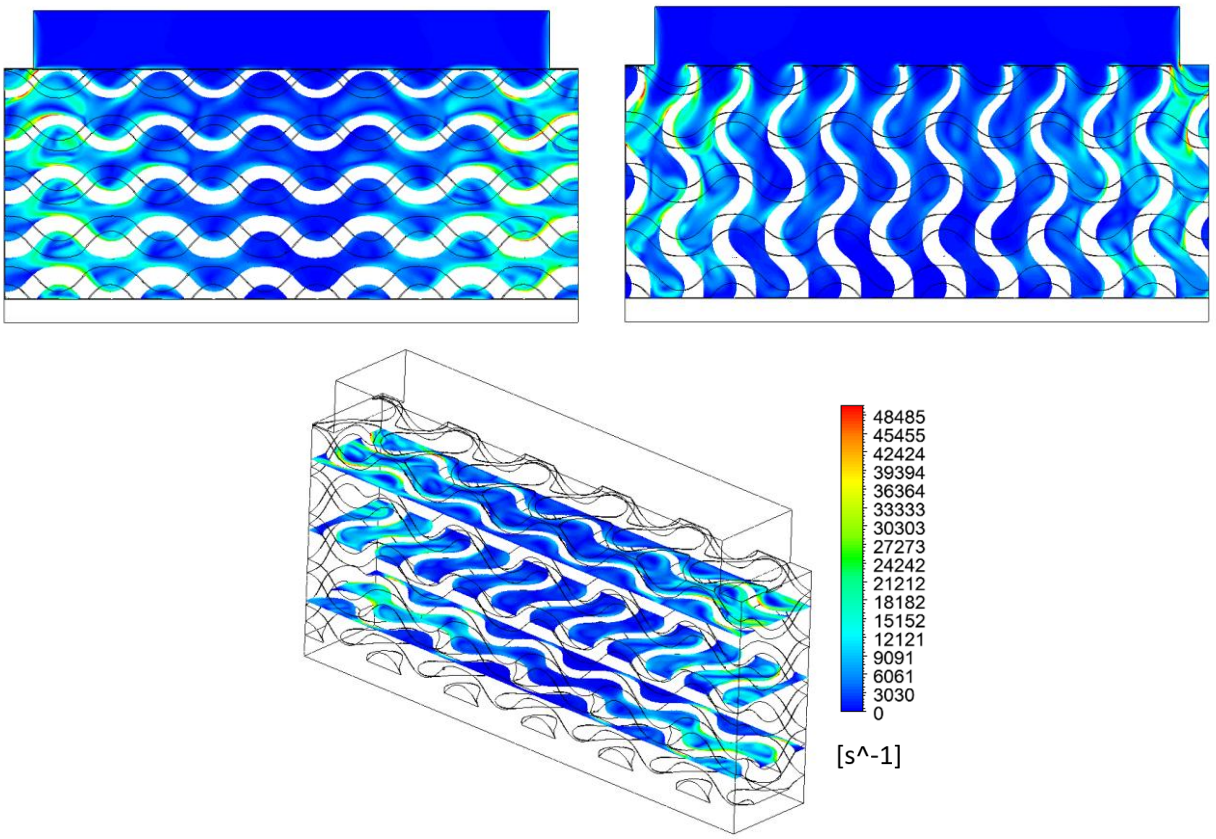


**Figure 92:** Vorticity for 9 mm slot configuration with an inlet velocity of 0.4 m/s.

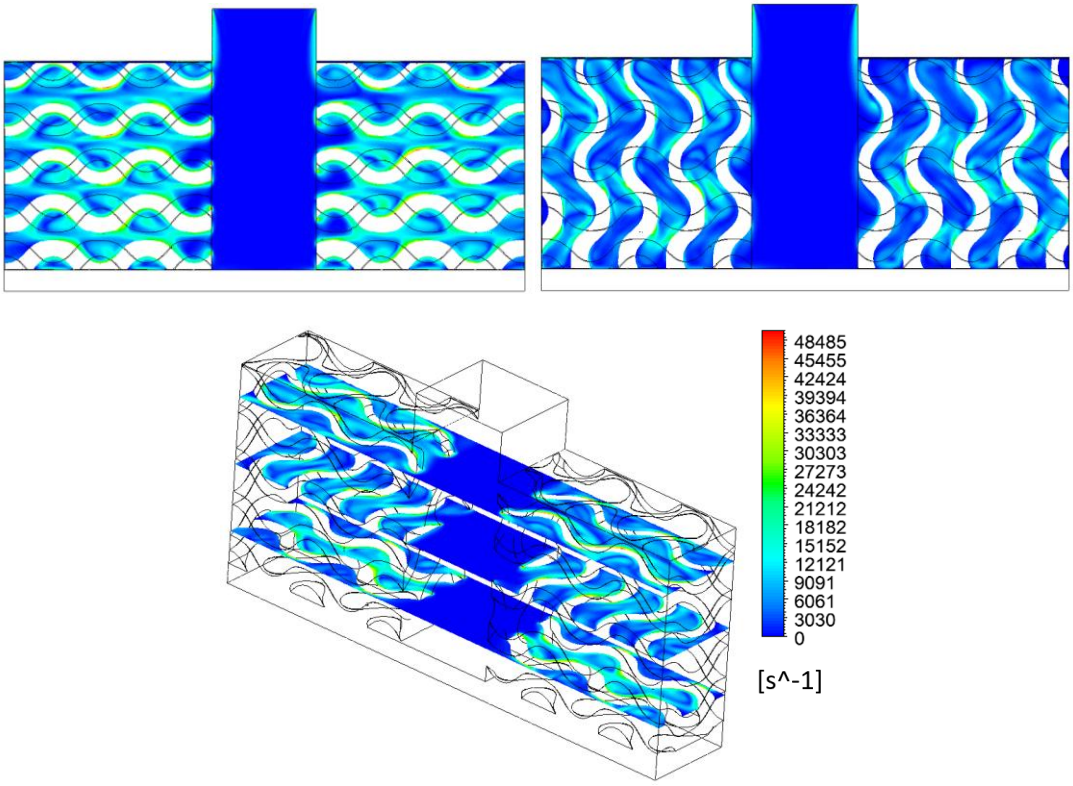


**Figure 93:** Vorticity for 2 mm slot configuration with an inlet velocity of 1.2 m/s.

The vorticity results for the parallel flow configuration are shown in Figure 94. Vorticity is present throughout the TPMS geometry from inlet to outlet and is homogeneously distributed. The vorticity patterns in the vertical and horizontal channels resemble those of the 2 mm slot configuration, resulting in a similar Nu value, as shown in Figure 87. However, unlike the 2 mm slot configuration, high vorticity is observed near the surfaces when the flow turns through curves.

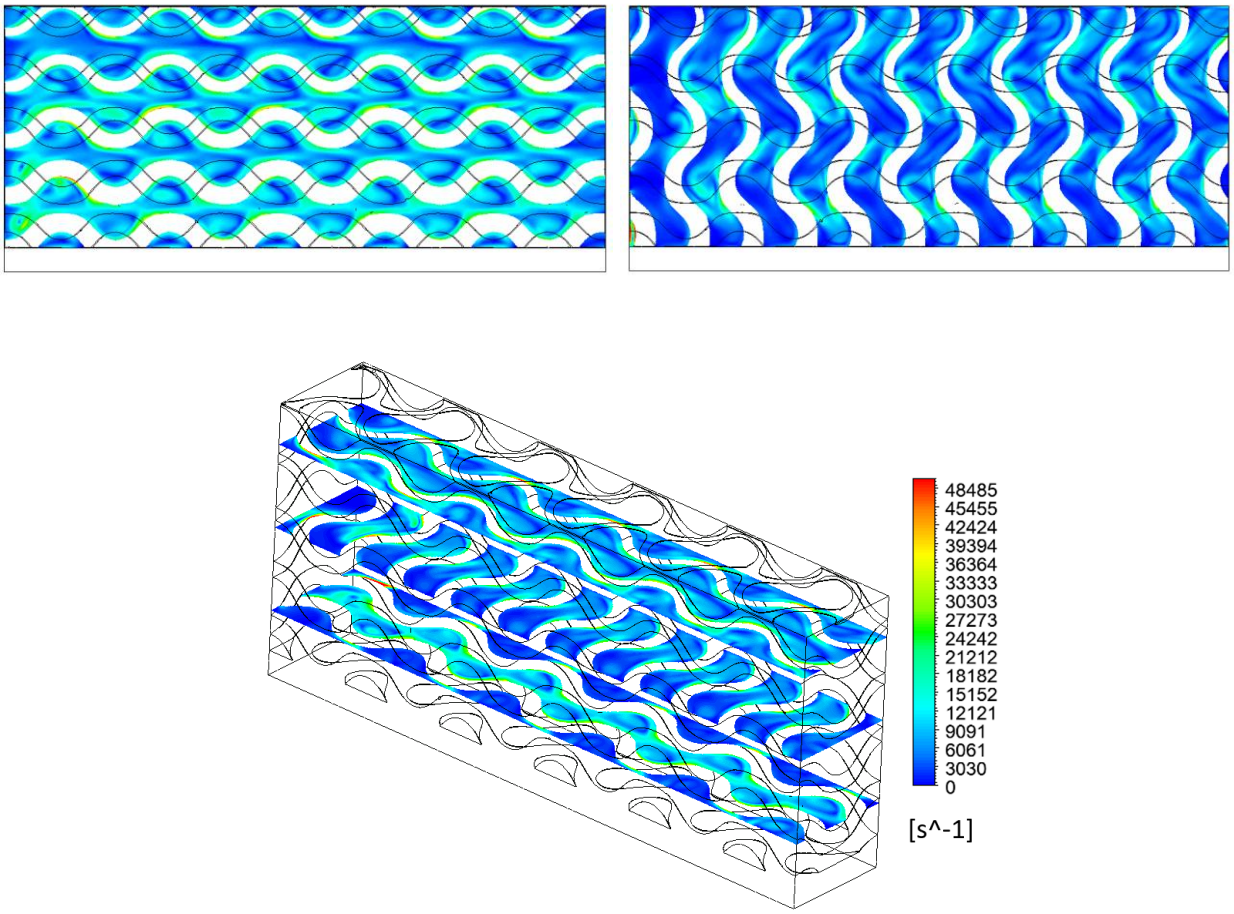


**Figure 94:** Vorticity for parallel flow configuration with an inlet velocity of 0.4 m/s.

The temperature contours of the solid and fluid regions for the 9 mm slot configuration are shown in Figure 95. The temperature at the center of the heated surface is slightly higher than at the sides due to the flow being directed toward the outlet before reaching the heated surface. Additionally, the thermal boundary layers are very close to each other in the lower sections, particularly at the center, which is undesirable for efficient heat transfer. This occurs due to the lack of vorticity in these regions, leading to an increased thermal boundary layer thickness.

The temperature distribution in the fluid and solid regions for the 2 mm slot configuration is shown in Figure 96. Unexpectedly, the heated surface facing the impingement flow exhibits noticeably higher temperatures. Given that the heat sources are usually located at the center of the heated surface, this configuration may lead to higher chip temperatures. The thermal boundary layers do not overlap significantly, indicating efficient heat transfer.

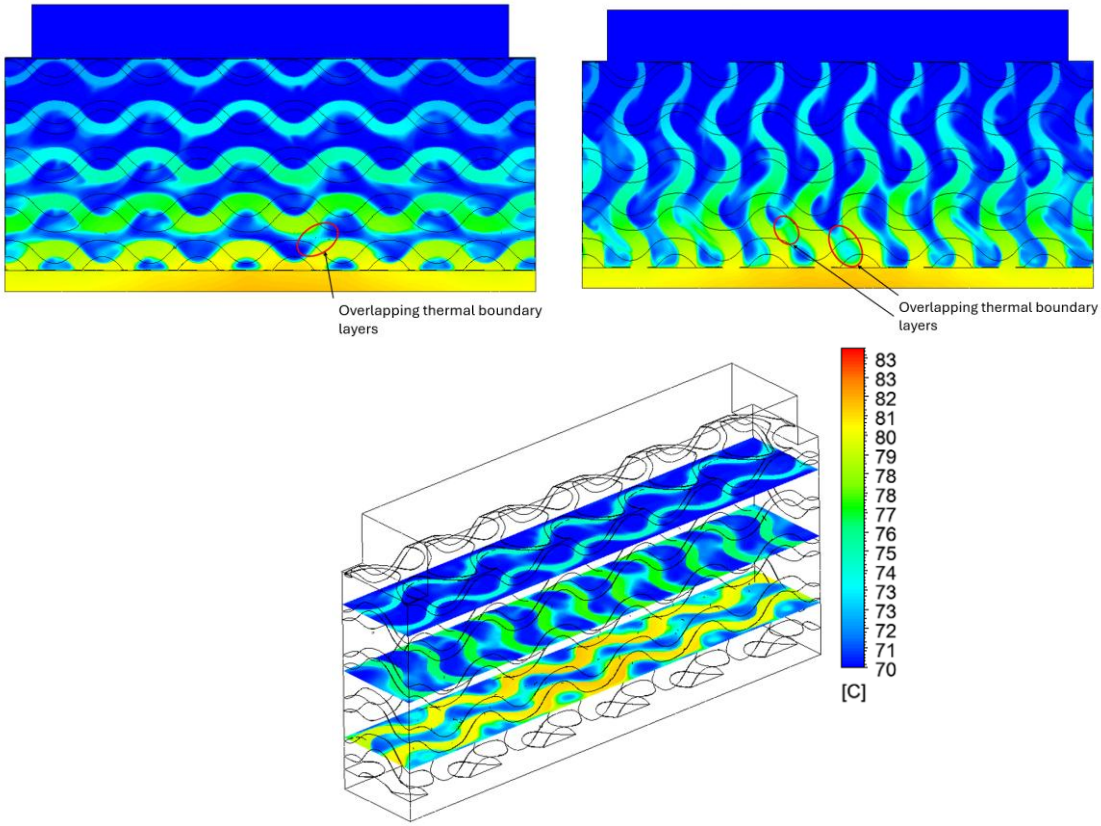


**Figure 95:** Temperature contours of solid and fluid for 9 mm slot configuration with an inlet velocity of 0.4 m/s.

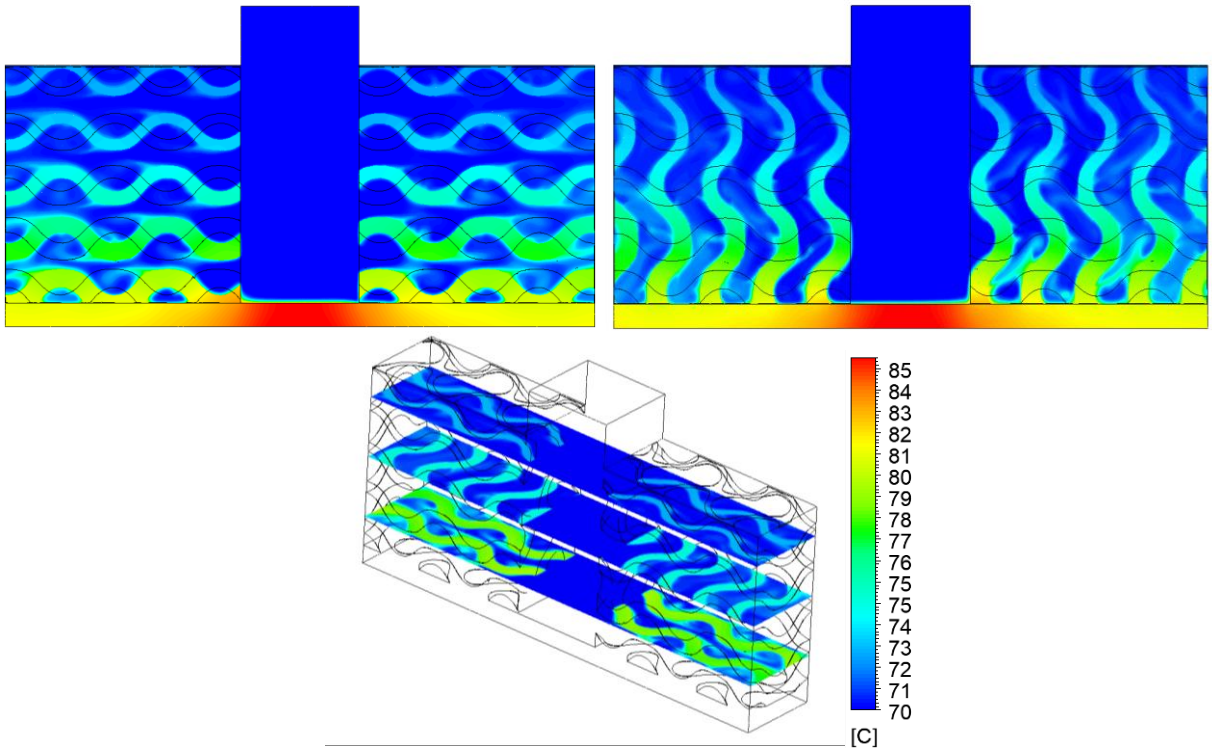


**Figure 96:** Temperature distribution in solid and fluid for 2 mm slot configuration with an inlet velocity of 1.2 m/s.

The temperature distribution in the solid and fluid regions for the parallel flow configuration is shown in Figure 97. The temperature of the heated surface increases along the flow as the fluid temperature rises. Additionally, the fluid temperature is higher in the lower sections of the geometry. As the flow progresses, the thermal boundary layers become indistinct, particularly at the lower right section of the geometry, even though the fluid temperature increases significantly.

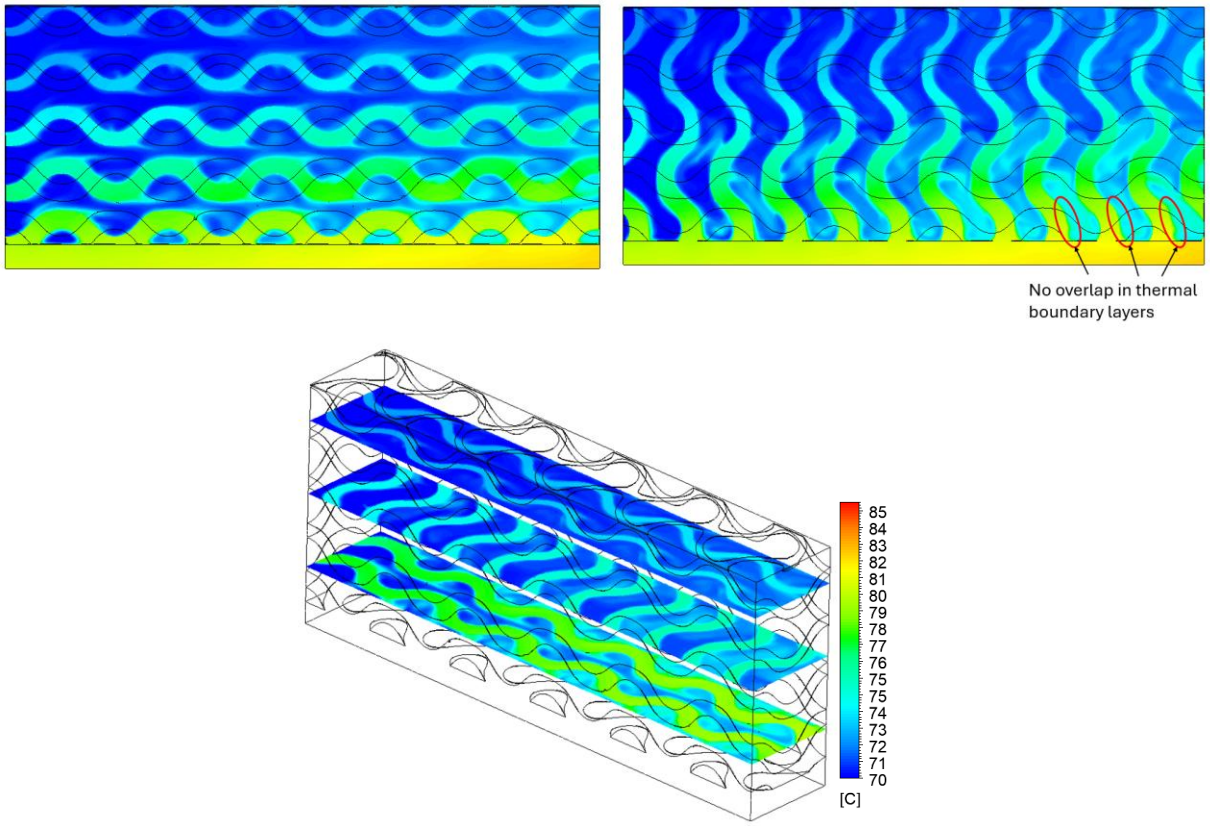


**Figure 97:** Temperature distribution in solid and fluid for parallel flow configuration with an inlet velocity of 0.4 m/s.

## 8. Validation of an Internal Permanent Magnet Motor LPTN

### Summary

In this project task, the Lumped Parameter Thermal Network (LPTN) model of the Nissan Leaf motor is developed. This LPTN will then be used to model the integration of the developed end-winding cooling system in this thesis. The main objective of the task is to validate this LPTN against the FEA model as well as experimental data.

As we are focused on cooling the end-winding, only the stator will be considered for the rest of the work. We propose a different approach by analyzing temperature profiles along three different paths of the motor, with particular attention to the end-windings region and the different contact

interfaces in the stator, as they will directly impact the performance of the developed end-winding cooling system.

Each thermal parameter of our LPTN is clearly investigated, and the relations between the LPTN parameters and FEA parameters are given. Moreover, the sensitivity of the main thermal parameters is computed. The thermal parameters with the highest influence on the increase in motor temperatures were identified through this sensitivity analysis.

**Method**

The Nissan Leaf Electric Motor from Nissan Motor Co. Ltd. is our reference for all geometric, material, and thermal parameters used in this chapter. The only active cooling system in the Nissan Leaf motor is an external water jacket composed of 3 channels in series made of aluminum. The water jacket coolant is Water-Ethylene Glycol (WEG).

The experimental results used in this task are taken from previous experiments in [13]. In these experiments, the windings were supplied with DC current (voltage of 1.4V and current of 165 amps) and the rotor was removed from the motor. The total heat generation from the 3 phases of the motor was 567 W. The only heat rejection system was the water-jacket. The latter was filled with WEG coolant at 50% volume of water. The flow rate was 10 L/min. Insulation was used to reduce natural convection from the external surfaces directly exposed to ambient air (end-windings, inner stator, housing). The boundary conditions of these experiments are shown in Figure 98.

Temperatures were measured with K-type thermocouples. The location of each thermocouple is shown in Figure 98 (black and white crosses). All temperature points in the cross-section plane, Figure 98, except the Housing temperature points, are measured in two other cross-section planes rotated by 120° and 240° with respect to the motor axial axis.

For this task, we consider that a temperature label can be the same for different thermocouples or temperatures by assuming stator symmetries. A set of temperature points having the same label means they should all have the same temperature value based on the assumed symmetries in the models defined thereafter. For instance, we assume that End-windings Inside temperature points have the same value for both rear and front-end-windings. Similarly, we consider that the Stator inner face temperature points have the same temperature along the axial length of the tooth. These assumptions are made to enable a consistent comparison between experimental data and modeling results.

By assuming these symmetries, we end up with only five different temperatures to be compared against the modeling results. In fact, inserting thermocouples inside the stator or the windings requires dismantling the laminations or the slot windings, which would cause a different thermal behavior of the machine. This represents one of the main difficulties for model validation against experimental temperature values. However, in order to validate the LPTN model well, we still need to know if the temperatures inside the stator and the slot windings are consistent. Therefore,

the LPTN temperature outputs are also compared to the FEA modeling results of the complete stator.

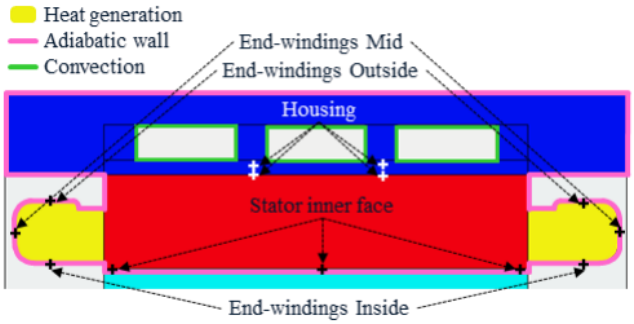


**Figure 98:** Thermocouple locations on the Leaf motor stator and their associated labels, using Motor-CAD® environment. Heat generation and boundary conditions are shown as well.

We used the same motor geometry and boundary conditions in the FEA model as for the experiments. The same power loss input (567 W) was used, and radiation and convection to ambient air were neglected. Table 17 gives thermal conductivities for each material involved in the model, thermal contact conductance at each interface, and the water-jacket thermal properties.

**Table 17:** Thermal conductivities along each direction of a cylindrical system and thermal contact conductance used for the FEA model along with water jacket thermal properties.

| **Thermal conductivity $[W.m^{-1}.K^{-1}]$** | | | |
|---|---|---|---|
| | Radial | Tangential | Axial |
| Stator Laminations | 21.9 | 21.9 | 1.77 |
| Slot-Windings | 0.99 | 0.99 | 292 |
| End-Windings | 0.76 | 202 | 101 |
| Slot liner | 0.18 | 0.18 | 0.18 |
| Aluminum | 167 | 167 | 167 |
| **Thermal contact conductance $[W.m^{-2}.K^{-1}]$** | | | |
| Slot-Windings \| Liner | | | 1645 |
| Liner \| Laminations | | | 556 |
| Laminations \| Housing | | | 5555 |
| **Water-jacket cooling system** | | | |
| Heat transfer coefficient $[W.m^{-2}.K^{-1}]$ | | | 1428 |
| Flow rate $[L.min^{-1}]$ | | | 10.0 |
| Coolant mean temperature [°C] | | | 65 |

The water-jacket heat-transfer coefficient is derived from a CFD/HT simulation of the complete water-jacket channels in [49]. The coolant mean temperature value in the water-jacket is also taken from [49]. The tests in [14, 15] were conducted based on the Nissan Leaf motor parts. This makes the evaluation of the FEA model thermal parameters more accurate than deducing these from a

different motor. We must note that the values for Slot-Windings-to-Liner and Liner-to-Laminations thermal contact conductances are not exactly the same values as those provided in [49]. Indeed, NREL provided slightly different values which were not published yet. These values are preliminary results which require further confirmation.

Two pictures of the FEA model mesh are shown in Figure 7. The average mesh size was fixed at 2.7 mm. This choice relies on a mesh independence study. For this independence study, computing time and maximum temperature versus mesh size results were obtained (see Figure 8). Red labelled markers in Figure 8 correspond to the final average mesh size of the FEA model. With this final mesh size of 2.7 mm, the numerical results are accurate to within 0.4%.

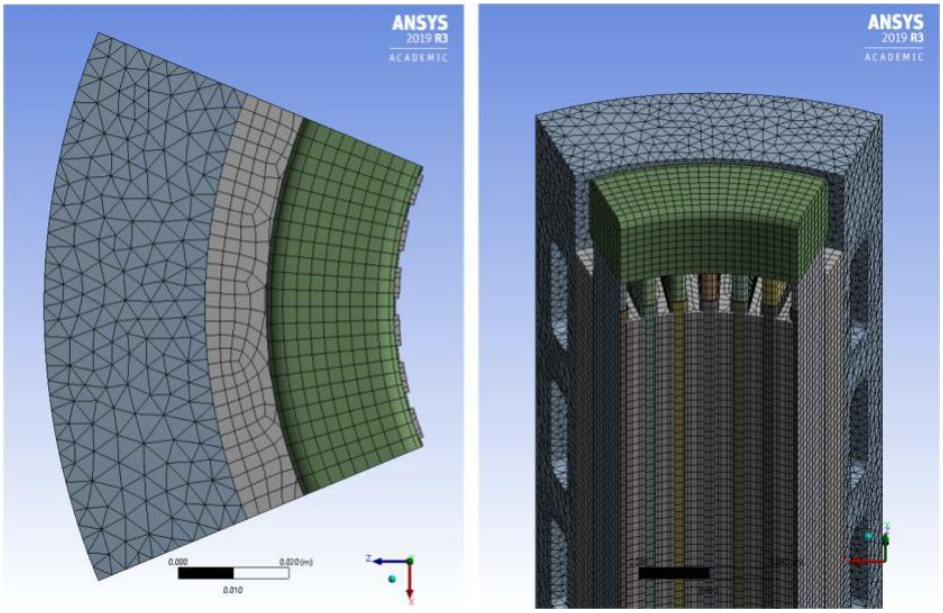


**Figure 99**: Mesh of the FEA model (average size of 2.7 mm).

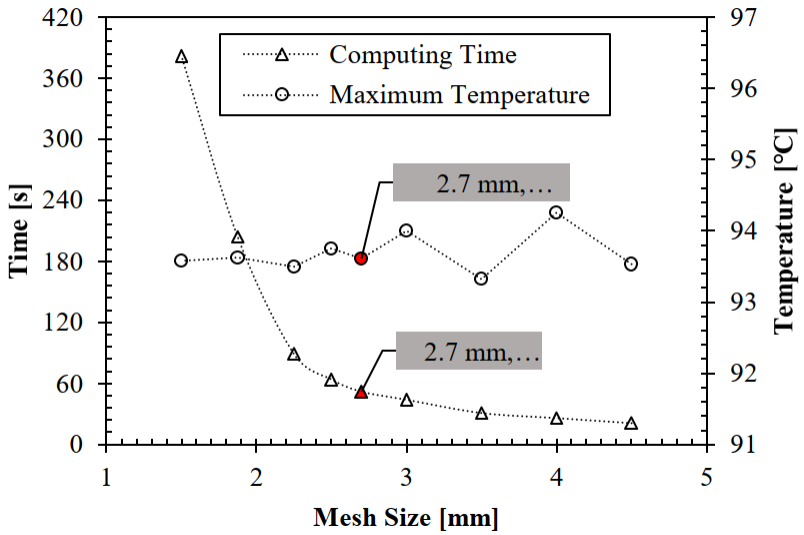


**Figure 100:** Computing time and maximum temperature of the FEA model with respect to mesh size.

The LPTN model was created using Motor-CAD® software environment, where the electric motor geometry is designed first. All dimensions from the FEA model were kept for the LTPN model. **Figure 101** shows cross-sectional views of the geometry. The radial and axial views are shown on the left and right, respectively. A simplified version of the LPTN defined from this geometry is given in Figure 102. Each colored resistance accounts for the thermal conduction through a given part of the stator. The white resistances account for thermal contact resistance at the interface between two parts of the stator. Each node of the network represents a temperature and the sources of the circuit correspond to the copper losses generated inside the windings (567 W). The LPTN main parameters are defined thereafter.

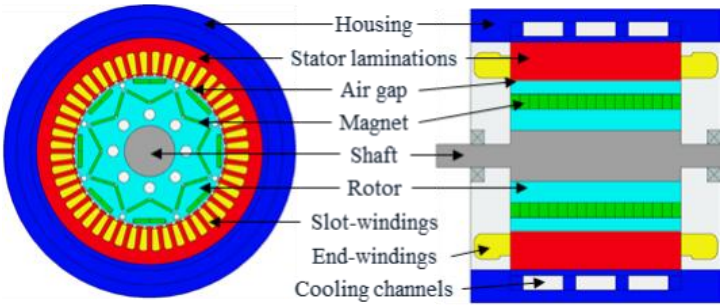


**Figure 101:** Nissan Leaf motor geometry in Motor-CAD® environment: radial cross-sectional view on the left, axial cross-sectional view on the right.

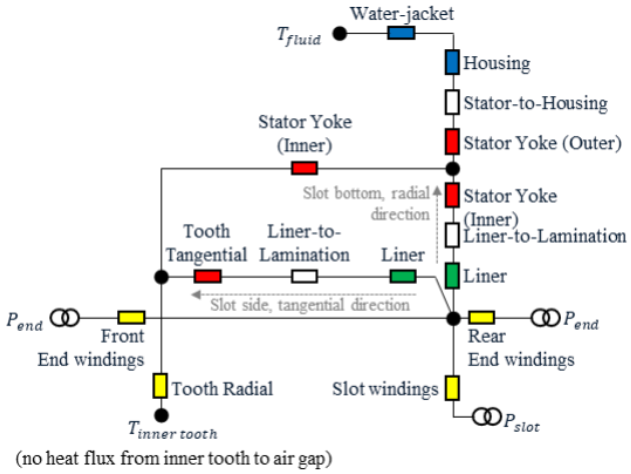


**Figure 102:** Simplified representation of the stator LPTN model (based on Motor-CAD® schematic).

The copper wires used for the windings have a diameter $Dc$ = 0.800 $mm$ and a total diameter (including insulation) $D$ = 0.885 $mm$. Maximizing the number of wires that can fit inside a single slot of the Leaf motor leads to a maximum copper slot fill of 52%.

In the LPTN, the slot-windings are represented as a set of cuboids. The cuboid material includes the copper from the wire, the wire insulation, and the impregnation material. One cuboid contour is highlighted in Figure 103b. One can notice that each cuboid can have a different height or width. However, they all have the same axial length equal to the length of the active windings which is

also the length of the stator. Using cuboids instead of individual wires allows to have a much faster model. Moreover, this cuboid model is not affected by the randomness of the wire distribution in the slot.

The internal resistance values between the face nodes and the center node are calculated from the equivalent thermal conductivities of the wire and impregnation material along each axis. In order to compare LPTN results with FEA results, we used user-defined equivalent thermal conductivities, the values of which are given in Table 17.

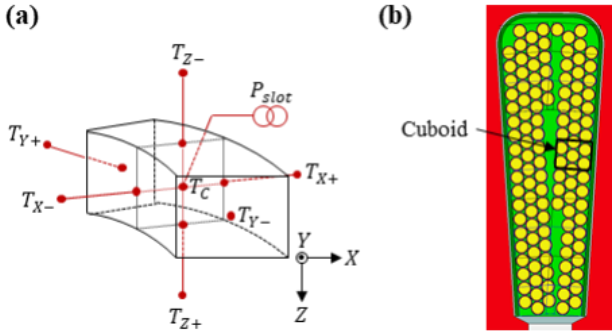


**Figure 103:** Slot-windings cuboids: (a) 3D model representation, (b) in-plane representation within Motor-CAD® environment.

End-windings are modeled as a single toroid. The thermal resistance at the interface between each end-turn and the end-winding shape irregularities are therefore not considered. End-windings are modeled by 10 cuboids connected to the slot-winding cuboids on $T_{Z\pm}$ nodes. As a significant portion of a single wire in the end-winding is oriented along the tangential direction, the thermal conductivity along this tangential direction is significantly increased compared to the slot-winding thermal conductivity along the same direction. However, the thermal conductivity along the axial direction is decreased. This observation explains the different thermal conductivity values given in Table 17. As FEA and LPTN models must be accurately compared, user-defined values of end-winding thermal conductivities (taken from Table 17) were used inside Motor-CAD®.

Thermal contact resistances are the most critical parameters in the LPTN model, as they are the main source of error due to manufacturing process uncertainties. For example, the stator's external surface roughness significantly impacts the effective thermal contact conductance between the lamination stack and the housing. Usually, a stator-to-housing air gap is used to account for the surface roughness. An air gap value for a good contact at the lamination-housing interface is around 0.01 $mm$. If we convert this air gap into an equivalent thermal contact conductance, we obtain a stator-to-housing conductance of 3,171 $W.m^{-2}.°C^{-1}$ for the Leaf motor.

In Motor-CAD®, in order to represent the equivalent thermal contact resistance of the liner, an additional thin impregnation layer is considered between the liner and the laminations. The impregnation thermal conductivity combined with a goodness factor can represent the thermal conductance. Consequently, in the LPTN, the thermal resistance associated with $GLiner$ is defined as the equivalent resistance of a 0.1 mm layer of impregnation between the liner and the stator

lamination multiplied by a goodness factor of 0.051. The very low value of this goodness factor shows that considering perfect contact with the liner is questionable if an accurate LPTN is needed.

Several explanations for the low thermal contact conductance at the liner interface may exist. First, the roughness of the lamination stack surface and liner surface could increase the mean gap between these surfaces and, therefore, increase the resistance. Second, due to a relatively high viscosity of the varnish during the winding impregnation process, there may be stuck air bubbles between the winding and the liner, further deteriorating the contact goodness. Third, there is no additional pressure on the liner that would improve the effective contact area with the laminations or the windings.

In Figure 102, two resistors are associated with the liner-to-lamination contact resistance: one is for the contact with the tooth slot side, and the other is for the contact with the slot bottom.

**Results**

After performing the LPTN simulations, we compared in Figure 104 the temperatures from experiments and the LPTN at the same locations. Labels used for each bar in Figure 104 come from Figure 6. The same reference temperature of 65 °C (coolant mean temperature) is used for both LPTN and experiments. As a reminder from Figure 98, one temperature corresponds to the average at different points from symmetry considerations. Thus, one can derive the standard deviation for each of the five labeled temperatures in Figure 104. These standard deviations are represented by error bars in Figure 104. Standard deviations for each temperature associated with the end-windings are larger than for the Housing or the Stator inner face. Whereas the housing or the stator can be considered orthotropic materials, end-windings are made of several bent wires with various trajectories assembled with impregnation, which can contain air bubbles. Moreover, there are non-equal spaces between end-turns. Therefore, end-windings are highly anisotropic, and the assumed symmetry along the tangential direction of the end-windings implies these larger standard deviations.

In order to compare LPTN and experimental results, we can compute the relative error between LPTN and experimental results for each temperature. End-windings suffer from the highest relative error. Indeed, characterizing end-windings as a single toroid involves significant simplifications as, in the real end-windings, there are three layers of end-turns along the radial axis accounting for the three phases. In these end-turns, wires are curved to go from one slot to another and create a loop, which makes the thermal conductivity of end-windings highly position-dependent. As a result, considering a fixed thermal conductivity along each axis of a cylindrical coordinate system in a single toroid is a strong simplification compared to real end-windings. Consequently, this yields the temperature differences between the LPTN and the experiments. Despite all these simplifications, we obtained a maximum relative error of 3.6%, which demonstrates a good agreement between experimental data and LPTN results. Accordingly, we can claim that the LPTN model is able to accurately predict the steady-state temperatures of the Nissan Leaf motor.

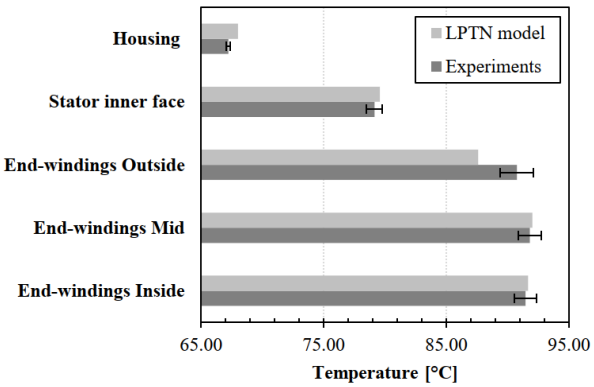


**Figure 104:** Measured temperatures compared to LPTN output temperatures at 5 different points of the stator. Coolant mean temperature of 65 °C is used for both LPTN and experiments.

The results from the FEA steady-state thermal analysis are shown in Figure 105. The comparison between LPTN and FEA models relies on temperature profiles along three different paths represented in Figure 106. Path (1) crosses the slot-windings and stops at the cooling channel wall, path (2) crosses the tooth and stops at the cooling channel wall and path (3) crosses the mid plane of the end-windings along the radial direction.

In order to have a better visualization for the comparison, temperature profiles from FEA and LPTN are given in Figure 107a for path (1), Figure 107b for path (2) and Figure 107c for path (3). For each of these figures, temperatures from experiments (see Figure 104) have also been reported. As presented in the previous section, LPTN representation of windings is based on cuboid structure. For Figure 107a and Figure 107c, the cuboid temperature node that was used for the plots is $T_c$ (see Figure 103), namely the temperature of the cuboid's center node. In order to have an idea of the temperature extremum for each cuboid, the maximum and minimum temperature envelope has been plotted as grey dotted lines on both Figure 107a and Figure 107c. These envelopes are associated with the cuboid model in the LPTN, which is only used for windings, thus, the dotted line is plotted only for the slot-windings part on Figure 107a. Looking at the domain between these two envelopes is more relevant when comparing the LPTN model to experimental data or the FEA model since the plot of $T_C$ temperature does not necessarily correspond to the exact same temperature point in the FEA model or in the experiments.

The maximum relative error between LPTN and FEA models for each path is given in Table 18. The overall maximum relative error is about 2% which makes the LPTN highly consistent with the FEA results for the regions where we have critical temperatures in a motor, namely slot-windings, stator tooth, and end-windings. This confirms the ability of the LPTN to replace an FEA model for steady-state thermal analysis of an electric machine. The computational time for the LPTN steady-state analysis is about 4 seconds, whereas the FEA computational time, with the same computer configuration, is about 52 seconds. However, the LPTN inherent structure provides far coarser temperature resolution than the FEA model.

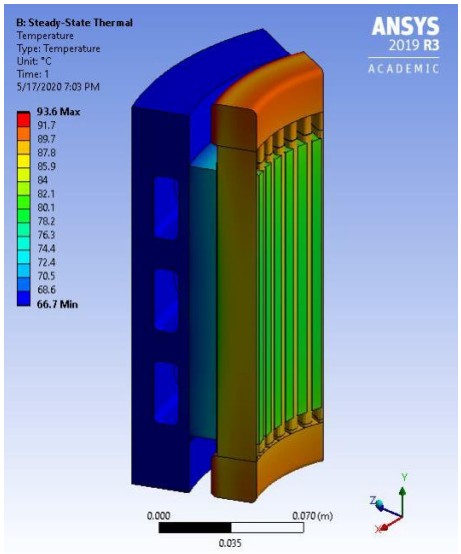


**Figure 105:** Stator temperatures from FEA steady-state thermal simulation.

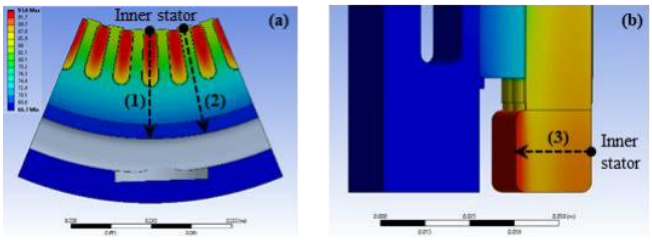


**Figure 106:** Temperature profile paths: (a) path (1) and path (2) locations in the midplane cross-section view of the stator and (b) path (3) location in the axial cross-section view of the stator.

The thermal design of an electric motor is mainly focused on the highest temperature in each of its parts. Indeed, especially for the stator, the thermal limit is fixed by the temperature limit of the windings due to the deterioration of the wire insulation. As a result, having a number of temperature points is not essential as long as the maximum temperature values in each part are accurately predicted. The accuracy has been shown to be significantly high, especially along path (2). For this path, we are only crossing stator laminations and the housing. Stator laminations can be accurately modeled within an LPTN as they are composed of steadily distributed silicon iron sheets

**Table 18:** Maximum relative error between FEA and LPTN model temperature profiles.

| Path | Error |
|---|---|
| (1) → slot-windings | 0.95 % |
| (2) → stator tooth | 0.52 % |
| (3) → end-windings | 2.08 % |

The highest error occurs in the end-windings (Figure 107c). We have already discussed the difference between end-windings LPTN model with a single toroid and fixed orthotropic thermal conductivity and the real end-windings in the LPTN model and experimental data section. The FEA model also uses a single toroid and fixed orthotropic thermal conductivity; however, the LPTN and FEA temperature profiles are reversed in the region beyond 17 mm from the inner stator.

The reason for this temperature rise in the FEA model comes from the low radial thermal conductivity value compared to the axial, and tangential thermal conductivities in the end-windings, see Table 17. For a more detailed explanation, end-windings volume can be represented as a combination of two volumes $\mathcal{V}_1$ and $\mathcal{V}_2$ as shown in Figure 108. Here $\mathcal{V}_2$ is the volume beyond 17 mm. As can be noticed in Figure 19, the heat flux $q_2$ from $\mathcal{V}_2$ to $\mathcal{V}_1$ occurs along the radial direction and unlike $\mathcal{V}_1$, $\mathcal{V}_2$ is not directly connected to the slot-windings. As a result, the heat produced in $\mathcal{V}_2$ leaves through surface $A_2$ (convection is neglected). Yet, the thermal conductivity along the radial direction is much lower than that along the axial direction – the direction of heat flux $q_1$ from $\mathcal{V}_1$ to the slot-windings.This results in a temperature increase in $\mathcal{V}_2$ away from $A_2$ in the radial direction. However, from Figure 107c, the temperature is decreasing within $\mathcal{V}_2$ for the LPTN model. Indeed, as for the slot-windings, end-windings are represented as a set of cuboids within the LPTN model, each connected to the slot-windings cuboids on their $T_{Z\pm}$ nodes (see Figure 12). It means all cuboids are directly connected to the slot-windings, and thus, there is no equivalent volume $\mathcal{V}_2$, as for the FEA, which is not directly connected to the end-windings. Within the LPTN, the end-windings are represented as a single volume $\mathcal{V}_1$. This explains why LPTN temperature profile is still decreasing as we go beyond the bottom of the slot-winding.

Eventually, in Figure 107c, the LPTN predictions are closer to the experiments. This is consistent since all wires that are in volume $\mathcal{V}_2$ come from the slot-windings. Thus, in the real end-windings, heat flux follows the curved path of the wires, which makes volume $\mathcal{V}_2$ directly connected to the slot-windings; hence, the lower temperatures are experimentally observed outside of the windings.

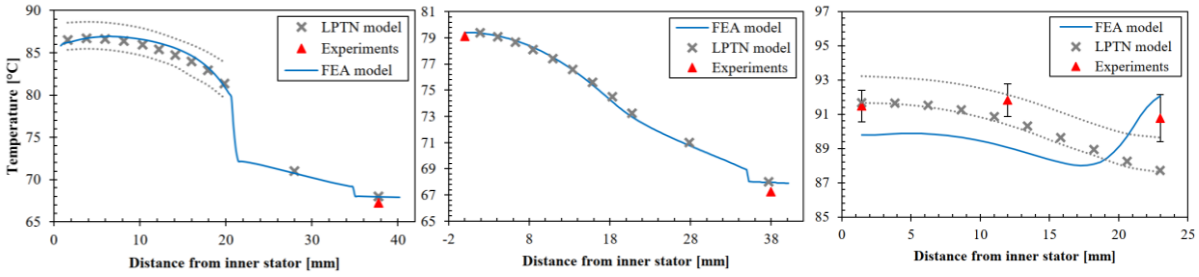


(a) (b) (c)

**Figure 107:** Temperature profiles along a slot following (a) path (1) (b) path (2) (c) path (3). Profiles are given for the FEA model, LPTN model and experimental data.

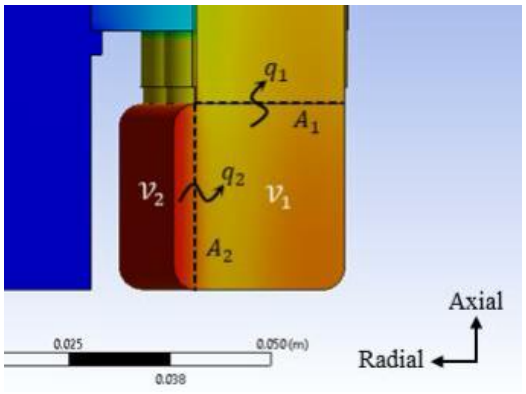


**Figure 108:** End-windings heat flux and volume separation.

A sensitivity analysis using the LPTN can help identify the resistances most responsible for the temperature rise in the stator. Usually, for a sensitivity analysis, the thermophysical properties of the different materials are considered. However, because both thermal conductances and thermal conductivities are considered here, the present sensitivity analysis is based on their equivalent thermal resistance. The final thermal parameters and their associated thermal resistance names chosen for the present sensitivity analysis are given in Table 19.

**Table 19:** List of thermal resistances used for the sensitivity analysis and their related initial thermal parameter.

| Thermal resistance | Associated thermal parameter |
|---|---|
| R [Liner Contact] | Liner-to-lamination thermal contact conductance |
| R [Liner] | Liner thermal conductivity |
| R [Slot-Windings] | Slot-windings equivalent thermal conductivity |
| R [Water-Jacket] | Channels heat transfer coefficient |
| R [Housing Contact] | Housing-to-lamination thermal contact conductance |
| R [Housing] | Housing thermal conductivity |

The LPTN used for the sensitivity analysis was based on a 20% and 50% value reduction for each thermal resistance in Table 19. The sensitivity was assessed by computing the temperature difference $\Delta T$ between the winding maximum temperature with initial resistances and the winding maximum temperature with the new reduced resistance. Figure 109 presents the sensitivity analysis results for each resistance and percentage reduction.

Figure 109 shows that the Liner Contact resistance has the highest influence on the temperature variation of the motor, followed by the Liner resistance. This high influence of the liner relates to the highest temperature decrease (≈ 7°C), at 21 mm from the inner stator in Figure 107a. This temperature decrease occurs along a very short distance, less than 1 mm, corresponding to the liner area.

The liner influence is due to the low thermal conductivity of the liner compared to other thermal conductivities involved (see Table 17). Also, this influence comes from the low contact thermal conductance of the liner compared to other thermal conductances like the stator-to-housing contact conductance. Although the difference between contact thermal conductance of the liner compared to other conductances seems quite high, it remains consistent. Indeed, stator-to-housing thermal resistance is essentially caused by laminations roughness. At the lamination-to-liner interface, this same roughness is responsible for a decrease in the contact conductance. However, imperfections during impregnation process, as well as remaining air between the liner and the laminations significantly impact further reduction of the liner contact conductance.

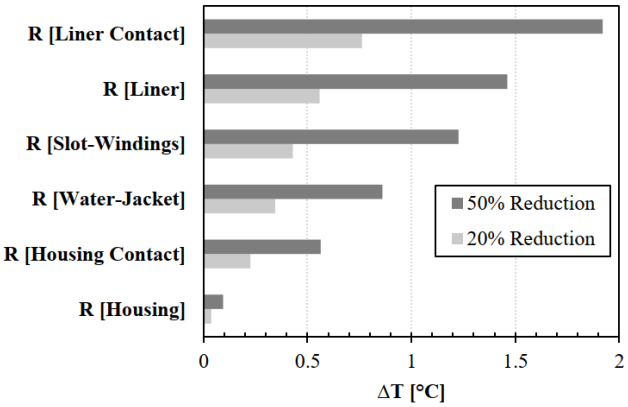


**Figure 109:** Sensitivity analysis of the LPTN thermal resistances for 20 % and 50 % value reductions.

It is worth noticing that Water-Jacket resistance sensitivity is less than half of the Liner Contact resistance sensitivity. This shows that improving the heat transfer coefficient of a cooling jacket system outside of the slot-windings has some limitations in terms of maximum temperature reduction. This is particularly illustrated in Figure 110. The limitation of increasing the heat transfer coefficient is represented by the dashed line asymptote equal to 91.50 °C. Therefore, the maximum temperature difference between the current heat transfer coefficient (1,428 $W.m^{-2}.°C^{-1}$) and an infinite heat transfer coefficient is about 1.7 °C.

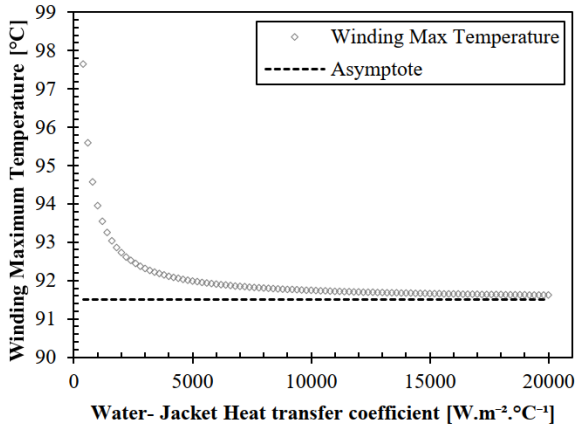


**Figure 110:** Winding maximum temperature as a function of water-jacket heat transfer coefficient. Results are computed with our LPTN model.

From the previous observations, we can draw an important conclusion. The next-generation cooling systems that will make IPM motors reach high power densities must be between the liner and the windings. According to the sensitivity analysis, improving the water-jacket heat transfer coefficient or the stator-to-housing conductance will not provide enough temperature decrease in the windings. With this analysis, one can understand that the next generation of high-density electric motors must have direct winding cooling.

## 9. Design, Testing and Modelling of the End-winding Channel

### Method

The end-winding channel design was based on the geometry of the Nissan Leaf motor. This motor has distributed windings, as most of the motors inside electric vehicles. Consequently, the toroid formed by the end-turns is quite compact, which makes it difficult to push a channel inside the windings. Moreover, during electric machine manufacturing, once wound, the windings are impregnated with a varnish material which is then cured, creating a solid toroid that cannot be deformed to insert channels. Thus, putting channels inside the windings would require changing the impregnation process of the winding. If we want our solution to be suitable for mass production, we need to have a cooling system that can be assembled in the motor after the impregnation process.

The coolant flowing through the channel must be the WEG mixture, as we want to keep the same coolant used for the water jacket. This WEG is electrically conductive. Consequently, we must have a perfectly sealed channel to prevent any WEG leak on the windings. Furthermore, the thermal resistance between the coolant and the end-windings needs to be as low as possible to ensure a good heat transfer. This implies that the channel walls should be as thin as possible and as close as possible to the windings. However, we must ensure a minimum wall thickness for the channel to withstand the internal pressure from the coolant at high flow rates. The pressure requirement was fixed at 15 psi based on the cooling loop total pressure.

The wall of the channel cannot be made of conductive material, as we are touching the end-windings, and we may have risks of short circuits. Moreover, this non-conductive material should be equal to the maximum temperature rating from the wire insulation class given by the NEMA standard. We have considered a class F rating for the windings, leading to a maximum operating temperature of 155°C. Eventually, the contact area between the channel and the end-winding needs to be as high as possible to enhance the heat transfer from the windings to the coolant.

In addition to the requirements listed in the research task 6, the design of the end-winding channel has been limited by cost, time, and equipment constraints. We had only 3 months to create and test the end-winding channel prototype at NREL. Due to these time and cost constraints, and as we needed several iterations on the channel dimensions before being able to test the final prototype, we could not outsource the fabrication of the end-winding channel. Consequently, we had to use the available equipment from NREL to manufacture the end-winding channel prototype.

In order to maximize the surface contact area between the channel and the end-windings, we decided to design the channel as a U-shape surrounding the end-windings. With this U-shape, we are in contact with the inner side, outer side, and top side of the end-windings while having an easy insertion process.

The material for the channel needed to be non-conductive with a high temperature operating point of 155°C. PEEK material and ULTEM are two polymers that have a wide operating temperature range. In our case, both PEEK and ULTEM have maximum operating temperatures higher than the maximum operating temperature of the winding (155 °C). In terms of equipment, the easiest way to create a prototype and iterate quickly on different sizes and shapes is to use a 3D printing process. However, NREL had only a 3D printer capable of printing ULTEM 9085 parts. As a result, we decided to go with ULTEM 9085 material for the fabrication of the end-winding channel. ULTEM 9085 has a heat deflection at 264 psi of 153 °C and a glass transition temperature of 186 °C according to Stratasys manufacturer. As ULTEM is a high-operating-temperature material, Fused Deposition Modeling (FDM) is the preferred 3D printing technology for this material. FDM consists of a thermoplastic filament connected to a heated extruder head, which moves along each Cartesian axis of a 3D space. The part is extruded layer by layer. The thickness of one layer is limited by the diameter of the filament and the deposition speed.

3D printing is a fast iteration process, but it comes with some disadvantages in terms of design possibilities. Indeed, our first idea was to 3D print the channel as a single body as seen in Figure 22. However, 3D printing this geometry would have required a support structure inside the channel cavity to support the top wall of the channel

perpendicular to the 3D printing direction. This support structure inside the channel would have increased the pressure drop significantly, as well as the risk of low-quality sealing of the channel wall. Consequently, we decided to split this single body into two parts.

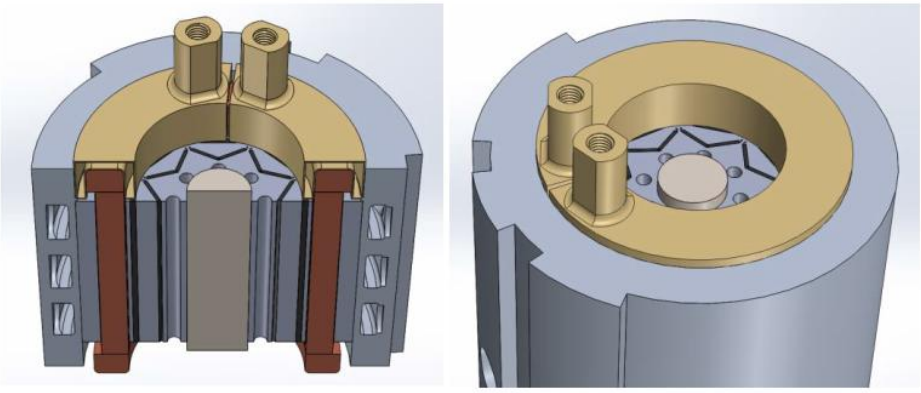

**Figure 111:** Initial design of the end-winding channel.

The two resulting parts are shown in Figure 112 and Figure 113. The bottom part is inserted inside the end-windings. This part includes the U-shape cavity for the fluid to flow all around the end-windings. The top part is then fixed to the housing and pushed against the bottom part to ensure that the complete assembly is sealed. The inlet and outlet of the end-winding channel are located

on the top part as shown in Figure 112. This was the easiest way to connect the end-winding channel to the rest of the coolant loop. However, in a fully integrated solution, these inlet and outlet could come directly from the housing and enter the channel from the outer side of the U-shape wall. On the left picture of Figure 113, one can see that the cavity has a separation wall which prevents the fluid from the inlet to be mixed with the fluid from the outlet.

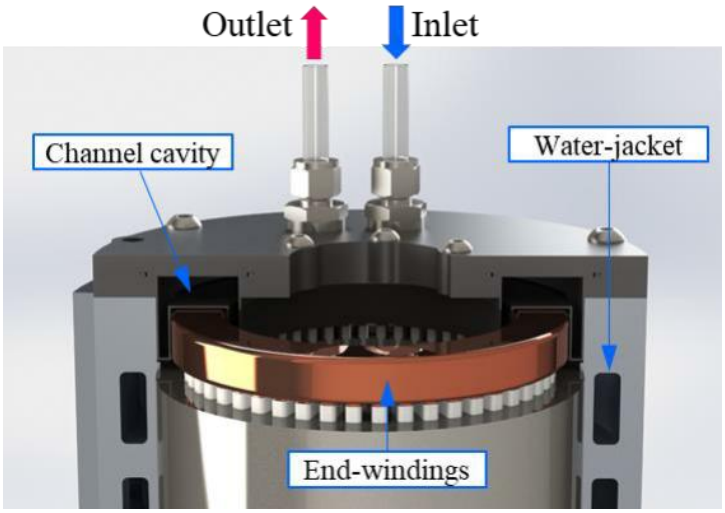


**Figure 112:** Cross-sectional view of the final assembly of the end-winding channel and the Nissan Leaf motor

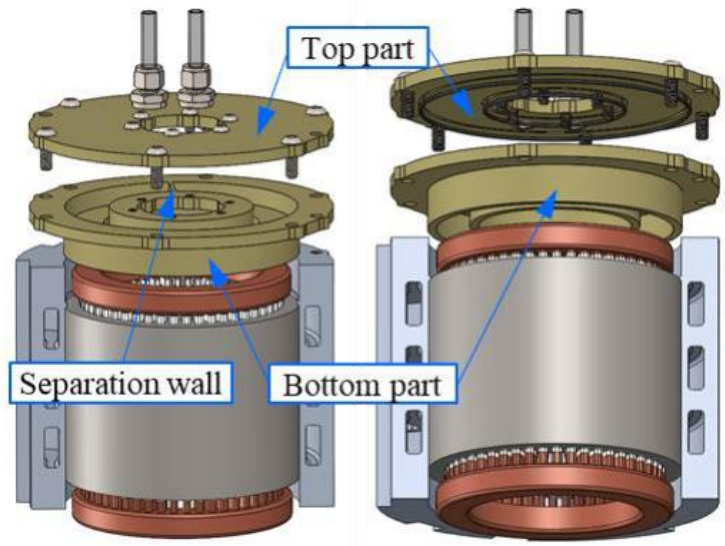


**Figure 113:** Final design of the end-winding channel. The bottom part with the U-shape cavity is pushed to the end-windings and the top part is fixed to the bottom part and the housing.

The final dimensions of the end-winding channel are shown in mm. Figure 114. As we can see, the left and right sides of the U-shape channel have an internal thickness of 4.7 mm. We were limited by the distance between the housing and the channel. In a fully integrated design, we would increase the gap between the housing and the end-winding channels to increase the thickness of the channel sides to further reduce the pressure drop across the end-winding channel.

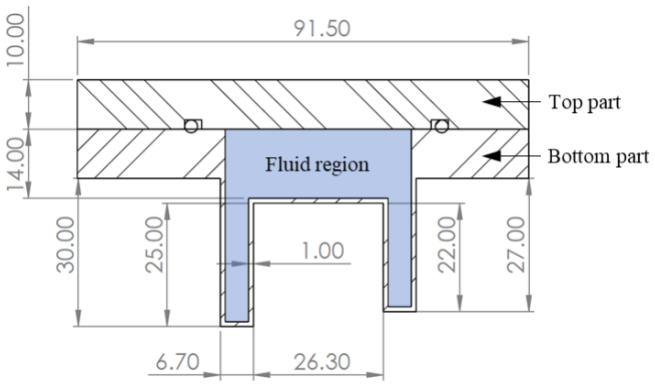


**Figure 114:** End-winding channel cross-sectional view with dimensions in mm.

The end-winding channel must be perfectly sealed to prevent any WEG coolant from touching the end-windings. Our solution presents two different sealing challenges. The first challenge is the sealing of the parts themselves. Indeed, the optimization of the filament deposition in the FDM process is not enough to ensure the watertightness of the 3D-printed parts. Tiny air gaps still exist between the deposited filaments, especially at the corners, and when two contours with different curvatures are next to each other. The second challenge is the sealing of the bottom and top part assembly. We must ensure that we have a perfect sealing when pushing the top part against the bottom part. Our solutions for these two challenges are presented hereafter.

In order to seal a 3D-printed part, the small air gaps between the filaments need to be filled so that the part becomes a solid block. To meet the pressure requirement, the Stratasys team recommends using a two-part epoxy to make the 3D printed part watertight. Two types of epoxy are proposed: Loctite E-20HP Hysol Epoxy from Henkel Adhesive Technologies and the TC-1614 Epoxy from BJB Enterprises. Only the TC-1614 meets the temperature requirement for our application. Indeed, according to the TC-1614 Datasheet, this epoxy withstands temperatures up to 177 °C, which is beyond our maximum temperature of 155 °C. Moreover, the TC-1614 epoxy has been especially developed for 3D printed part sealing, which was another reason to select this epoxy.

The TC-1614 is a low-viscosity two-part epoxy. A two-part epoxy is composed of a resin part and a hardener part. The resin and hardener are both liquid at ambient temperature. When this resin and hardener are mixed, they form a viscous epoxy that becomes solid after a few hours of curing. The principle of 3D printed part sealing with this type of epoxy is simple. After mixing the resin and the hardener, the still-liquid epoxy is applied to the 3D printed part. The epoxy penetrates the part and fills all the small air gaps. The epoxy cures inside the part, and we eventually obtained a composite part made of epoxy and ULTEM with no air gap. Nevertheless, the final complete process for 3D-printing part sealing with TC-1614 is more complex as it requires intermediate steps to ensure a good sealing quality and a good surface finish of the part.

The first approach to seal the bottom and top part assembly was to use a static O-ring face sealing between these two parts. Two glands were designed on the outer and inner sides of the channel on the top part. These glands and the two O-rings used for the assembly can be seen on the right

picture in Figure 113 or in the cross-sectional view in Figure 114. When using an O-ring solution, the surface finish of the gland surface should be lower than 63 µm (RMS value) for the side surfaces of the gland and 32 µm (RMS value) for the bottom surface of the gland according to Parker O-ring Handbook. However, these values are lower than the typical roughness obtained with a 3D-printing process. Indeed, according to the roughness study of 3D-printed parts using ULTEM 9085 from Fischer and Schöppner, the roughness for surfaces parallel to the extrusion direction (corresponding to a build angle of 90 degree as defined in their paper) is around 100 µm while the roughness for surfaces perpendicular to the extrusion direction (corresponding to a build angle of 0 degree as defined in their paper) is around 150 µm.

To improve the surface finish of the parts, we decided to sand them using sanding sheets from medium to fine grit. This sanding step was performed once each part was filled with epoxy following the sealing process. Only the surfaces in contact with each other and the surfaces of the gland were sanded with care. For the other surfaces, surface finish did not have an impact on the sealing quality of the top and bottom part assembly. The result of the sanding surface finish can be seen in Figure 115 for the top and bottom parts. The matte surfaces correspond to the sanded surfaces while the glossy surface on the left picture is the original surface coated with epoxy. One can notice that the surface finish is really good on the visible sanded surface of the picture. While we have not measured the exact surface roughness, it obvious via touch, that we have a surface roughness lower than the maximum roughness recommended in the O-ring handbook.

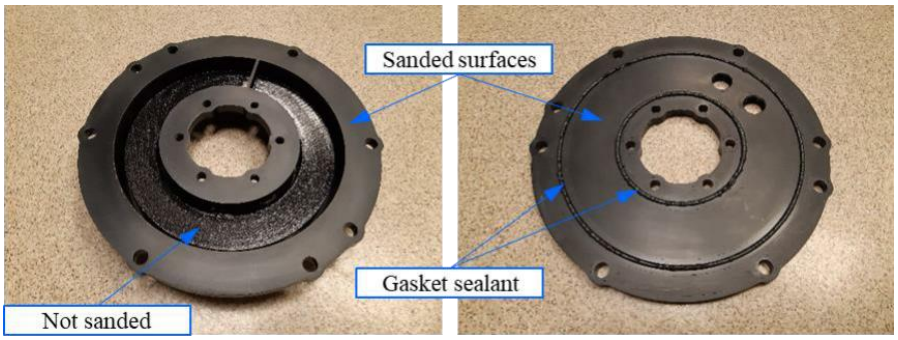


**Figure 115:** Bottom (left) and top (right) parts of the end-winding channel after sealing with epoxy and sanding surface finish.

While the surface finish of the contact surfaces looks good enough to use an O-ring solution, we were not able to achieve the same finish quality for the gland. Indeed, using sanding sheet to smooth each surface of the gland was difficult and correctly sanding the corners of the gland was impossible. Consequently, we could still potentially have a leak at one of the O-ring after bolting the top part to the bottom part. To test the channel assembly sealed with O-rings before using it for the test, we used a Fluke 718 300G pressure calibrator. This pressure calibrator was connected to the outlet of the end-winding channel, and the inlet was closed using an endcap fitting as shown in Figure 116. We just used this calibrator to have an accurate measurement of the pressure we were creating inside the channel by using the manual pump of the calibrator. Soapy water was applied to each external surface of the assembly to easily detect any leaks.


**Figure 116:** End-winding channel airtightness test setup

After increasing the pressure inside the channel using the manual pump, we detected a leak at 9 psi from the outer edge, at the interface between the bottom and top part. As a reminder from our design requirements, the channel must withstand a maximum pressure of 15 psi. Even though this test was measuring airtightness instead of watertightness, we could not take the risk of using an O-ring for the top and bottom part assembly, knowing that we had an air leak at 9 psi. Increasing the number of bolts would have probably solved this sealing issue, but we were constrained by the number of available holes in the Nissan Leaf housing. Thus, to solve this issue, we decided to replace the O-ring with a silicone gasket sealant commonly used in the automotive industry, namely the LOCTITE 5900 from Henkel Adhesive Technologies. We applied this silicone sealant in the glands of the top part as can be seen in Figure 115. Then, we bolted the top part to the bottom part and let the sealant cure at ambient temperature for one day. We performed the same airtightness test shown Figure 116 for the new assembly with the gasket sealant, and we did not detect any leak at 20 psi. This solution was validated, and the end-winding channel was ready to be fixed to the Nissan Leaf Housing. Two photos of the final end-winding channel assembly are shown in Figure 117.

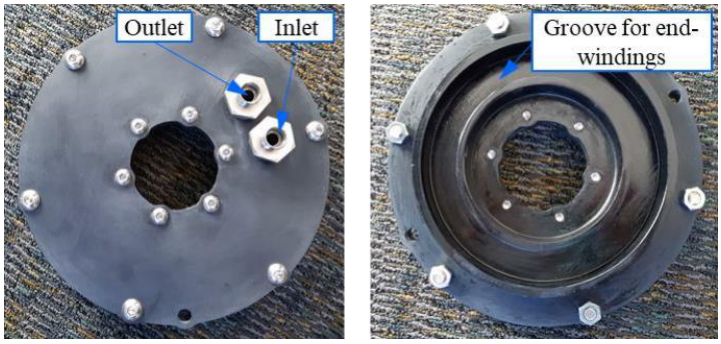


**Figure 117:** Final end-winding channel assembly

The end-windings have a very irregular geometry due to the coil winding manufacturing process used for typical round wires. This can be observed in Figure 118. For instance, the gap between the outer side of the end-windings and the inner side of the housing is not constant. The difference between the minimum gap and the maximum gap is more than 1 mm, which can have a significant

impact on the heat transfer between the end-windings and the channel. This gap variation also exists on the inner side of the end-winding. Compressing the end-windings to form a better rectangular shape would help reduce the geometric irregularity. However, the motor we had was a purchased motor with windings already impregnated. Therefore, the end-windings were forming a very solid block that could not be reshaped.

**Figure 118:** Nissan Leaf end-winding rear side view

For our cooling system to be used with this type of distributed windings, we then had to improve the contact between the channel wall and the end windings to reduce the associated thermal resistance. For electronic cooling, a thermal paste is typically used between the hot electric component casing and the cold plate to have a better thermal contact. We decided to use this same technique by applying a thermal paste between the channel walls and the end-windings. After comparing different options, we ended up using a thermally conductive cure-in-place silicone compound from Parker Chomerics called THERM-A-FORM™ CIP35. This silicone compound is particularly suitable for complex shapes, it does not require high compressive force, can cure at ambient temperature, and has a high thermal conductivity of 3.5 $W.m^{-1}.K^{-1}$. These are the main reasons for using this product.

As we did not know exactly what amount of silicone would be required to fill the irregular gap between the channel walls and the end-windings, we decided to spread the silicone compound on the end-windings and then push the channel assembly on the end-windings. This would allow the excess potting to be pushed to the laminations of the stator. The potting was applied by hand, and a spatula was used to smooth the surface. Two photos of the end-winding with the silicone compound, just before inserting the channel, are shown in Figure 119. Alternatively, if the final amount of silicone required to fill the gap between the channel and the winding is known, it would be better to put the compound on the channel walls first and then push the channel assembly on the end-windings. In this case, we would use much less compound than what we have used for our experiments. It is difficult to have a good estimate of the effective compound volume in the end-winding region. We estimate we had ~250 $cm^3$ of silicone compound in the end-windings.

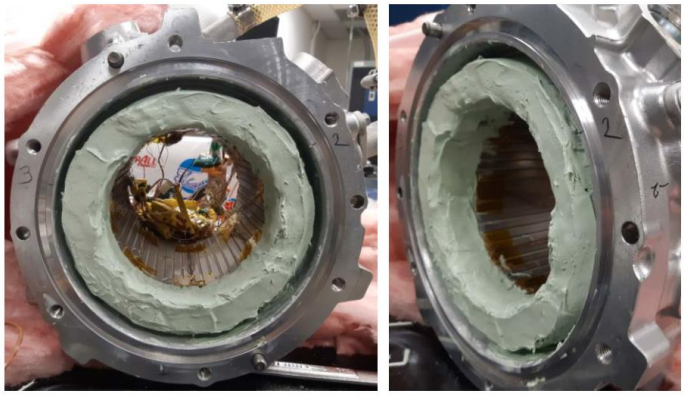

**Figure 119:** Thermally conductive silicone compound on end-windings.

After applying the silicone to the end-windings, we pushed the end-winding channel assembly into the end-windings. We let the silicone compound cure in place for one day. The final assembly of the channel and the motor can be seen in Figure 120. The silicone layer in between the top of the end-windings and the channel prevented us from pushing the channel up to the end-windings. As a result, we still had a gap of ~2 mm between the housing and the channel flange.

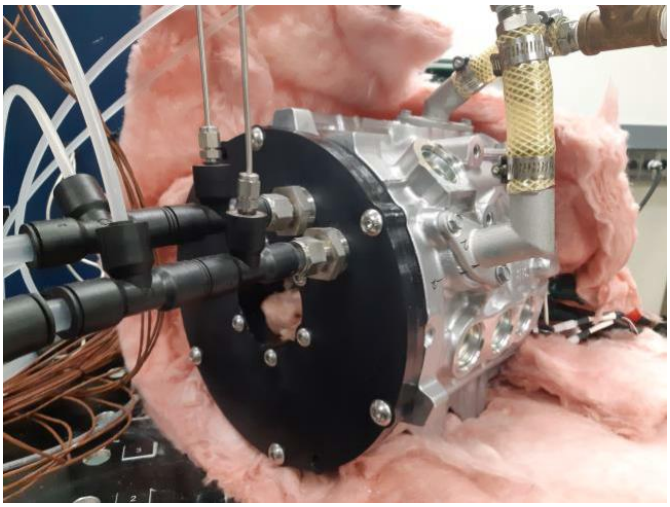

**Figure 120:** Final assembly of the end-winding channel to the Nissan Leaf motor

Both the end-winding channel and water-jacket of the motor assembly were connected to the same cooling loop shown in Figure 121. The fluid used in this cooling loop was WEG mixture with 50% volume of water. The temperature of the fluid is stabilized at 65 ℃ for the experiments by utilizing a chiller/heater circulator connected to the bath. The water-jacket and end-winding channel fluid paths are connected in parallel to control the flow through each path individually. The flow was controlled by changing the position of the manual valves shown on the schematic (Figure 121). The total flow was set by changing the pump speed. The channel valve and the water-jacket valve are then used to control the flow balance between the end-winding channel and the water-jacket. The total flow could be adjusted using the bypass valve, as changing the pump speed does not provide an accurate control of the flow in the loop.

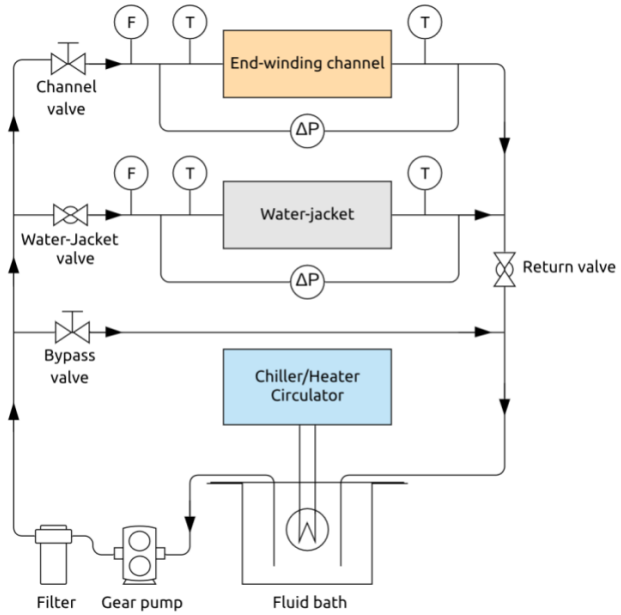


**Figure 121:** Cooling loop schematic

In this cooling loop, we have two flow meters measuring the volumetric flow rate across the end-winding channel and the water jacket. The pressure drop across each cooling system was also monitored via two pressure drop sensors. Also, the temperatures at the inlet and outlet of each cooling system were measured using K-type thermocouples.

The end-winding channel cooling system was located on the rear end-winding side. As a result, we wanted to maximize the number of thermocouples in this area to accurately measure the temperature distribution on the end-winding surfaces. To guide our choice of the thermocouple locations, we decided to run DC current through each phase of the motor using one power supply per phase (same configuration as for the experiments). Each phase was supplied with the same current. No cooling loop was used. The objective of this quick test was to understand the temperature distribution in the end-windings using a FLIR thermal camera. Based on the information from the image that we got from the thermal camera (see Figure 122), we decided to divide the end-windings into 8 sections corresponding to the motor pole number. In each section, the same temperatures were measured:

• Temperature at the rear end-winding outer surface normal to the radial direction of the motor (labelled “Rear End Outer”).
• Temperature at the rear end-winding inner surface normal to the radial direction of the motor (labelled “Rear End Inner”).
• Temperature at the rear end-winding top surface normal to the axial direction of the motor (labelled “Rear End Top”).
• Temperature inside the gap between the two end-turns in the middle of the end-winding (labelled “Rear End Inside”).

The location of each thermocouple, following the temperature definitions given above, is shown in Figure 122. Each number represents one section. The inlet and outlet of the end-winding channel are represented by a red disc and a blue disc, respectively. The picture in this figure is the distribution image captured with the thermal camera. Thus, a total of 32 temperatures are measured in the rear end-windings, which allows us to capture the temperature range on each side of the end-windings. As these end-windings were already impregnated, it was not possible to have a thermocouple inserted directly inside the end-windings to capture the maximal internal temperature. However, having end-windings impregnated using the real manufacturing process from the factory allows to have a good representation of the impregnation quality.

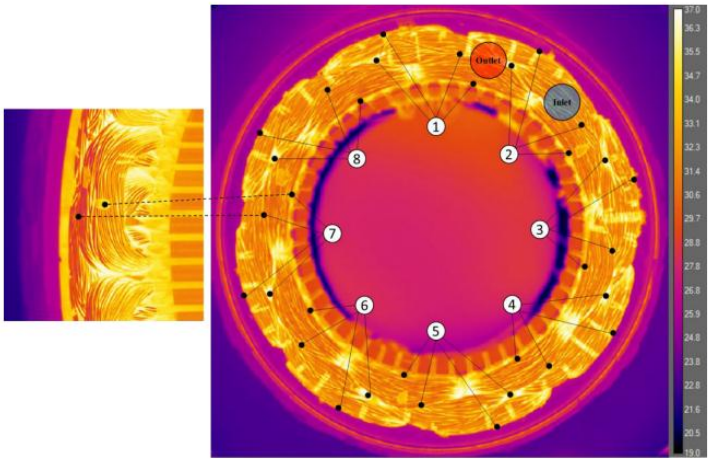


**Figure 122:** Thermocouple location and temperature distribution in the rear end-windings.

The end-windings are divided into 8 equal sections. The red disc and blue disc represent the outlet and inlet of the end-winding channel, respectively. In addition to these 32 thermocouples, we placed 2 thermocouples on the front end-winding inner surface and top surface in sections 2 and 8, as well as a thermocouple at the ring terminal of termination wires.

The thermocouples used in the experiments are K-type thermocouples. All thermocouples were calibrated using a reference probe, leading to a maximum uncertainty of ± 0.1°C for a temperature range from 20°C to 120°C. The thermocouples were fixed on surfaces using a thermally conductive epoxy from Omega.

The complete experimental setup for the motor cooling testing is shown in Figure 123. At the bottom of the photo, we can see the bath containing WEG coolant and the heater/cooler circulator which stabilizes the temperature of the bath. Just after the bath, we have the pump, at the bottom left corner. The rest of the cooling loop is behind the blue panel of the bench. On the right of this panel, we have the water-jacket valve which is connected to the water-jacket inlet. The gate valve with a red handwheel is the end-winding channel valve. The flow meter, pressure sensors and thermocouples are connected to a National Instrument's CompactDAQ data acquisition system which can be seen at the right of the screen in Figure 123.

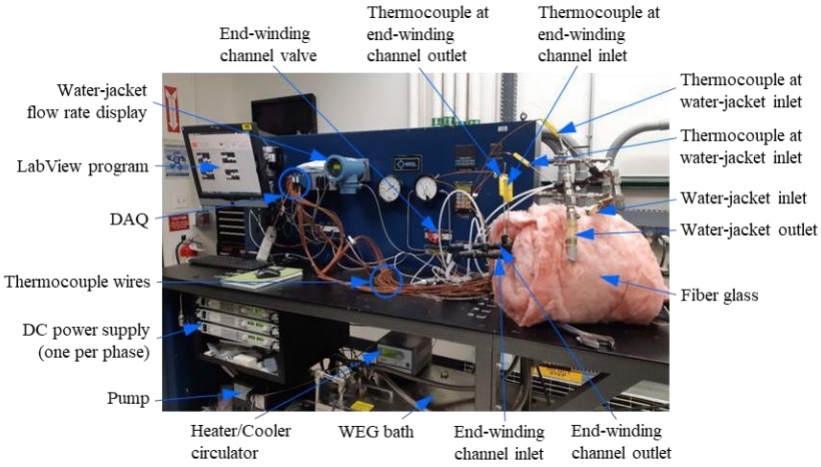


**Figure 123:** Experimental apparatus for motor cooling testing using end-winding channel and water-jacket cooling systems.

The water jacket, the front side, and the rear side of the motor were covered with fiberglass to minimize natural air convection on the external surface of the motor. The rotor was removed from our experiments and replaced with fiberglass. Due to this, we could consider all external surfaces previously in contact with air as adiabatic. Each phase of the stator was supplied with a stabilized DC current of 160 A with a Y configuration (see schematic in Figure 124). We used one power supply per phase to ensure a good current balance between each phase. These power supplies were Agilent technologies N5762A (8V/165A, 1320W), and they can be seen just above the pump, on the left side of the photo in Figure 123.

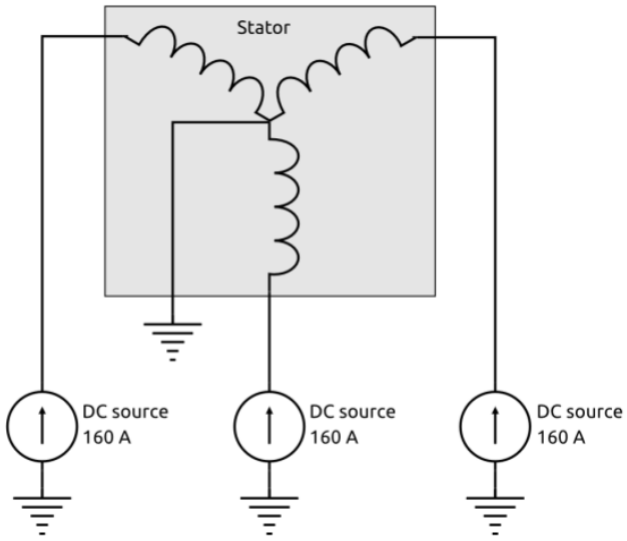


**Figure 124:** Stator phase connection to DC power supply using Y configuration.

Finally, the experiments were monitored and controlled with a LabVIEW program connected to the DAQ system and the power supplies. Flow rates, pressure drops, thermocouple temperatures, phase current, phase voltage, and electric power were monitored in this LabVIEW program. The fixed parameters and variables in these experiments are given in Table 20.

**Table 20:** Fixed parameters and variables for motor cooling experiments.

| **Fixed parameter** | **Value** |
|---|---|
| Fluid temperature in the bath [°C] | 65°C |
| DC current per phase [A] | 160 A |
| Total input power [W] | 530 W |
| **Variable** | **Values** |
| Water-jacket flow rate [L/min] | 3, 6, 10 |
| End-winding channel flow rate [L/min] | 3, 6, 10 |

The only variable in these experiments was the flow rates in the end-winding channel and the water jacket. To understand the impact of using the end-winding channel cooling system on the stator temperatures, we needed a first set of tests without the end-winding channel, using the water-jacket cooling system only (at 3, 6, and 10 L/min). Moreover, in order to characterize the influence of end-winding channel flow rate on the winding temperature independently from the water-jacket flow rate, we decided to change the flow rate of the end-winding channel while keeping the same water-jacket flow rate. As a result, we had a total of 12 tests, as shown in the test matrix from Table 21.

**Table 21:** Test matrix for motor cooling experiments

| **Test number** | **Water-jacket flow rate [L/min]** | **End-winding channel flow rate [L/min]** |
|---|---|---|
| Test 1 | 3 | None |
| Test 2 | 6 | None |
| Test 3 | 10 | None |
| Test 4 | 3 | 3 |
| Test 5 | 3 | 6 |
| Test 6 | 3 | 10 |
| Test 7 | 6 | 3 |
| Test 8 | 6 | 6 |
| Test 9 | 6 | 10 |
| Test 10 | 10 | 3 |
| Test 11 | 10 | 6 |
| Test 12 | 10 | 10 |

The first step of the experimental procedure was to stabilize the WEG coolant temperature in the bath at 65 °C while running the pump. The power supplies are off for this first step. As the stator was insulated using fiberglass, the thermocouples were all indicating a temperature around 65 °C when we had reached steady state. Steady state was defined as the state for which the thermocouple temperature change was less than ± 0.1 °C for a 10 min time interval. This ± 0.1 °C corresponds to the maximum thermocouple calibration uncertainty.

Once the temperature reached steady state, we turned on the power supplies at a fixed current of 160 A. We were recording the transient time frame only for tests 2, 7, 8, and 9 for a fixed flow rate of 6 L/min in the Water-Jacket. For all the other tests, we were just monitoring the transient temperatures in a plot window of the LabVIEW program. Once we reached a steady state for the end-winding temperatures, we recorded 120 samples with a 1-second time step. After recording the 120 samples, we moved to the next test by changing the flow rates accordingly. As the flow was changed, so did the temperatures. Therefore, when moving from one test to another, we had to wait for the new temperature steady state. The ambient temperature in the lab was not monitored as we had a fully insulated stator. Therefore, the ambient temperature for our motor was considered to be the inlet temperature of the coolant.

**Results**

In this section, the results of our experiments are provided from test 1 to test 12 at steady state. As the main objective of this test is to compare the impact of the new end-winding channel on the end-winding temperatures, the temperatures of interest for this section are the temperatures from the 32 thermocouples in the rear end-windings shown in Figure 122. The temperatures are computed for each test in Table 21, and the results are shown in Figure 125.

For any surface $k$, the graphs show that, as we are increasing the flow rate in the water-jacket without end-winding channel, the end-winding temperature decreases. Indeed, the heat absorbed by the fluid is proportional to the mass flow rate of the fluid in the water jacket. We observed the same phenomenon when the end-winding channels are connected. However, the impact of the water-jacket flow rate on the end-winding temperature decrease is less significant in this case. Some part of the heat produced by the rear end-windings is directly absorbed by the end-winding channel. However, this does not necessarily mean that the overall impact of the water-jacket mass flow rate on the winding temperatures is less significant. Indeed, the slot-winding temperatures are probably still significantly impacted by the water-jacket flow rate. However, we did not have measurements inside the slot-windings to assess how the slot-winding temperatures were affected when including the end-winding channel cooling system.

When using the end-winding channel, one could expect that the end-winding temperatures at each surface would gradually increase as we are far from the inlet, where we have the lowest coolant temperature. However, for a fixed flow rate through the water-jacket and end-winding channel, the temperature distribution is not conservative when moving from one section to another. For example, we have the highest top surface temperature in section 3 (from graph (c)) whereas we have the lowest outer surface temperature in the same section (from graph (a)). Moreover, the maximum fluid temperature difference between the outlet and inlet of the end-winding channel is lower than 1 °C, while the end-winding temperature difference between one section and another in Figure 125 can be higher than 2 °C. Therefore, the temperature variations from one section to another are not directly due to the coolant temperature increase as it flows around the end-windings. Additionally, the temperature variation from one section to another looks almost

random. The source of this variation could then be due to the uncertainty of the temperature measurements.

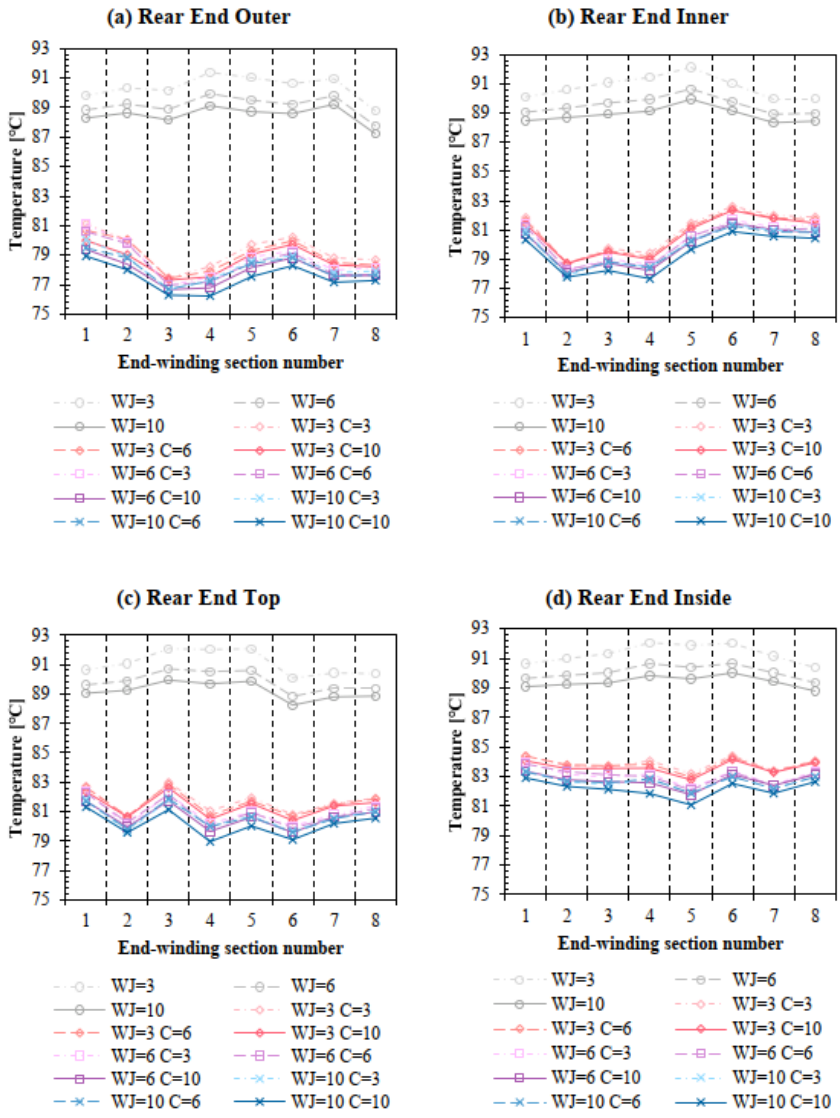


**Figure 125:** Steady state mean temperatures in the rear end-windings for each end-winding section and each flow rate (L/min) in the water-jacket ("WJ") and end-winding channel ("C"). For example, "WJ=3 C=3" is equivalent to: Water-jacket flow rate = 3 L/min and End-winding channel flow rate = 3 L/min.

The first source of error could be the randomness of the wire distribution in the end-windings, coupled with the thermocouple location. Indeed, we can observe in Figure 34 that the temperature on the top surface is not uniform. For example, if we place the thermocouple at the top of one wire or between two wires, this will already affect the effective measured temperature. Moreover, we may not have placed the thermocouple for one surface at the exact same location from one section to another, especially for the outer surface, which was difficult to access. A second source of error is the shape difference between one end-turn from two different sections. Finally, a third source of

error could be the thickness of the highly conductive epoxy between the thermocouple and the end-windings. This thickness is inevitably changing from one thermocouple to another.

Due to the randomness of this temperature variation from one section to another, we have decided to take the arithmetic average of all section temperatures for each surface instead of the individual temperatures.

In Figure 126, we can better compare the temperatures at each surface of the end-windings. When the end-winding channel is not used, the temperature values from one end-winding surface to another are close. Indeed, without an end-winding channel, the external surfaces are directly in contact with air, which has a very low thermal conductivity. Thus, the heat flow from each end-winding surface to the ambient air is close to zero at steady state.

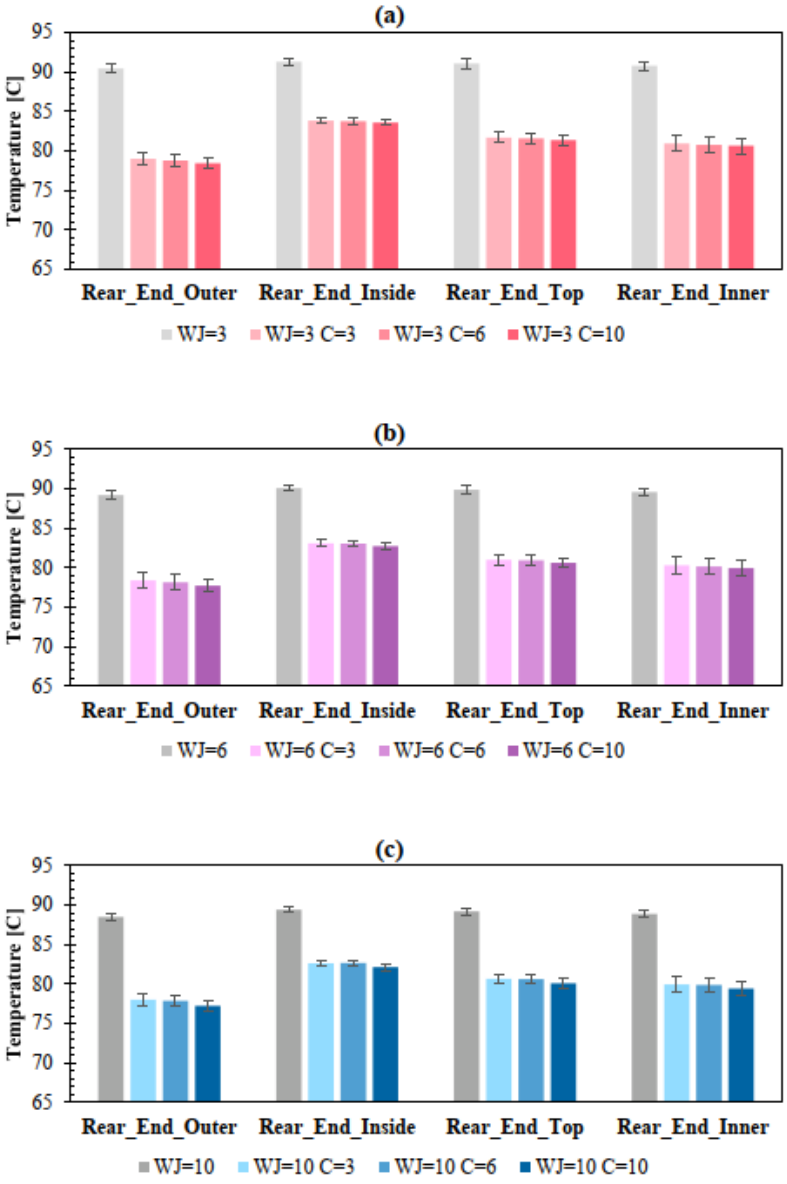


**Figure 126:** Mean end-winding temperature on the outer, inside, top and inner surfaces for a water-jacket flow rate of 3 L/min (a), 6 L/min (b) and 10 L/min (c).

As expected, when the end-winding channel is used, the inside temperatures are the highest. Indeed, the distance between the inside surface and the channel wall is higher than for other surfaces, leading to a higher thermal resistance. Besides, for a fixed water-jacket flow rate, the end-winding temperature difference for a 3 L/min flow rate and a 10 L/min flow rate in the end-winding channel is less than 1°C. Thus, we are able to significantly reduce the end-winding temperatures even at lower flow rates, resulting in lower hydraulic power requirements.

To quantify the effective performance of the end-winding channel cooling system, a temperature rate of decrease $\xi^k$ has been defined for each surface $k$ of the end-windings. The values of $\xi^k$ at each flow rate of the water-jacket and the end-winding channel are shown in Figure 127. For each value, error bars are given. These error bars represent the extended uncertainty $U_c(\xi^k)$ using propagation of uncertainty from temperature measurements. The maximum value of $\xi$ is 47% while the overall lowest value is 28%. However, this lower value is measured on the inside surface, which, again, is far from the end-winding channel wall compared to the other surfaces. Therefore, if we only consider the closest end-winding surfaces to the channel wall, namely "outer", "inner", and "top" surfaces, the lowest $\xi$ is 35%. These numbers demonstrate a very good cooling capability of the end-winding channel.

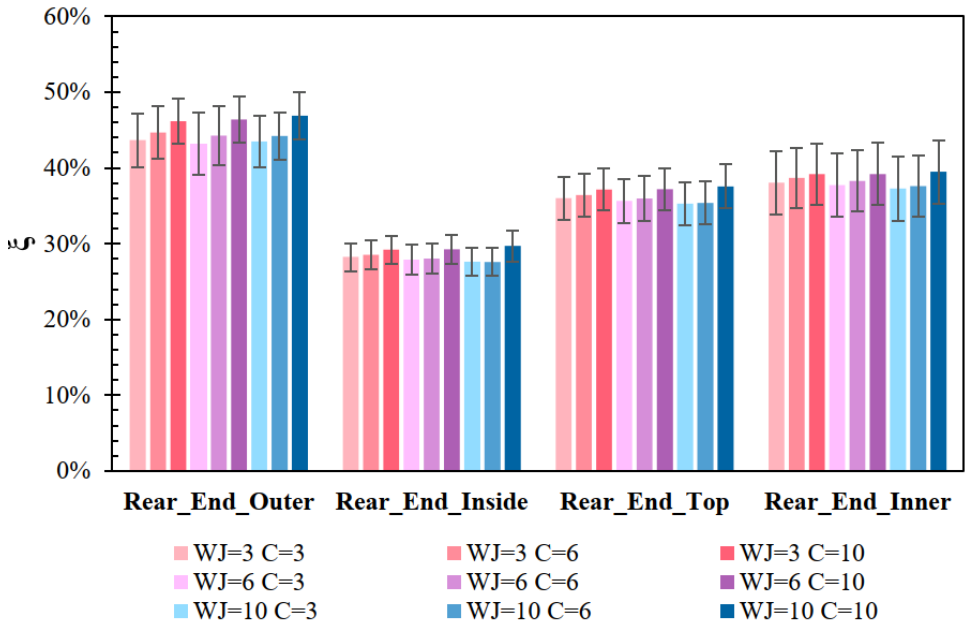


**Figure 127: $\xi$** values for each end-winding section ***k*** and each flow rate (L/min) in the water-jacket ("WJ") and end-winding channel ("C").

This high rate of temperature decrease is due to two major factors. The first factor is the coolant proximity to the end-windings. This coolant has a temperature of 65 °C at the inlet, and the temperature difference between the inlet and outlet is negligible in our experiments (less than 1 °C at the lowest flow rate). Therefore, considering the Newton's law of cooling, the temperature difference between the end-winding surface and the coolant is maximized. Moreover, the U-shape

of the channel maximizes the area of the heat transfer. The remaining parameter which represents the second major factor is the overall heat transfer coefficient $U$ between the end-winding external surfaces and the coolant. This parameter is the most critical for our cooling system. While the low thermal conductivity of the ULTEM material is limiting the maximum value of $U$, the highly conductive silicone compound used at the interface between the channel wall and the end-windings plays a key role in improving the value of $U$. Without this silicone compound, the airgap between the channel wall and the end-windings would drastically reduce the performance of the cooling system.

As a reminder, the end-winding channel is only used at the rear end-windings, which means the front end-winding does not have any direct cooling system. Assuming the end-winding channel system is also integrated in the front end-winding, we would probably have the same rate of decrease for the front of the end-windings. Reducing the overall winding temperature for the same electric power input means that the electric motor power density is increased. Indeed, the fixed maximum temperature of the winding will be reached for a higher electric power input if the end-winding channel is used on both the front and rear end-windings.

This first prototype was supposed to be a proof of concept, constrained by time and resources. Many improvements could be made to this design to increase $U$. By using another manufacturing process for the end-winding channel, the thickness of the channel wall could be reduced. ULTEM 9085 has a very high strength compared to other traditional polymers. Consequently, the wall thickness could be reduced without compromising the capability of the channel to withstand the internal pressure. $U$ could also be improved by using a material with higher thermal conductivity. We assumed that using metallic material like aluminum would present a risk of short-circuit as the end-windings are very close to the channel wall. However, further investigation is needed, and it may be possible to use metallic material by ensuring a minimum distance between the wall and the end-windings. The combination of a lower wall thickness and use of metallic material for the channel could lead to even better cooling performance.

The temperatures $T_{inlet}$ and $T_{oulet}$ and their difference $\Delta T$ are given in Table 22 for both the water-jacket and the end-winding channel at different flow rates (test 4 to 12).

Overall, the values of $\Delta T$ are low: less than 1 °C for the end-winding channel and less than 3 °C for the water-jacket. This is due to a low value of the total power input that we are using (around 530 W). In the real application, this value can go up to the maximum power of the motor, 80 kW. This is more than 100 times the total power input from our experiments, which means the $\Delta T$ value can go much higher than what we have for these experiments.

$q_{fluid}$ has been computed for both the water-jacket and the end-winding channel for each different flow rates (test 4 to 12). As we have only DC current in our experiments all the electric power is converted into heat. Consequently, $q_{fluid}$ can be compared to the total electric power from the power supplies to know which part of the heat is absorbed by the fluid. The results of this

comparison are given in Figure 128. The error bars correspond to the sum of extended uncertainty $U_c(q_{fluid})$ for the water-jacket and end-winding channel.

**Table 22:** Temperature at the inlet and outlet and the resulting $\boldsymbol{\Delta T}$ for both the water-jacket and the end-winding channel from test 4 to 12.

| | Water-jacket | | | End-winding channel | | |
|---|---|---|---|---|---|---|
| | $T_{outlet}$ [°C] | $T_{inlet}$ [°C] | $\Delta T$ [°C] | $T_{outlet}$ [°C] | $T_{inlet}$ [°C] | $\Delta T$ [°C] |
| **WJ=3 C=3** | 64.0 | 66.2 | -2.2 | 63.9 | 64.4 | -0.4 |
| **WJ=3 C=6** | 64.1 | 66.3 | -2.2 | 64.4 | 64.8 | -0.3 |
| **WJ=3 C=10** | 64.3 | 66.5 | -2.1 | 64.8 | 65.0 | -0.3 |
| **WJ=6 C=3** | 64.6 | 65.6 | -1.0 | 64.0 | 64.6 | -0.5 |
| **WJ=6 C=6** | 64.5 | 65.6 | -1.1 | 64.4 | 64.8 | -0.4 |
| **WJ=6 C=10** | 64.8 | 65.9 | -1.1 | 64.8 | 65.1 | -0.2 |
| **WJ=10 C=3** | 64.8 | 65.5 | -0.7 | 64.2 | 64.6 | -0.4 |
| **WJ=10 C=6** | 65.0 | 65.7 | -0.7 | 64.7 | 65.0 | -0.3 |
| **WJ=10 C=10** | 65.0 | 65.6 | -0.6 | 64.9 | 65.1 | -0.2 |

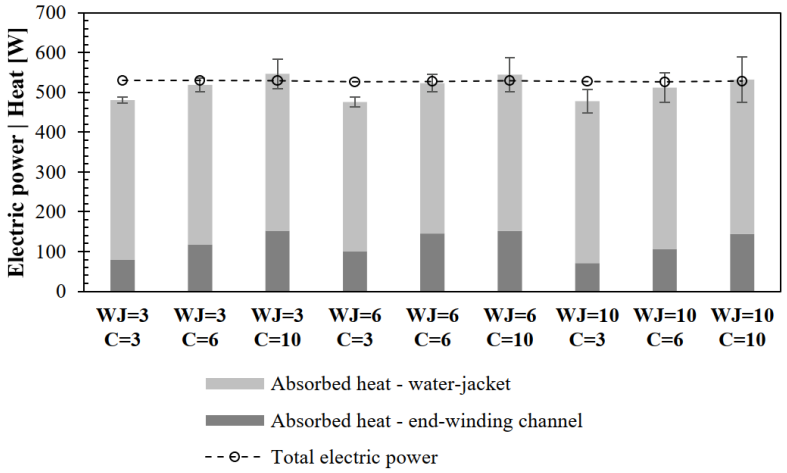


**Figure 128:** Absorbed heat in the water-jacket and the end-winding channel compared to the total electric power input at each flow rate (L/min) in the water-jacket ("WJ") and end-winding channel ("C").

If the motor was perfectly insulated when using the fiberglass for the experiments, all the heat generated by the windings should be absorbed by the fluid based on heat flow conservation. However, in Figure 128, for a fixed flow rate of 3 L/min in the water-jacket, the total heat absorbed by the fluid is lower than the total heat input by around 9%. A reasonable explanation for this gap would be heat dissipation to ambient air. Indeed, the thermal insulation of the motor with fiberglass is not perfect. As the water-jacket flow rates increase, the cooling systems are able to absorb more heat. However, at the highest flow rates for the water-jacket, the calculated absorbed heat is higher than the total heat input of the system. This is probably due to measurement uncertainty. Indeed, the higher the total flow rate, the lower the $\Delta T$ and the higher the error.

This is the reason why the size of the error bars grows as we look at higher flow rates in Figure 128. Moreover, in the uncertainty analysis for $U_c(q_{fluid})$, we only consider the uncertainty of the thermocouples and the flow sensor; however, other parameters must be affecting the temperature measurements, such as the height of the thermocouple in the tube, the local flow turbulence, tiny air bubbles stuck in the T fittings. Consequently, the total uncertainty is probably higher $U_c(q_{fluid})$. Therefore, the exact value of the absorbed heat should be carefully interpreted.

The heat absorbed by the fluid in the end-winding channel represents a minimum of 15% and a maximum of 28% of the heat absorbed by the fluid in the water-jacket. The minimum is reached when the flow rate in the water-jacket is maximum and the flow rate in the end-winding channel is minimum ("WJ=10, C=3") whereas the maximum is reached when the flow rate in the water-jacket is minimum and the flow rate in the end-winding channel is maximum ("WJ=3, C=10"). From the value of the volume ratio $\alpha$ = 62 %, we can deduce that the total power generated at the rear end-windings is about 19 % of the total power input. Consequently, if $V \geq 6$ L/min in the end-winding channel and for any other tested flow rate in the water-jacket, the end-winding channel cooling system is able to absorb all the heat from the end-windings, which is exactly what it was meant for. Again, improvements in the material and wall thickness of the end-winding channel could allow for a further increase in this performance. Different flow configurations could also be investigated to optimize this cooling system.

In order to predict the global performance of the motor with this new end-winding channel cooling system and optimize its design, we must integrate the end-winding channel in our LPTN model. The first step of the process is to derive the heat transfer coefficient $h_{EWC}$ characterizing the convective heat transfer between the fluid and the channel wall. As we do not have temperature measurements at the wall in contact with the fluid, we need to compute $h_{EWC}$ using a CFD model of the channel fluid domain. The CFD model and the results for $h_{EWC}$ are presented in the following sections.

The end-winding channel fluid domain was only used in the CFD model. This fluid domain is shown in Figure 129. The cross-section of the fluid domain has the same dimensions as the internal U-shape from Figure 114. The flow is considered a turbulent flow (detailed explanation in the following paragraphs). Therefore, the entrance length $L_{entrance}$ was chosen to be 10 times the inlet tube inner diameter $D_{inlet}$. This rule for the entrance length allows to have a fully developed flow before entering the U-shape channel.

The final version of the CFD model was created using ANSYS 2020 R2 software with ANSYS Meshing and Fluent packages. As we have a liquid coolant, the fluid is considered as incompressible. Before selecting the viscous model for this study, we calculated the value of the $Re$ for the three different flow rates tested in our experiments (3 L/min, 6 L/min and 10 L/min) and at two different areas of the end-winding channel: at the inlet tube cross section and in the U-shape channel cross section. WEG (50%-50% by volume of water and ethylene glycol) properties for a temperature of 65°C are given in Table 8.

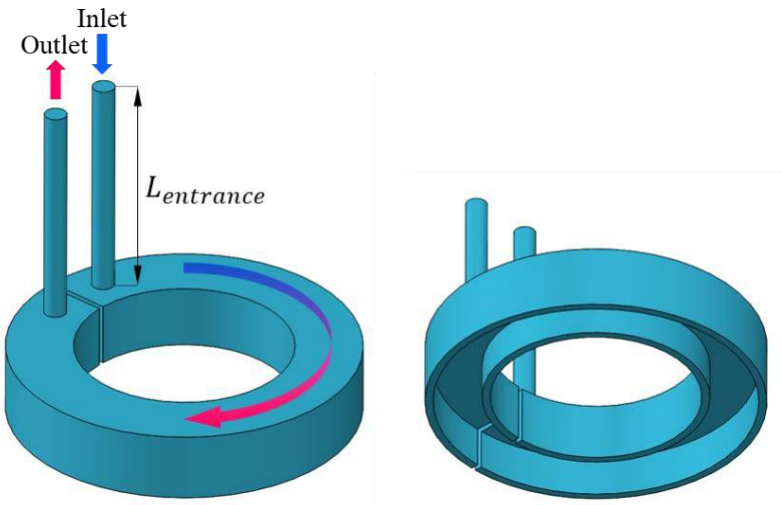


**Figure 129:** CFD model fluid domain geometry

**Table 23:** WEG with 50% volume of water properties at 65°C.

| WEG property | Value |
|---|---|
| Density [kg/m$^{3}$] | 1048 |
| Specific heat [J.kg$^{-1}$.K$^{-1}$] | 3449 |
| Thermal conductivity [W.m$^{-1}$.K$^{-1}$] | 0.390 |
| Viscosity [cP] | 1.319 |

The $Re$ values at three different flow rates and for both the inlet tube and U-shape channel are calculated. The $Re$ values and their associated velocities are reported in Table 10. The transition from laminar to turbulent flow in pipes is usually characterized by a critical Reynolds number $Re_{crit}$. In straight pipes, $Re_{crit} \approx 2100$, but for the curved U-shape, this $Re_{crit}$ is higher according to helical pipe correlation [14]. From the $Re$ values in Table 24. The flow in the inlet tube can always be considered as turbulent, while the flow in our channels is always laminar if we consider the $Re_{crit}$ due to the curved pipe. As we have a turbulent regime in our inlet and outlet pipe, and considering the complexity of the U-shape cross-section of the channel, a turbulent model was used for our CFD model.

After comparing different types of turbulent model available in ANSYS Fluent by looking at the different residuals and temperature, pressure and mass flow convergence, we decided to use the SST k-ω model where k is the turbulent kinetic energy and ω is the specific rate of dissipation of k into internal thermal energy. This turbulence model is solving for the Reynolds-Average Navier-Stokes (RANS) equations describing turbulent flow as well as the transport equation for k and ω. In addition to the RANS equations, we are also solving for the energy equation in order to compute the temperature distribution in the fluid and derive $h_{EWC}$.

**Table 24:** Velocity and $\boldsymbol{Re}$ values at the inlet tube and U-shape channel for different flow rates.

| | Inlet tube | | U-shape channel | |
|---|---|---|---|---|
| **Flow rate [L/min]** | $\boldsymbol{u}$ **[m/s]** | $\boldsymbol{Re}$ | $\boldsymbol{u}$ **[m/s]** | $\boldsymbol{Re}$ |
| 3.0 | 0.395 | 3985 | 0.065 | 782 |
| 6.0 | 0.789 | 7970 | 0.131 | 1563 |
| 10.0 | 1.316 | 13284 | 0.218 | 2606 |

At the inlet, we have a uniform velocity boundary condition. The value of this velocity can be found in Table 24 under "Inlet tube". The outlet is a fixed pressure boundary condition at 0 Pa. All the other external surfaces are considered as 1 mm-thick walls with no-slip conditions. When considering a roughness height equal to half of a ULTEM filament width, we did not have a significant impact on $h_{EWC}$ value. Therefore, we decided to simplify the model and have no roughness at the wall.

We assumed the heat transfer on outside surfaces (shown in grey in Figure 130) to be negligible compared to the inside surfaces in direct contact with the end-winding (shown in red Figure 130). Therefore, all walls were considered as adiabatic except for the outer, inner, and top side of the channel as shown in Figure 130. A constant heat flux is applied at these three surfaces. The applied heat flux $q_{wall}$ value is equal to the heat absorbed by the fluid given in Figure 128 for each flow rate, divided by the total combined area of the outer, inner, and top surfaces. We decided to take the absorbed heat value for a fixed water-jacket flow rate of 10 L/min. The resulting heat flux values are 1861 W/m$^2$, 2800 W/m$^2$, and 3787 W/m$^2$ for an end-winding channel flow rate of 3 L/min, 6 L/min and 10L/min respectively.

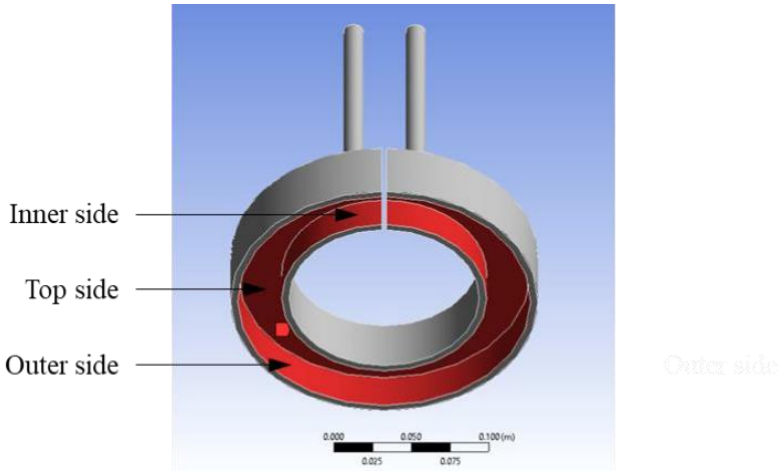


**Figure 130:** Channel surfaces considered for the heat transfer between channel walls and the end-windings.

The fluid domain mesh had a total of ~955,000 cells. Pictures of the mesh are shown in Figure 131. The base size of the mesh is 2 mm, and the boundary layer has 7 layers for a total thickness

of 1.3 mm. The thickness and the number of cells were chosen after a few iterations to obtain a convenient value of y+ lower than 4 at the wall and a fine mesh on the outer and inner sides of the channel. Indeed, we wanted to make sure we did not have significant temperature or velocity gradients between two consecutive cells in the viscous sublayer. The final mesh was chosen after a mesh independence study based on the computed heat transfer coefficient $h_{EWC}$ and the pressure drop between the inlet and the outlet. The results of this mesh independence study are given in Figure 132.

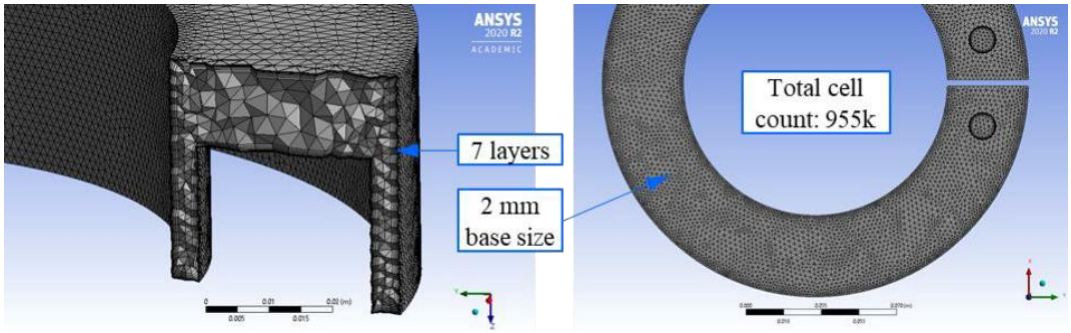


**Figure 131:** Fluid domain mesh

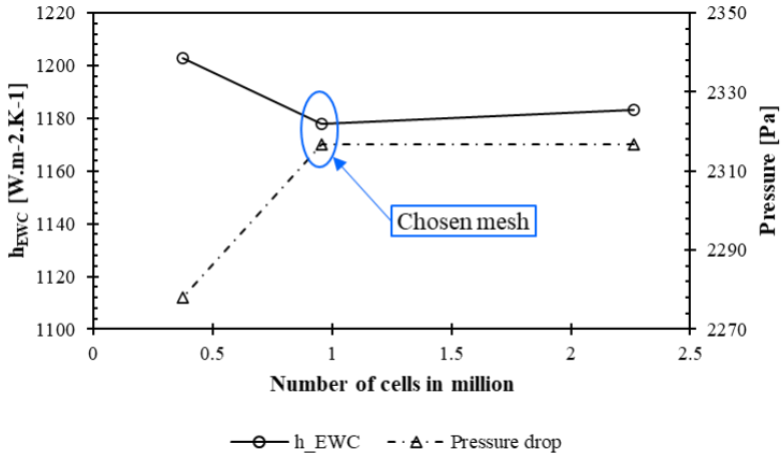


**Figure 132:** Mesh independence study, $h_{EWC}$ and total pressure drop with respect to the total number of cells in the CFD model.

The steady-state simulations of the end-winding channel fluid domain were performed for a flow rate of 3 L/min, 6 L/min and 10 L/min. The wall temperatures as well as the velocity streamlines for a flow rate of 10 L/min in the end-winding channel obtained from the steady-state simulation are shown in Figure 133. In Figure 133a, the external wall temperature is almost equal to the fluid average temperature as we have considered these walls to be adiabatic. However, the inside, outer, inner, and top walls show a much higher temperature increase especially on the outer wall as we get closer to the outlet of the channel. The values of each heat transfer coefficient are given in Table 25.

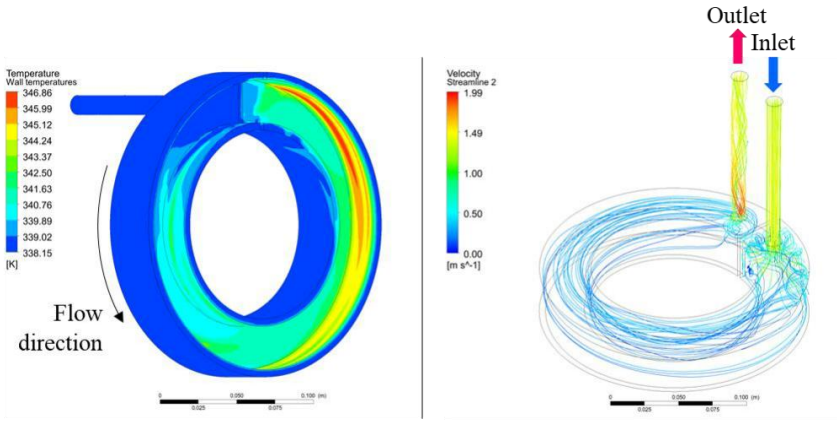


(a) Wall temperatures (b) Velocity streamlines

**Figure 133:** Wall temperatures (a) and Velocity streamlines (b) from steady-state simulation of the end-winding channel fluid domain for a flow rate of 10 L/min.

**Table 25:** Heat transfer coefficients derived from CFD steady-state simulation for three different flow rates.

| Flow rate [L/min] | $h_{EWC}$ [W.m$^{-2}$.K$^{-1}$] | $h_{EWC_{inner}}$ [W.m$^{-2}$.K$^{-1}$] | $h_{EWC_{outer}}$ [W.m$^{-2}$.K$^{-1}$] | $h_{EWC_{top}}$ [W.m$^{-2}$.K$^{-1}$] |
|---|---|---|---|---|
| 3.0 | 546 | 612 | 413 | 742 |
| 6.0 | 839 | 1043 | 639 | 1042 |
| 10.0 | 1177 | 1472 | 889 | 1483 |

In order to predict the impact of the end-winding channel on the performance of the end-winding channel, and possibly compare it to other cooling systems, we must integrate the end-winding channel component into our LPTN model. This integration includes creating an equivalent resistance network representing the end-winding channel and calibrating the parameters of the end-winding channel resistances to match the experimental results. These steps are presented in the section below.

The end-winding channel equivalent network is represented by three resistances, $R_{outer}$, $R_{inner}$ and $R_{top}$ as shown in Figure 134. The values for $h_{EWCi}$ are taken from the CFD results given in Table 25. The areas $A_{outer}$, $A_{inner}$ and $A_{top}$ corresponds to the area of the surfaces represented in red in Figure 130. In Figure 134, the thickness of the potting and channel wall are not representative of the real dimensions. In the real motor assembly, the distance between the channel wall and the end-windings is small enough to consider that the change in area from the wall to the end-windings is negligible. Eventually, $L_{poti}$ and $L_{channel}$ are the thicknesses of the potting layer and the channel wall, respectively. $L_{channel}$ is equal to 1 mm. However, $L_{poti}$ is almost impossible to measure accurately as the end-windings are not perfect flat surfaces as shown in Figure 118. For instance, on the outer side, the winding coming from the slot are curved to reach to top surface and then go back to the next slot. Therefore, the potting thickness is a function of both axial and tangential

coordinates and can differ from one surface to another. Besides, the equivalent thickness of the potting may be different from one side to another, hence the $L_{poti}$ dependence on the surface $i$.

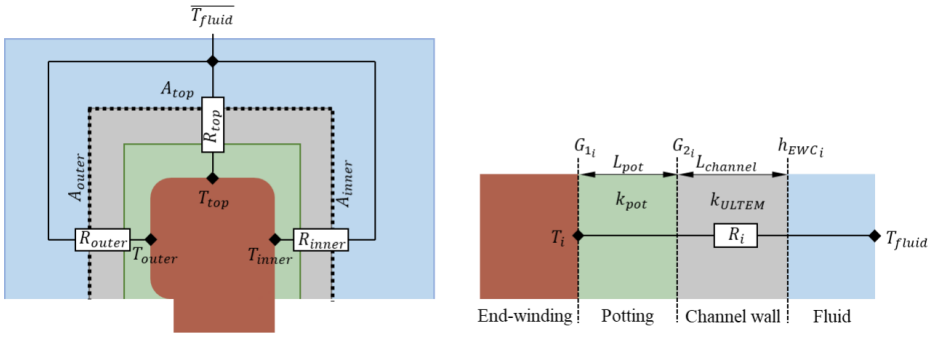


**Figure 134:** End-winding channel equivalent resistance network

The calibration consists of changing the values of our unknown in the expression of the end-winding channel network resistances to minimize the error ε between the LPTN and experimental temperatures.

The calibration was conducted using an optimization script in Python with the Sequential Least Square Quadratic Programming (SLSQP) constrained optimization algorithm. The calibration process using this Python script is shown in Figure 135.

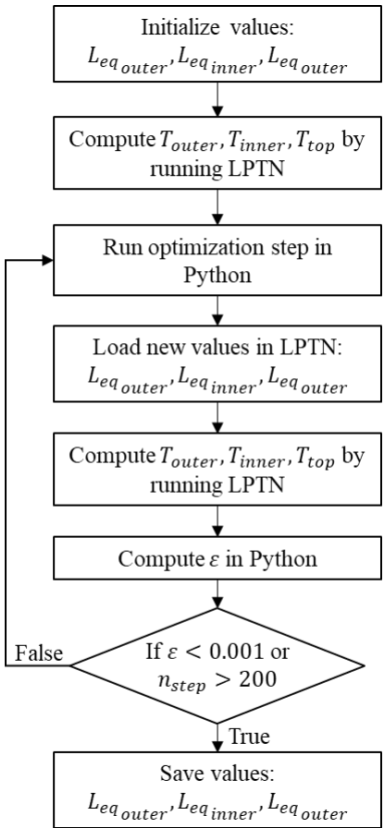


**Figure 135:** Calibration algorithm using LPTN in Motor-CAD® and the Python script.

## 10. Evaluation of In-slot Heat Exchanger Performance via Component-level Modeling

### Summary

In this project task, the motor in focus and the direct winding cooling solutions being explored are described, and the evaluation methodology is introduced.

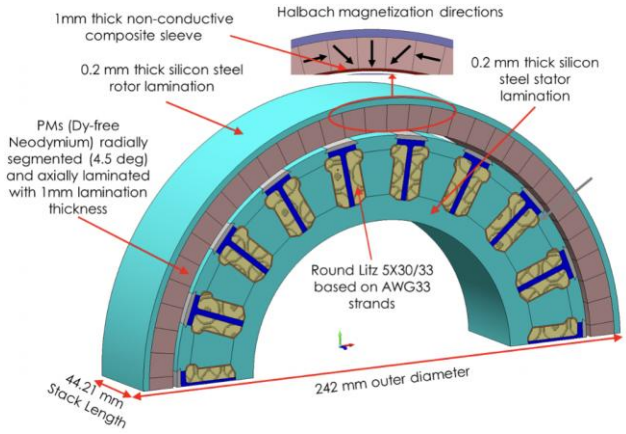


**Figure 136:** High-power-density motor design proposed to meet U.S. DRIVE program goals [13]

The innovations in this work are detailed in the context of a high-speed, high-power density non-HRE permanent magnet (PM) traction motor being designed and developed jointly by ORNL and NREL. This motor was designed to meet the U.S. DRIVE program specifications - primarily, a power density of 50 kW/L, and a 100 kW peak-55 kW continuous power output. Historically, high motor torque density, power density, and efficiency have been achieved for PM synchronous traction motors using heavy rare-earth

(HRE) magnet material such as Dysprosium (Dy). However, due to the price and globalsupply volatility of Dy and other HRE materials, Dy-free non-HRE-based PM materials have been developed and commercialized.

It was noteworthy that an outer-rotor design was chosen for this motor for several reasons. An outer-rotor motor allowed for easy integration of power electronics within the inner hollow volume of the stator. The rotor had a robust construction, with a continuous band of magnets around the inner diameter of the rotor and no extra voids (as opposed to a typical internal permanent magnet (IPM) machine, where a few magnets are embedded in select locations within the rotor, in a discontinuous manner). This provided natural support for magnet retention against centrifugal forces during operation. Since the airgap was at the radially outermost location with this topology, this further facilitated higher torque density than the other two candidates. Moreover, this topology had the lowest active volume (1.88 L) of the three candidates and was the only topology to satisfy the 50 kW/L power density target. In this manner, the chosen motor design met the targeted peak power and torque density and quality requirements (see Table 26), while exhibiting resistance to demagnetization within a 12% design margin.

The motor design is pictured in Figure 136. However, given as-yet-unpublished results acquired since [13], certain updates have been considered to the motor drive specifications. The relevant updated parameters, relating to the "peak torque condition" operating point selected for the motor-level model, are presented in Table 26 and form the baseline for this work.

**Table 26:** Key Motor Specifications (adapted from [15])

| | |
|---|---|
| Peak Power (kW) | 100 |
| Peak Torque (N.m) | 163 |
| Maximum speed (RPM) | $\leq$ 20000 |
| Maximum efficiency (%) | $>$ 97 |
| Number of stator slots | 18 |
| Number of poles | 16 |
| Maximum current (A) | 387.75 |
| Battery operating voltage (Vdc) | 650 |

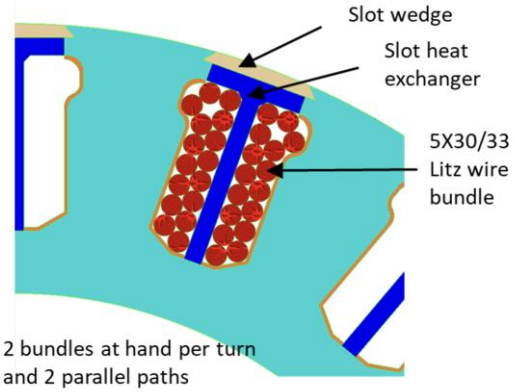


**Figure 137:** In-slot configuration for proposed motor showing placement of in-slot heat exchanger

Although the outer-rotor topology leads to a higher power density, the windings are positioned radially inward, in contrast to inner-rotor motors. This limits the ability of housing coolant jackets to cool the windings and necessitates a different cooling solution for windings. Hence, the baseline cooling solution chosen for this motor, Figure 137, is an in-slot liquid-cooled HX that sits adjacent to and in between adjacent copper windings inside the slot. The design is based on the 3-D-DWHX design. As seen in Figure 138, the coolant enters from the split top channels and changes direction and profile at the closed axial end, entering the bottom channel via the internal return feature. Subsequently, it is guided by the S-shaped microfeature towards the outlet, which is on the same axial end as the inlet. This baseline design is primarily optimized for the portion of the winding loop within the axial stator slot length or the in-slot windings. However, due to the heat exchanger's straight axial profile, it is not optimally designed to address the curved end windings that protrude from the slot, as shown in Figure 139 (baseline design on left). Given the relative inflexibility of critical parameters for the motor, such as the slot shape and lamination stack, and geometric constraints that would make a separate coolant flow path and additional manifolds specific to end-winding cooling infeasible, a modified design for the HX that integrates end-winding cooling into the same singular flow path is considered.

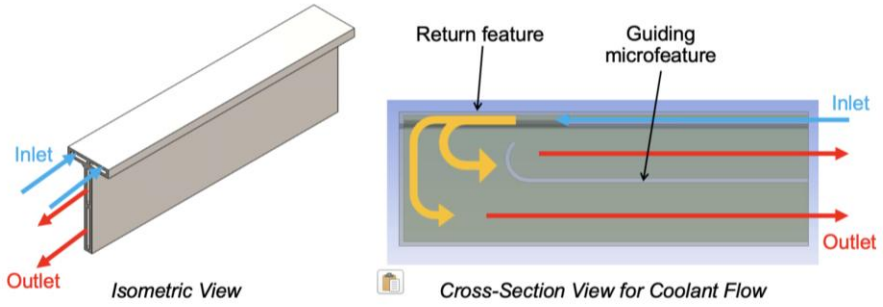


**Figure 138:** Isometric (L) and cross-sectional (R) views of baseline design of in-slot HX, showing coolant flow path.

In order to simultaneously address end-winding cooling, the proposed design uses a modification to the baseline design, at the closed axial end downstream of the inlet, seen in Figure 140. The length of the HX extending axially from the stator slot is curved around the end windings using the "tapered revolve" function in SolidWorks, such that the cooling channel follows the profile of the winding loop even as it extends outside the slot, as shown in Figure 139. Hence, the thermal conduction resistance from the end windings to the coolant flow is reduced as with the windings inside the slot. An internal return feature similar to that in the baseline design is maintained at the end of the curved portion of the HX, to connect the flow from the top channels (inlet side) to the bottom channel (outlet side) and eliminate the need for multiple manifolds. This design change has several advantages. Firstly, the proposed design requires no change to the slot shape since the 'T-shaped' cross-section of the HX inside the slot remains unchanged. There is also no modification to parameters such as the stator stack length or slot fill factor, which are also critical to the electromagnetic performance of the motor. Moreover, the end windings and in-slot windings are cooled simultaneously without the need for an additional coolant flow path or manifold specifically for the end windings, and the flow rate can be adjusted to further enhance cooling, given the additional contact with the winding loop.

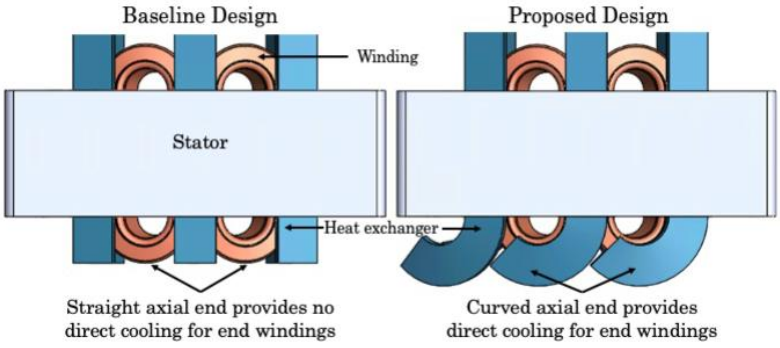


**Figure 139:** Baseline (L) and Proposed (R) Design positioning with respect to windings and stator stack.

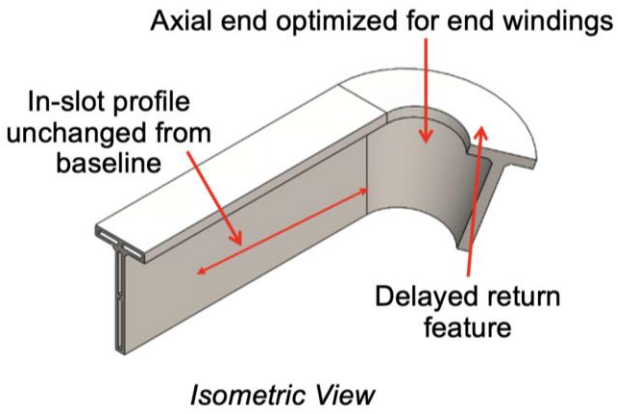


**Figure 140:** Isometric view of proposed design of in-slot HX.

The thermal performance of the HX designs needs evaluation and comparison at component-level –through metrics such as pressure drop and effective heat transfer coefficient – as well as in terms of the relative impact the designs have at a motor- or sub-motor-level. To address this need, a multiscale evaluation framework for motor thermal analysis is presented in Figure 141. This framework requires various packages in Ansys (or their counterparts).

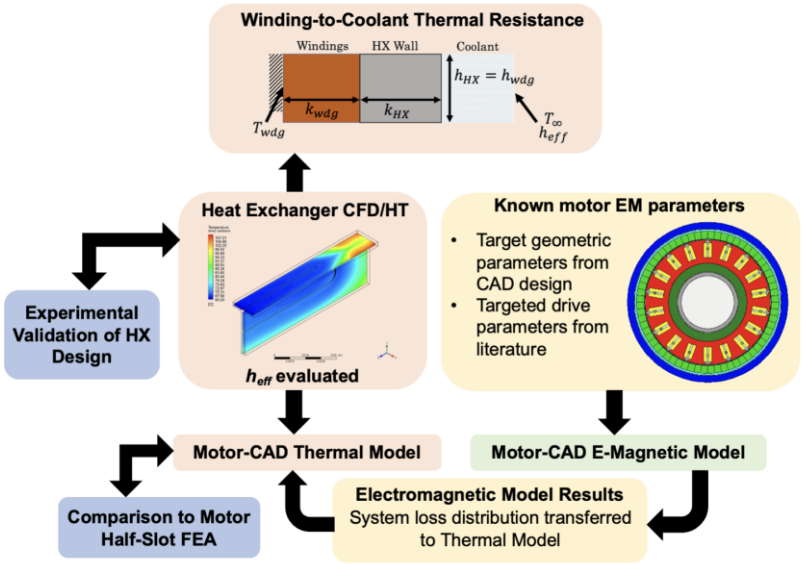


**Figure 141:** Multiscale Modeling Framework for Motor Thermal Analysis with Baseline and Proposed Cooling Solutions

First, component-level CFD/HT analysis is conducted to determine metrics for heat transfer effectiveness of the cooling solution in question, such as the effective convective heat transfer coefficient ($h_{eff}$). The analysis also explores trends in heat with parameters such as the coolant flow rate and the heat load configuration. The component-level results and trends are validated experimentally with a subscale test using prototypes of the baseline and proposed HX designs. The component-level metrics can be subsequently fed into various motor-level and sub-motor-level analyses.

The motor-level impact of the proposed HX design is first evaluated agnostic of the operating input drive parameters or thermal conditions. For this, the calculation of a "winding-to-coolant (WTC) thermal resistance" or $R_{th,w-c}$, that measures the ease of heat flow from the motor hotspot (windings) to the heat sink (coolant flow) is proposed. This analysis can be similarly conducted for any cooling solution targeting a specific component/thermal hotspot of the motor. Subsequently, the 'universal' results can be contextualized using motor-level thermal modeling. First, a reduced-order motor analysis conducted using Ansys Motor-CAD is carried out. The features of Motor-CAD that make this an attractive choice are (1) the ability to configure custom cooling solutions by editing the inbuilt thermal networks, (2) delivery of rapid steady-state motor-level thermal insights, and (3) the ability to (partially) achieve electrothermal coupling between targeted drive parameters and consequent thermal insights. The motor-level analysis is initialized by specifying these targeted drive parameters for any chosen electromagnetic operating point in the E-Magnetic model. The reduced-order E-Magnetic model evaluates electromagnetic performance insights at that operating point. The resulting system power loss distribution data for the specified operating point are leveraged to drive the thermal model, where cooling solutions are configured based on the known parameters and post-processed results from the component-level CFD analysis (primarily $h_{eff}$). The thermal model is then solved near-instantaneously to provide estimated motor-level thermal insights, with temperature distribution provided for various components subject to the specified cooling solution. The accuracy of the reduced-order motor-level MotorCAD model results can be assessed through comparison to a full numerical FEA model of a half slot of the motor, developed at NREL. While this FEA model has far finer spatial resolution, and likely higher accuracy, the trade-offs are significant computational costs and time. Hence, the Motor-CAD modelling framework is being explored as a rapid evaluation method for new, proposed cooling solutions for motors, such as the proposed HX design in focus. Here, this multiscale evaluation framework is implemented to evaluate and compare the relative performances of the baseline and proposed HX designs as heat transfer geometries and as motor cooling components. The experimental validation of the component-level analysis reveals the virtues and challenges of comprehensive validation, and this can be used to refine the specifics of future motorette testing experimental validation of the motor-level results. The framework can thus be modified and implemented to evaluate any new, proposed cooling solution in terms of its predicted impact at a multiscale level.

For both HX designs, the average heat transfer coefficient ($h_{eff}$) was evaluated as the metric of component-level heat transfer performance. $h_{eff}$ was desired because it could be easily leveraged as an input parameter to drive our motor-level thermal models. It is calculated using the Number of Transfer Units (NTU) method for HX effectiveness.

To numerically evaluate the component-level hydrodynamic and thermal performance metrics, a CFD/HT model was created in Ansys Fluent for each design. The modelled system constituted the solid-phase HX flooded with the coolant (DI water) flowing from inlet to outlet inside it, and disregarded the manifold for ease of computation. The fluid-HX system was discretized using tetrahedral meshing and 10 inflation layers where the fluid interfaced with the inside walls of the

HX, to adequately resolve the boundary layers. An image of the generated mesh through a cross-section of the flooded HX geometry, for a characteristic element size of 0.35 mm is shown in Figure 142. Body sizing is 0.35mm, and 10 inflation layers can be seen for the fluid phase at the fluid-HX interface at the inner wall.

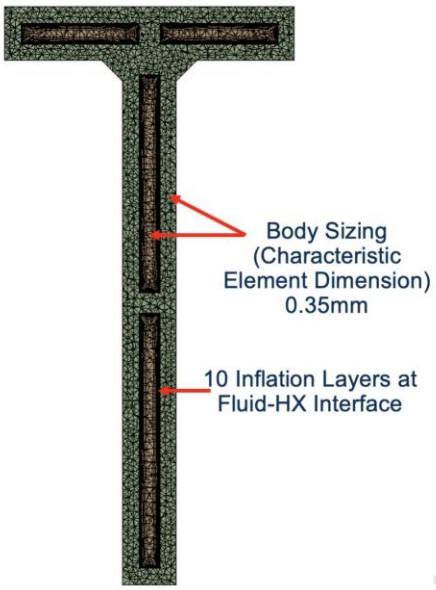


**Figure 142:** Mesh shown in cross-section plane through CFD geometry of flooded HX.

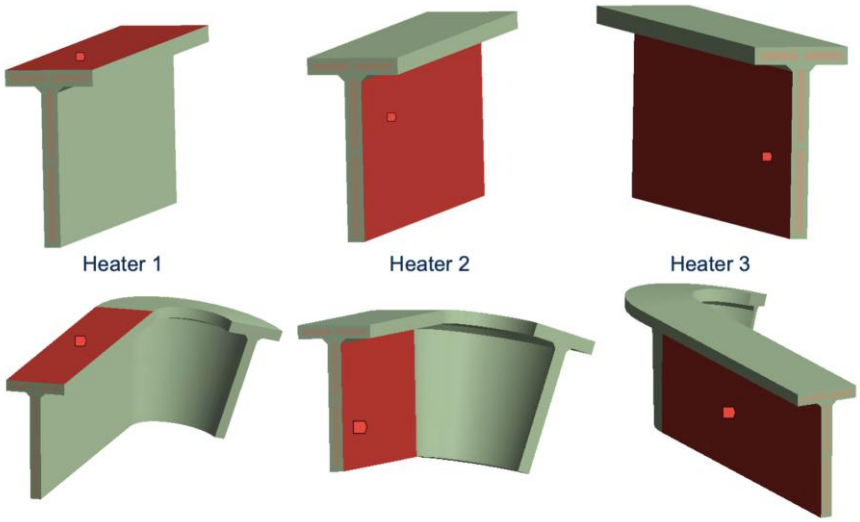


**Figure 143:** Heat loads configured on HX surface groups in preliminary CFD/HT simulation.

Heat fluxes were applied to the various HX outer walls as outlined in Figure 143 for both designs. These fluxes simulated heat loads from polyamide patch heaters, considered as the heat load for the experimental validation. The flux specified for each surface was limited by the maximum rated power of each heater, corresponding to a rated $I_{max}$ of 0.7 A. Given this, 3 current levels ranging from 0.5 A to 0.68 A were chosen.

The realizable k-ϵ SST model was subsequently configured and solved. First, system parameters such as maximum system temperature $T_{max}$ and inlet pressure $Pi_n$ (for an outlet pressure of 0 Pa) were monitored for converged simulations with decreasing "body sizing"(characteristic element length) - and thus, increasing numbers of mesh elements - for a mesh independence study, as pictured in Figure 144 (baseline design with flow rate of 0.555 lpm). Figure 144 shows that the model results achieved mesh size independence past an element size of 0.5 mm, so all further simulations were conducted at a body sizing of 0.35 mm to ensure reasonable computing time.

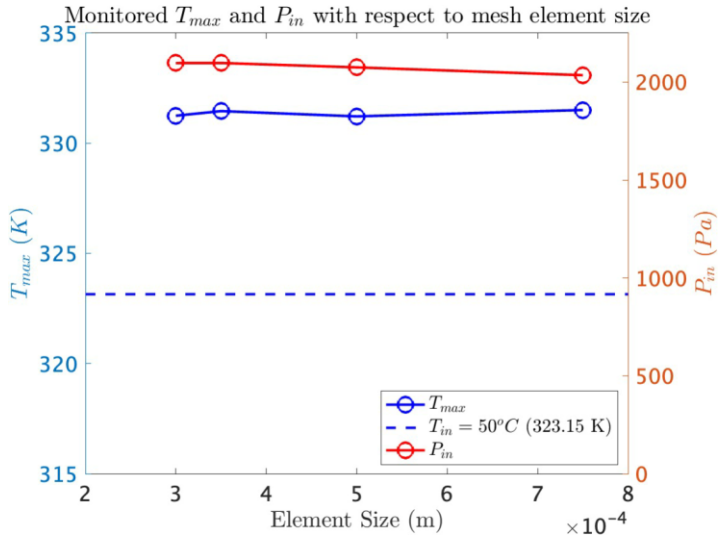


**Figure 144:** Mesh independence monitors $T_{max}$ and $P_{in}$ with respect to mesh element size for DI water simulation, with a flow rate of 0.555 lpm.

Figure 145 and Figure 146 show the thermal contours at the fluid-HX interface for both designs, for a coolant flow rate of 0.555 lpm and system heat loads of 54.1 W (corresponding to I = 0.68 A for each heater). The proposed design has a $\Delta T_{max}$ of 2.65 °Cat the fluid-HX interface, compared to 7.97 °C for the baseline design, for the same total heat input to the system. The proposed design evidently exhibits greater temperature uniformity, due to the longer flow path for the coolant increasing the contact area with the windings that distributes the heat loads from the windings across a much large surface of the HX. The slightly modified return feature in the proposed design also reduces the pronounced hotspots (seen in red/orange) in the baseline design due to dead flow zones. These qualitative disparities in the two designs persisted across all flow rates and heat flux levels.

Additionally, the fluid flow through both HX designs was also assessed to ensure the feasibility of the proposed design. For the critical flow rate of 0.555 lpm, the pressure drop across the baseline design of the HX was found to be 2.10 kPa, while the pressure drop across the proposed design is 4.70 kPa. While there was an increase of 124% in pressure drop with the proposed design, both these differential pressures are relatively low in a practical context, as was later seen in the analogous experimental results. The higher pressure drop in the proposed design may be a result of a slightly smaller return feature cavity, and in turn forces the coolant to flow closer to the axial extremities at the closed end, reducing the presence of the dead flow zones and leading to the

aforementioned greater temperature uniformity. For each flow rate and heat load level, the simulation results were post-processed to evaluate $h_{eff.}$ The fluid flow and heat transfer metrics were assessed across the various $\dot{Q}$ magnitudes and flow rates to determine anticipated trends.

**Table 27:** $h_{eff}$ vs. $\dot{Q}$ for the flow rate of 0.555 lpm

| $I_{heater}$ $(A)$ | $\dot{Q}$ $(W)$ | $T_{max}$(K) | $P_{in}$ $(Pa)$ | $h_{eff}$ $(W/m^2K)$ |
|---|---|---|---|---|
| 0.68A | 54.06 | 331.46 | 2097.4 | 3151.86 |
| 0.59A | 40.592 | 329.45 | 2097.8 | 3130.86 |
| 0.5A | 29.1 | 327.66 | 2097.8 | 3128.09 |

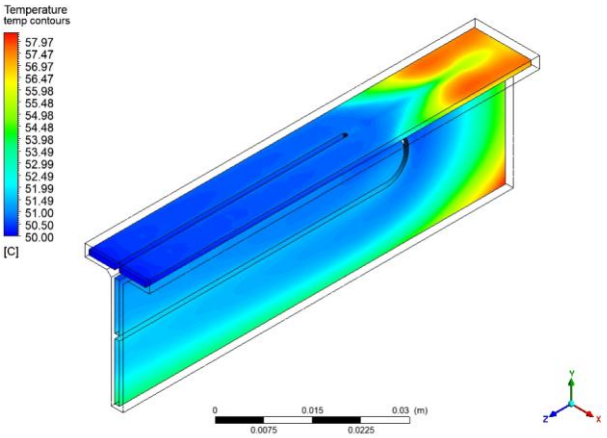


**Figure 145:** Thermal contours at fluid-HX interface for baseline HX design.

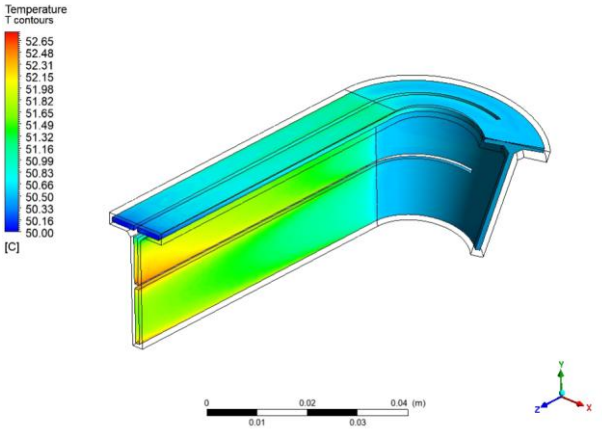


**Figure 146:** Thermal contours at fluid-HX interface for proposed HX design.

Table 27 shows the variation of $h_{eff}$ with the scaling of $\dot{Q}$ between 29.1 W ($I_{heater}$ =0.5 A) and 54.06 W ($I_{heater}$ = 0.68 A), with the actual proportion and configuration of heat load application for each surface remaining consistent, for the baseline case with flow rate of 0.555 lpm. The results revealed that for the chosen heating configuration, the CFD/HT results across the three heat load levels had a low standard deviation of 0.41%. It was thus hypothesized that $h_{eff}$ is agnostic to the magnitude of the heat flux provided for any chosen heating configuration.

Figure 147 shows the variation of $h_{eff}$ for both designs, with varying coolant flow rates between 0.2 lpm and 5 lpm. The results revealed that for both designs, $h_{eff}$ exhibited logarithmic growth with increasing flow rate, i.e., a rapid initial increase, followed by a gradual approach towards an asymptotic value at very high flow rates. More crucially, while the proposed design had a slightly lower $h_{eff}$ at very low flow rates, its curve soon rose above that of the baseline design. At the critical flow rate of 0.555 lpm, the baseline design had an $h_{eff}$ of 3151.86 W/m$^2$K, while the proposed design had an $h_{eff}$ of 3662.78 W/m$^2$K- which was a 16.2% increase. This suggests that, assuming consistent conductive thermal resistances through the HX wall across all flow rates, the convective capabilities of the proposed design outperformed those of the baseline past a threshold flow rate of ≈ 0.4 lpm.

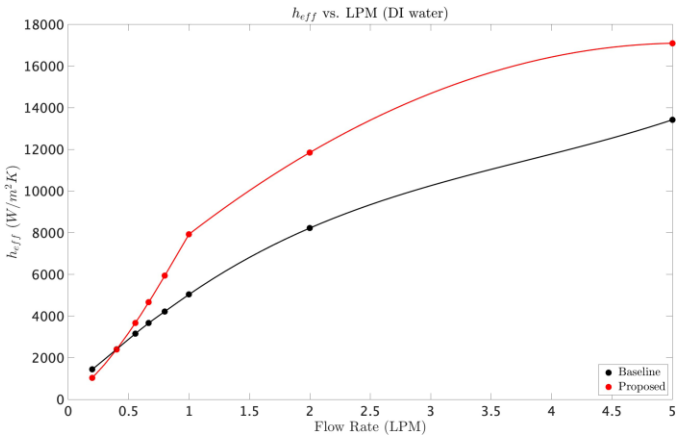


**Figure 147:** Variation in $h_{eff}$ with flow rate for both HX designs.

When considering the net gains from the HX design change, it is also important to consider the relative pumping power required for achieving a certain $h_{eff}$ with each design. The relationship between $P_{pump}$ and flow rate was analyzed from the CFD/HT results for both designs, as shown in Figure 148. The results of this analysis revealed that due to the higher pressure drop seen in the proposed design, the pumping power required for the proposed design was approximately twice that for the baseline design at the lowest tested flow rate of 0.2 lpm, and only increased with increasing flow rates. At the critical flow rate of 0.555 lpm, the pumping power required for the proposed design was 224% of that required for the baseline design, and this disparity continued to increase for flow rates past 1 lpm, as seen in Figure 149. This indicated that any enhancement in $h_{eff}$ would be counteracted by an increase in pumping power requirements, reducing the feasibility of this design change for use at higher coolant flow rates.

While the CFD/HT analysis with DI water and experimental validation confirmed the superior thermal performance of the proposed HX design, the HX-level results required minor adjustments prior to scaling up for a motor-level analysis. These were as follows:

• It was desired to obtain projected CFD/HT results for $h_{eff}$ for the ideal coolant of choice, WEG 50/50. Hence, the CFD/HT simulations were repeated with the same heat load and model settings, but with the coolant being WEG50/50, entering the inlet of the HX at 65 °C. The thermophysical properties of WEG50/50 chosen for the simulation were assumed to be temperature-dependent

between 30°C and 130 °C. However, for the $h_{eff}$ calculation, constant properties tabulated in Table 28 were assumed.

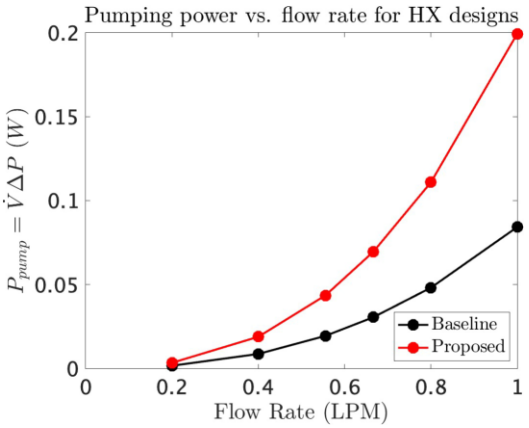


**Figure 148:** Variation in pumping power with flow rate for both HX designs, in the 0.2 lpm-1 lpm range.

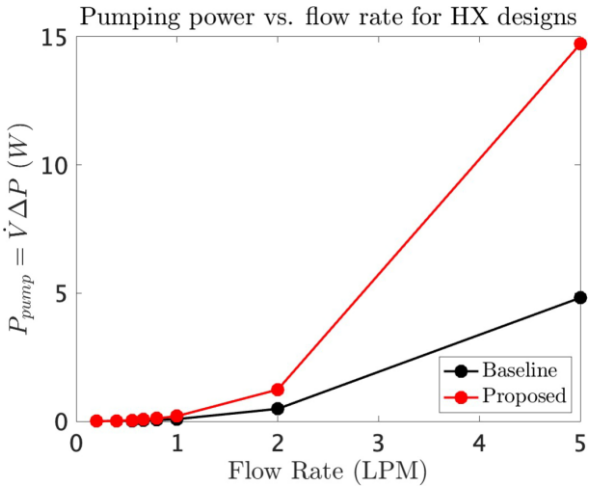


**Figure 149:** Variation in pumping power with flow rate for both HX designs.

**Table 28:** Thermophysical Properties of WEG 50/50 Used for CFD/HT Analysis Post-Processing

| Density $\rho\ (kg/m^3)$ | Specific Heat $C_p\ (J/kg.K)$ |
|---|---|
| 1050 | 3386.1 |

Given that it was not feasible to measure HX inner wall temperatures for $T_{surf,ave}$, the outer wall temperatures were considered in our DI water analysis and validation. However, choosing the outer wall temperature for $T_{surf,ave}$ meant that the resulting $R"_{th,NTU}$ value incorporated the thermal resistance for conduction through the HX wall. Hence, this prevented accurately determining a purely convective heat flux, where $T_{surf,ave}$ would ideally be measured at the inner wall. Figure 150 shows a 1D planar thermal resistance network that further elucidates this limitation. Hence, the WEG50/50 CFD/HT post-processing was adjusted to calculate $T_{surf,ave}$ at the HX inner wall instead. This would allow for the $h_{eff}$ to be a true reflection of the convective heat transfer capabilities of the HX. This modification would also aid motor-level analyses, where the conduction and convection resistances would be distinct from each other. Additionally, it would allow for fair

comparisons with state-of-the-art technologies and past analyses of similar HX designs, since convection-based thermal resistances are agnostic to the thermal conductivities of the various materials used for the prototypes.

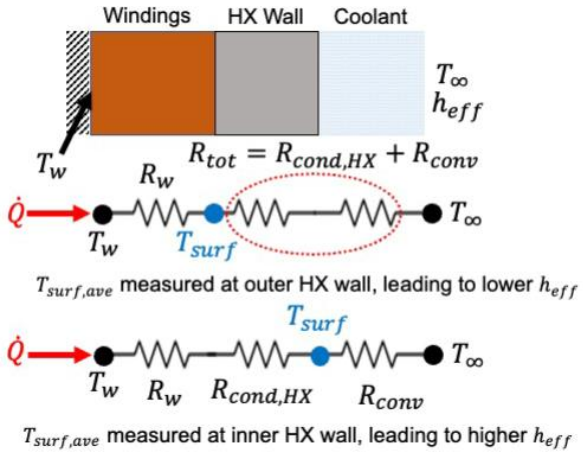


**Figure 150:** 1-D planar thermal network model for a linearly temperature dependent heat load across the HX wall. The upper network shows the limitation of the prior simulations,that capture a larger thermal resistance including the conduction resistance through the HX wall. The lower network shows how measuring $T_{surf,ave}$ at the inner wall allows a better estimation of convective $h_{eff}$.

The temperature contours are seen in Figure 151 and Figure 152. For the maximum heat load of 54.1W as in Table 3.1 and a flow rate of 0.555 lpm, the maximum temperature at the fluid-HX interface in the proposed design was 3.03 °C higher than the inlet temperature, which was 68.8% lower than the baseline design (maximum increase of 9.71 °C). The increased temperature uniformity, reduction of pronounced hotspots due to dead flow zones and other qualitative insights remained consistent as in Figure 145-Figure 146 despite the coolant fluid change. The post-processed calculations of $h_{eff}$ at 0.555 lpm revealed an $h_{eff}$ of 3276 W/m$^2$K for the proposed design, which was 23% higher than that of the baseline design (2664 W/m$^2$K).of 3276 W/m$^2$K for the proposed design, which was 23% higher than that of the baseline design (2664 W/m$^2$K).

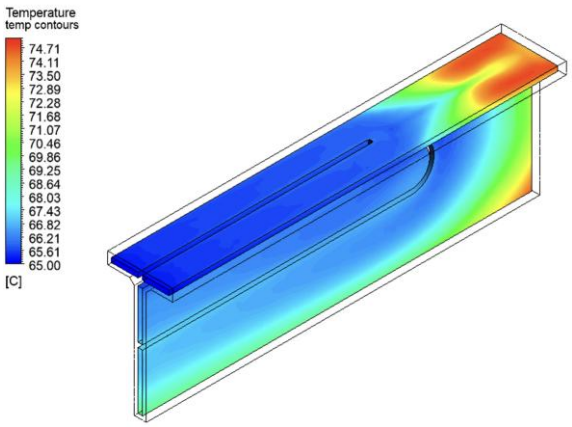


**Figure 151:** Thermal contours at the coolant-HX interface for the WEG 50/50 CFD/HT simulation run for the baseline design.

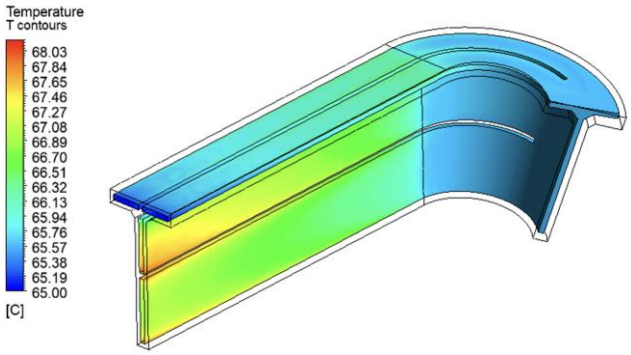


**Figure 152:** Thermal contours at the coolant-HX interface for the WEG 50/50 CFD/HT simulation run for the proposed design.

Figure 153 shows the trends in $h_{eff}$ for both the baseline and proposed designs with changing flow rate. Like with the DI water simulations, the proposed design showed an enhanced $h_{eff}$ at all flow rates past the threshold of 0.4 lpm. Subsequently, **Figure *154*** pictures the adjusted results for $h_{eff}$ for the case where $T_{surf,ave}$ was measured at the inner wall of the HX. As can be seen, choosing the inner wall for $T_{surf,ave}$ computation excluded the effects of conductive thermal resistance through the HX wall, leading to lower values of $R"_{th,NTU}$ . As the flow rate increased, the convective impact became more dominant for both HX designs, and higher heff were seen than with the outer wall temperature-based trends seen in Figure 153. The inner wall results were particularly useful when leveraging $h_{eff}$ to evaluate motor-level impact of each HX design.

The CFD/HT simulated results were validated experimentally through subscale testing of the baseline and proposed HX designs, using additively manufactured LithaLox 350 HP alumina prototypes provided by Lithoz America. Alumina was chosen due to its ability to withstand high temperatures, poor electrical conductivity, and high thermal conductivity.

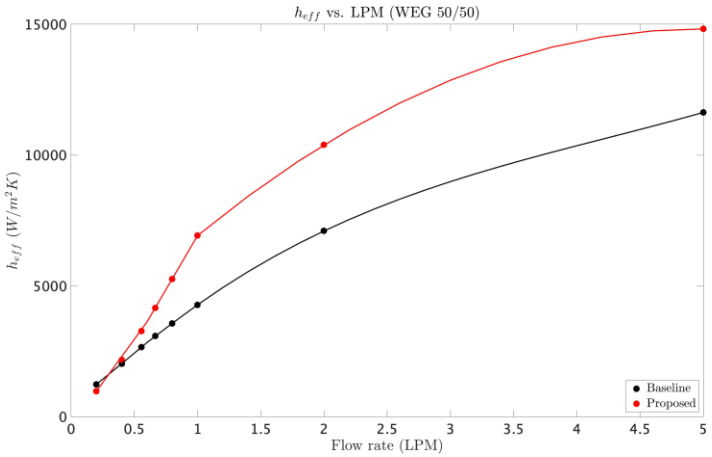


**Figure 153:** Figure 3.12: CFD/HT trends for $h_{eff}$ with respect to flow rate for both HX designs, showing higher heff for proposed design past approximately 0.4 lpm.

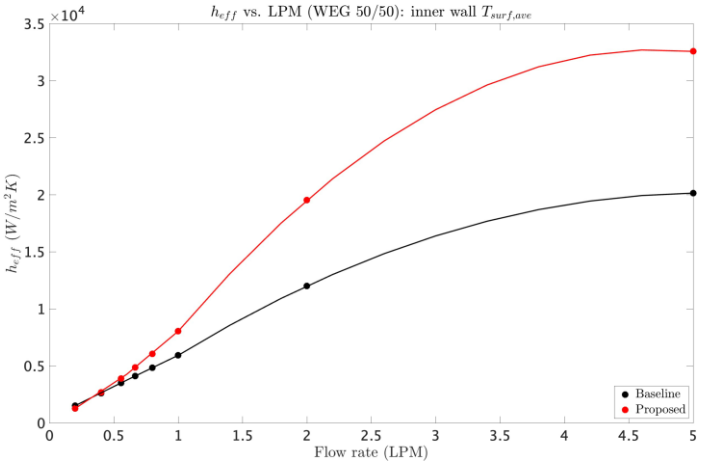


**Figure 154:** CFD/HT trends for $h_{eff}$ with respect to flow rate for both HX designs where $T_{surf,ave}$ is measured at the HX inner wall.

The system heat loads were provided by polyamide patch heaters adhered to the major walls of the HX surfaces via aluminium heat spreader plates. Each heater was rated for 28 V/0.7 A and a maximum power output of ≈ 20 W, so each heater was connected to a separate power supply to maximize the possible heat input to the system. The coolant used was deionized (DI) water, due to its ready availability in the laboratory. A schematic of the testing loop is pictured in Figure 155, and the actual thermal testing loop (set up at Georgia Tech) is pictured in Figure 156.

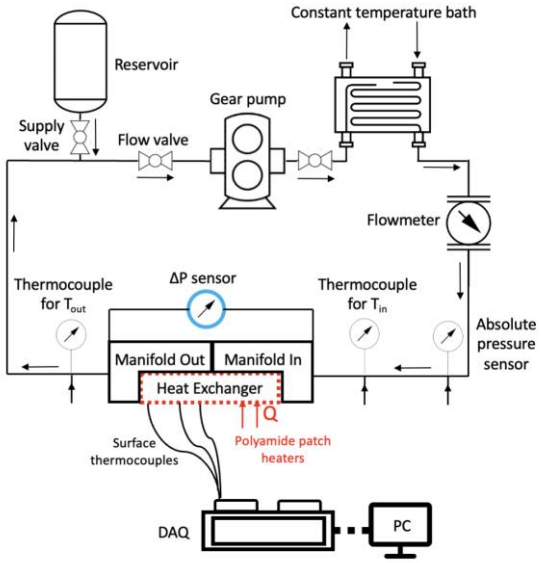


**Figure 155:** Figure 3.14: Schematic of thermal testing loop for component-level HX effectiveness testing, as set up at Georgia Institute of Technology.

While the CFD/HT analysis with DI water and experimental validation confirmed the superior thermal performance of the proposed HX design, the HX-level results required minor adjustments prior to scaling up for a motor-level analysis. These were as follows:

• It was desired to obtain projected CFD/HT results for $h_{eff}$ for the ideal coolant of choice, WEG 50/50. Hence, the CFD/HT simulations were repeated with the same heat load and model settings, but with the coolant being WEG50/50, entering the inlet of the HX at 65 °C. The thermophysical properties of WEG50/50 chosen for the simulation were assumed to be temperature-dependent between 30°C and 130 °C. However, for the $h_{eff}$ calculation, constant properties tabulated in Table 28 were assumed.

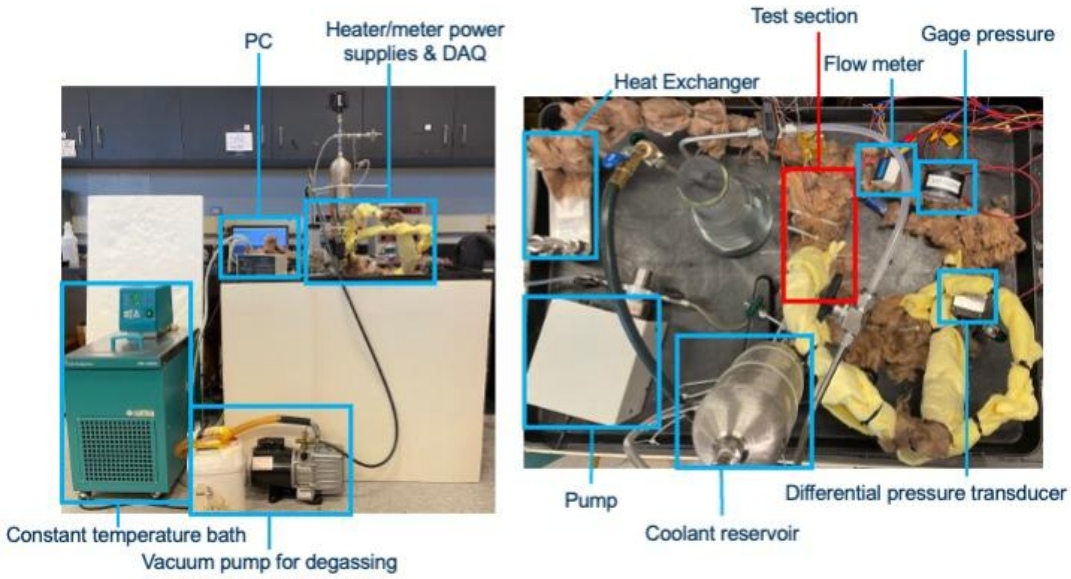


**Figure 156:** Actual thermal testing loop setup for component-level HX effectiveness testing, at Georgia Institute of Technology.

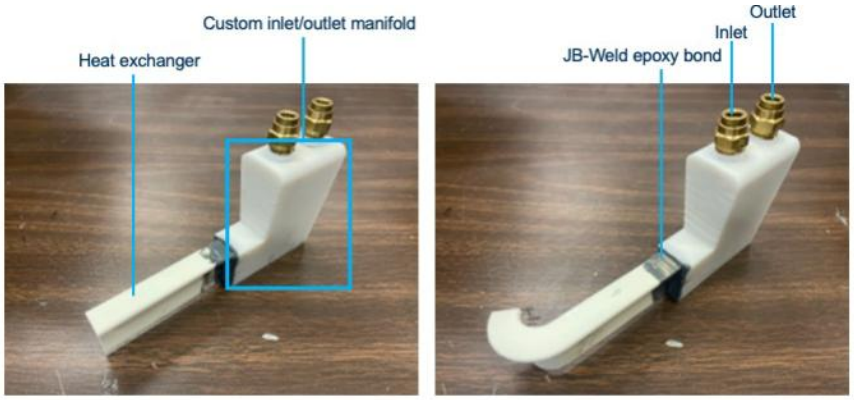


**Figure 157:** Test sections for both HX designs with attached inlet/outlet manifold for coolant supply

The test section was connected to the testing loop, parallel with the differential pressure transducer. At both the inlet (1) and outlet of the manifold (2), AWG 14-sized T-typethermocouple probes were inserted to measure $T_{in}$ and $T_{out}$ for the LMTD and energy balance calculations. Five (5) AWG 24-sized T-type thermocouples were placed on the outer surface of the HX, approximately equally spaced along the flow path of the coolant. These thermocouples measured the outer surface

temperature of the HX, in order to estimate $T_{surf,ave}$. Since it was not feasible to place thermocouples on the inside surface walls of the HX, $T_{surf,ave}$ was measured at the outer surface wall. Uncertainty analysis was conducted for the thermocouple temperature measurements, and the uncertainty in each steady-state temperature measurement was found to be ≈ 0.0291 °C.

**Table 29:** Details and placement of polyamide patch heaters providing heat loads on the HX.

| Heater No. | Heater Placement | Power Supply | Estimated $Q_{out,max}$ [W] |
|---|---|---|---|
| 1 | Top horizontal | Agilent N5752A | 17.9 |
| 2 | Vertical side wall 1 | Instek PR-3060D | 17.8 |
| 3 | Vertical side wall 2 | Instek PR-3060D | 18.4 |

Table 29 lists the power supply models, corresponding heater placements, and maximum heat input ($I_{heater}$ = 0.68 A). The total maximum heat input to the insulated system from the 3 heaters was ≈ 54.1 W, found by summing the individual $Q_{out,max}$ from all the heaters. The test section and all the tubing from the brazen-plate HX (for inlet temperature regulation) to the inlet of the test section were insulated using 0.0508 m-thick fiberglass insulation and cable ties. This mitigated heat losses from the system to the surroundings. Following this, the trial was conducted for each HX design as follows:

• The DAQ collected data for all thermocouples, the flow meter, and the differential pressure transducer at a sample rate of 1 Hz. The chiller/temperature regulator was switched on and its setpoint was set to 50 °C.

• The flow meter calibration data was interpolated to determine the expected voltage value for the chosen coolant flow rate.

• The pump was turned on and de-gassed if this had not already been done prior. The pump was slowly tuned while monitoring the DAQ for the interpolated output voltage value, to ensure the correct flow rate.

• The power supplies connected to 3 heaters were turned on, and gradually tuned to the chosen input voltage and current. The thermocouple temperatures were monitored throughout to ensure safety and prevent any accidental overheating-based hazards.

• The DAQ was monitored to ensure steady-state temperature. Note: Steady-state temperature was defined as $\Delta T < 0.2$ °C for 20 min of data collection.

• At the chosen flow rate/heat load data point, steady-state data was collected at the chosen sampling rate (this translated to 1200 steady-state samples). Once recorded, the DAQ was stopped and the raw data was exported for measurement calibration and subsequent post-processing.

• All 3 heater power levels were tested for the same flow rate fine tuning, to ensure flow rate uniformity. For any other flow rate of interest, steps 2-3 were repeated while keeping the heaters active, and the system temperatures were once again allowed to reach steady state before recording data.

• For the turn-down procedure, the power supplies to the heaters were switched off before switching off the pump to stop coolant flow.

The measured data for $T_{in}$, $T_{out}$, $T_{surf,ave}$ and Q, and the known thermophysical properties of water subsequently facilitated the effective convective heat transfer coefficient calculation.

The DI water CFD/HT simulation results and trends were experimentally validated using the raw data obtained from the setup. The major limiting factor dictating the feasible operating conditions for our experimental trials was thermocouple uncertainty relative to the temperature differences being measured ($\Delta T_i$ and $\Delta T_o$). At a combination of higher flow rates and low heat load levels, $\Delta T_i$ and $\Delta T_o$ would approach values smaller than the uncertainty in measured thermocouple data, leading to unreliable derived results for LMTD, and subsequently, $h_{eff}$ . Hence, combinations of flow rates were chosen so as to ensure that $\Delta T \geq 0.5$ °C, which was approximately the uncertainty in the raw thermocouple data. The choice of flow rate and heat load level ranges was further justified upon conducting an uncertainty analysis of the results, as described towards the end of this section.

• Flow rates: 0.8 lpm led to a minimum $\Delta T \approx 0.52$ °C. Hence, CFD/HT results for the following flow rates were validated - 0.2, 0.4, 0.555, 0.666 and 0.8 lpm.

• Heater load levels: 0.5 A (≈ 29 W total) led to a minimum $\Delta T \approx 0.52$ °C. Hence, 3 different heat load levels corresponding to the following current levels were tested -0.5 A (≈ 29 W total), 0.59 A (≈ 40.5 W total) and 0.68 A (≈ 54 W total). The upper limit was dictated by the maximum allowable rated current through each heater, which was 0.7 A.

An energy balance calculation was conducted to confirm effective thermal insulation of the test setup. The known input power from the heaters ($\dot{Q}_{in} = Q$ ) was compared against the heat removal rate by the coolant in the HX ($\dot{Q}_{out}$). $\dot{Q}_{out}$ was calculated.

Figure 158 and Figure 159 show the results of the energy balance for all the data points for both the baseline and proposed HX designs. The expected ΔT is denoted by the colored lines, while the experimentally observed ΔT for the corresponding heat load levels are overlaid with solid circular markers of the same color (0.5 A - blue, 0.59 A - red, 0.68A - green). Meanwhile, the black curve shows the CFD/HT result for the maximum heatload case. It was evident from Figure 158 and Figure 159 that the CFD/HT, expected and observed experimental results were all well aligned. Figure 160 further quantifies this by plotting the percentage error between the ΔT expected from energy balance or CFD/HTand observed experimental ΔT across all experimental trials. The observed ΔT exhibited agreement to within 7.6% and 13.8% for the baseline and proposed design trials, with low average errors of 1.6% and 2.9%, respectively. Potential sources of this error include thermocouple measurement uncertainty, or from minor system heat losses due to imperfect insulation leading to small unforeseen air gaps around the test section and small amounts of heat conduction through the low-conductivity manifold (which has a thermal conductivity of 0.52 W/m.K). While these minor losses were unavoidable despite careful setup due to the described

systematic and human error, they were low enough to consider the energy balance reasonably satisfied.

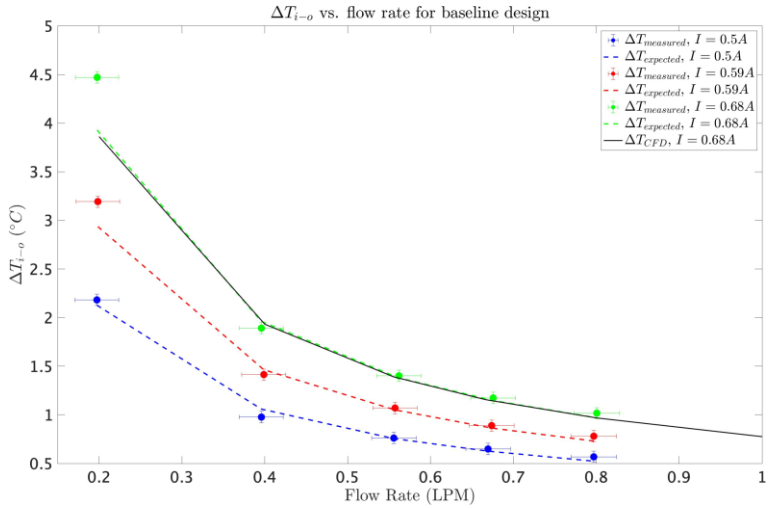


**Figure 158:** CFD/HT and experimental values for $\Delta T_{i-o}$ for baseline design

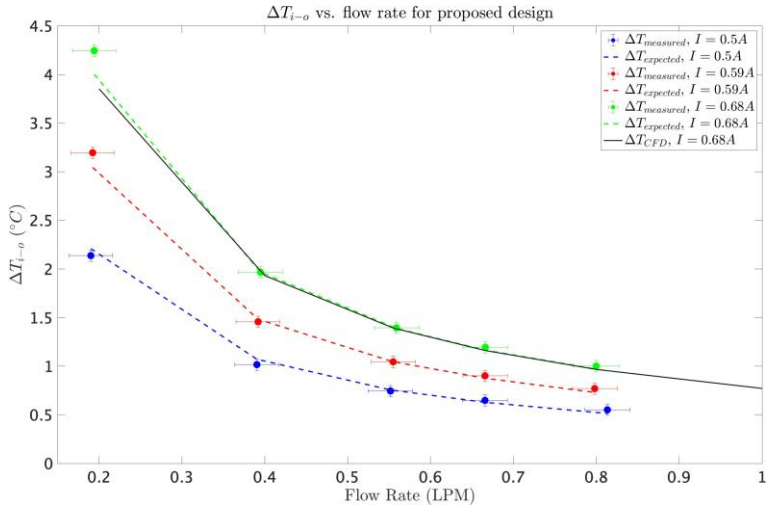


**Figure 159:** CFD/HT and experimental values for $\Delta T_{i-o}$ for the proposed design

Prior to analyzing heat transfer trends, we looked to validate trends in the differential pressure drop for the test section of each HX design. The time-averaged differential pressure transducer data was converted to a pressure drop reading in Pascals using the device calibration data for each data point. The resulting experimental pressure drop data are plotted against the corresponding CFD/HT trends for both designs in Figure 161 and Figure 162.The pressure drop results for the proposed design were evidently more straightforward to analyze, since they were experimentally observed to be reasonably aligned with the expected CFD/HT result. The maximum error in the experimental result was -38%, observed at the flow rate of 0.2 lpm, and the average magnitude of the error between the experimental and CFD/HT results was 17.1%. The slight disparity between the CFD/HT and experimentally measured pressure drops was likely because the CFD/HT considered the pressure drop across the HX alone, while in the experimental setup, the pressure drop was

measured across the complete test section. This included the pressure drop due to the manifold, which had sudden flow profile changes between the 1/2" (0.0127 m) NPT-sized flow cavity at the manifold inlet and outlet, and the much smaller 1 mm-wide HX flow channel interfacing with the HX inlet and outlet. Additionally, the pressure drop may have been further impacted by the presence of flexible teflon tubing between the test section and the pressure transducer. However, for the baseline design test section, the experimental pressure drop values exhibited relatively poor agreement with the CFD/HT result. The error was relatively small at low flow rates but increased drastically with rising flow rates, reaching a maximum of 174% at the flow rate of 0.8 lpm. This suggested the presence of one or more small local obstructions along the coolant flow path. These may have occurred due to material overhang during the HX additive manufacturing process, or from remnant resin particles from the manifold threading accidentally travelling into and becoming trapped in the channel. Alternatively, the contraction could have occurred due to interference of the JB-Weld epoxy at the manifold-HX bond line, where improperly applied epoxy could have caused an unforeseen contraction impeding coolant flow.

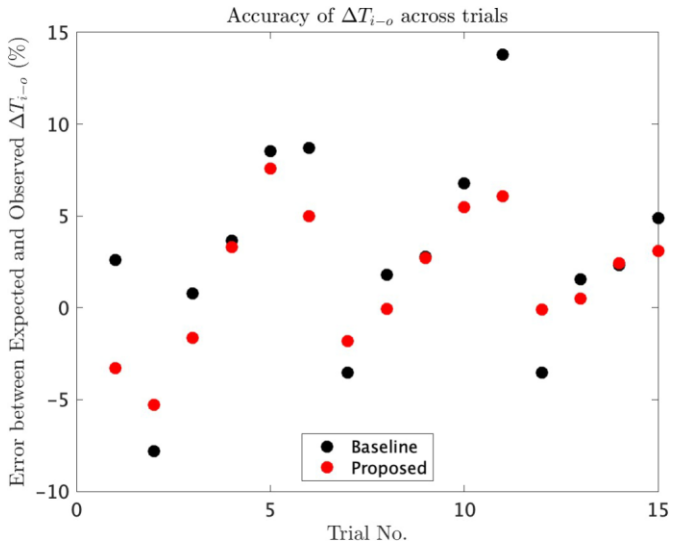


**Figure 160:** Percentage errors in observed $\Delta T_{i-o}$ across all trials

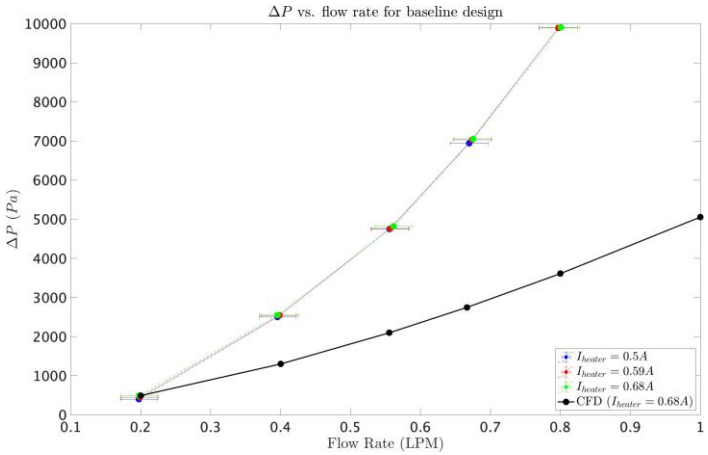


**Figure 161:** Differential pressure drop across baseline design test section

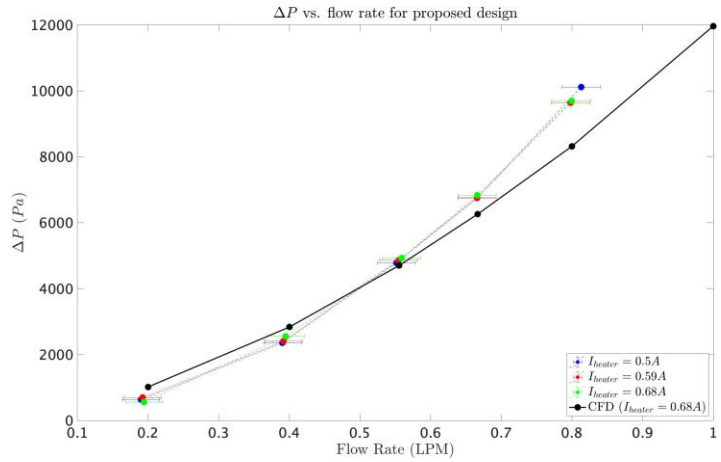


**Figure 162:** Differential pressure drop across proposed design test section

To confirm our hypothesis, the bond lines and flow channels for both designs were visualized using X-ray imaging. The X-ray scan was post-processed using the Image Processing Toolbox in Matlab, and converted from surface data to patch data using the patch-Surf() command in Matlab. Subsequently, they were written to .stl files using the inbuiltstlwrite() function. The resulting .stl files were viewed in MeshLab, and further cleaned and reduced using the 'Remove Isolated Elements (wrt diameter)' (to remove improperly resolved stray voxels at the scanned volume boundaries) and Quadric Edge Collapse Decimation to view, zoom and pan the images within the computational constraints of the system. Figure 163-Figure 165 show some salient results of the MeshLab visualizations for both the baseline and proposed designs.

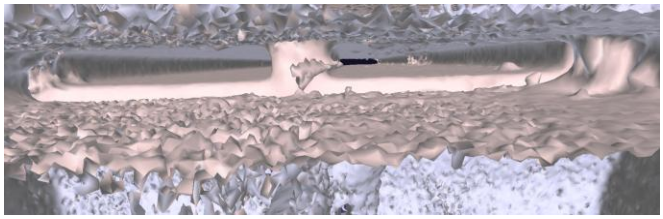

**Figure 163:** X-ray scan result visualized in MeshLab for baseline HX design showing bondline obstructions.

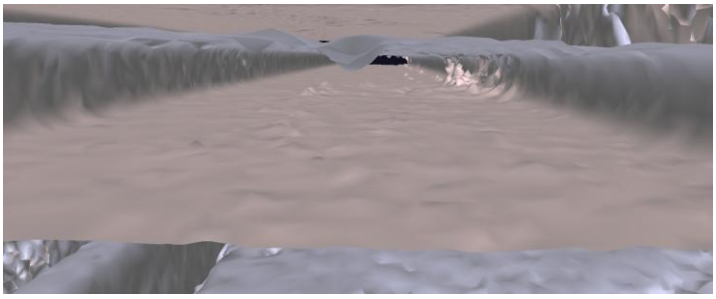

**Figure 164:** X-ray scan result visualized in MeshLab for baseline HX design showing inletchannel obstructions further into flow path.

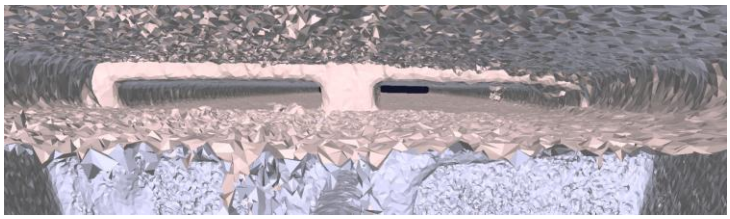

**Figure 165:** X-ray scan result visualized in MeshLab for proposed HX design showingmuch fewer bond line obstructions.

The baseline design X-ray scans (Figure 163 and Figure 164) displayed significant interference of the epoxy at the inlet bond line, and further obstructions along the inside of the right inlet channel. This deposition was likely due to smeared and hardened epoxy, or due to overhang during HX manufacture. These were the likely cause of the elevated experimental pressure drop. In contrast, there were far fewer obstructions at these locations in the case of the proposed design, justifying the greater alignment between the experimental and predicted CFD/HT trends.

Post calibration, the time-averaged steady-state experimental results for each data point were post-processed to calculate experimental values of $h_{eff}$. Figure 166 and Figure 167 show the experimental data for $h_{eff}$ versus flow rate, compared to the predicted CFD/HT results, for the baseline and proposed designs, respectively. The experimental trendlines were separately plotted based on the heat load level ($\dot{Q}$) provided to the system (blue - 0.5 A, red - 0.59 A, green - 0.68 A). The experimental results across all trials showed agreement to within maximum errors of 17.2% for the baseline design and 18.7% for the proposed design, relative to the CFD/HT results. The corresponding average error magnitudes for the baseline and proposed design trials were 5.6% and 9.5%, respectively.

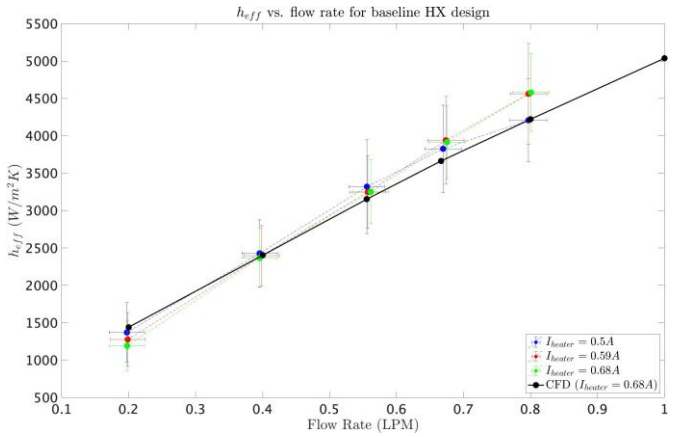


**Figure 166:** Post-processed results for $h_{eff}$ from experimental data for baseline design.

The resulting experimental trends in $h_{eff}$ versus flow rate align well with predicted trends from CFD/HT analysis. It is worth noting that at the higher flow rates for both designs for the data points with low heater current (0.5A), trendlines for both designs show a slight deviation from the remaining experimental trends, with outliers being seen especially for the 0.5 A, 0.8 lpm data points (in blue). This illustrated the potentially reduced reliability of the results obtained at higher flow rates and low heat load levels, due to the temperature differences being measured being close

to or just less than the rated uncertainty in the thermocouples. This explained the upper limit on feasible flow rates being ≈ 0.8 lpm for this validation setup.

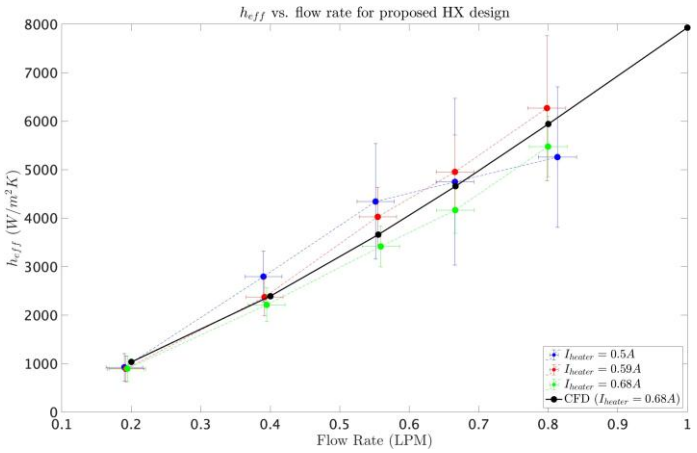


**Figure 167:** Post-processed results for $h_{eff}$ from experimental data for proposed design.

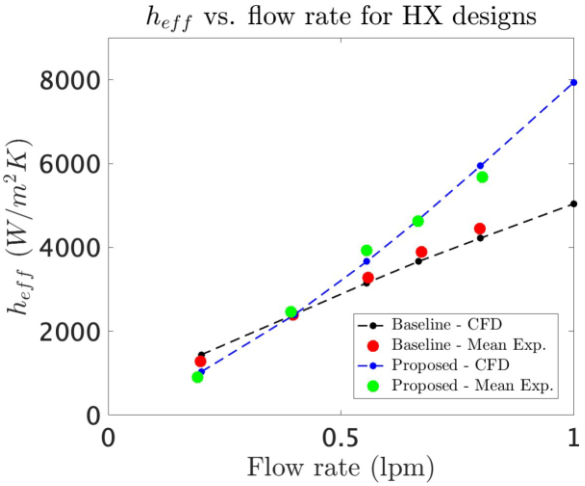


**Figure 168:** Experimental versus CFD/HT $h_{eff}$ versus flow rate for both HX designs

Subsequently, we calculated the standard deviation in the $h_{eff}$ results across the 3 heat load levels at each flow rate (for both designs). For the baseline design, the heat-load-averaged experimental results had a maximum standard deviation of 7.0% (with an average of 3.1%). For the proposed design, the maximum standard deviation was 12.2% (with an average of 8.9%). The low relative standard deviations reasonably confirmed that for the chosen heating configuration, $h_{eff}$ is not dependent on the heat load level $\dot{Q}$.

Having confirmed the negligible impact of heat load level, the results at each flow rate were averaged across all heat load levels. At the critical flow rate of 0.555 lpm, the heat-load-averaged $h_{eff}$ for the proposed design was found to be 3931 W/m$^2$K (7.3% error from the CFD/HT result), while the corresponding value for the baseline was found to be 3273 W/m$^2$K (3.8% error from the CFD/HT result). Hence, at the critical flow rate, the experimental $h_{eff}$ exhibited a 20.1% enhancement with the proposed design (compared to 16.2% from CFD/HT). Figure 3.27

subsequently shows the trends in $h_{eff}$ with flow rate for both designs, averaged across the 3 heat load level trials. As can be seen in the figure, the average experimental trend closely mirrors the CFD trends, and also clearly shows the enhanced heat transfer capability with the proposed HX design beyond a minimum threshold flow rate of ≈ 0.4 lpm. The heat-load-averaged experimental results across all flow rates showed agreement to within 11.1% (baseline design) and 12.7% (proposed design) relative to the CFD/HT results, with error averaging 5.4% and 5.6% for the two designs, respectively.

Uncertainty analysis was conducted for the experimentally obtained $h_{eff}$. The resulting uncertainties in $h_{eff}$ or $U(h_{eff})$ were plotted as error bars in Figure 166-Figure 167. The average relative uncertainties in $h_{eff}$ across all trials, or $\%U(h_{eff})$, were 17.7% and 21.4% for the baseline and proposed designs, respectively. Although the uncertainties in measured temperatures (0.0291 °C), flow rates (≈ 3.3%) and pressure drops (≈ 0.6%) were relatively small, $\%U(h_{eff})$ was derived by propagating relative uncertainties from multiple measured quantities (7 thermocouple measurements + 1 mass flow rate reading), which compounded step-wise. In fact, *U(LMTD)* (since *LMTD* was a function of 7 thermocouple readings) was found to contribute heavily to $U(h_{eff})$, due to the likelihood of very small *LMTD* values for the same absolute thermocouple uncertainties (leading to larger $\%U(T_i)$). The reliance of $\%U(h_{eff})$ on %U(LMTD) for both designs is better visualized in Figure 169, with the solid markers denoting mean relative uncertainty and error bars denoting minimum/maximum relative uncertainties across flow rates for a given design and heat load level. Figure 169 elucidates some noteworthy practical trends for the experimental data. First, a clear correlation was observed between the average $\%U(h_{eff})$ and heat load level for both designs. As the heat load level decreased, the 0.59 A (red) and 0.5 A (blue) data points for both designs showed increases in %U(LMTD) and $\%U(h_{eff})$. The lowest mean$\%U(h_{eff})$ was observed at the highest heat load level (0.68A, in green) for both designs- averaging 16.3% and 16.0% for the baseline and proposed design, respectively. Hence, while our CFD/HT analysis showed that heat load level had a negligible impact on the value of $h_{eff}$, it was shown practically that the most reliable set of results was obtained at the highest heat load level (0.68 A).

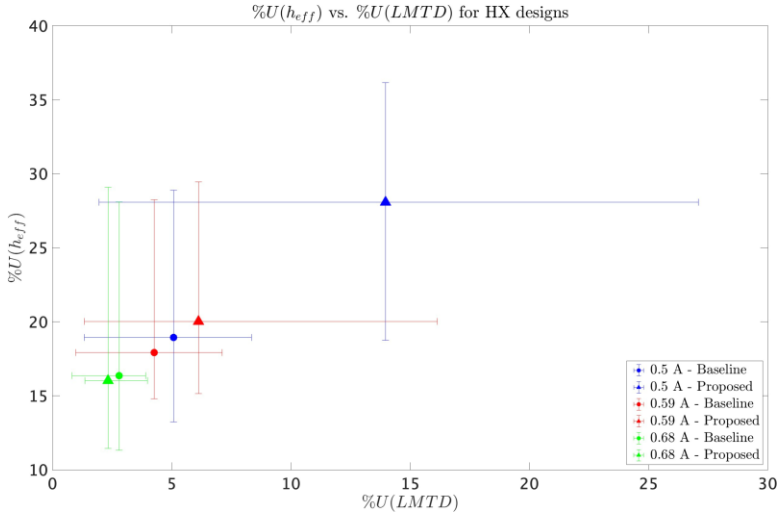


**Figure 169:** $\%U(h_{eff})$ versus %U(LMTD) for tested heat load levels both designs.

Secondly, as heat load decreased, the mean and maximum %U(LMTD) and %U($h_{eff}$) increased far more for the proposed design (maximum of 36.2% uncertainty at 0.5 A level) than for the baseline design (maximum of 28.9% uncertainty at 0.5 A level). This was due to the fact the proposed design leads to lower LMTD values for the same set of flow rate, thus indicating greater temperature uniformity and leading to higher $h_{eff}$. Hence, while the lower LMTD with the proposed design is a desirable result from a thermal performance standpoint, its experimental validation led to slightly less reliable results than with the baseline design, especially at the lower heat load levels. The relatively low %U($h_{eff}$) for the 0.68 A heat load case - 16.3% and 16.0% average uncertainty for the baseline and proposed design data points, respectively, indicated that the 0.68 A results most reliably validated the CFD/HT results. The 0.5 A and 0.59 A results subsequently served as an additional confirmation of the experimental validation. The trends in %U($h_{eff}$) with respect to heat load level hence made evident the virtues of future experimental validation with higher heat fluxes, where the relative uncertainty in LMTD would be even lower at the same set of flow rates. Since %U($h_{eff}$) tended to increase with flow rate across all heat load levels, the use of a more powerful heat load source could also enable validation at flow rates > 0.8 lpm without incurring large relative uncertainties. However, applying a higher heat load was not as straightforward as merely selecting more powerful patch heaters, since the patch heater size increased with its power output. In fact, the 20 W patch heaters chosen for this experiment were the most powerful patch heater option that satisfied the upper size limit of the HX surfaces they were applied to. These practical limitations in heat sources for the experimental validation limited the flow rate range for testing, and the resultant relative uncertainties.

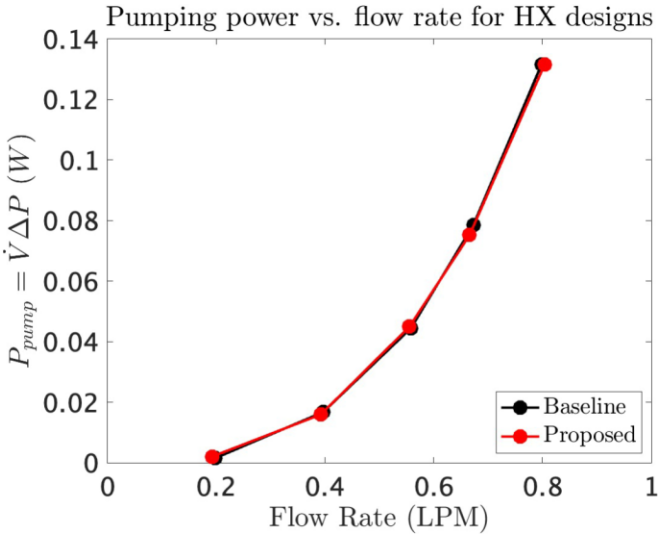


**Figure 170:** Experimental trends for pumping power requirements with respect to flow rate for both HX designs.

While it was desired to validate the predicted pumping power trends for each design, the higher experimental pressure drop in the baseline test section expectedly led to increased pumping power requirements for the baseline design than was predicted with the CFD/HT analysis. Figure 170 plots the pumping power, averaged across all heat load levels for each flow rate, against flow rate.

It is evident from the graph that due to the increased pressure drop in the baseline design, the pumping power requirements for both designs were almost equal.

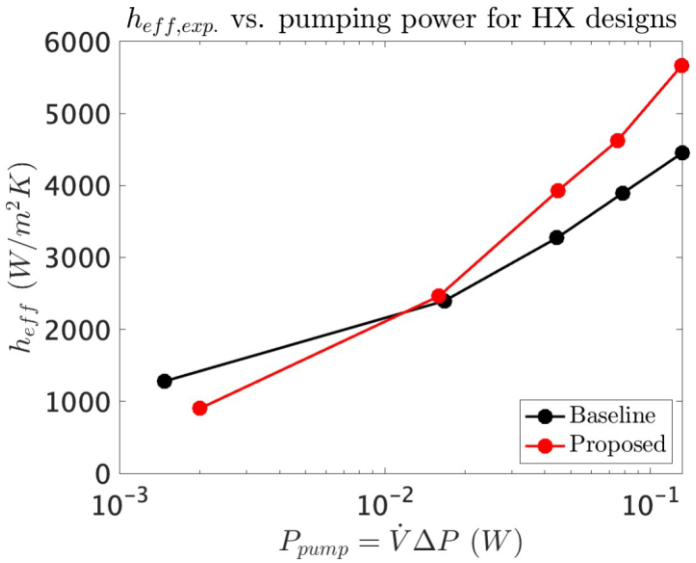


**Figure 171:** Experimental trends for $h_{eff}$ with respect to experimental pumping power requirements for both HX designs.

Given the very similar pumping powers for both designs, the feasibility and energetics of use with each design were largely the same in this instance. Hence, the comparison of $h_{eff}$ with each design came with no trade-offs, and it could be seen that past the minimum threshold of 0.4 lpm, the $h_{eff}$ for the proposed design was higher than that for the baseline design for very similar pumping power requirements. This indicated the benefits of using the proposed design for cooling the motor. However, in the future, a more careful assembly of the baseline test section would ensure no unexpected contributors to an elevated pressure drop, leading to more successful validation of the pumping power comparison.

## 11. Evaluation of In-slot Heat Exchanger Performance via Motor-Level Modeling

### Summary

In this project task, the various approaches for motor-level thermal analysis of the two HX designs are presented.

It was first desired to express the thermal performance enhancement with the proposed HX design in a universal, operating condition-agnostic sense. For this, the metric used was the "winding-to-coolant (WTC) thermal resistance" or $R_{th,wtc}$ that estimates thermal resistance from the hotspot of the motor (windings) to the heat sink (coolant flow). Our calculations provided us with a value for $R_{th,NTU} = R"_{th,NTU}/A$, which was assumed as convective thermal resistance when $T_{surf,ave}$ was measured at the HX inner wall. The convective $R_{th,NTU}$ was subsequently combined with conduction resistances for the windings and the HX wall to estimate $R_{th,wtc}$ for each design. The simplified thermal resistance network governing the winding-to-coolant concept is pictured in

Figure 172 and drew from similar analyses conducted. For simplicity, the impact of contact resistances between the various phases and minor air gaps in the potting material was neglected.

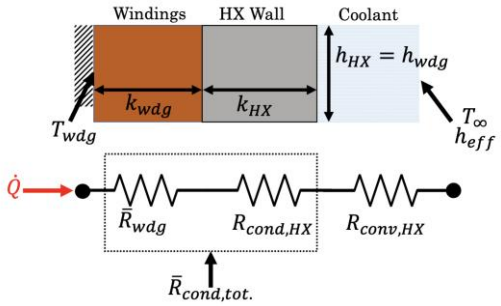


**Figure 172:** Simplified 1-D representation of the thermal network model showing constituents of the winding-to-coolant thermal resistance for the HX designs.

The mean winding-to-coolant thermal resistance was calculated as detailed in the following equation:

$$\bar{R}_{th,wtc} = \frac{1}{3}\bar{R}_{wdg} + R_{cond.,HX} + R_{conv.,HX}$$

where $R_{conv.,HX} = R_{th,NTU}$ from our CFD/HT post-processing, with $T_{surf,ave}$ being measured at the HX inner wall. $R_{cond.,HX}$ was the thermal resistance for conduction through the HX wall, and was calculated using following equation:

$$R_{cond.,HX} = \frac{W_{HX}}{k_{HX} H_{HX} l_{ax,HX}}$$

where $W_{HX}$ = 0.8 mm (known HX wall thickness), $k_{HX}$ = 37 W/m.K (Lithalox 350 HP alumina), and $H_{HX} \approx$ 30.414 mm was estimated by measuring the total effective contact 'height' between the HX wall and the windings in the motor CAD design. $l_{ax,HX}$ was the average 'axial' path length of the coolant from the open to closed axial end of each HX design - 85 mm for the baseline, and ≈ 102 mm for the proposed design (20% greater based on the CAD designs). Lastly, $R_{wdg}$ was calculated using the following equation:

$$\bar{R}_{wdg} = \frac{W_{wdg}}{k_{wdg} H_{wdg} l_{cont.,wdg-HX}}$$

where $W_{wdg} \approx$ 4.87mm and $H_{wdg} = H_{HX}$. $k_{wdg}$ was estimated as the effective conductivity for copper conductors ($k_c$ = 389 W/m.K) and high-conductivity potting ($k_p$ =3 W/m.K) for the targeted fill factor $v_c$ = 0.353. This effective conductivity, found to be ≈ 139.3 W/m.K, was calculated using the parallel estimation formula for two-part composite materials.

Finally, $l_{cont.,wdg-HX}$ was the axial contact length between the winding loop and the HX outer wall. For the baseline design, $l_{cont.,wdg-HX}$ = 42.756 mm, and for the proposed design, $l_{cont.,wdg-HX}$ = 75.6 mm - due to the increased contact in the end-winding region for the proposed design.

**Table 30:** Analytical thermal network results for flow rate-independent resistances and quantities

| | Baseline Design | Proposed Design | $\Delta R$ with Proposed Design |
|---|---|---|---|
| $R_{cond,HX}\ (K/W)$ | 0.00836 | 0.00697 | -16.7% |
| $\bar{R}_{wdg}\ (K/W)$ | 0.02691 | 0.01523 | -43.4% |

Table 30 lists the results of the two conduction resistances through the windings and HX wall, which were constant and flow rate-independent. The greater contact area between the windings and the HX, as well as the longer 'axial' length of the proposed HX design, led to reduced conduction resistances. The total conduction resistance, or $1/3.R_{wdg} + R_{cond.,HX}$, was 0.0120 K/W for the proposed design compared to 0.0173 K/W for the baseline design- a reduction of around 30.5%.

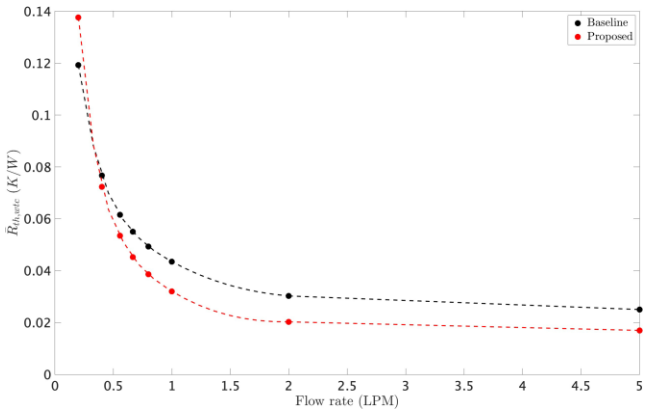


**Figure 173:** Analytically estimated winding-to-coolant thermal resistance $\bar{R}_{th,wtc}$ with re-spect to flow rate, for both HX designs.

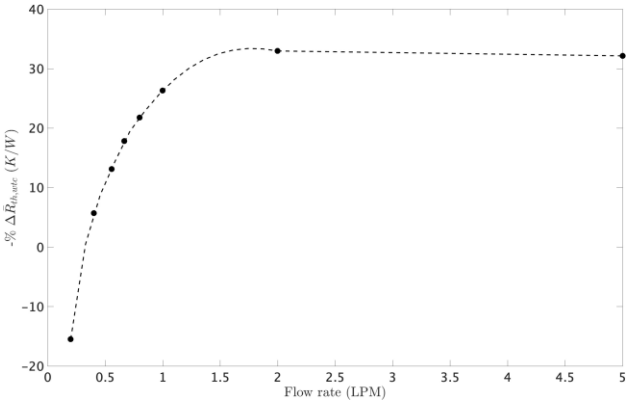


**Figure 174:** Percentage reduction in $R_{th,wtc}$ with the HX design change from baseline to proposed design, as a function of flow rate.

Subsequently, Figure 173 shows the trends in $R_{th,wtc}$ for both HX designs with respect to flow rate. For flow rates approximately ≥ 0.4 lpm, the winding-to-coolant thermal resistance was lower for

the proposed design. Moreover, as flow rates increased, the contribution of convective resistance $R_{conv,HX}$ reduced asymptotically to negligibly small values. Hence, the $R_{th,wtc}$ trendlines for both designs asymptotically approached their respective total conduction resistance values ($1/3.R_{wdg}$ + $R_{cond.,HX}$) at very large flow rates.

The percentage reduction in $R_{th,wtc}$ with the change from baseline to proposed design was plotted against flow rate in Figure 174. It can be seen that at ≈ 2 lpm, the reduction in winding-to-coolant resistance reached a theoretical maximum ≈ 33%, where the convective resistance was 30% lower for the proposed design than for the baseline design. With flow rates increasing past 2 lpm, the thermal resistance 'enhancement' asymptotically approached 30.5% -the flow rate-independent enhancement in total conduction resistance. This suggested that this proposed design had a theoretical maximum thermal performance gain relative to the baseline design, leveraging optimal conductive and convective enhancements at an intermediate flow rate between 0.2 lpm-2 lpm. Hence, our motor thermal models would likely exhibit maximum winding and end winding temperature reductions in this flow rate range.

The trends in $R_{th,wtc}$ enhancement were leveraged to estimate the resulting enhancement in theoretical maximum root mean square (RMS) current density through the windings in a single slot, which is directly related to the motor power density.

Subsequently, $R_{th,wtc,max}$ was plotted against flow rate for both HX designs in Figure 175.The trend observed in Figure 175 were justifiably similar to those in Figure 173**Figure 175**, with the $R_{th,wtc,max}$ being lower for the proposed design than the baseline for flow rates > ≈ 0.4 lpm. Next, it was assumed that the theoretical upper limit for winding and end-winding temperatures was the National Electrical Manufacturers Association (NEMA) Class F in-sulation temperature limit, or 155 °C. Considering this limit to be $T_{hotspot}$, the allowable heat generation in the windings, $\dot{g}$, in W, was calculated as a function of flow rate for each HX design.

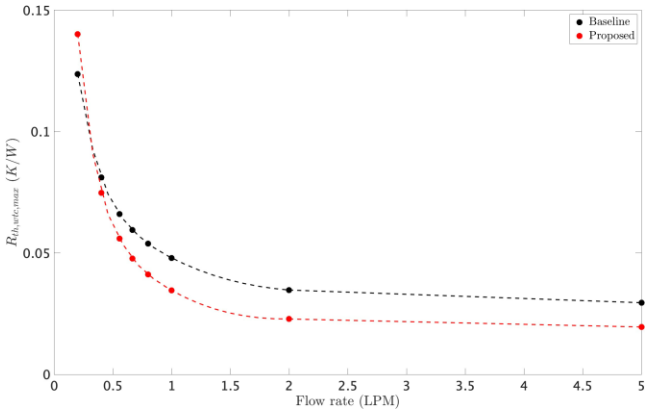


**Figure 175:** Analytically estimated winding-to-coolant thermal resistance associated with winding hotspot $R_{th,wtc,max}$ with respect to flow rate, for both HX designs.

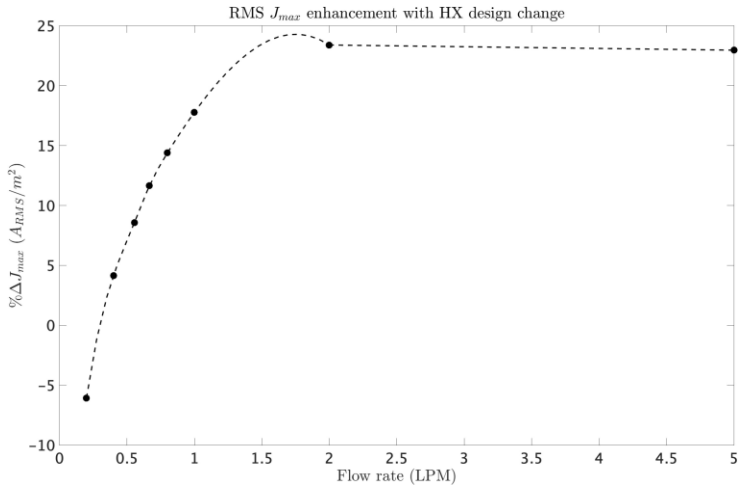


**Figure 176:** Figure 4.5: Theoretical enhancement in maximum allowable RMS Jmax with respect toflow rate, resulting from the change in HX design from baseline to proposed.

$\%\Delta J_{max}$ was subsequently plotted against flow rate, as pictured in Figure 176. The trend in $\%\Delta J_{max}$ closely resembled that for the percentage reduction in $R_{th,wtc}$ in Figure 174. At a flow rate ≈ 1.8 lpm, the proposed design allowed for a maximum increase of 24% in allowable current density while maintaining winding temperatures below the Class F insulation limit. Similar to the trend in Figure 174, at flow rates > 2 lpm, the convective performance enhancement with the proposed design diminished, leading to $\%\Delta J_{max}$ approaching ≈ 22%.

This result indicated that for flow rates > 0.4 lpm, the proposed design enabled the motor to be run at a higher winding RMS current density per slot (up to ≈ 24%), and consequently deliver a greater power density, without breaching the practical temperature limits of windings and insulation.

The reduced-order model was developed in the Motor-CAD software environment. First, the motor geometry was configured in the 'Geometry' tab using the 'BPMOR' motor type, with all the critical dimensions being provided by the motor design as viewed in CAD or the FEA model. The radial and axial views of the configured geometry are pictured in Figure 177 and Figure 178, respectively.

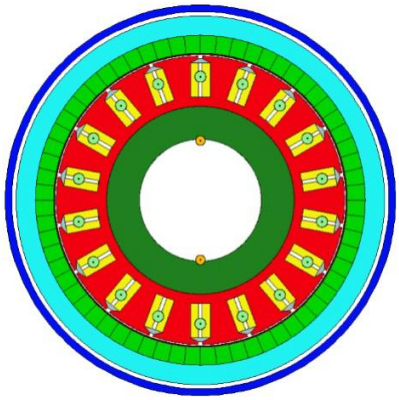

**Figure 177:** Radial view of motor geometry in Motor-CAD.

Next, the in-slot configuration was detailed. In Winding > Pattern, the winding pattern for the motor was configured with lap winding and a left/right path type. Three (3) phases, 8 turns, 2 parallel paths, and 2 winding layers were specified as per the targeted specifications. Subsequently, in Winding > Definition, the winding wire specifications were configured. Additionally, a central vertical divider of width 2.6 mm (consistent with the HX bottom channel) was configured for HX cooling, by choosing Divider Type as 'Solid Divider (Rectangular – Side/Side)'. The resulting in-slot winding configuration is pictured in Figure 179.

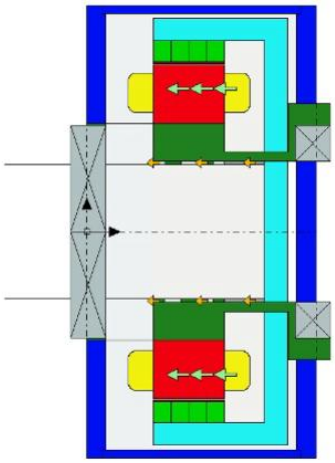

**Figure 178:** Axial view of motor geometry in Motor-CAD.

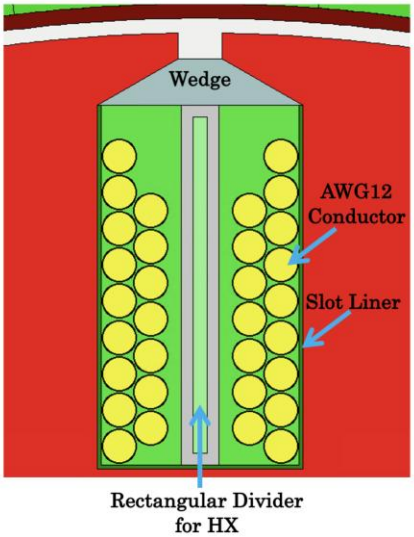


**Figure 179:** In-slot Winding Configuration in Motor-CAD.

Following this, the drive parameters for the chosen "peak torque condition" operating point are configured in the Calculation tab. Peak torque condition was chosen since parallel electromagnetic model results were available for this operating point. The shaft speed was 6667 RPM, and the current (RMS) and voltage were specified as listed in Table 26. The phase advance was 8.61 electrical degrees. The magnetization was a Halbach Sinusoidal array. The box for Torque was selected under 'On Load'. Lastly, the E-Magnetic Losses → Thermal option was chosen under E-Magnetic ↔ Thermal Coupling to transfer the loss distribution from the E-Magnetic model results

to the Thermal model. Upon solving, the steady-state electromagnetic performance insights at the peak torque operating point were viewed in the E-Magnetics, Output Data, and Graphs tabs. Figure 180 shows the contours for magnetic flux density (B[T]) in the stator for the operating point. The contours and the corresponding range of B resulting from this reduced-order model agreed with analogous peak torque contours in Raminosoa et. al. [15], with $B_{max}$ agreeing to within 0.6%. The Motor-CAD peak torque was 166.3 N.m with 1.2% torque ripple, had a reasonably small error of 2% relative to 163 N.m with 1.3% ripple in [13]. The output power, power factor (0.818), and efficiency (96.4%) also demonstrated similarly good alignment. This indicated that the loss distribution results were also reasonably reliable. These results were transferred as a driving input to the Thermal model.

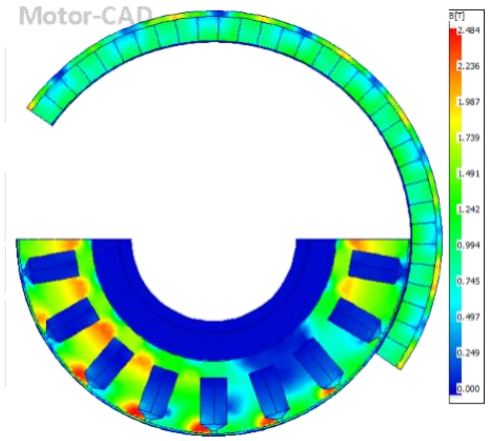


**Figure 180:** Magnetic loading (B[T]) under peak torque condition resulting from Motor-CAD E-Magnetic model.

Upon changing the model type to Thermal, the transferred loss distribution was visible in Input Data > Losses. Table 31 details the loss distribution values.

**Table 31:** Distribution of Motor-CAD Losses for Peak Torque Condition Transferred to Thermal Model

| Motor Loss Type | Motor-CAD Loss ($W$) |
|---|---|
| Armature Copper | 2748 |
| Stator Back Iron | 172.7 |
| Stator Tooth | 519.4 |
| Magnet Eddy Current | 475.5 |
| Rotor Back Iron | 4.774 |

In Input Data > Cooling, HX cooling solution was configured via the 'Slot WaterJacket' option. In the 'Slot Water Jacket' tab, WEG 50/50 was chosen as the fluid with an inlet temperature of 65 °C. The flow rate for the entire motor (18 × the flow rate through 1 HX) was specified based on the flow rate tested, and 18 parallel paths were defined for divided flow through each HX. The 'Flow in Divider' option was selected to specify flow through the rectangular divider. Lastly, under the Heat Transfer specifications, the $h_{eff}$ for the selected flow rate was defined as the convection coefficient, for the chosen HX design. Additionally, air cooling was configured at the innermost

radial layer using the 'Shaft Spiral Groove' option, with a convection coefficient of 10 W/m$^2$K.The thermophysical properties of targeted custom materials were in Input Data > Materials and were assigned to the corresponding motor components. The reduced-order Motor-CAD model does not have full thermal contour-level resolution comparable with FEA, but affords some flexibility provided in Settings > Models, where the stator slot can be discretized into1-9 axial slices. Three (3) axial slices were chosen for our model. Subsequently, the steady-state thermal model was solved in the Calculation tab, and the results were viewed in the Temperatures and Output Data tabs.

Upon solving the steady-state thermal model, the Temperatures and Output Data tabs instantaneously displayed thermal results. The thermal distributions for the motor in radial and axial views are pictured in Figure 181 and Figure 182 respectively for HX cooling with 0.555 lpm flow rate. The Output Data tab listed the temperatures of various motor components. Since this was a low-resolution model, most components (e.g., magnets) were treated as point nodes in the inbuilt thermal network with a singular characteristic temperature. However, in-slot winding and end-winding temperatures were discretized into the specified axial slices (as seen in Figure 182). Hence, the model estimated maximum, average, and minimum winding/end-winding temperatures.


**Figure 181:** Radial thermal distribution result for HX with 0.555 lpm flow rate in AnsysMotor-CAD.

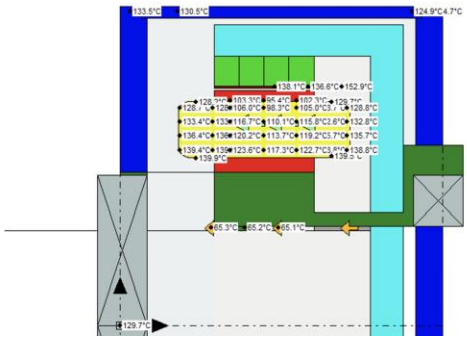

**Figure 182:** Axial thermal distribution result for HX with 0.555 lpm flow rate in Ansys Motor-CAD.

For our analysis, we focused on winding and end-winding temperatures for both HX designs across all HX coolant flow rates. These are shown in Figure 183 for the windings and Figure 184 for the end windings, respectively. The circular markers denote average temperatures, while the tops of the error bar denote maximum temperatures. The proposed design led to lower winding and end-winding temperatures than the baseline design, with the maximum hotspot temperature reduction occurring at 0.4 lpm, where winding hotspot temperatures reduced by 5.17 °C and end-winding hotspot temperatures reduced by 5.15 °C. Following the results, at larger flow rates, the relative performance enhancement of the proposed HX design due to convection diminished, and the black (baseline) and red curves (proposed) moved closer to each other.

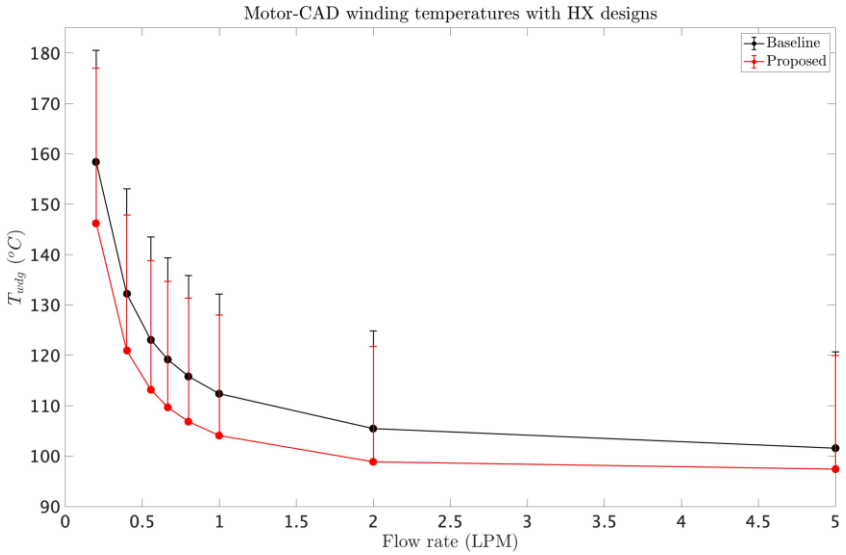


**Figure 183:** Winding temperatures with respect to flow rate for both HX designs as evalu-ated by the Motor-CAD model.

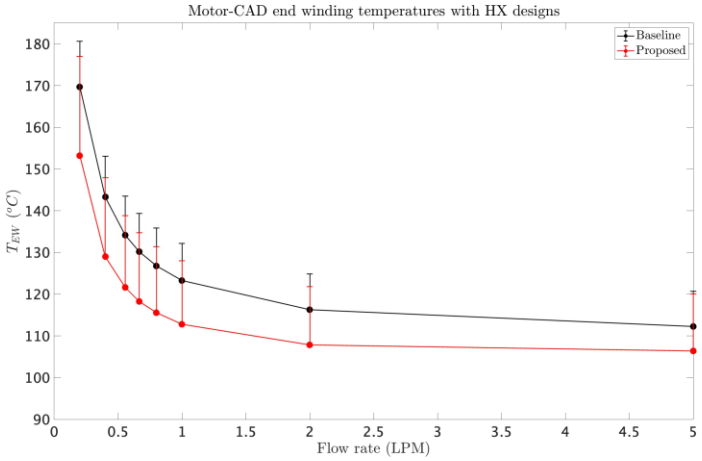


**Figure 184:** End-winding temperatures with respect to flow rate for both HX designs asevaluated by the Motor-CAD model.

Parallel to the Motor-CAD model, a highly accurate, to scale numerical FEA model was set up for a half-slot radial slice (10°) of the motor. The heat loads for the FEA mode in Ansys Mechanical are set up as internal volumetric heat generation values in the heat-generating components [W/m$^3$].

In order to compare thermal distributions for the same operating point across both models, the loss distribution generated for the peak torque operating point in Motor-CAD was converted to volumetric generation values. The values were subsequently adjusted by the mass factor, which was the ratio of the heat-generating component's mass in the FEA model to the component's mass as configured in the Motor-CAD model. Since the Motor-CAD geometry was based on a pre-defined 'BPMOR' template, the shape, dimensions (and thus, mass) of heat-generating components such as the stator and windings were not exactly configured as with the FEA model (which leveraged the accurate CAD design of the motor). Hence, the mass factor was applied to adjust for the differing disparities in the component thermal capacities and thus mitigate errors in the resulting temperature distributions across the two models. Table 32 details show the internal heat generation values computed for the FEA model.

**Table 32:** Conversion of Motor-CAD Losses for Peak Torque Condition to Mass-Adjusted Heat Generation Values for FEA Model

| Loss Type | M-C Loss ($W$) | FEA Vol. ($m^3$) | FEA Gen. ($W/m^3$) | $\frac{m_{FEA}}{m_{MC}}$ | Adjusted FEA Gen. ($W/m^3$) |
|---|---|---|---|---|---|
| Armature Copper | 2748 | $4.125 \times 10^{-4}$ | $6.663 \times 10^{6}$ | 0.466 | $3.102 \times 10^{6}$ |
| Stator Back Iron | 172.7 | $2.005 \times 10^{-4}$ | $8.611 \times 10^{5}$ | 0.630 | $5.421 \times 10^{5}$ |
| Stator Tooth | 519.4 | $3.249 \times 10^{-4}$ | $1.599 \times 10^{6}$ | 1.333 | $2.132 \times 10^{6}$ |
| Magnet Eddy | 475.5 | $3.610 \times 10^{-4}$ | $1.317 \times 10^{6}$ | 1.126 | $1.483 \times 10^{6}$ |
| Rotor Back Iron | 4.774 | $9.631 \times 10^{-5}$ | 49571 | 5.087 | $2.522 \times 10^{5}$ |

HX cooling was applied by selecting the inner walls of the HX, and specifying the $h_{eff}$ corresponding to the flow rate being tested as a heat transfer boundary condition. The FEA model was subsequently solved to generate steady-state results.

The results of the high-resolution FEA simulations for the two HX designs were obtained as smooth thermal contours for the motor components. The winding thermal contours for both HX designs were isolated to analyze trends with HX coolant flow rate, and are pictured for the critical flow rate of 0.555 lpm in Figure 185. In the proposed design, the maximum temperature is reduced by 5.91 °C in the in-slot windings and 5.82 °C in the end windings, while the corresponding average temperature is reduced by 6.02 °C and 6.61 °C, respectively.

Similar to Figure 183 - Figure 184, the maximum and average winding and end winding temperatures are shown in Figure 186 and Figure 187, respectively. Once again, the circular markers denote average temperatures, while the tops of the error bars denote maximum temperatures. The proposed design consistently led to reduced winding and end-winding temperatures across all flow rates. As seen with the analyses, the convective performance enhancement of the proposed HX design diminished at large flow rates as the thermal convection resistances reduced to asymptotically low values in both designs, leaving only the constant enhancement from conductive thermal resistance reduction with the proposed design.

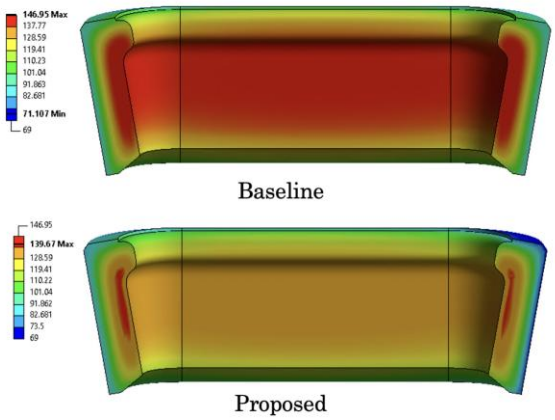


**Figure 185:** Thermal contours in windings for baseline (top) and proposed (bottom) HX designs with 0.555 lpm flow rate in Ansys Mechanical FEA model of motor half-slot.

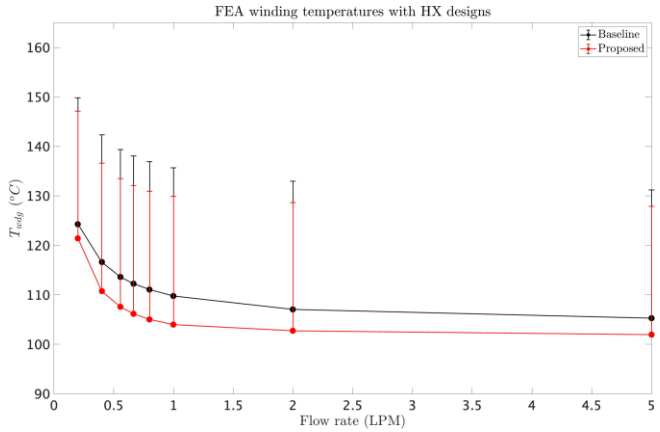


**Figure 186:** Winding temperatures with respect to flow rate for both HX designs as evalu-ated by the FEA model.

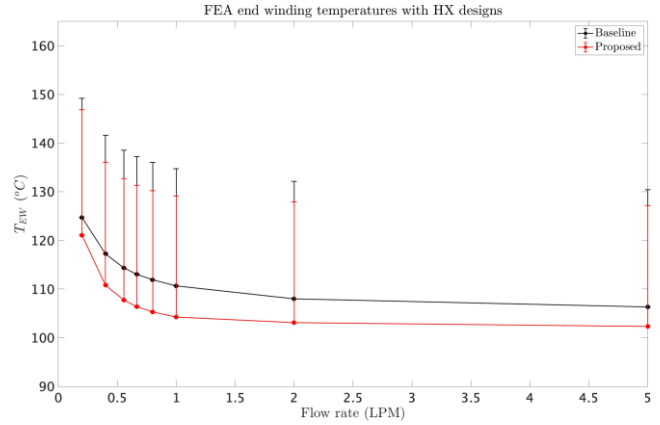


**Figure 187:** End-winding temperatures with respect to flow rate for both HX designs asevaluated by the FEA model.

We desired to evaluate the effectiveness and accuracy of the Motor-CAD model for the HX cooling solution, relative to the full numerical FEA model. Figure 188 and Figure 189 plot the reduction in maximum winding and end-winding temperatures, respectively, with the HX design change, as

found by the FEA and Motor-CAD models. Both figures showed general trends with flow rate that support the analytical calculations. The maximum temperature decrease with the design change was observed in the intermediate flow rate regime of 0.2 lpm-2 lpm for both models. The thermal performance gains were reduced at higher flow rates beyond 2 lpm, as the marginal benefits from reducing convection thermal resistance were negligible. Despite the similar trends across models, there were significant errors in the Motor-CAD thermal model results relative to the FEA model. A mixture of geometric and software limitations contributed to these errors in the Motor-CAD model. The Motor-CAD

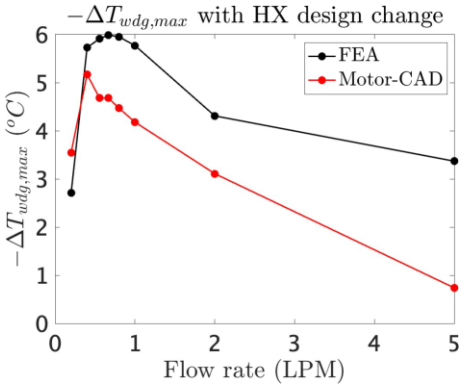


**Figure 188:** Reduction in winding temperature maximum caused by the HX design change,as evaluated by both the FEA and Motor-CAD models.

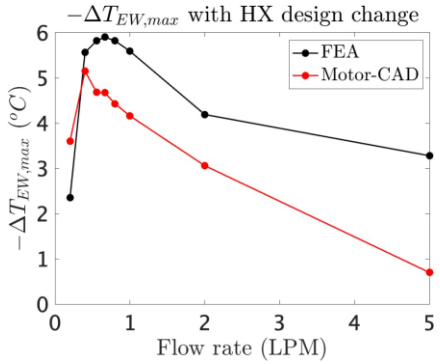


**Figure 189:** Reduction in end-winding temperature maximum caused by the HX design change, as evaluated by both the FEA and Motor-CAD models.

The thermal model package cannot compute custom geometries (unlike the E-Magnetic package), so the geometry used for thermal calculations was inexact. There were crucial inaccuracies in the estimated slot shape and winding type (since circular Litz wire was unavailable), leading to errors in accurately quantifying the winding-to-coolant thermal network. Additionally, certain custom design aspects of the motor were missing in the Motor-CAD template, such as a full-axial-length rotor extension and potting compound in the end-winding cavity. This led to further inaccuracies in the inbuilt thermal network in the Motor-CAD model. The geometric limitations also led to further mass discrepancies in the motor that were not completely accounted for by the mass factor

adjustment. The full motor in the Motor-CAD model had a total mass of 19.34 kg, which had a 48% error from the 37.10 kg mass for the accurate CAD-based motor geometry in the FEA model. Hence, the mass factors in Table 32 only partially bridged the bulk thermal capacity disparities between the models. Specifically, discrepancies in mass (and thus, thermal capacity) for the non-heat-generating components across the two models were neglected. This created differences in the whole motor's 'bulk' thermal capacity across models, and led to differing thermal distributions across all components. For example, the FEA motor geometry likely had a greater bulk thermal capacity, causing lower temperature sensitivity to thermal performance of the cooling solution. This was evidenced by the lower FEA winding and end-winding temperatures relative to Motor-CAD at low flow rates of 0.2-0.4 lpm.

## REFERENCES


[1] A. Kara-Slimane, D. Juve, E. Leblond, and D. Treheux, "Joining of AlN with metals and alloys," *Journal of the European Ceramic Society,* vol. 20, no. 11, pp. 1829-1836, 2000.

[2] P. D. File, "Joint committee on powder diffraction standards," *ASTM, Philadelphia, Pa,* pp. 9-185, 1967.

[3] A. Sheng *et al.*, "Ultrahigh temperature copper-ceramic flexible hybrid electronics," *Nano Letters,* vol. 21, no. 21, pp. 9279-9284, 2021.

[4] S. Khuje *et al.*, "High-Temperature Oxidation-Resistant Printed Copper Conductors," *Advanced Electronic Materials,* vol. 9, no. 3, p. 2200979, 2023.

[5] E. N. Schmierer and A. Razani, "Self-consistent open-celled metal foam model for thermal applications," 2006.

[6] A. Inayat, H. Freund, T. Zeiser, and W. Schwieger, "Determining the specific surface area of ceramic foams: The tetrakaidecahedra model revisited," *Chemical Engineering Science,* vol. 66, no. 6, pp. 1179-1188, 2011.

[7] X. Feng, G. Moreno, and K. Bennion, "Thermal Performance Benchmarking," National Renewable Energy Lab.(NREL), Golden, CO (United States), 2016.

[8] A. Ferrari, M. Magnini, and J. R. Thome, "Numerical analysis of slug flow boiling in square microchannels," *International Journal of Heat and Mass Transfer,* vol. 123, pp. 928-944, 2018.

[9] K. K. Wong and K. C. Leong, "Nucleate flow boiling enhancement on engineered three-dimensional porous metallic structures in FC-72," *Applied Thermal Engineering,* vol. 159, p. 113846, 2019.

[10] D. W. Kim, A. Bar-Cohen, and B. Han, "Forced convection and flow boiling of a dielectric liquid in a foam-filled channel," in *2008 11th Intersociety Conference on Thermal and Thermomechanical Phenomena in Electronic Systems*, 2008: IEEE, pp. 86-94.

[11] O. Al-Ketan, M. Ali, M. Khalil, R. Rowshan, K. Khan, and R. Abu Al-Rub, "Forced convection CFD analysis of architected and 3D printable heat sinks based on triply periodic minimal surfaces," *Journal of Thermal Science and Engineering Applications,* pp. 1-33, 2020.

[12] D. Deng, L. Chen, X. Chen, and G. Pi, "Heat transfer and pressure drop of a periodic expanded-constrained microchannels heat sink," *International Journal of Heat and Mass Transfer,* vol. 140, pp. 678-690, 2019.

[13] G. Moreno, "Thermal performance benchmarking: Annual report," National Renewable Energy Lab.(NREL), Golden, CO (United States), 2016.

[14] P. Srinivasan, S. Nandapurkar, and F. Holland, "Friction factors for coils," *Transactions of the Institution of Chemical Engineers and the Chemical Engineer,* vol. 48, no. 4-6, pp. T156-+, 1970.
[15] T. Raminosoa, R. Wiles, J. E. Cousineau, K. Bennion, and J. Wilkins, "A high-speed high-power-density non-heavy rare-earth permanent magnet traction motor," in *2020 IEEE Energy Conversion Congress and Exposition (ECCE)*, 2020: IEEE, pp. 61-67.

## List of Figures

## List of Tables